Cape Peninsula
University of Technology

AN IMPROVED PLASMA ENERGY CONVERSION SYSTEM FOR ELECTRIC POWER GENERATION

by

AYOKUNLE OLUWASEUN AYELESO

Thesis submitted in fulfilment of the requirements for the degree

Doctor of Engineering: Electrical Engineering

in the Faculty of Engineering

at the Cape Peninsula University of Technology

Supervisor: Prof. M.T.E Kahn

Bellville

June 2018

DECLARATION

I, Ayokunle Oluwaseun Ayeleso, declare that the contents of this dissertation/thesis represent my own unaided work, and that the dissertation/thesis has not previously been submitted for academic examination towards any qualification. Furthermore, it represents my own opinions and not necessarily those of the Cape Peninsula University of Technology (CPUT).

Signed **Date**

ABSTRACT

The generation of electricity through the conventional conversion system such as thermal and hydroelectric plants may no longer be sufficient to meet the increasing demands and usage. One of the major reasons for shortage supply of electric power is due to the lack of fossil fuel and other conventional resources that are currently being used in Africa. In addition, the conversion process of the conventional system often causes pollution which contributes to global warming. Therefore, there is a need for this research to develop novel and alternative methods of generating electric power. Among these methods is the Magnetohydrodynamics (MHD) conversion system, which is a direct energy conversion system. In this system, plasma or ionised gas is directly converted into electric power with generating efficiency of about 62 %. The conversion process of the MHD system is based on the principle of Faraday's Law of electromagnetism and fluid dynamics. The focus of the present study is to investigate alternative methods through which an MHD power generator can be coupled to the existing thermal plants in South Africa. In doing so, the thermal cycle efficiency of these conventional plants can be improved. Another goal of this study is to investigate the behaviour of an MHD generator prototype under exposure to plasma through simulation and experimentation in a laboratory setting.

The optimum power obtained when coupling MHD topping units to the South Africa Ankerlig and Gourikwa power plants (combined-cycle MHD gas-steam turbine, CCMGST) showed that the thermal cycle efficiency of these stations has improved. Moreover, at both CCMGST stations, large loss of energy is minimised, and the supplementary power generated could be used by commercial and industrial users. Similarly, from the simulation of the viscous flow of an ionised propane fluid inside a rectangular duct, in which the duct is configured to act as generator (MHD mode) and accelerator (Magnetoplasmadynamic, MPD, mode), the results showed that when the intensities of the applied magnetic fields are increased, the Lorentz forces are increased. This ultimately slowed down the field vectors of the fluid to lower values at the center of the duct. The selected remanent flux densities which are used to decelerate the motion of the field vectors are 1.12 T, 1.32 T and 1.41 T. Additionally, when electrical potentials are imposed to the duct electrode walls, the interaction between the magnetic fields and the fluid produce optimum magnitude of the flow velocity. The magnetic flux density results obtained in the simulation serve as a guide towards the selected magnet remanent flux density value used in the experiments.

From the simulation results of the inductively coupled plasma torch, the temperature and velocity magnitude of plasma at the torch outlet are 9000 K and 6 m/s, respectively. Similarly, from the simulation results of the DC arc plasma torches observed from literature, the temperature of plasma at the torches outlet ranged from 7900 K to 30000 K while the velocity magnitude of plasma exiting the outlet of these torches ranged from 317 m/s to 3000 m/s. Subsequently, the above plasma temperatures and velocities together with 1 Ω, 100 Ω and 470 Ω external load resistors are modelled theoretically to the MHD generator and the optimum power is obtained when 1 Ω load resistor is placed across the generator electrodes.

A rectangular MHD generator with round electrodes were constructed and configured in segmented and continuous electrode modes for the realisation of this project. The round segmented electrodes were used in order to minimise experimental uncertainty that could arise from complex designs and structures. The aim is to characterise the generator electric response to typical plasma from a DC arc source located at the Department of Electrical, Electronic and Computer Engineering, Cape Peninsula University of Technology, Cape Town (South Africa).

The DC arc plasma measurements were performed under steady state conditions. Due to the nature of the physical processes of the arcing, the measurements encountered challenges in terms of noise present in the laboratory. To reduce these high noise levels, the measurement circuit through a differential terminal configuration within the NI USB-6002 DAQ device was used to capture the voltage difference across the electrodes. Subsequently, the study looked at both time and frequency domain analyses as avenues to mitigate the effect of noise on the measurements. In all experiments, the absolute time-average of each measured terminal voltage across 1 Ω, 100 Ω and 470 Ω load resistors was obtained.

The frequency content of the measured terminal voltages was also observed through performing a Fast Fourier Transform (FFT) on the time signals. This analysis was done to determine the frequencies involved in the voltage signals. The frequency patterns of the absolute of the measured terminal voltages showed consistency after performing the post-processing with FFT. Significant harmonics were observed at frequencies between 0 Hz and 700 Hz.

Comparing the result obtained in the experiments, the actual terminal voltages measured from the continuous electrodes and the middle-segmented electrodes were similar. In all the experiments conducted, the maximum power (0.203 mW) was obtained when 1 Ω resistor was connected to the middle-segmented electrodes. From the outcome of these results, it can be deduced that in both numerical and experimental studies the optimum power is produced when 1 Ω resistor is used. Conclusively, these results validate the measurement approach and operation of MHD generator with segmented electrodes and could be used to design a large MHD unit that can be incorporated to the conventional thermal plants.

ACKNOWLEDGEMENTS

I wish to thank:

- The Almighty God, for giving me the grace to reach this far.
- My supervisor, Professor M.T.E Kahn for his supervision, guidance, contribution and encouragement throughout the thesis write up.
- The Cape Peninsula University of Technology for providing the funding for purchasing the equipment used during the experiments. Without them the project will not have been completed.
- The Department of Electrical Electronics & Computer Engineering for providing some of the equipment and the test facilities used for this project.
- The Council for Scientific and Industrial Research (CSIR) for sponsoring my studies at the Cape Peninsula University of Technology.
- The Center for Postgraduate Studies (CPGS) at the Cape Peninsula University of Technology for their support.
- My colleagues in the Department of Electrical Engineering, Cape Peninsula University of Technology, Bellville campus for the support, the guidance and the encouragement I received from them.
- My wife, Mrs Alinde Berenice Ayeleso, for her support and encouragement during the time of my studies. Her lovely advice and moral support have helped me to the conclusion of the project.
- Mr Akim Aminou for his contribution and support towards my studies.
- Mr Abegunde Akinola for his support and contribution towards my studies.

The financial assistance of the Council for Scientific and Industrial Research (CSIR) and the Center for Postgraduate Studies (CPGS) towards this research are acknowledged. Opinions expressed in this thesis and the conclusions arrived at, are those of the author, and not necessarily to be attributed to the Council for Scientific and Industrial Research (CSIR).

DEDICATION

This research is dedicated to:

The almighty God

My lovely wife
Mrs Alinde Berenice Ayeleso

My parent's
Chief & Mrs P.B. AYELESO

RESEARCH OUTPUTS

Published Articles:

1) Journal name: Journal of King Saud University – Science
   Title: Modelling of a combustible ionised gas in thermal power plants using MHD conversion system in South Africa.

2) Journal name: Journal of Energy Technology Research
   Title: Modelling of an MHD system to investigate an ionised gas flow inside a rectangular duct.

3) Journal name: Transylvanian Review
   Title: Theoretical Modelling of an MHD Generator with External Loads Coupled to a Thermal Power Plant.

4) Journal name: Acta Polytechnica: Journal of Advanced Engineering
   Title: Experimental Characterization of a Magnetohydrodynamic Power Generator under Dc Arc Plasma

5) Journal name: IEEE Conference proceeding publication
   Title: Computational fluid domain simulation of MHD flow of an ionized gas inside a rectangular duct.

6) Journal name: IEEE Conference proceeding publication
   Title: Plasma Energy Conversion System for Electric Power Generation.

Conference proceedings:

7) Conference name: Proceedings of ISER International Conference
   Title: Characteristics behaviour of a combustible coal volatile gas flow along a rectangular duct for power generation.

TABLE OF CONTENTS

LIST OF FIGURES

LIST OF TABLES

GLOSSARY

Symbols	Definition/Explanation
A	Electrode surface area
A_m	Magnetic vector potential
B	Magnetic field
B_r	Constant
C_p	Specific heat capacity
D_e	Electrical flux density
D_h	Hydraulic diameter
e	Electric charge
E	Electrical field strength
E_e	Electron energy
E	Electric field
E_m	Electric field intensity
EMF	Electromagnetic force
E_{kav}	Average kinetic energy of electrons
$E_{K\ electrons}$	Electron kinetic energy
E_{tr}	Energy transfer
F	Lorentz force
$\mathrm{F}(v)$	Maxwellian electron velocity distribution function
H	Magnetic field strength
H_a	Hartmann's number
l	Distance between the electrodes
I_{mhd}	Current
J	Total current density
k	Turbulence kinetic energy
K_B	Boltzmann's constant
k_t	Thermal conductivity

m_e	Electron mass
m_i	Ion mass
m_h	Mass of the heavy particles
m_{in}	Mass of particles which losing energy
N	Interaction parameters
n_e	Electron density
n_i	Ion density
$N_{electrons}$	Number of electrons
N_p	Number of particles
ρ	Fluid density
P	Gas pressure
P_{max}	Maximum power
P_{out}	Output power
q	Heat flow
Q	Heat flow rate,
r	Electric resistivity.
R	External Load resistor
R_e	Reynolds number
R_{em}	Magnetic Reynolds number
t	Time
T	Temperature
T_d	The dissociation temperature
T_e	Electron temperature
$\boldsymbol{T_g}$	Gas temperature
T_i	Ion temperature
T_{ion}	Ionisation temperature
$\boldsymbol{T_p}$	Plasma temperature
T_r	Radiation temperature

v	Plasma or particle velocity
V_{actual}	Actual voltage
V	Output voltage
w	Angular frequency
ω_p	Plasma frequency
σ	Electrical conductivity
λ_D	Debye length
λ_e	Collision mean free paths
N_P	Debye number
ε	Dissipation rate
ε_o	Permittivity of free space
ε_r	Medium relative permittivity
δ_{H_a}	Thickness of the viscous limit layer
μ	Dynamic viscosity
μ_o	Magnetic permeability,
μ_r	Relative permeability
μ_T	Turbulent viscosity
φ	Electrical potential
η	Conversion efficiency
k	Electrical load factor

GLOSSARY

Terms/Abbreviation	Definition/Explanation
AC	Alternating current
B	Remanent flux density
C	Copper coil
cat	Carrier tube
CCGST	Combined-cycle gas-steam turbines
CD	Computational domain
CDPES	Centre for Distributed Power and Electronics System
cet	Central tube
CCMGST	Combined-cycle MHD gas-steam turbine
CME	Coronal mass ejection
CPUT	Cape Peninsula University of Technology
CTE	Complete thermodynamics equilibrium
DAQ	Data acquisition device
DOFs	Degrees of freedom
DC	Direct current
DPP	Discharge produced plasma
ECR	Electron cyclotron resonance
EUV	Extreme Ultraviolet
FDP	Flame discharge plasma
GDP	Gas discharge plasma
GT	Gas turbine
HF	High Frequency
HRSG	Heat recovery steam generator
HW	Helicon wave
ICP	Inductively coupled plasma
LEO	Low Earth Orbit
LPP	Laser produced plasma

LTE	Local thermal equilibrium
MHD	Magnetohydrodynamics
MIP	Microwave induced plasma
MPD	Magnetoplasmadynamics
NI	National Instrument
NM	Neodymium magnets
non-LTE	Non-local thermal equilibrium
OCGT	Open-cycle gas turbines
PSI	Pound-force per square inch
RFI	Radio frequency inductive
RIE	Reactive ion etcher
UVA	Ultraviolet A
UVB	Ultraviolet B
UVC	Ultraviolet C
VARB	Van Allen Radiation Belt
Vcags	Velocity of the carrier gas
Vcegs	Velocity of the central gas
Vsgs	Velocity of the sheath gas
VUV	Vacuum ultraviolet
SAMA	South Atlantic Magnetic Anomaly
st	Sheath tube

CHAPTER ONE: GENERAL INTRODUCTION

1.1 Introduction

Power consumption is becoming one of the major challenges affecting many industrial and commercial users. Therefore, there is a need for more research in order to discover new technologies which can be used for converting different forms of energy into electric power. The Centre for Distributed Power and Electronics System (CDPES) at the Cape Peninsula University of Technology (CPUT) is actively involved in the development of energy technologies in South Africa. These technologies include renewable energy, distributed system and energy usage.

The aim of the CDPES is in line with the focus of the South African Government to promote efficient use of energy and to develop quality energy research. Another aim of the CDPES is to develop power converters for renewable energy sources and investigate inter-connectivity of distributed resources with microgrids and electric power systems. The students, staff at CDPES are currently investigating different energy conversion technologies for electric power generation. The focus of the present study is to develop an alternative method that could be used for converting plasma energy into electric power.

1.2 Research background and awareness of the problem

The lack of fossil fuel and other conventional resources that are currently being used for power generation in Africa are not sufficient for industrial applications and usage (Ajith & Jinshah, 2013:1; Anumaka, 2014:1072; Masood *et al*., 2014:1356-1357). This shortage of electricity supply has led to the use of load shedding schedules to regulate power consumption in many countries around the world, including South Africa. However, this approach has negative impacts on the national economy and has caused damages to basic systems and equipment's.

One of the major reasons for the shortage supply of electricity in Africa is due to the fact that most facilities still use fossil fuel and other resources with conventional systems such as thermal, hydro and nuclear to generate electricity. In these systems, the potential energy of primary sources such as fuel, coal, natural gas and liquefied petroleum gas are first converted into mechanical energy before being converted into electrical energy with considerably low output efficiency of about 40 to 45 %. In addition, the generation and maintenance of electric power through the conventional system require huge capital cost and usually raise several environmental concerns such as pollution. As a result, there is a need to discover new methods in which electricity can be produced efficiently in Africa.

One of these methods is the use of direct energy conversion system such as the Magnetohydrodynamics, MHD, system (Ajith & Jinshah, 2013:1-3; Mayo & Mills, 2002:1). In the MHD conversion system, plasma or other forms of energy can be directly converted into electricity without passing through any mechanical stage (Khan *et al*., 2014:81; Ajith & Jinshah, 2013:1-3).

Considering the steadily increasing demands for electricity in South Africa, there is need for improvement on the efficiency of the existing conventional systems. Therefore, this present research investigates alternative methods through which an MHD power generator can be coupled to the conventional power plants in South Africa. In doing so, the thermal cycle efficiency of these plants can be improved. Another focus of this study is to investigate the behaviour of an MHD power generator prototype when exposed to DC arc plasma, in a laboratory environment, mimicking the actual plasma environment. Figure 1.1 depicts the stages of the direct energy conversion system.

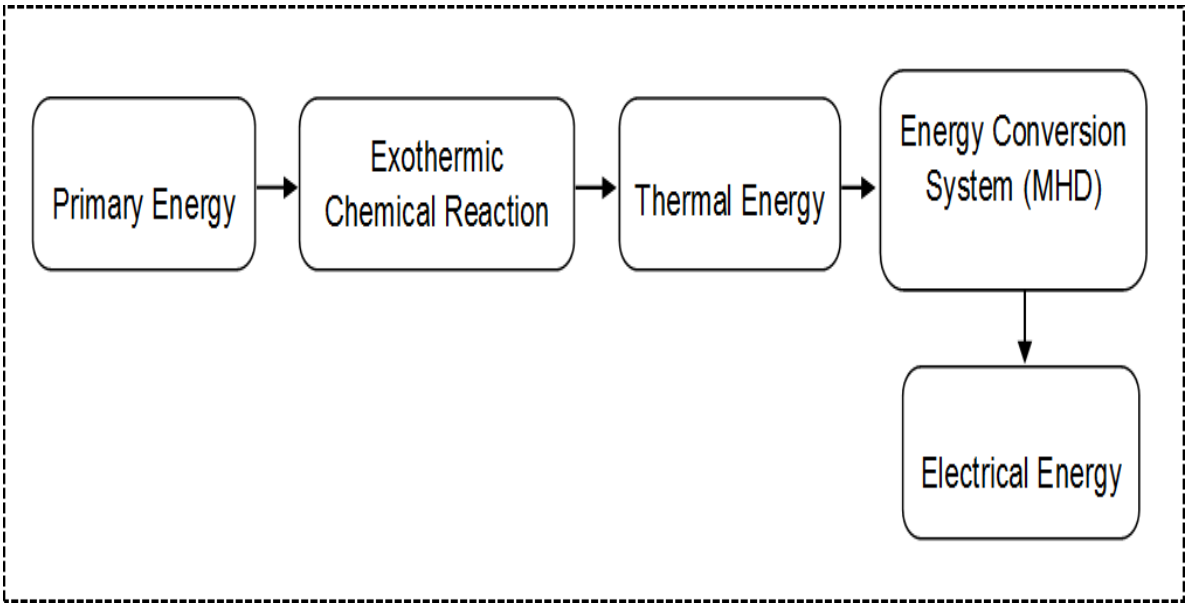

Figure 1.1: The stages of the direct energy conversion system

1.3 Research statement

In recent times, the generation of electric power using hydroelectric and thermal energies is faced with several challenges. Therefore, alternative sources of energy are being sought such as plasma energy. For this purpose, the aim of the present research is to develop an MHD generator that can be used to generate electric power using plasma. This device electric response to a DC arc plasma will be investigated.

1.4 Objectives of the research

In view of the above,

- The possibility of coupling an MHD conversion system to the existing conventional systems will be examined.
- The principle of using the Faraday's Law of electromagnetism and fluid (plasma) dynamics in MHD conversion system will be investigated through numeric computational studies and the development of an MHD power generator prototype.
- The testing of such device will be performed using the available plasma facilities.
- Attention is given to the practical challenges associated with these tests to facilitate further research on plasma conversion system.

1.5 Investigative questions

The investigation questions to guide the research are:

- Which direct energy conversion system can be used to generate electric power using plasma?
- How can this system be implemented in order to improve on the efficiency of the existing conventional system?
- Which high temperature gases and seeded substances can be used to create plasma?
- Which materials can be used to develop the MHD power generator prototype?
- Which plasma facilities are available in the Western Cape region to carry out the research experiment?

1.6 Significance of the research

This research will:

- Contributes to the body of knowledge on plasma energy in relation to electric power generation.
- Results in the development of an MHD conversion system which could be used to produce a reliable electric power.
- Establish possible methods through which the MHD power generator could be used alongside the existing conventional power plants to produce electric power for commercial and industrial applications.
- Lays a foundation for further research on plasma conversion system.

1.7 Research delineation

This research focuses on the conversion of plasma energy into electrical energy, with emphasis on the modelling, development and testing of the MHD power generator prototype. Plasma facilities are limited in the Western Cape region. For this reason, the tests are carried out using the DC arc plasma source located at the Department of Electrical, Electronic & Computer Engineering, CPUT, Cape Town (South Africa).

1.8 Research methodology

The following investigation methods are followed to achieve the objectives of the research.

Literature review: Relevant literature were consulted in order to have a broad understanding of the research field.

Experiment and *evaluation*: The experimental setup is designed to test the functionality of the MHD power generator prototype when exposed to DC arc plasma. This entails subjecting the device to both plasma and magnetic fields and observing its electric current responses.

Critical analysis of findings: The functionality test results are analysed and compared with literature. There is also a critical discussion on the testing laboratories.

1.9 Summary of chapters

- Chapter One gives a general introduction and overview of what the project is about. The research problem, research statement, research objectives, investigative questions, significance and delineation of the research have been discussed.

- Chapter Two reviews the literature supporting the research. The chapter focuses on the theory of plasma and its ability to be applied to various industrial applications. The chapter also reviews the theoretical aspect of a direct energy conversion system with an overview of the different categories of MHD system as well as a short introduction of the MPD system.

- Chapter Three covers the numerical simulations relating to the flow of an ionised gas inside a rectangular MHD duct based on the principle of Faraday's Law of electromagnetism and fluid dynamics. The magnetic flux density results obtained from these simulations serve as a guide towards the selection of the magnet remanent flux density value used in the MHD experiments. During the simulation, the duct is configured to act as generator and accelerator.

- Chapter Four covers the coupling of the MHD power generator to the South Africa Ankerlig and Gourikwa power stations through the use of a convergent-divergent nozzle. The chapter begins by performing a 2-D numerical modelling of a combustible fluid through this nozzle. Thereafter, the fluid velocity obtained at the exit of the nozzle and several MHD parameters (models 1, 2, 3 and 4) coupled to the power stations were modelled theoretically. The chapter concludes by discussing the gross output power obtained from the power plants.

- Chapter Five covers the modelling and simulation of thermal plasma torch. The chapter begins by performing a 2D numerical modelling of an inductively coupled plasma torch. The chapter also summarises several numerical modellings from literature in relation to the DC arc plasma and inductively coupled plasma torches. The plasma temperatures and velocities obtained from these torches are modelled theoretically to the MHD power generator with three external load resistors values. Thereafter, the optimum powers are computed and summarized.

- Chapter Six covers the development of the MHD power generator prototype and the experimental test setup. In this setup, two different generator configurations, namely the continuous and the segmented electrodes are considered. Additionally, the MHD generator prototype connected to three external load resistors values are tested with a DC arc plasma source and the results obtained from the experiments conducted are analysed and discussed. The chapter concludes by comparing the experimental results with literature.

- Chapter Seven concludes the study. It summarises the key findings and also provides recommendations for future research.

CHAPTER TWO: LITERATURE REVIEW

2.1 Introduction

This chapter reviews the literature supporting the research. The chapter focuses on the theory of plasma and direct energy conversion system such as the magnetohydrodynamics (MHD) and the magnetoplasmadynamics (MPD) systems. A theoretical overview of the categories of the MHD conversion system is given.

2.2 Plasma

Plasma is a quasi-neutral gas of charged and neutral particles which displays collective behaviours (Chen, 1984:3; Grill, 1994:3; Weyde, 2006:17; Escobar, 2009:2; Asselin, 2011:19−20). When the temperature of a gas is increased to higher levels, the gas becomes ionised and electrons are separated from the atoms of the gas (Miyamoto, 2000:1; Böhlmark, 2006:5; Rucker, 2008:6). Subsequently, the gas becomes electrically conductive and forms plasma.

Plasma can be found in the Earth and other planetary bodies such as stars and solar systems trapped within their respective magnetic fields (Barth *et al*., 2003:466). Moreover, low temperature plasmas can be used inside the MHD generator to produce electric power if seeded with alkali metals (potassium nitrate, rubidium, caesium, sodium and lithium) (Ajith & Jinshah, 2013:3; Masood *et al*., 2014:1358). These alkali metals are required because of their high electrical conductivity, which make them to ionise easily at lower temperatures. The temperature of plasma species such as electrons, ions and neutrals are always equal in thermal equilibrium state (Grill, 1994:8). Likewise, the electron density and the ion density are always equal in the quasi-neutral state of plasma (Grill, 1994:5; Asselin, 2011:20).

2.3 Plasma parameters

Plasma can be described by parameters such as plasma velocity, v, electron temperature, T_e, ion temperature, T_i, Debye length, λ_D, ion density, n_i, electron density, n_e, and plasma frequency, ω_p. These parameters are discussed in the following sections.

2.3.1 Plasma velocity

The average velocity of plasma particles in thermal equilibrium state depends on temperature, T, as given by equation 2.1 (Grill, 1994:4),

$$v = \sqrt{\frac{K_B T}{m}} \quad , \qquad \textbf{Equation 2.1}$$

where T [K] is the gas temperature, K_B= 1.38 x 10^{-23} [J/K] is Boltzmann's constant and m [kg] is the particle mass.

2.3.2 Energy transfer between electrons and heavy particles

Plasma particles usually cause collisions among themselves when they are in motion. These collisions can be divided into two categories: elastic and inelastic collisions. In the elastic collision, particles such as electrons and heavy particles (neutral atoms, ions, and neutral molecular fragments) collide with each other, and the collision does not result to the excitation of the heavy particles (Grill, 1994:5). In this case, the energy transfer, E_{tr}, is given by equation 2.2 (Grill, 1994:5−7),

$$E_{tr} = \frac{2m_e}{m_h} E_e , \qquad \textbf{Equation 2.2}$$

where E_e [J] is the electron energy, m_h [kg] is the mass of the heavy particles and m_e [kg] is the electron mass.

On the other hand, inelastic collision is collision which occurs between electrons and heavy particles, and the collision result to the excitation, ionisation and dissociation of the heavy particles. In this case, the energy transfer is given by equation 2.3 (Grill, 1994:5−7),

$$E_{tr} = \frac{m_h}{m_{in} + m_h} E , \qquad \textbf{Equation 2.3}$$

where $m_{in} = m_e << m_h$ is the mass of particles losing energy.

Furthermore, in the inelastic collision between electrons and heavy particles, the electrons transfer most of their energy to the heavy particles. Thus, creating energetic plasma species. Heavy particles can also disperse their energy through radiation.

2.3.3 Plasma temperature

Plasma is a mixture of particles, each with different mass, temperature and electric charge (Grill, 1994:7). When a plasma temperature is increased, the mean translational energy of each species within the plasma is increased. Plasma can also be characterised using the specific average temperature of each species which include the ion temperature and the electron temperature (Grill, 1994:7−8).

Furthermore, some heavy particle species such as the excitation temperature, T_{ex}, the dissociation temperature, T_d, the ionisation temperature, T_{ion}, and the radiation temperature, T_r can have several temperatures at the same time. All these temperatures must be equal to one another in order for the plasma to attain a thermal equilibrium state, as given by equation 2.4 (Grill, 1994:8),

$$T_{ex} = T_{ion} = T_d = T_r = T_e \,. \qquad \textbf{Equation 2.4}$$

In thermal equilibrium state, the velocity distribution of plasma particles is Maxwellian. Therefore, the one-dimensional Maxwellian electron velocity distribution function, $\mathrm{F}(v)$, is given by equation 2.5 (Chen, 1984:4; Boulos *et al*., 2013:2),

$$\mathrm{F}(v) = B_r \cdot exp\left(-\frac{\frac{1}{2} m_e v^2}{K_B T_e} \right) . \qquad \textbf{Equation 2.5}$$

The relationship between the constant B_r and the electron density is given by equation 2.6 (Chen, 1984:4; Miyamoto, 2000:7),

$$B_r = n_e \left(\frac{m_e}{2\pi K_B T_e} \right)^{1/2} , \qquad \textbf{Equation 2.6}$$

where,

$$n_e = \int_{-\infty}^{\infty} \mathrm{F}(v) dv \,. \qquad \textbf{Equation 2.7}$$

Figure 2.1 shows a typical Maxwellian electron velocity distribution. The distribution is mostly characterised by the temperature of the electrons (Boulos *et al*., 2013:2).

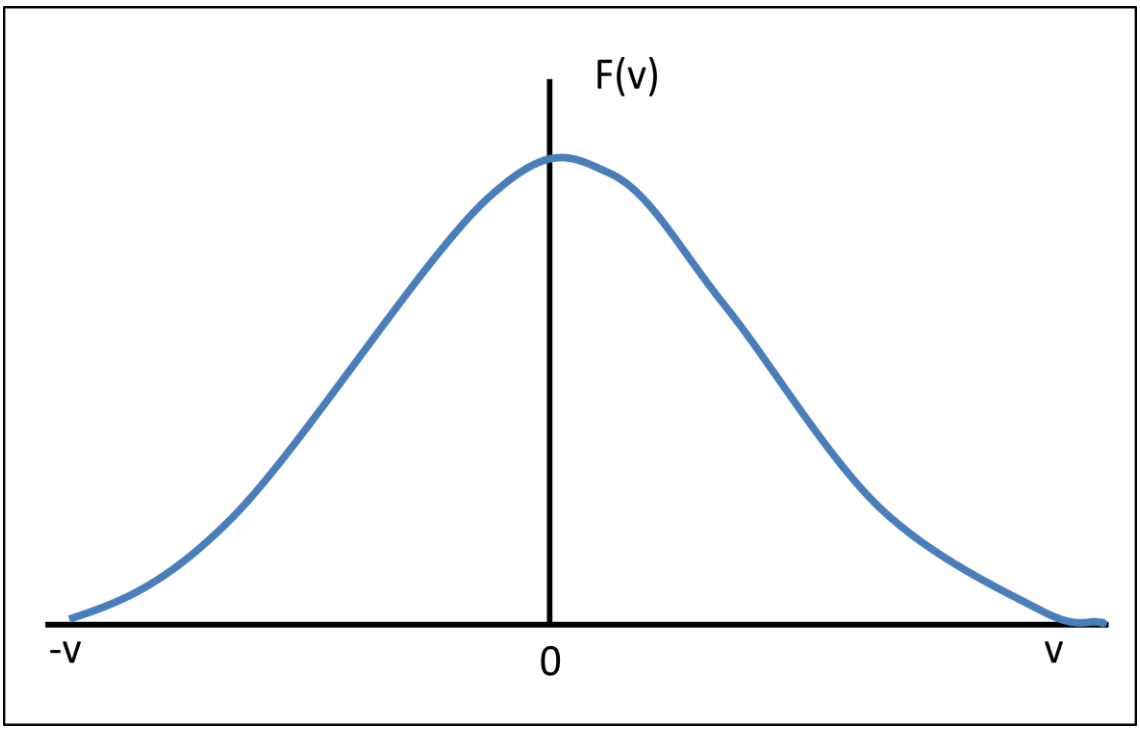

Figure 2.1: Schematic illustration of the Maxwellian electron velocity distribution (Adapted from Chen, 1984:5; Sinclair, 2005:4).

From Figure 2.1, the average kinetic energy of electrons (E_{kav}) in the Maxwellian distribution is given by equation 2.8 (Chen, 1984:5; Sinclair, 2005:4),

$$E_{kav} = \frac{1}{2} K_B T_e \,. \qquad \textbf{Equation 2.8}$$

The average kinetic energy of the electrons in equation 2.8 can be extended to three dimensions, as given by equation 2.9,

$$E_{kav} = \frac{3}{2} K_B T_e \,. \qquad \textbf{Equation 2.9}$$

From equation 2.9, the electron temperature is equivalent to one electron volt (eV) divided by Boltzmann's constant, as given by equation 2.10 (Sinclair, 2005:5),

$$K_B T_e = 1\text{eV} = 1.6 \times 10^{-19} \text{ J}, \qquad \textbf{Equation 2.10}$$

$$T_e = \frac{1 \text{ eV}}{K_B} = 11604 \text{ K}.$$

2.3.4 Debye length

Another parameter which is often used when working on plasma is the Debye length, λ_D. Considering a situation where two oppositely charged electrodes are immersed in the plasma; electrons will drift towards to the positively charged electrode while ions will drift towards the negatively charged electrode. This procedure creates a sheath (clouds of particles) around the electrodes and, hence, prevents an electric field from forming inside the plasma. The Debye length is often used to determine how large the sheath region around the electrodes surface can extend inside the plasma. This phenomenon is called Debye shielding (Sinclair, 2005:2). The thickness of the sheath depends on the electron density and the electron temperature, as given by equation 2.11 (Grill, 1994:12−13; Düsterer, 2002:21),

$$\lambda_D = \sqrt{\frac{\varepsilon_o K_B T_e}{n_e e^2}}\,, \qquad \textbf{Equation 2.11}$$

where *e* is the electron charge.

From equation 2.11, when the electron density increases, the Debye length also decreases because there is more presence of electrons inside every layer of the plasma. Additionally, since the Debye length is inversely proportional to the electron density, more dense plasma would have a smaller Debye length. This shows that the denser the plasma, the more the electrons that can participate in the shielding (Chen, 1984:10). Moreover, if the plasma particles are more energetic, the Debye length will increase, and the screening effect will be felt further away from the electrodes. Thus, the hot plasma (high temperature) will have larger Debye length due to their increased velocities and random movement of electrons. The Debye length is also useful in magnetohydrodynamics system (section 2.5.1) since it defines the characteristics length through which plasma is electrically neutral. It also defines the minimum size a system must have to exhibit plasma behaviour and any plasma that falls below this size can no longer be assumed to have charge neutrality (Chen, 1984:10).

For a Debye shielding to occur, there must be sufficient number of electrons (Debye number, N_P) in a Debye sphere (sphere with radius of Debye length) to effectively shield particles from deviating from neutrality (Grill, 1994:13). The Debye number measures the quality of the plasma and it also shows how many charged particles are participating in the Debye shielding. The larger the particles, the smaller their re-arrangement will be to shield charge and cancelling out electric fields. To determine the Debye number of electrons within plasma, the number density is integrated across the Debye sphere and is given by equation 2.12 (Chen, 1984:11).

$$N_p = n_e \frac{4}{3}\pi\lambda_D{}^3 \quad . \qquad \textbf{Equation 2.12}$$

Substituting the Debye length expression (equation 2.11) into equation 2.12, the Debye number then becomes,

$$N_p = \frac{4\pi}{3} \cdot \frac{\left(\varepsilon_o k_b T_e\right)^{3/2}}{e^3 \left(n_e\right)^{1/2}} . \qquad \textbf{Equation 2.13}$$

From equation 2.13, the Debye number is scaled in such a way that the electron temperature and electron density are inversely proportional to one another. Therefore, when $N_p > 1$, the mean kinetic energy of electrons is greater than their mean electrostatic potential energy. The 4π/3 term is often dropped when considering order of magnitude. Plasma separation using the Debye number can be divided into two categories; diffuse-hot plasma with large Debye number, and dense-cold plasma with low Debye number (moderately fewer particles in a Debye sphere).

A plasma consisting of a large Debye number will generally have collective behaviours with electromagnetic force dominating over collisions while a plasma consisting of a low Debye number will have these collective behaviours sunk out by binary collisions (Chen, 1984:10-11). The solar wind and astrophysical plasmas fall within the low-density plasma. Whereas, for laboratory plasmas, their behaviour is basically different from other types of plasma.

2.3.5 Plasma frequency

When the charge neutrality of a plasma is perturbed, the electrons, because of their small mass, respond faster than the ions to the electric force created. The response of these electrons can be characterised by oscillations and the frequency at which every electron oscillate in the plasma is given by equation 2.14 (Grill, 1994:16; Miyamoto, 2000:8; Düsterer, 2002:21),

$$\omega_p = \left(\frac{n_e e^2}{m_e \varepsilon_o}\right)^{1/2} , \qquad \textbf{Equation 2.14}$$

where ω_p [rad/s] is the frequency of the plasma.

2.4 Types of plasma

Plasma can occur naturally in space or be created under controlled conditions in a laboratory setting for specific applications such as spectrochemistry and power generation (Grill, 1994:20). In the entire universe, plasma (electrified gas) constitutes approximately 99% of matter with chemically reactive species such as electrons, ions, and neutrals (Boulos *et al*., 2013:1-5; Nehra *et al*., 2008:54). An example of a natural occurring plasma is lightening while a fluorescent light is a manmade plasma.

In the laboratory, plasma can be generated using plasma torches and microwave devices with high heat flux commonly used for material processing and waste treatment (Venkatramani *et al.,* 2002:258). Some of the plasma that can be created in a laboratory include direct current (DC) arc plasma, reactive ion etcher (RIE) plasma, flame discharge plasma (FDP), inductively coupled plasma (ICP), electron cyclotron resonance (ECR) plasma, radio frequency inductive (RFI) plasma, helicon wave (HW) plasma and microwave induced plasma (MIP) (Chen, 1995: 2166-2168). These plasmas vary according to their temperatures and number densities (Edson & Cohen, n.d.). Moreover, plasmas are often distinguished according to the level of their temperature: high (50000 K – 10^6 K) and low (≤ 50000 K). The low temperature plasma can be grouped into thermal and non-thermal plasmas.

In the thermal plasma, the gas phase is high enough to ionize other matters (solid & liquid). Electrons, ions and neutrals species produced as a result of this ionization are considered to be in quasi-equilibrium state. The temperature of the thermal plasma species remains the same even when used in activities that required high energy such as hot fusion (Valinčius *et al*., 2012:4-5; Abubakar *et al.,* 2016:63-64). Furthermore, most electrons produced using thermal plasma devices usually transferred their energy to heavy particles (ions and neutrals) during elastic collision, in which resulted to plasma jet (Zhukov & Zasypkin, 2007:3).

In the non-thermal plasma, electrons, ions and neutrals are not in thermodynamic equilibrium because electrons have much higher temperatures than both ions and neutrals, which operate at nearly room temperature. Moreover, the non-thermal plasma species have different temperatures and their velocity distribution does not obey the Maxwellian distribution (Abubakar *et al.,* 2016:64). The non-thermal plasma characteristics include low gas temperature, strong thermodynamic non-equilibrium state, high selectivity and occurrence of reactive chemical species. They can also be used to treat polymers, bio-tissues and any other heat sensitive materials (Nehra *et al*., 2008: 54-55). Figure 2.2 and Table 2.1 depict the flow diagram of different types of plasma and their characteristics.

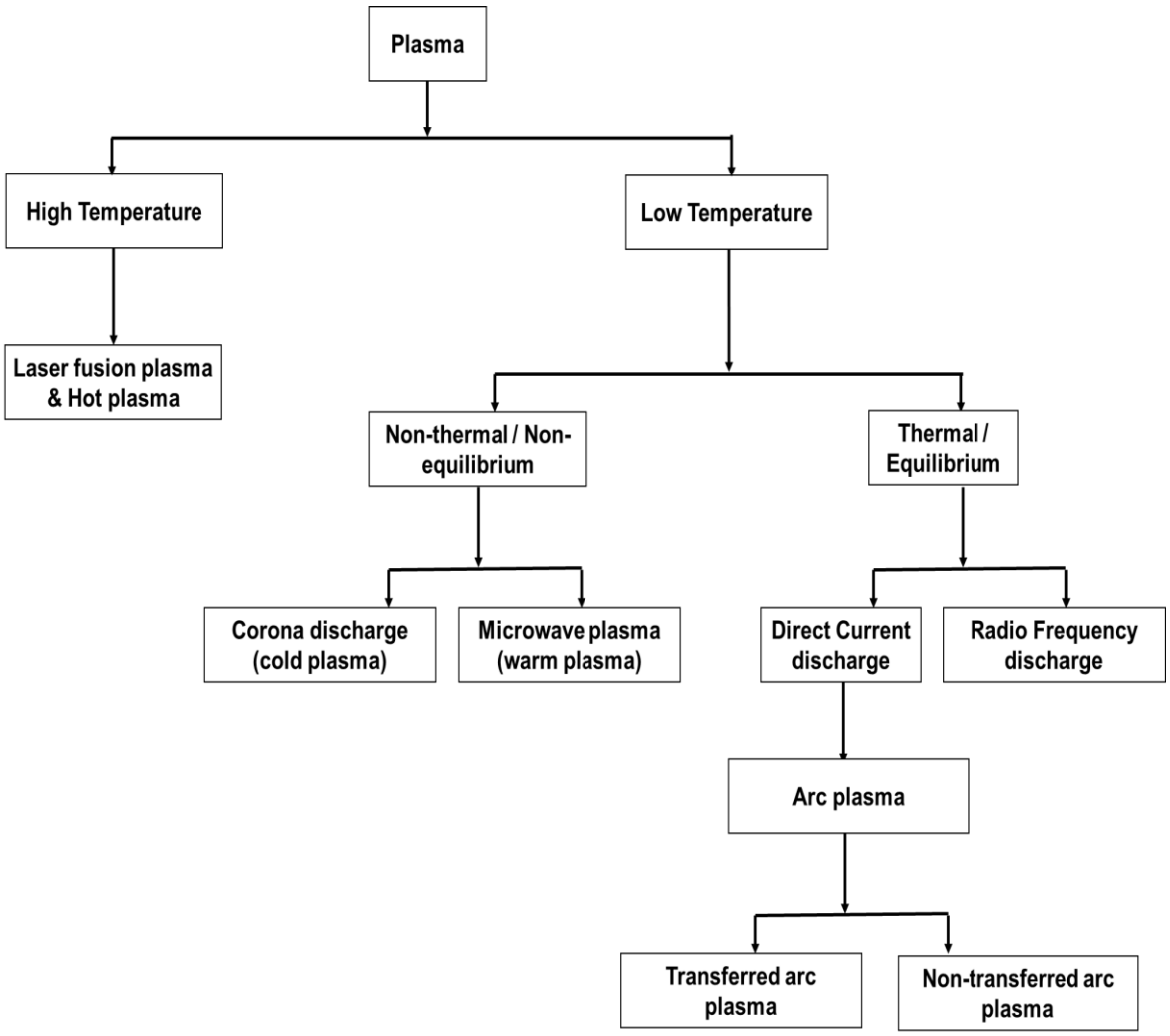

Figure 2.2: Types of plasma
(Adapted from Abubakar *et al.,* 2016:64).

Table 2.1: **Characteristics of different types of plasma (Adapted from Nehra *et al.,* 2008:54-55; Abubakar *et al.,* 2016:64;)**

Properties	**High temperature plasma**	**Low temperature plasma**	
		Thermal plasma	**Non-thermal plasma**
Plasma state	$T_e \approx T_i \approx T_g$	$T_e \approx T_i \approx T_g$	$T_e \approx T_i \approx T_g$
Plasma temperature	$T_p = 10^6 - 10^8$ K	$T_p \leq 2 \times 10^4$ K	$T_p = 300 - 10^3$ K
Electron density	$n_e \geq 10^{20}$ m^{-3}	$n_e \geq 10^{20}$ m^{-3}	$n_e \approx 10^{10}$ m^{-3}
Plasma pressure	Cover a wide range	$\approx$101 kPa	≤ 10 kPa
Examples	Laser fusion plasma	Arc plasma, radio frequency discharge	Glow & corona plasma
Applications	Energy, military	Solid waste treatment, ceramic processing, plasma cutting and welding.	Air pollution control and polymer coatings

Note: T_g = gas temperature, T_p = plasma temperature

From Table 2.1, the high and low temperature plasmas can be converted into a useful electric power for industrial applications. The electric power generated from these plasmas can also be used in vehicles, houses, military, satellites and energy companies. Examples of thermal plasma are gas discharge and gas laser plasmas while non-thermal plasma examples are solar wind, aurora and earth's ionosphere plasmas (Bogaerts *et al.,* 2002:610; Yongcheol & Han, 2010:183; Boulos *et al*., 2013:6). Figure 2.3 depicts the temperature and number density of typical plasmas.

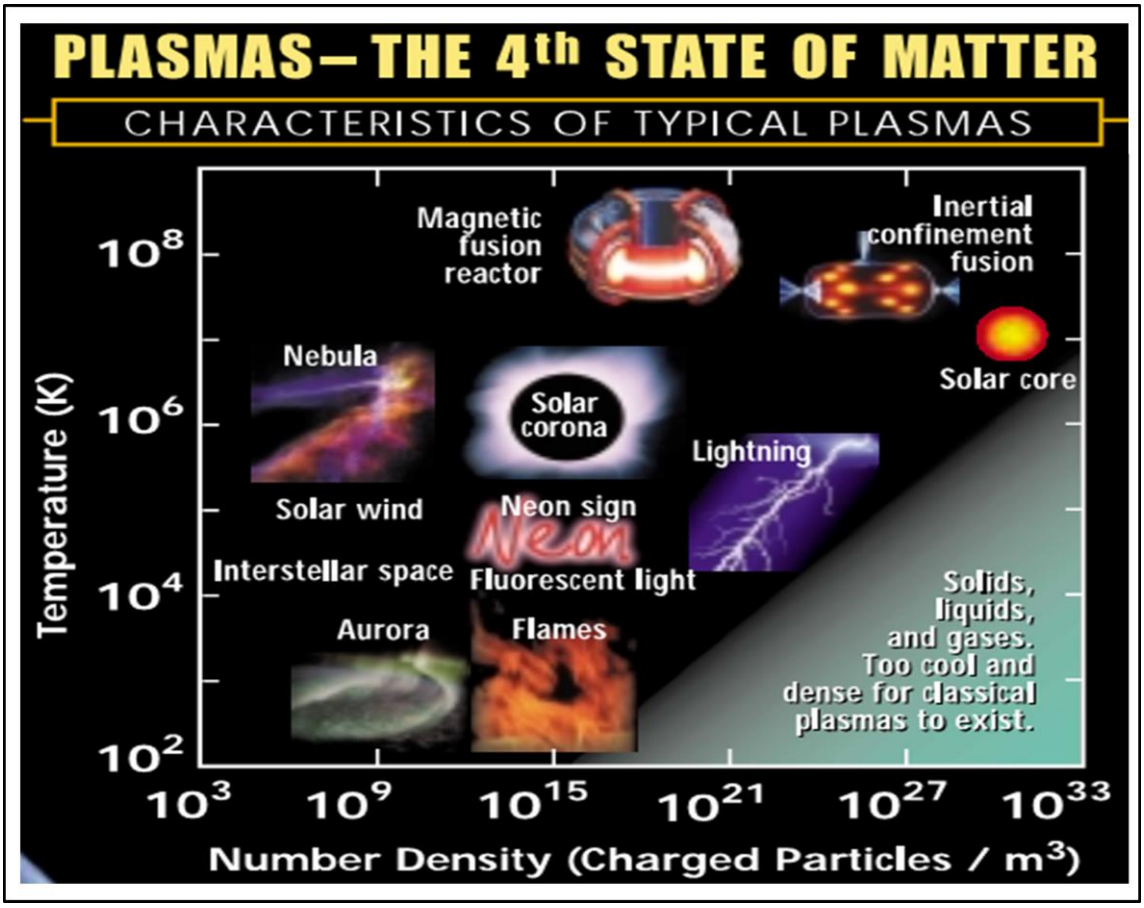

Figure 2.3: The temperature and number density of typical plasmas (From Edson & Cohen, n.d.).

2.4.1 Gas discharge plasma

The gas discharge plasma (GDP) can be obtained from a low temperature gas (≤ 50 000 K) produced by flames, welding arc, cutting arc, mercury rectifier, neon and fluorescent lights, hydrogen thyratrons, ignitions, spark gaps and lightning discharges (Chen, 1984:13; Budtz-Jorgensen, 2001:5; Castell *et al.,* 2004:1734; Callen, 2006:5; Merlino, 2007:1078; Arora *et al.,* 2014:1). These gases are mostly used for Discharge produced plasma (DPP) applications (Ota *et al.,* 2006:4). From Figure 2.2, the GDP is divided into two categories: local thermal equilibrium (LTE) and non-local thermal equilibrium (non-LTE) plasma.

2.4.1.1 Local thermal equilibrium plasma

The LTE plasma can be generated from direct current, radio frequency (RF) and microwave electric discharge sources. All these thermal plasmas have equal temperatures except for radiation temperature (Grill, 1994:20-21; Czapka *et al.,* 2008:1314; Boulos *et al*., 2013:5). The temperature and pressure of the gas molecules used for the generation of thermal plasma are approximately 2 x 10^4 K and 101 kPa, respectively (Budtz-Jorgensen, 2001:6). Moreover, the temperature of plasmas, with low gas ionisation is about 1 eV to 2 eV (Bonizzoni & Vassallo, 2002:327). An example of a thermal plasma is a DC arc discharge device. This type of plasma can be created by passing a direct current through a gas or air (Boulos *et al*., 2013:43; Abubakar *et al.,* 2016:65).

In the present study, air is used as the primary gas inside a DC arc plasma torch device. The advantage of this type of torch is that it uses air which is readily available instead of expensive inert gases such as argon and nitrogen. The arc plasma system begins when an electric arc and pressurized volume of the ionised air are forced through a small hole fitted between the cathode electrode inside the plasma torch head and the anode electrode. This confined, high velocity and temperature arc plasma stream cuts through the metal within a constricted nozzle area and a secondary air is used for the cooling of the torch (Figure 2.4) Valinčius *et al*., 2012:21. Furthermore, the plasma jet that is generated from the DC arc plasma discharge can either be a transferred arc (plasma cutter) or a non-transferred arc (plasma sprayer).

In the transferred arc plasma, the cathode is placed inside the plasma torch while the anode is placed outside the torch, as shown in Figure 2.4 (Abubakar *et al.,* 2016:65).

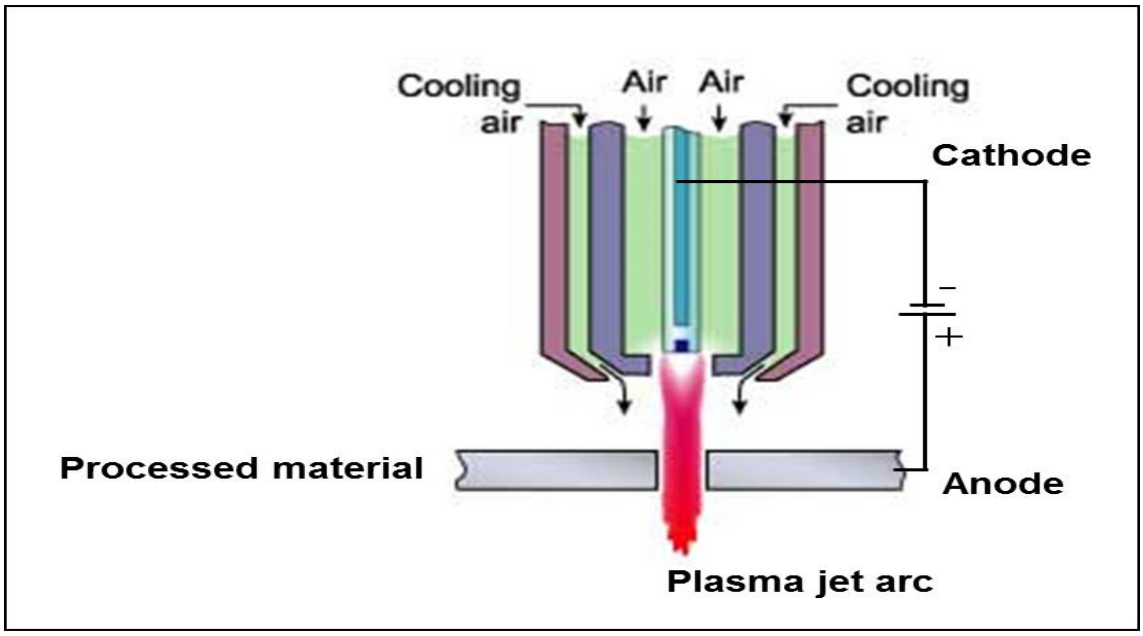

Figure 2.4: Transferred arc plasma torch
(Adapted from The Welding Institute, 2017).

From Figure 2.4, the cathode of the plasma torch is made of special consumable materials such as copper coated with hafnium or zirconium while the anode is made of high thermal conductivity metallic materials such as copper, silver and aluminium (Abubakar *et al.,* 2016:65). The electrodes configuration allows plasma to flow out of the air-cooled torch with high heating efficiency. The temperature of the gas jet exiting the plasma torch is about 5,000 °C or higher (5,273 K or higher) (Ducharme & Themelis, 2010:1-2). This high temperature is capable of heating the treated metallic materials (anode) and excite any chemical bonds within them.

The advantage of the transferred arc plasma is that it requires high temperatures and densities which allow high heat and high reactant transfer rate. Additionally, it has a smaller size which make it easy to be installed. The gases that can be used for the transferred arc plasma processing are air, argon (A_r), helium (H_e), oxygen (O_2), hydrogen (H_2) and nitrogen (N_2) (Trelles *et al.,* 2009:728).

In the non-transferred arc plasma, electric power is transformed into heat energy by means of electric discharges from cathode to anode of the air-cooled body of the plasma torch. A high temperature arc is then generated in between the electrodes. Subsequently, the high pressure of the flowing gas pushes the plasma out of the torch through its nozzle to create a plasma jet (Abubakar *et al.,* 2016:65). A schematic of the non-transferred arc torch is shown in Figure 2.5.

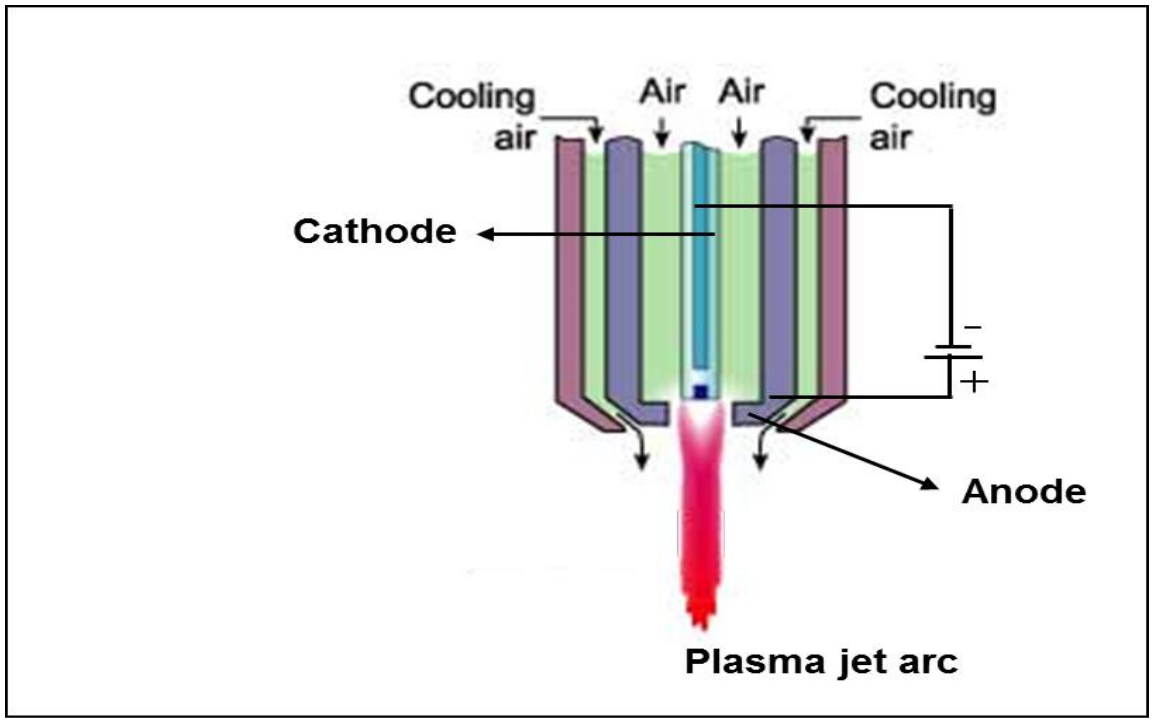

Figure 2.5: Non-transferred arc plasma torch (Adapted from The Welding Institute, 2017).

The advantage of non-transferred arc plasma is that power consumption and electrode degradation are very low. The non-transferred arc plasma torch also produces less noise and less vibration which result to more stable operation. One disadvantage of this type of torch is that the heating efficiency is very low compared to the transferred arc plasma (Table 2.2).

Table 2.2 lists the characteristic and performance comparison between the transferred-arc and non-transferred arc plasma torches.

Table 2.2: **Comparison between the transferred-arc and non-transferred arc plasma torches (Adapted from Abubakar *et al.,* 2016:64)**

Property	**Non-transferred arc plasma torch**	**Transferred arc plasma torch**
Energy density	Low.	High.
Heating efficiency	Between 50 & 75%.	Greater than 90%.
Peak temperature	Between 10,000 to 14,000K	Between 12,000 to 20,000K
Electrode separation	From few millimeters to about 5 centimeter.	From few centimeter to about 1 meter.
Relation with the processed material	The processed material is independent of the electric circuit.	The processed material form part of the electric circuit.
Plasma Projection	The plasma jet is projected out of the nozzle as flame.	The electrode is extended toward processed material.
Arc Location	Formed between the cathode and the air-cooled nozzle.	Formed between the cathode and the processed material (anode).
Application	It can be used for welding and ceramic metal plating.	It can be used for welding, cutting of metals and waste treatment.

Another type of LTE plasma is known as the Inductively Coupled Plasma (ICP). In this type of plasma, energy is supplied by induction coils current produced through a time varying magnetic field (electromagnetic induction). The ICP or radio frequency discharge technique was first used in 1960's for crystal growing. Recently, it has gained general acceptance in many types of applications among which include the detection of trace metals (Warra & Jimoh, 2011:41-42). The gases used for the generation of this type of plasma are mostly electrically conductive because they contain large concentration of ions and electrons. In addition, there are equal number of charged ions and electrons in each unit volume of plasma generated using the ICP method. To develop an ICP, two different geometries are often considered: planar and cylindrical.

For the planar geometry, the electrodes are made up of a flat metal coil which is looped in a spiral shape. Whereas, for the cylindrical geometry, the electrodes are made up of a cylinder metal coil which is looped in a helical spring shape (Batsala *et al.,* 2012:671-672). The ICP torch are mostly used within a water-cooled coil of a radio frequency generator. When operating this torch, a gas flow and RF coil fields must be activated. As the gas flows along

the RF field inside the torch, it becomes electrically conductive (plasma) due to the induced magnetic field. This generates a high frequency (HF) electric current within the heated coil electrodes (Warra & Jimoh, 2011:41-42). The density and temperature of the plasma generated with ICP torch can be maintained by continuously heating the gas with the required magnetic field strength (Warra & Jimoh, 2011:41-42).

The setup of an ICP torch consists of three silica concentric quart tubes known as the inner loop, intermediate loop, and outer loop. These quart tubes are used with concurrent flow of three gases (inner/carrier gas, intermediate/central gas and the outer/sheath gas) to insulate the plasma from other components within the torch system and also to prevent short-circuiting and torch meltdown (Figure 2.6).

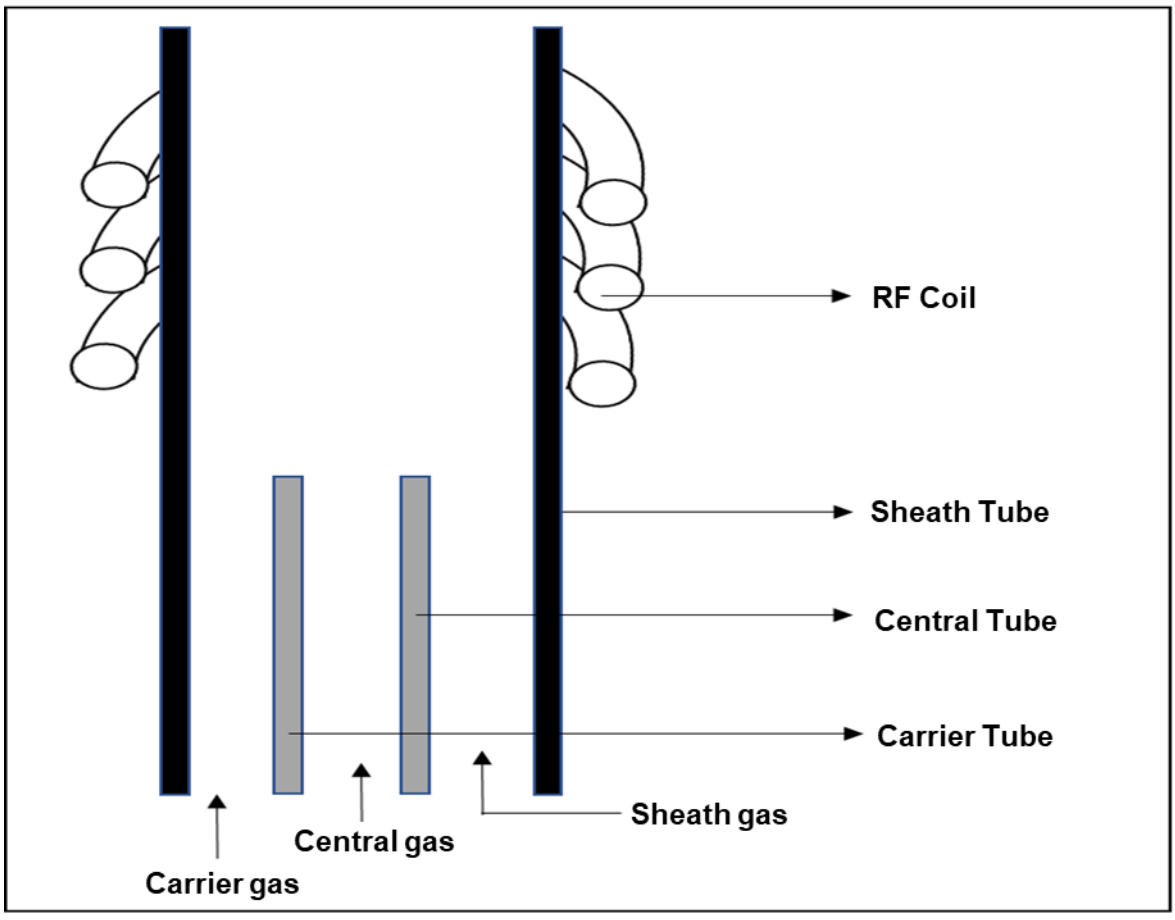

Figure 2.6: **Inductively coupled plasma torch geometry (Adapted from Solonenko, 2003:51-52).**

From Figure 2.6, the sheath gas (Argon or Nitrogen) is used for maintaining the plasma, stabilizing the plasma position and thermal isolation of the plasma from the sheath tube. Whereas, the carrier gas is used to transport the sample to the plasma. Argon gas is mostly used for both central and carrier gases.

The argon plasma discharge inside an ICP torch produces an ion source, with jet peak temperature and velocity magnitude of about 6000 °K to 10000 °K and 20 m/s to 80 m/s, respectively (Warra & Jimoh, 2011:41-42). In most ICP torches, the maximum excitation frequency ranged from 30 MHz to 40 MHz and the excitation power ranged from 15 kW to 30 kW (Solonenko, 2003:52). A typical ICP operation can be described using the principle of a transformer, in which a coil serves as primary coil and plasma acts as secondary coil with single turn (Dropmann *et al.,* 2013: 804-807).

In summary, due to the physical characteristics (vaporisation and ionisation) of thermal plasma, the plasma generated can be used for creation of new materials, destruction of toxic and harmful materials, treatments of materials, cutting of metallic materials, plasma spraying processes such as surface coating and casting of ores (Grill, 1994:21; Bonizzoni & Vassallo, 2002:327-330). They can also be used for applications which require heat energy in order to create anticorrosion, thermal barriers, antiwear coatings of thick films and electric power generation.

2.4.1.2 Non-Local thermal equilibrium plasma

The non-local thermal equilibrium plasma can be generated from microwave frequency, low power radio frequency and high voltage DC or alternating current (AC) sources placed inside a vacuum system (Singh *et al.,* 2014:7). This kind of plasma can cause physical and chemical reactions with gases at extremely low temperature because of their non-equilibrium properties. (Grill, 1994:21-22; Budtz-Jorgensen, 2001:7). In addition, the temperature of the electrons inside the non-LTE plasma is much greater than the temperature of the ions (Grill, 1994:22; Köritzer, 2013:9-10; Arora *et al.,* 2014:1; Singh *et al.,* 2014:7).

The non-LTE (cold) plasma can be used for material processing and also for applications which does not require high temperature, pressure (<10 kPa) and heat energy, such as etching and superficial modification of existing materials (Bogaerts *et al.,* 2002:610; Boulos *et al*., 2013:8). The non-LTE plasma can also be used to create surface chemistries and coatings which are uniquely different from the bulk material (Bonizzoni & Vassallo, 2002:327). An example of non-LTE application is when plasma particles such as ions and electrons interact with a target material and a superficial modification is made to the surface of the material (Bonizzoni & Vassallo, 2002:327-329).

Furthermore, an extreme ultraviolet (EUV) radiation can be produced when a magnetic or electric field is applied to non-LTE plasma. The electrons inside this plasma are accelerated to high temperatures (10^4 K - 10^5 K) which are sufficient enough to ionise the neutral molecules and atoms of the gas (Grill, 1994:21-22; Budtz-Jorgensen, 2001:7; Lyons, 2007:15−16; Arora *et al.,* 2014:1).

Some of the chemical elements used for non-LTE plasma processing are silicon (S_i) and nitrides, (Lieberman, 2003:4). Figure 2.7 depicts the density and energy of gas discharge plasmas.

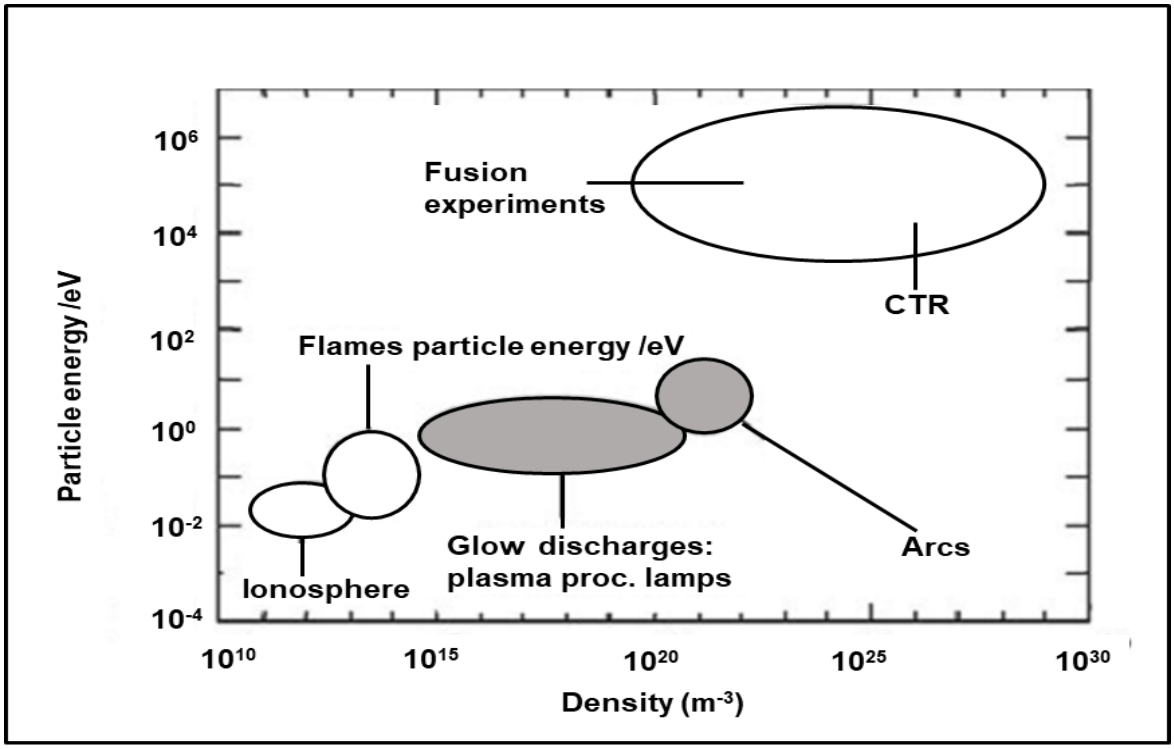

Figure 2.7: The 2D map of the density and energy of gas discharge plasmas (From Braithwait, 2000:519).

2.4.2 Gas laser plasma

Gas laser plasma can be generated through vaporisation and ionisation of a solid or liquid material (fuel) exposed to high density laser energy (Grill, 1994:4; Berkery & Choueiri, 2001:6). This type of plasma is often referred as the laser produced plasma (LPP) (Ota *et al.,* 2006:4). In LPP, the fuel materials (Xenon, tin, and lithium) are heated by a pulse laser to produced high temperature plasma. At about 13.5 nm wavelength, the LPP can also be used to generate high power EUV radiation from the hot plasma (20 eV - 50 eV) of Xenon, tin, and lithium (Grill, 1994:4; Ota *et al.,* 2006:4).

Figure 2.8 illustrates the mode of detection of EUV radiation source. In this figure, the EUV light source is collected by the collecting mirror and filtered to the intermediate focus. The intermediate focus is the channel through which the reflecting surface is illuminated. Moreover, the UV spectra are sub-divided into different groups: EUV (10 to 121 nm), Vacuum ultraviolet, VUV (10 to 200 nm), ultraviolet C (UVC) (100 to 280 nm), ultraviolet B (UVB) (280 to 315 nm) and ultraviolet A (UVA) (315 to 400 nm) (Tobiska & Nusinov, 2000:388; Tobiska & Nusinov, 2005:5−10).

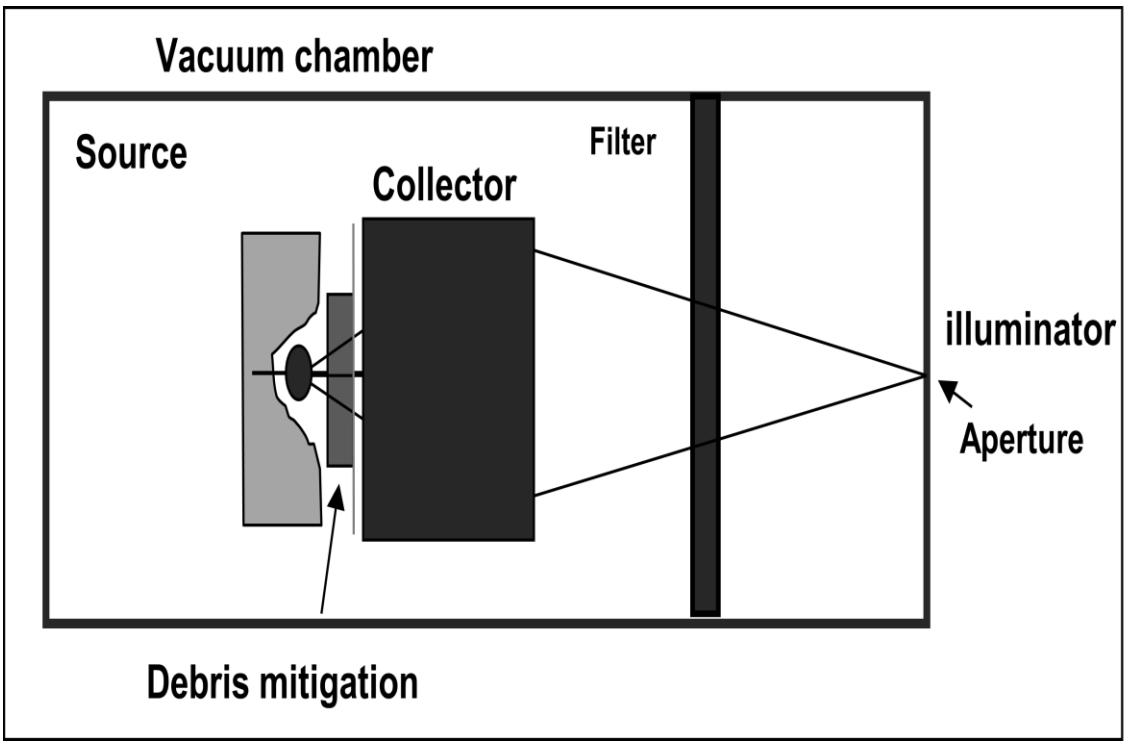

Figure 2.8: Extreme ultraviolet radiation source mode of detection (Adapted from Ota *et al.,* 2006:29).

2.4.3 Solar wind plasma

Solar wind plasma consists of stream of charged particles (protons, electrons and ions) emanating from the sun (Figure 2.9) (Grill, 1994:20: Richardson, 2010:83-86).

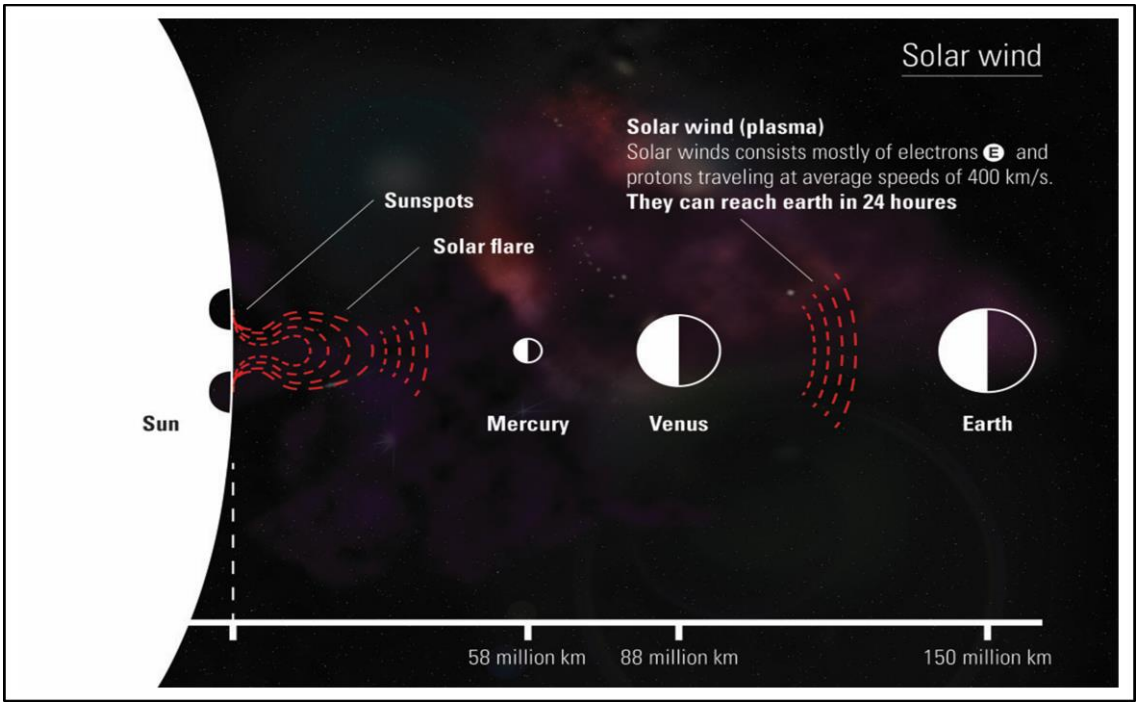

Figure 2.9: Solar wind plasma (From Iceland Aurora Films, 2014).

From Figure 2.9, the charged particles in the magnetosphere region are formed when the solar wind and the interplanetary plasma interact with the earth's magnetic field (Conde, 2014:18). The temperature and density of these particles are, respectively, 50 eV and 5 cm^{-3} (Grill, 1994:20).

In the North and South poles, the sun magnetic field lines are connected with the earth's geomagnetic field to form a spiral shape called parker spiral (Richardson, 2010:86). The charged particles' flowing along these magnetic field lines does not experience any deflecting force as they move towards the earth surface. The polar auroras are originated from these solar activities (Conde, 2014:18). Figure 2.10 depicts the deviation of charged particles from the earth surface by the earth magnetic field.

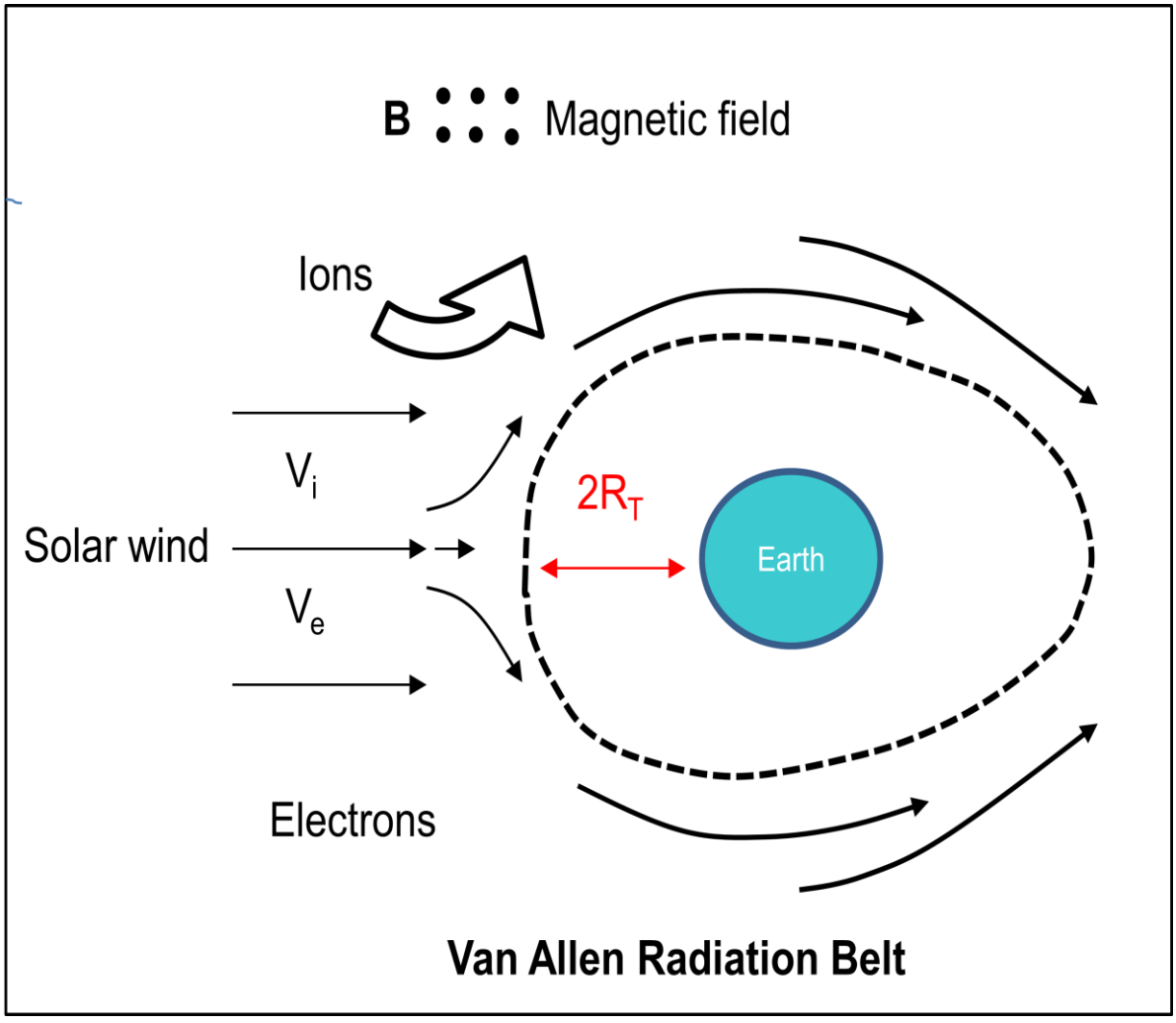

Figure 2.10: The deviation of charged particles by the earth magnetic field (Adapted from Siingh et al., 2005:638; Robin, 2006; Conde, 2014:18).

The magnetosphere, stellar interiors and other region of the atmospheres are hot enough to be in plasma state. For instance, the temperature at the center of the sun is approximately 2 keV (Grill, 1994:20; Budtz-Jorgensen, 2001:5). The solar corona, which is tenuous plasma, also has a temperature of approximately 200 eV. The interaction of particles at these temperatures are responsible for the sun's radiation (Chen, 1984:14-15).

Other plasma which behave like particles in space include Crab nebula and stars in the galaxy (0.5 eV - 7 eV). The outer layer of the galaxy stars plasma is partially ionised while the interior layer is completely ionised (Grill, 1994:20). The types of plasma that can be found within the galaxy stars are complete thermodynamics equilibrium (CTE) plasma.

2.4.4 Earth's ionosphere plasma

The formation of highly energetic charged particle begins within a layer of the Earth's atmosphere called the ionosphere. The ionosphere region extends approximately from an altitude of about 90 km to 1000 km above the Earth's surface and is often ionised by solar radiation (Kotova, 2007:409).

The solar radiation within the ionosphere layer is strong enough to dislodge electrons from molecules, thus, producing free electrons with positively charged ions (Escobar, 2009:7). The plasma investigated within this region is weakly ionised with a density of approximately 10^6 cm^{-3} and an electron temperature of approximately 0.1 eV (Grill, 1994:20). Each of the plasma in the ionosphere consists of both charged and neutral particles. Moreover, when the densities of these charged species are equal, they are neutrally charged.

Figure 2.11 depicts the densities of gases and atomic species within the ionosphere with respect to their altitudes.

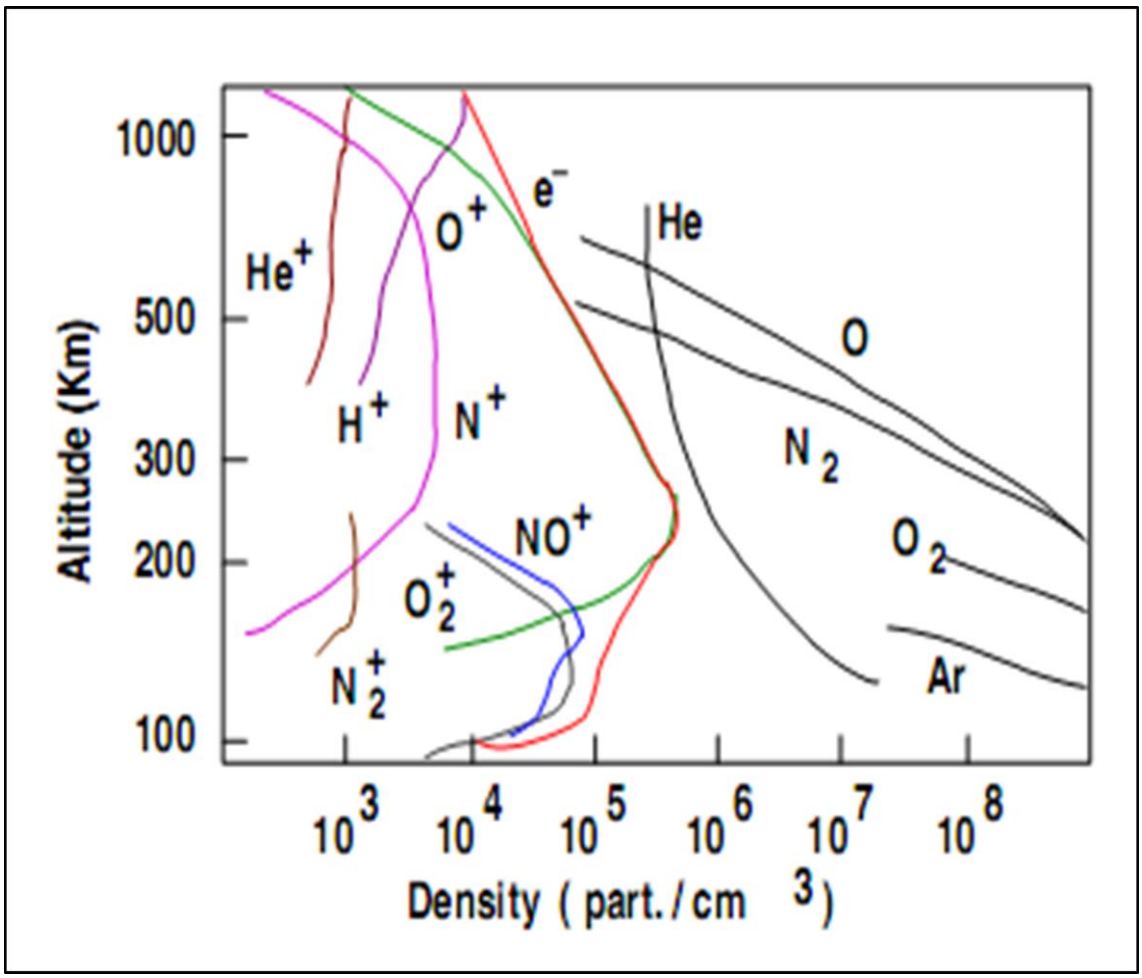

Figure 2.11: The densities of gas molecules and atomic species in the ionosphere with their altitudes (From Conde, 2014:19).

During solar storms (i.e. dissociation and recombination of the charged particles), the high energy charged particles (protons, electrons and ions) from the atomic species diffuse toward the Earth and their motion are often restricted and trapped by the Earth's magnetic field within the Van Allen Radiation Belt (VARB) region (Stassinopoulos & Raymond, 1988:1423).

The VARB region is symmetric to the Earth's magnetic axis, which is inclined to the Earth's rotational axis by 11° (Figure 2.12). The inner VARB come closest to the Earth's surface over the South Atlantic Ocean and farthest over the North Pacific Ocean (Heirtzler, 2002:1701; De Santis & Qamili, 2010:339; Casadio & Arino, 2011:1056; Ayeleso, 2014:6). Above the South Atlantic Ocean is the South Atlantic Magnetic Anomaly (SAMA) region where the Earth's magnetic field is very weak, and radiation found in this region is very high (Figure 2.12).

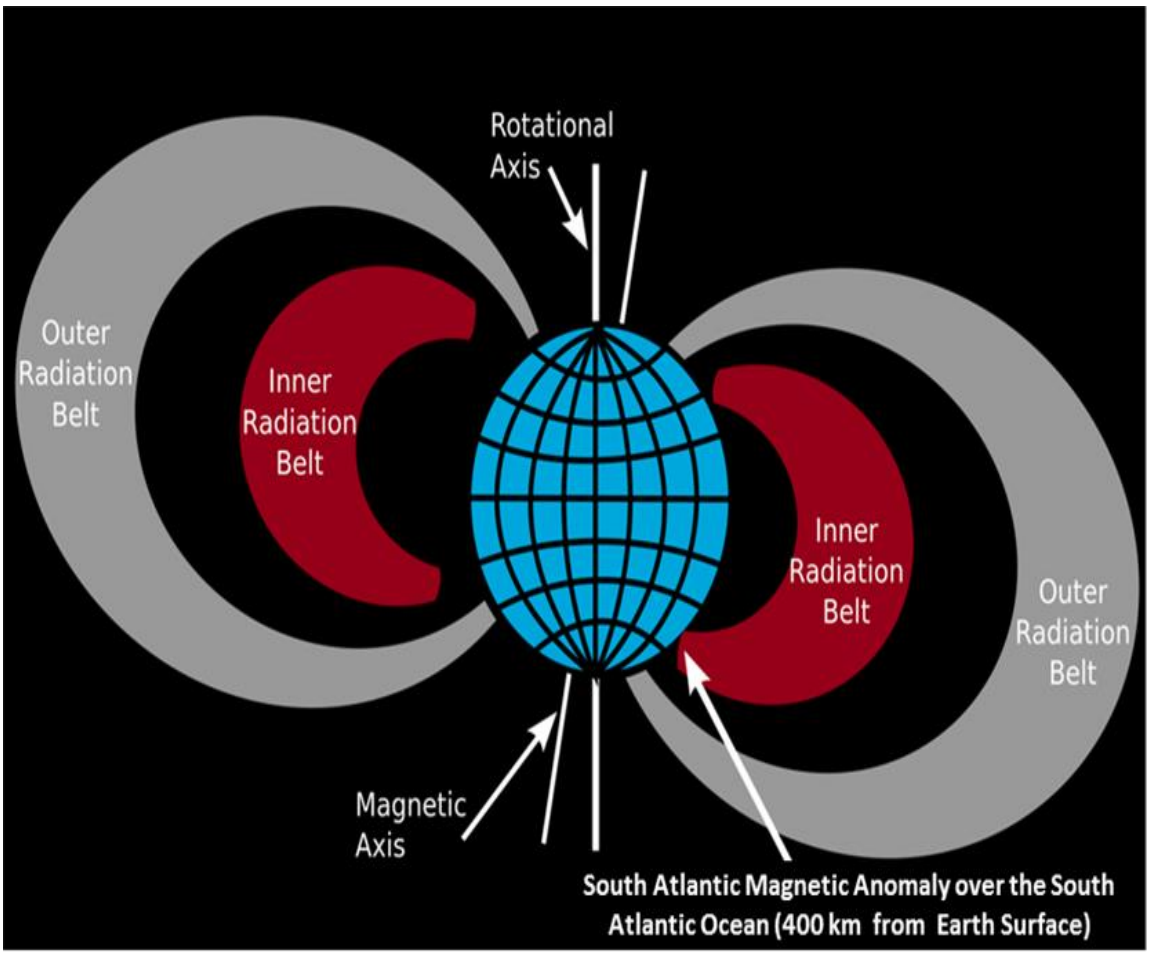

Figure 2.12: Schematic illustration of the South Atlantic Magnetic Anomaly (Adapted from Robin, 2006).

From Figure 2.12, the trapped charged particles, move in opposite directions because of their charge, i.e., electrons move towards the east while protons and heavy ions move towards the west within the Earth's magnetic field lines. The trapped electrons (below 10 MeV) are found in the inner and outer zone of the VARB (Figure 2.12). Whereas, the trapped protons (above 1 MeV) are found as the most penetrating radiation in the SAMA region. This is due to their intensive flux around the Low Earth Orbit (LEO) (Stassinopoulos & Raymond, 1988:1424−1425; Mavromichalaki *et al*., 2007:1089−1093).

The characteristic electron density in the VARB is between 10^6 m^{-3} and 10^{10} m^{-3} and the electron temperature is between 1 eV and 2 eV (Weyde, 2006:23; Kotova, 2007:409). Nearby the VARB, there is a region known as the plasmasphere (Figure 2.13). The plasmas that can be found in this area are extremely dense with a peak density of 10^{10} m^{-3} and cold temperature of approximately 1 eV (Figure 2.14) (Weyde, 2006:23; Kotova, 2007:409). The Electron density and temperature of plasma around the VARB regions are listed in Table 2.3.

Table 2.3: **Electron density and temperature of plasma around the VARB regions (Adapted from Weyde, 2006:23; Escobar, 2009:38)**

Plasma regions	Electron density [m^{-3}]	Electron Temperature [eV]	Debye Length [m]
Ionosphere	10^{12}	≈0.26	3.8×10^{-3}
Plasmasphere	10^{10}	≈1	74.3×10^{-3}
Magnetosphere	10^{7}	≈500	52.3
Solar wind	5×10^{6}	≈10	10.5

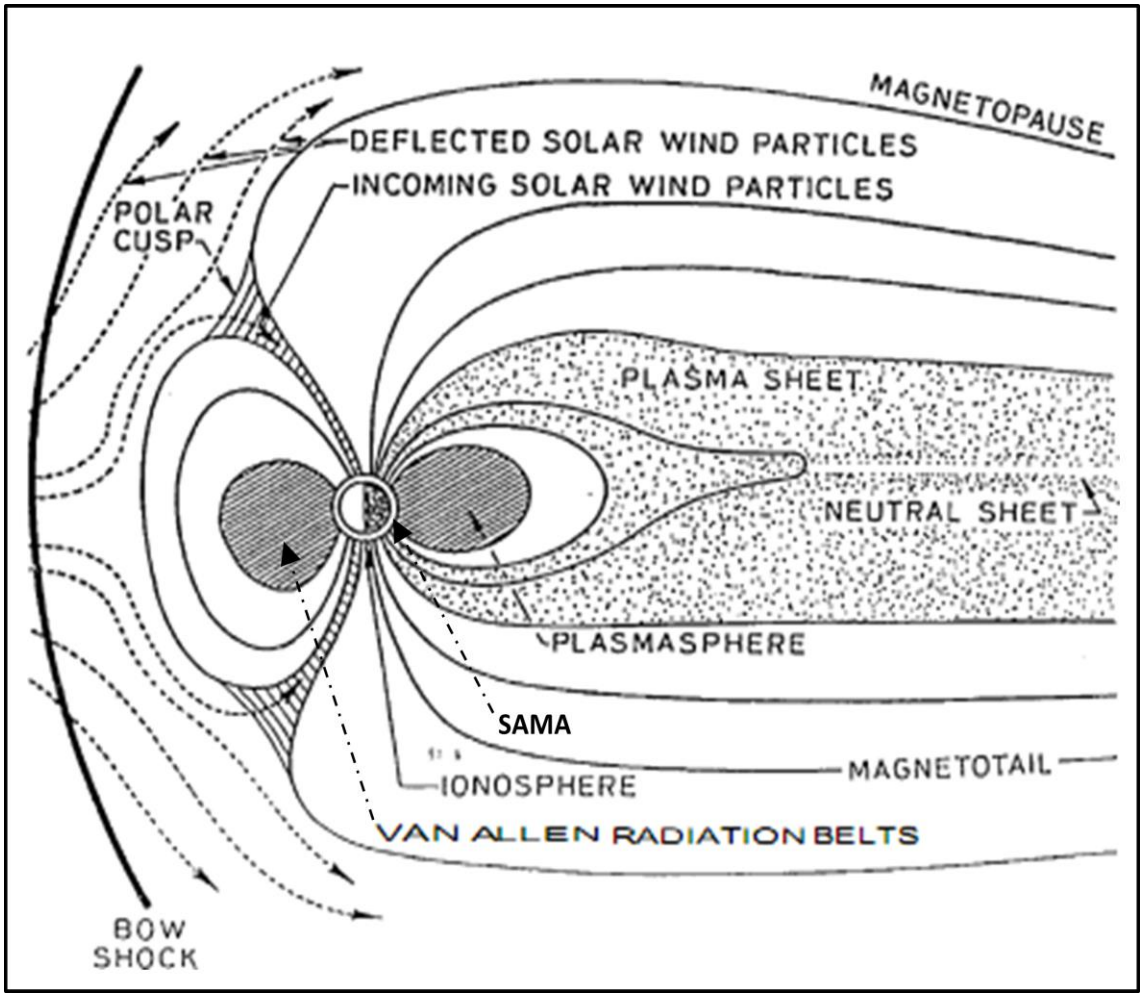

Figure 2.13: Schematic illustration of the VARB region showing the Earth's magnetosphere (Adapted from Siingh *et al*., 2005:638).

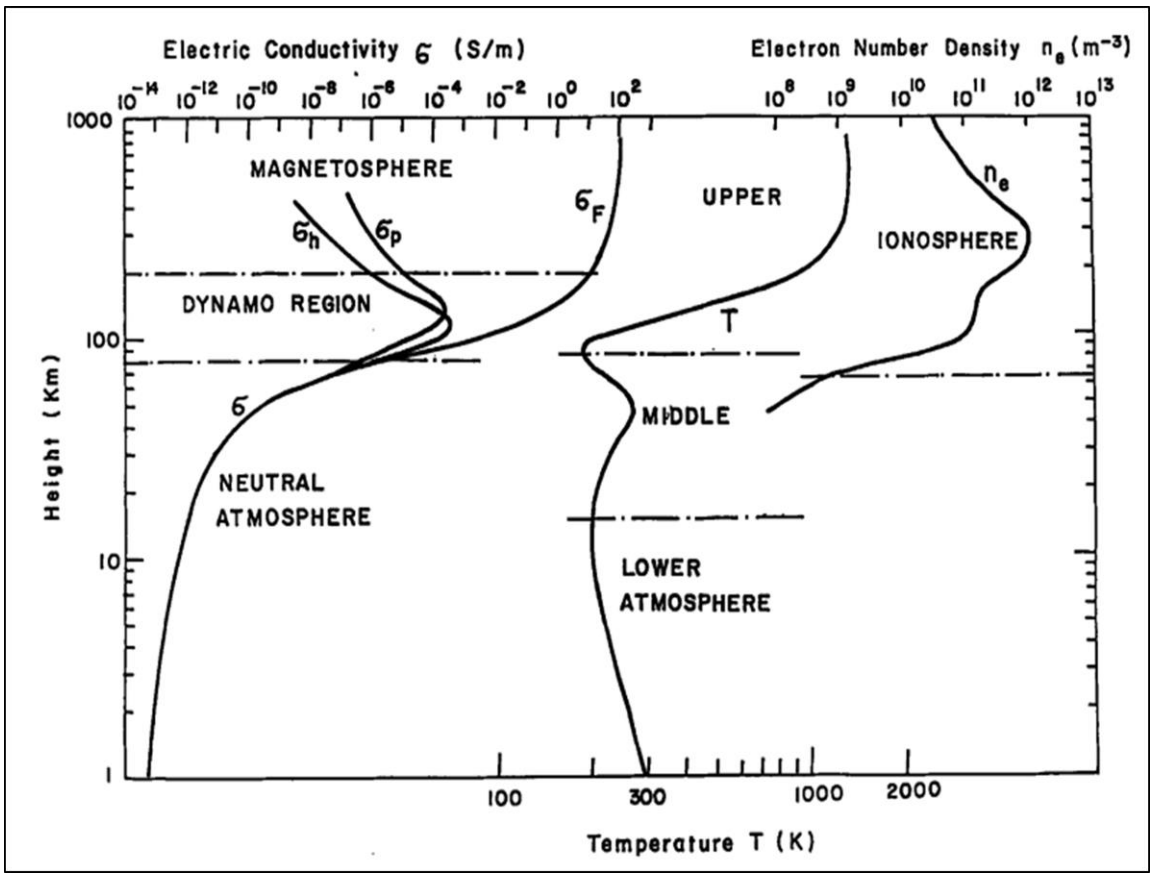

Figure 2.14: Schematic illustration of electron density and temperature around the Earth's magnetosphere and ionosphere (From Siingh *et al*., 2005:640).

Table 2.4 lists some of the gases and atomic species around the Earth's magnetosphere and the ionosphere regions, with their ionization energies (Escobar, 2009:7-8).

Table 2.4: Lists of gases and atomic species around the Earth's magnetosphere and the ionosphere regions, with their ionization energies

Species	Wavelength (nm)	Ionization Potential (eV)
NO	9.25	1340
O_2	12.08	1027
H_2O	12.60	985
O_3	12.80	970
H	13.59	912
O	13.61	911
CO_2	13.79	899
N	14.54	853
H_2	15.41	804
N_2	15.58	796
He	24.58	504

From Table 2.4, it can be seen that the specie with the smallest wavelength ionises more than the specie with the maximum wavelength. Moreover, the ionosphere is divided into three regions: the equatorial region, the mid-latitude region and the high-latitude region (Escobar, 2009:7).

In the equatorial region, the magnetic field is almost parallel to the earth surface. In the high-latitude region, Arctic and Antarctic circles dominate the major activities in the region. The high-latitude region is known as polar cap and aurora zone. The region between the high-latitude and the equatorial regions is known as the mid-latitude region (Escobar, 2009:7-8).

The ionosphere can also be grouped into three layers: D, E, and F layers (Chapman layers). The density of plasma increases in these layers with heights, as shown in Figure 2.15 and Table 2.5. The F-layer has the highest plasma density while the D-layer has the lowest plasma density (Escobar, 2009:7-8). Particles in the D-layer usually collide with themselves and the surrounding neutral particles.

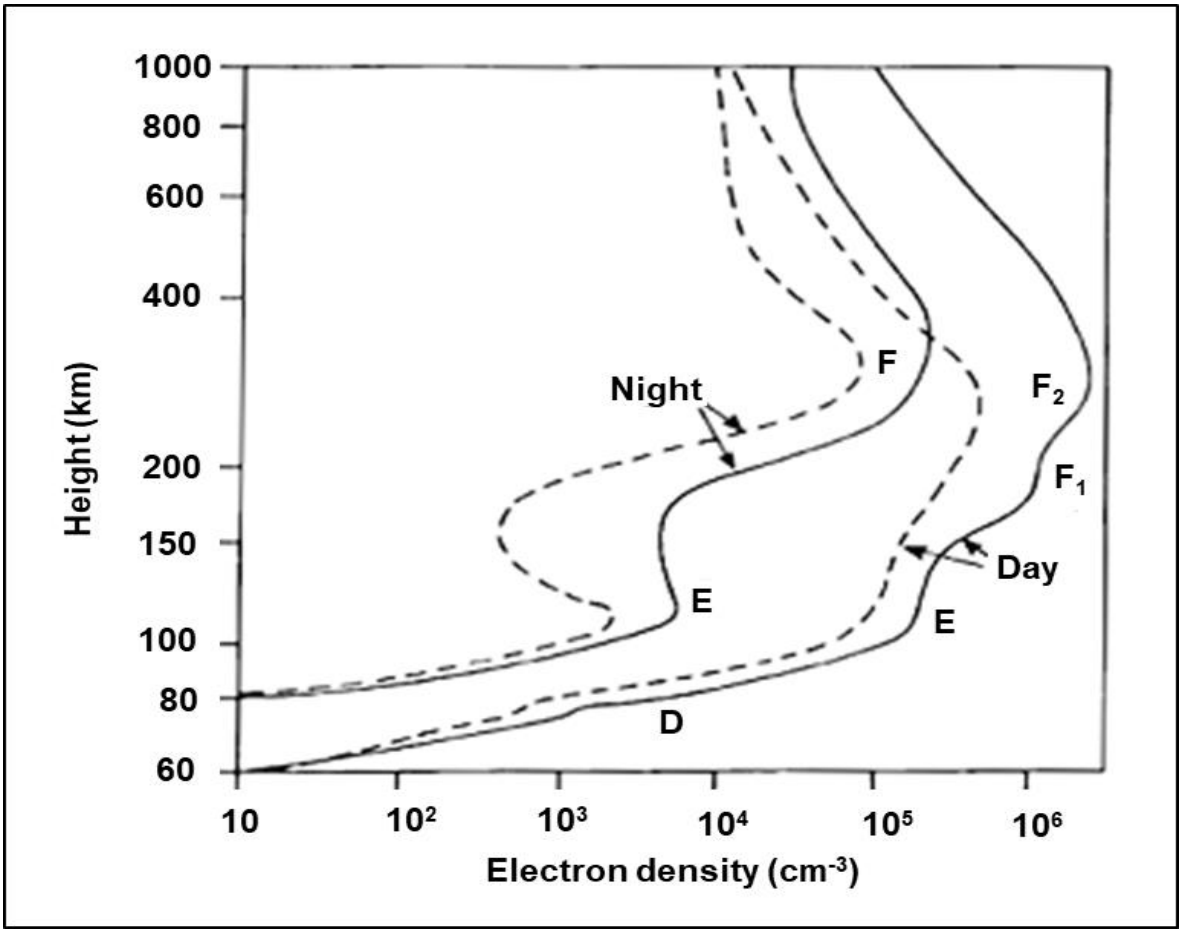

Figure 2.15: The density of electrons within the ionosphere region (From Escobar, 2009:8).

Table 2.5: The properties of plasma within the ionosphere region with selected altitudes

Plasma properties	Unit	Altitudes				
		150 km	**200 km**	**400 km**	**800 km**	**1200 km**
v	m/s	7.83×10^3	7.80×10^3	7.68×10^3	7.47×10^3	7.26×10^3
$n_{i,e}$	cm^{-3}	3.0×10^5	4.0×10^5	1.0×10^6	1.0×10^5	1.0×10^4
$K_B T_i$	K	700	1100	1600	2200	2600
$K_B T_e$	K	1000	2000	2800	3000	3000
m_i	Uma	28	24	20	14	10
λ_D	Cm	0.40	0.49	0.37	1.20	3.78
λ_e	Cm	5.0×10^5	1.0×10^5	1.0×10^5	1.0×10^6	1.0×10^7
P	Torr	3.75×10^3	7.5×10^{-10}	1.0×10^{-11}	-	-
T_g	K	635	859	993	-	-

From Table 2.5, n_i is the ion density, n_e is the electron density, λ_D is the Debye length, m_i is the mass of the ions, T_e is the electron temperature, T_i is the ion temperature, λ_e is the collision mean free paths, v is the particle velocity, P is the gas pressure and T_g is the gas temperature.

There are two major sources of ionisation in the ionosphere region: electromagnetic radiation and energetic particle precipitation. When ionising through electromagnetic radiation, the emitting spectrum ranges from X-ray to EUV radiation. The X-ray emission ranges from 0.1 nm to 17 nm (1 Å - 170 Å) while the EUV radiation emission ranges from 17 nm to 175 nm (170 Å - 1750 Å) (Escobar, 2009:8).

Furthermore, when ionising through energy particle precipitation, the charged particles which flow along the earth's magnetic field lines, greatly influence the behaviour of the high latitude ionosphere. These particles are protons and electrons (hydrogen ions, H^+). However, the equatorial and mid-latitudes are not seriously affected by these particles (Escobar, 2009:8).

2.4.5 Aurora plasma

The aurora lightning is one of the most common natural plasma discovered on earth (Dave & Joshi, 2010:177; Boulos *et al*., 2013:5). This plasma is a display of light, which usually occurs when the earth's magnetic field within the ionosphere interacts with the streams of charged particles emanating from the sun. During solar eclipse, a large flare (particles) of the sun, with coronal mass ejection (CME) of about 2 million Fahrenheit travels with solar wind and collides with gas molecules (oxygen and nitrogen) within the earth's atmosphere (Stern, 2002; Lilensten *et al.,* 2013:1-2).

As these particles collide with one another, the electrons within the magnetosphere region transfer their energy to the molecules of oxygen and nitrogen, making them to become electrically excited. Consequently, when the gas molecules return back to their initial state, they emit photons which display the aurora light (Figure 2.16) (Stern, 2002; Baranoski *et al.,* 2005:40; Axelsson *et al.,* 2012:1693; Laron, 2013).

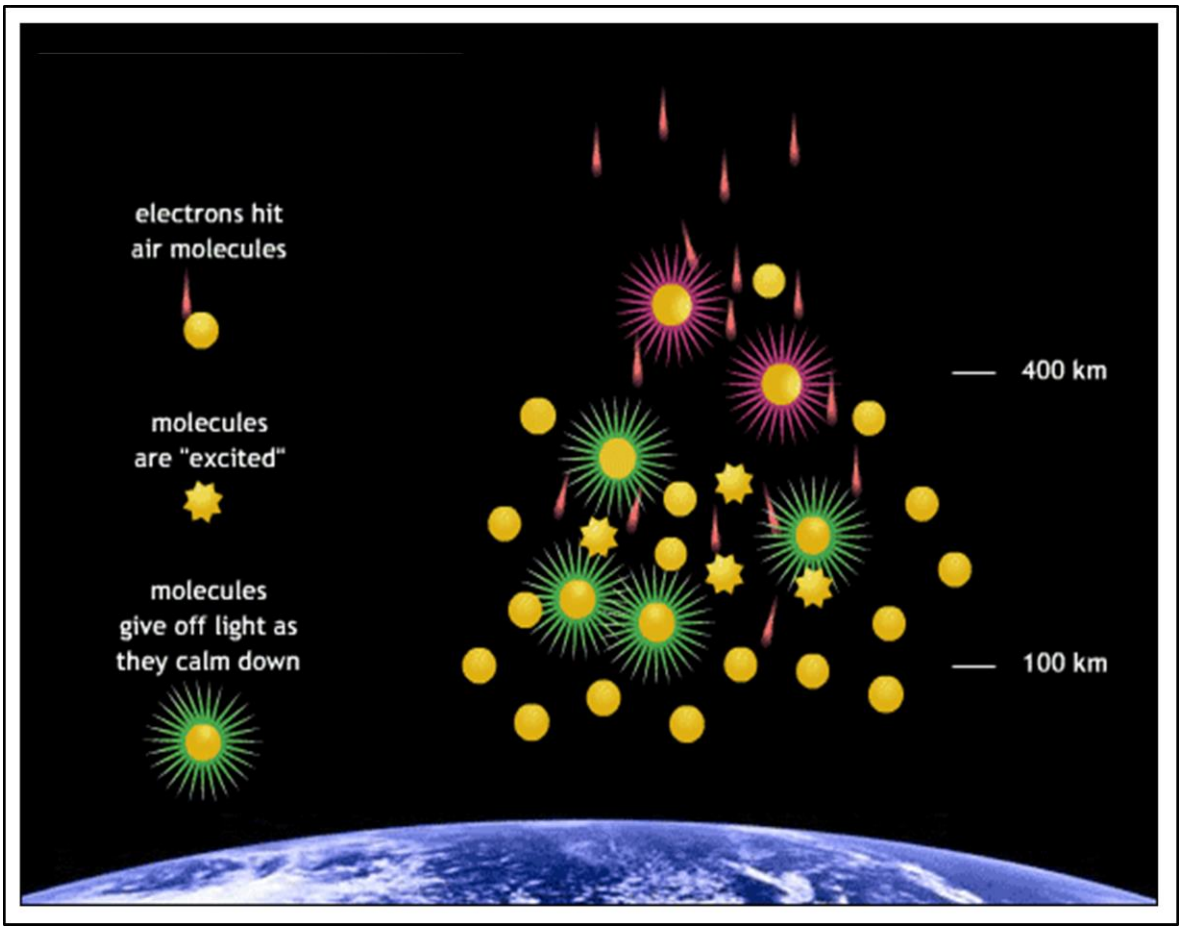

Figure 2.16: The emission of light from collisions between electrons and gas molecules (Adapted from Laron, 2013).

From Figure 2.16, the aurora originates at altitudes of about 100 km to 400 km above the earth surface in the Northern and Southern hemispheres. The lightning effect in the Northern hemisphere is called the aurora borealis while the lightning effect in the Southern hemisphere is called the aurora australis (Figure 2.17) (Arora *et al.,* 2014:1). The aurora borealis can be found in Alaska, North of Canada, North of Russia, South of Greenland, Southern Iceland, Northern Norway, Sweden, and Finland while the aurora australis can be found in New Zealand, South America and Australia (Brown, 2006; Iceland Aurora Films, 2014).

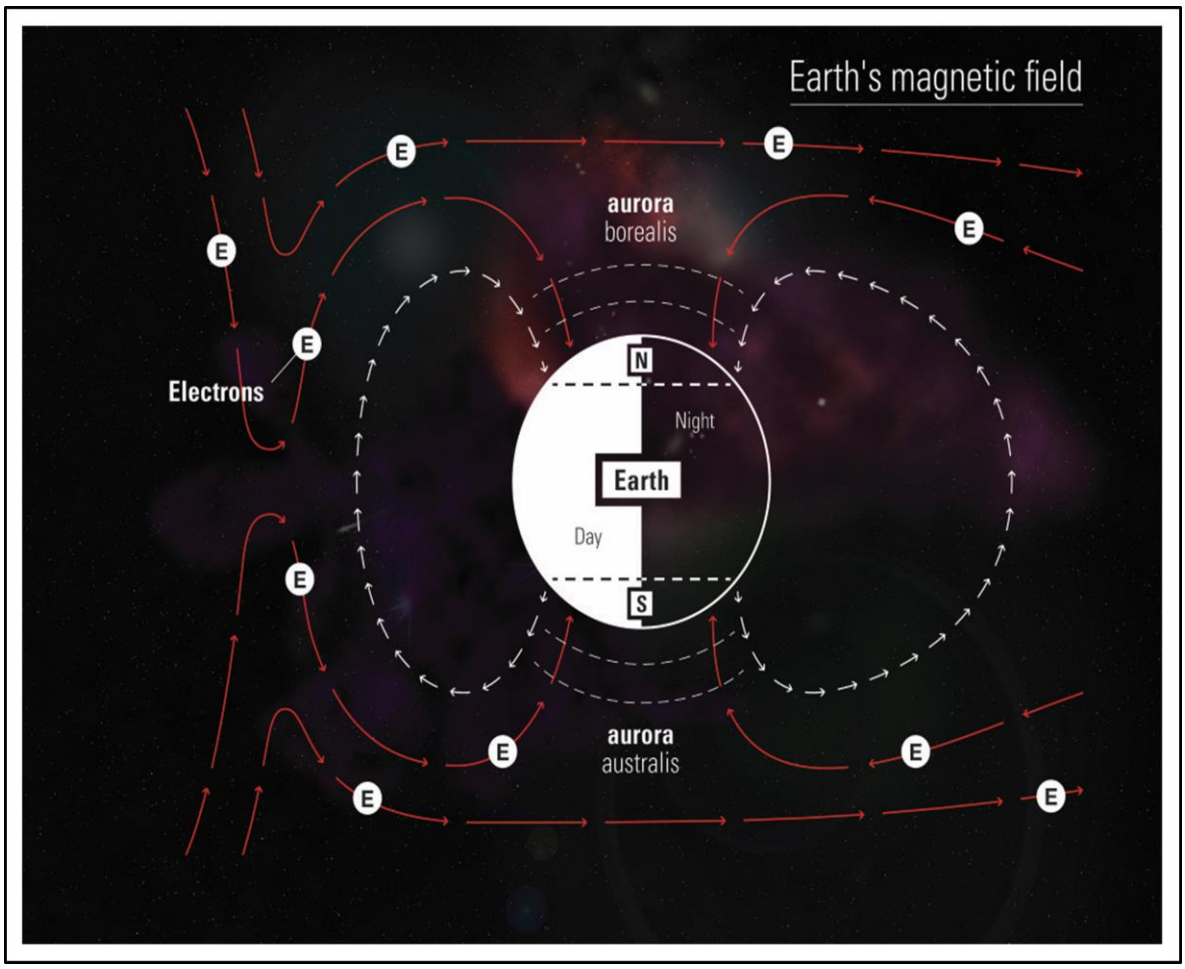

Figure 2.17: The aurora borealis and australis regions (From Iceland Aurora Films, 2014).

From Figure 2.17, the auroras (borealis and australis) positions show that the earth atmosphere and the ionosphere are energised by the current generated from the magnetosphere region. This current is usually discharged in the ionosphere region.

The intensity of the aurora light changes each night at a certain period of time. However, the best light display can be seen during the early hours in the morning. (Brown, 2006; Iceland Aurora Films, 2014). This glow of light can also appear at night as a long narrow arc shape with different intensities and colours such as green, red, blue, pink violet and white (Figure 2.18) (Axelsson *et al.,* 2012:1694; Baranoski *et al.,* 2005:41).

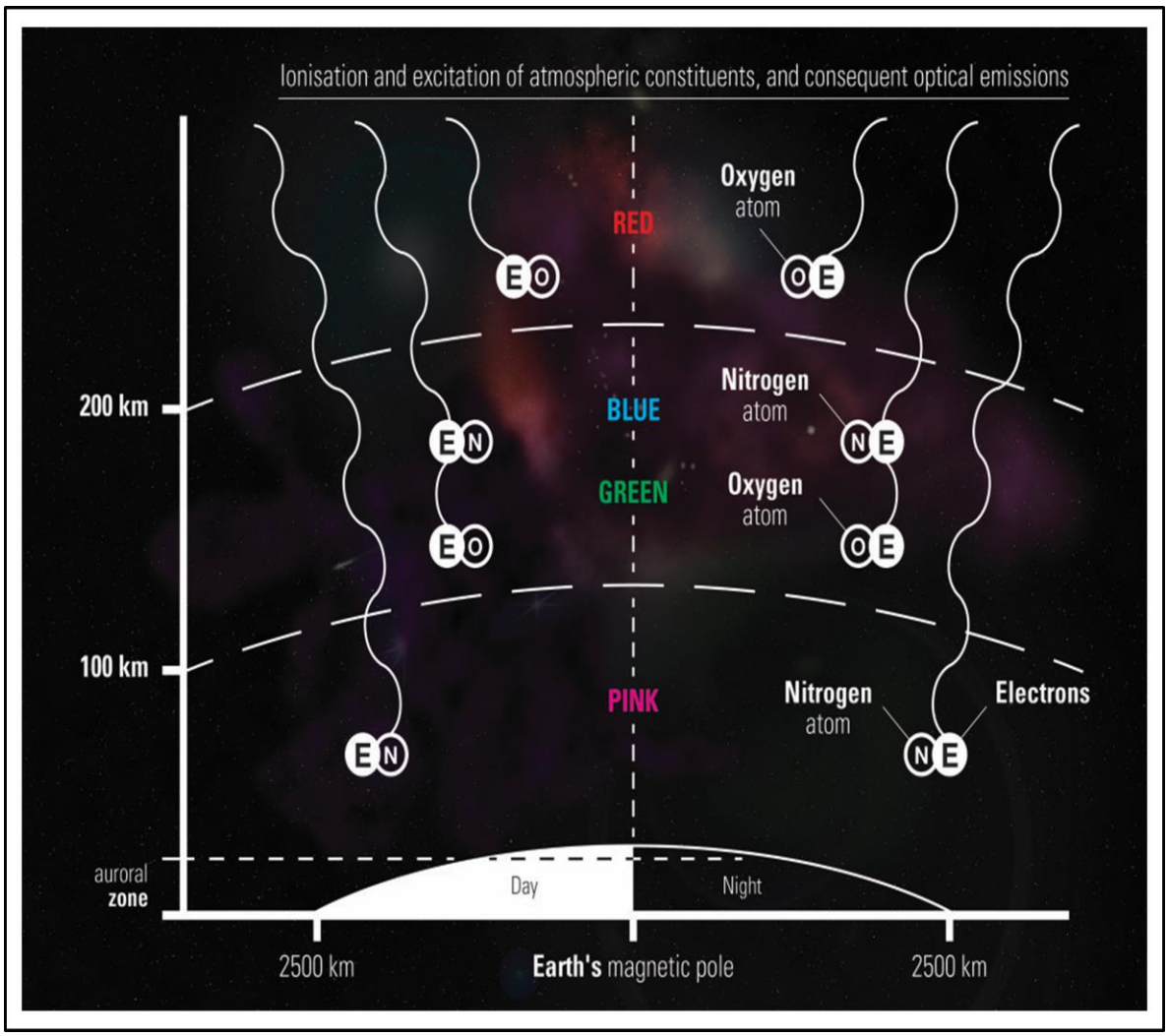

Figure 2.18: The auroras light colours with their altitudes (From Iceland Aurora Films, 2014).

From Figure 2.18, the brightness and visibility of the aurora light depend on the types of gas molecules colliding with the energetic electrons that drop out of the earth magnetic field lines in the magnetosphere region (Kletzing *et al.,* 2003:1). The green aurora appears to be the brightest of all the aurora lights. This light is emitted from an oxygen (O) atom at approximately 97 km altitude above the earth surface (Stern, 2002). The red aurora is emitted from an oxygen atom at high latitude of about 322 km. Furthermore, other lights such as the blue and pink auroras are, respectively, emitted from ionised and neutral nitrogen (N) atoms (Iceland Aurora Films, 2014).

The aurora plasma can be used as a natural source of energy for electric power generation. It can also be used to investigate the effects of nuclear explosions in the upper atmosphere (Baranoski *et al.,* 2005:38).

2.5 Direct energy conversion system

The direct energy conversion system can be grouped into two categories: The magnetohydrodynamics and magnetoplasmadynamics conversion systems.

2.5.1 Magnetohydrodynamics conversion system

The MHD conversion system was initially discovered by Michael Faraday and later extended by Ritchie in 1832 (Ritchie, 1932:279; Aoki *et al*., 2012:53; Parsodkar, 2015:541). This system is a distinctive method used for the generation of electric power based on the principle of Faraday's Law of electromagnetism and fluid (plasma) dynamics (Sedaghati *et al*., 2013:281; Masood *et al*., 2014:1357; Khan *et al*., 2014:82-83).

The operation of MHD system begins when a plasma (ionised gas) is injected from a combustion chamber and then flow through a convergent-divergent nozzle at high velocity before entering the MHD duct. Inside the MHD duct, the ionised fluid velocity is decelerated by a strong magnetic field, B, placed between two electrodes. The magnetic field also creates a retarding force that is perpendicular to the direction of the fluid (Parsodkar, 2015: 542). Subsequently, the positive and negative ions of the plasma are collected by electrodes placed at 90° to the induced magnetic field, thus, producing an electric current, as shown in Figure 2.19 (Li, *et al*., 2007; Okuno *et al*., 2011:1-2; Sedaghati *et al*., 2013:281; Masood *et al*., 2014:1357-1358; Khan *et al*., 2014:81-83; Ayeleso *et al*., 2015:206; Mgbachi, C.A., 2015:106).

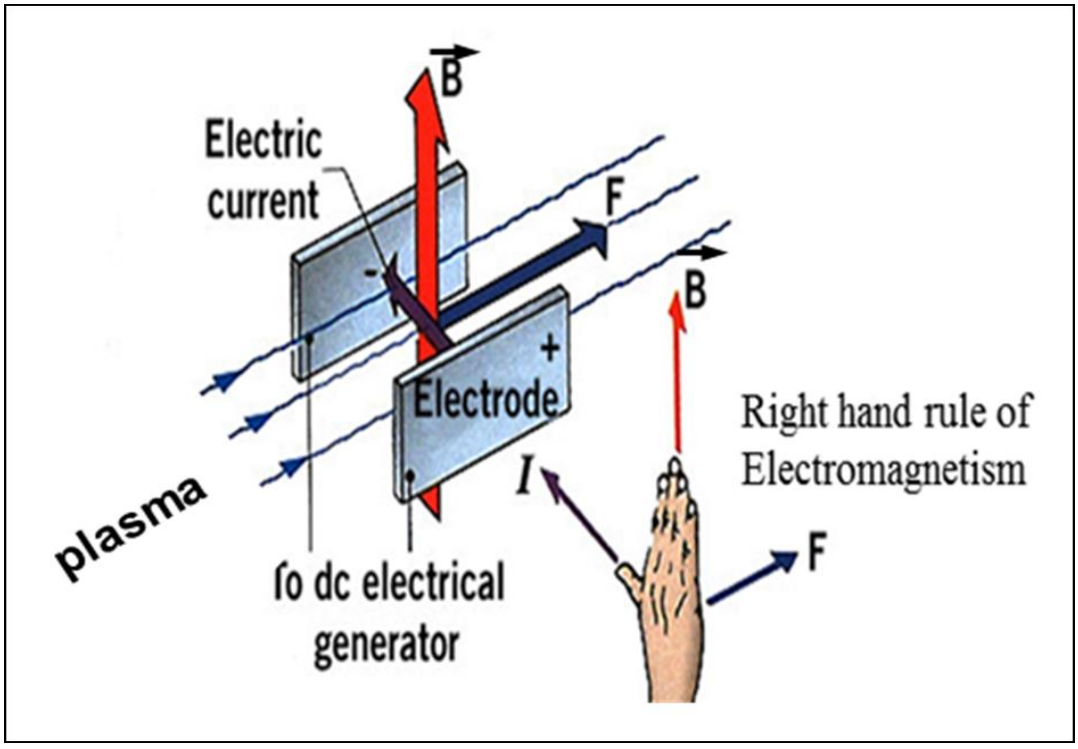

Figure 2.19: Principle of magnetohydrodynamics (From Masood et al., 2014:1357-1358).

From Figure 2.19, the Faraday's current is obtained as a result of the coupled effects between the dynamics of the electrically conducting fluid and the magnetic field. Moreover, the Faraday's current can also react with the applied magnetic field to create a Hall effect current perpendicular to the current itself (Ajith & Jinshah, 2013:1-3). The induced electric current, which is the sum of the axial current (Hall effect) and the radial current (Faraday's) can be captured using a series of insulated segmented electrodes skewed at an angle perpendicular to the fluid direction. This induced current is then measured through external loads connected to an inverter supplying the generated electricity (Mgbachi, C.A., 2015:106). The MHD system is useful in the field of Earth physics and industrial applications such as electromagnetic pumps, Ship propulsion in seawater, electromagnetic flowmeters, astrophysics (propulsion) and electric power generation (Lutz *et al*., 2003; Markusic *et al*., 2005:15).

The configuration of MHD power generator depends on how electrodes are positioned and connected. This system can be grouped into different categories: Faraday's generator with continuous electrodes, Faraday's generator with segmented electrodes, Hull generator, disc generator and series connected generator with discontinuous electrodes. Each group varies according to the way the electrodes are connected to the external load resistors (Ajith & Jinshah, 2013:1-3). The detailed procedure and implementation of all these types of Faraday's generators are discussed as follows:

- **MHD power generator with continuous electrodes**

The electrodes on each side of the Faraday's MHD duct can be connected together in continuous mode, as shown in Figure 2.20. In this configuration, the electrodes have the same potential and the fluid circuit is vertical to the flow of plasma. Consequently, the circuit components experience more long direction which causes large output losses.

Furthermore, the performance of the continuous electrodes is often deteriorated due to Hall effect and joule heating. The transverse component of the circuit is also reduced (Tillack & Morley, 1998:41-43; Sedaghati *et al*., 2013:282-283). The advantage of this method is that the electrodes and other materials such as the duct, the load resistor (*R*) and the magnets are simple to construct.

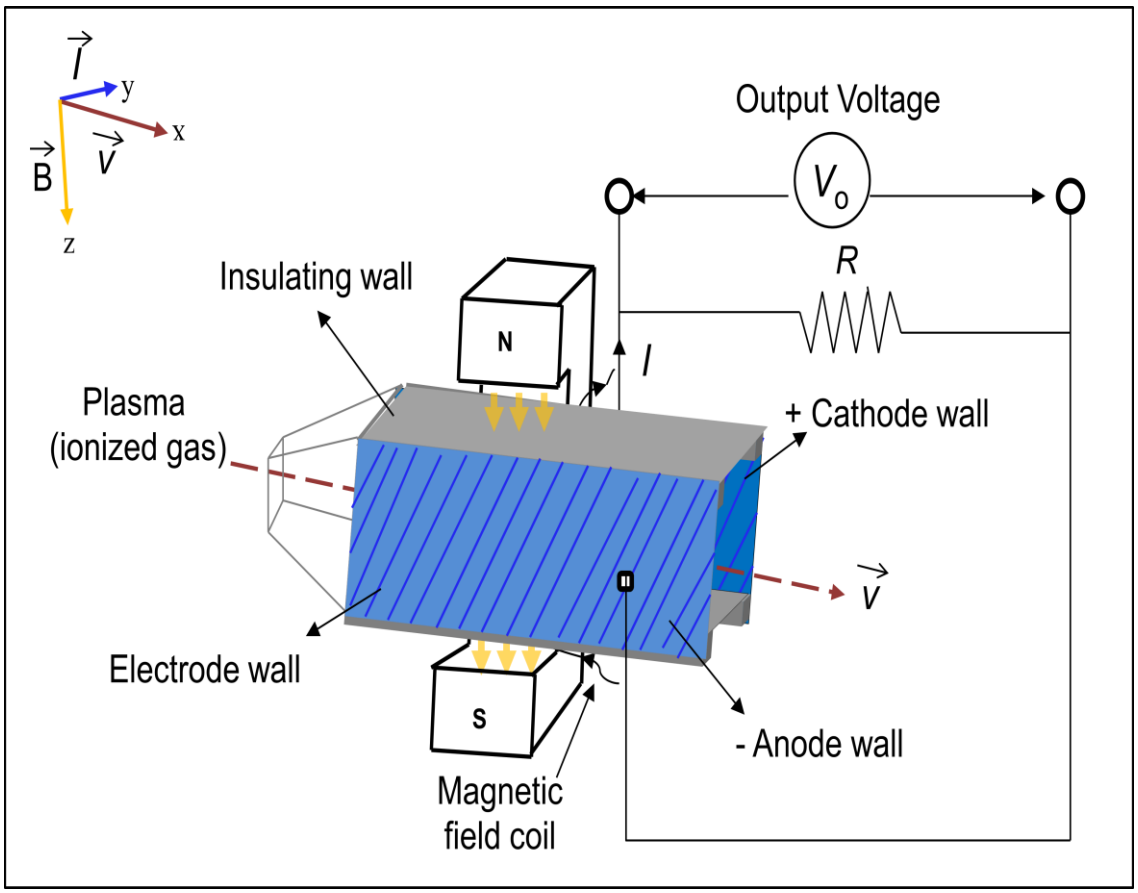

Figure 2.20: MHD power generator with continuous electrodes (Adapted from Masood *et al*., 2014:1358).

From Figure 2.20, in order to obtain good output voltage, *V*, the plasma gas (about 2000 K), must have a good electrical conductivity (Okuno *et al*., 2011:1-2; Anumaka, 2014:1072-1073). When the plasma flows through the MHD duct and a transversed magnetic field is applied, the charged particles inside the plasma experience an induced electric field, *E*, current, *I*, and retarding force, *F*, as given by equations 2.15, 2.16 and 2.17 (Ajith & Jinshah, 2013:3; Masood *et al*., 2014:1357; Khan *et al*., 2014:83),

$$E = v \times \mathrm{B}, \qquad \textbf{Equation 2.15}$$

where v is the particle velocity and B is the induced magnetic field.

The induced current is given by,

$$I = \sigma \times E, \qquad \textbf{Equation 2.16}$$

where σ is the plasma electrical conductivity.

The retarding Lorentz force, F , acting on the plasma is given by,

$$F = I \times \mathrm{B}\,. \qquad \textbf{Equation 2.17}$$

- **MHD generator with segmented electrodes**

The electrodes of the Faraday's MHD duct can also be connected in segmented modes, as shown in Figure 2.21. In this configuration, the electrodes are separated from one another with insulators and an external load resistor is connected to each electrode. In doing so, the potential difference of each of the circuit can be measured separately (Tillack & Morley, 1998:41-43; Sedaghati *et al*., 2013:282-283). The Hall effect difficulties experienced in the continuous electrodes mode can be alleviated in the segmented electrodes mode. The advantage of this method is that large losses are greatly minimised, and the electrodes are simple to construct.

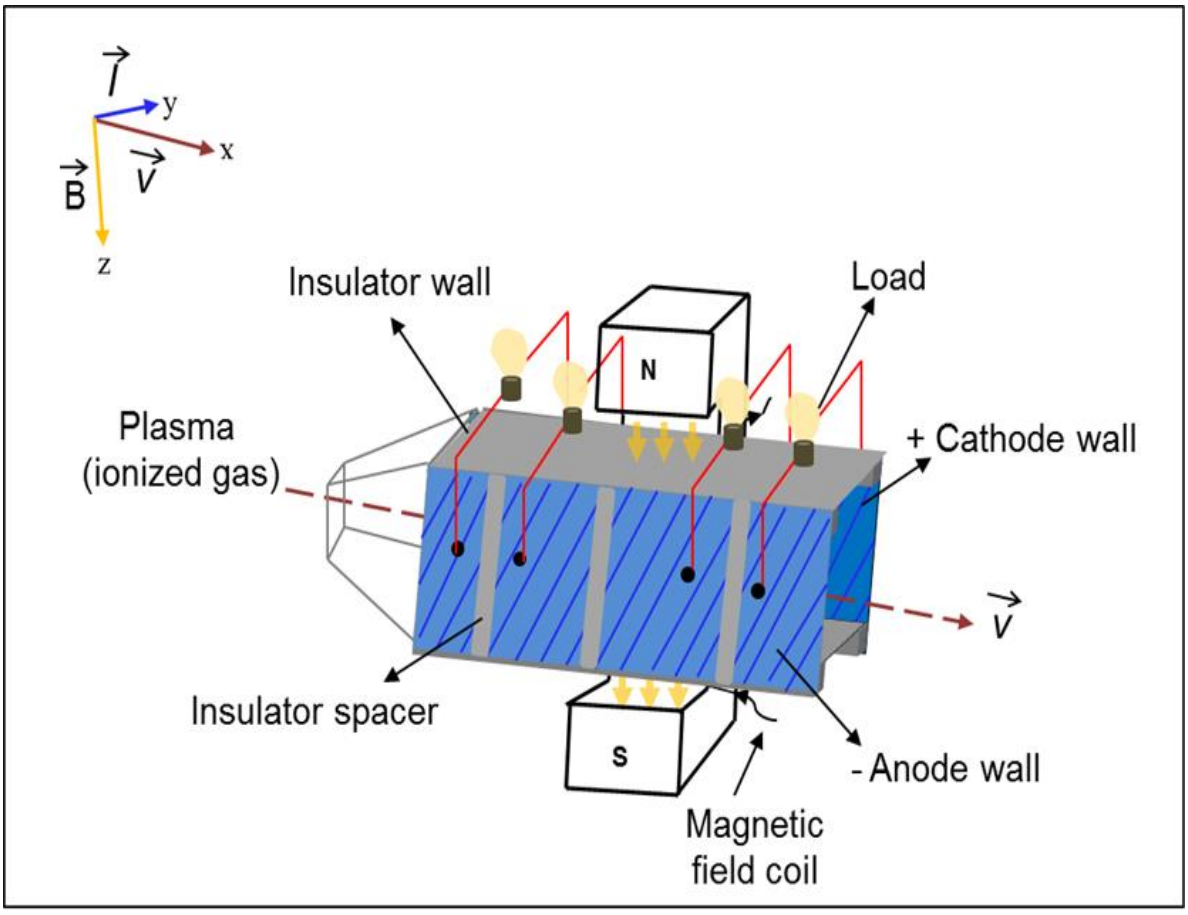

Figure 2.21: MHD power generator with segmented electrodes (Adapted from Masood *et al*., 2014:1358).

- **Hull generator**

The Hull generator design is shown in Figure 2.22. In this generator, the electrodes edges are connected together, and the load resistor is connected to the first and the last electrodes (Tillack & Morley, 1998:41-43; Sedaghati *et al*., 2013:282-283). When the load resistor is connected to the electrodes, an equipotential flow diagonally across the insulator walls. Consequently, the electrodes might wait for some period of time before it matches the equipotential. The output power from Hull generator is driven by the circuit electric fields.

Furthermore, this generator produces fewer losses than the Faraday's generator because the resulting output voltage is very high and shorting of the induced current is significantly reduced. The Hull generator is less efficient in terms of capturing high velocity plasma current unlike the Faraday's generator, which is very sensitive to plasma flow (Masood *et al*., 2014:1359).

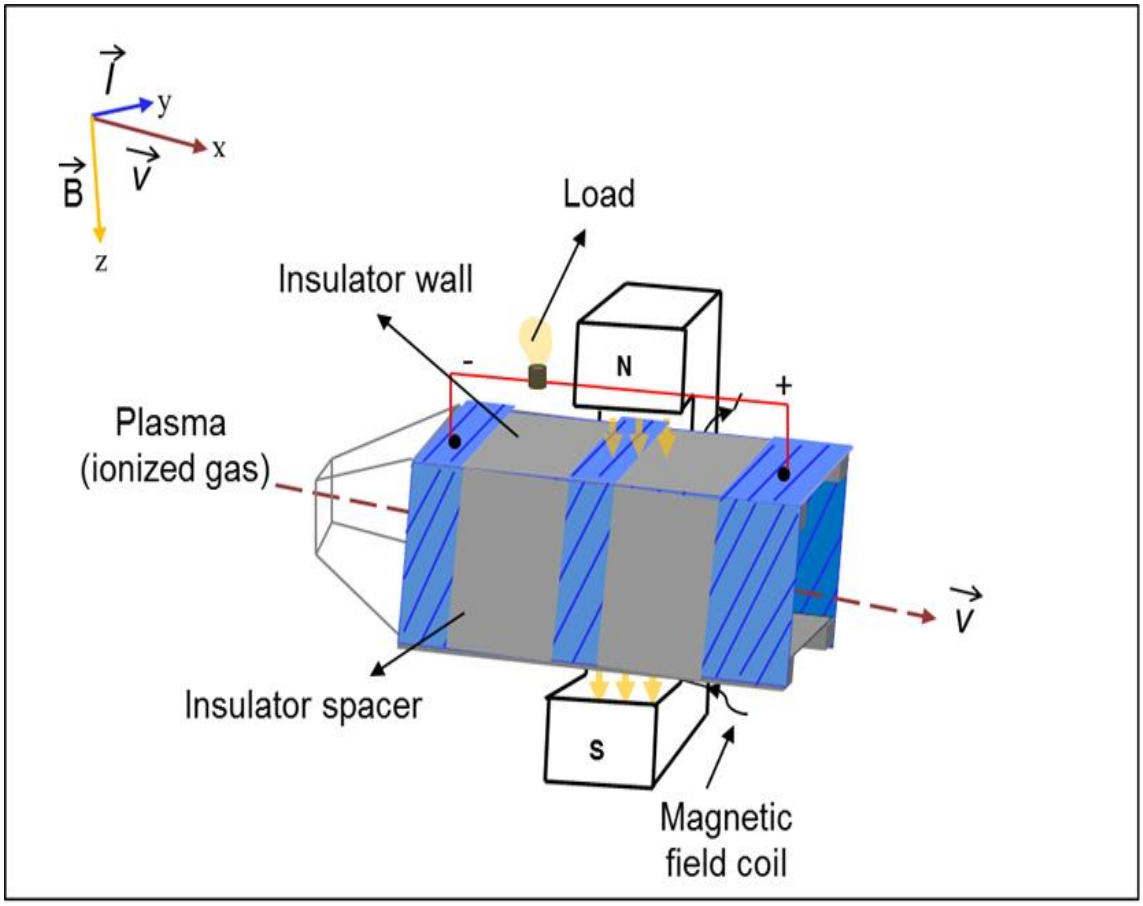

Figure 2.22: Hull generator
(Adapted from Masood *et al*., 2014:1358).

- **Series connected generator with discontinuous electrodes**

The series connected generator with discontinuous electrodes is shown in Figure 2.23. In this generator, the electrodes are connected diagonally, and the load is connected to the first and the last electrodes. Additionally, more loads can be connected to this generator if the insulator wall is arranged in the direction of electric field, (Tillack & Morley, 1998:43-44; Sedaghati *et al*., 2013:282-283).

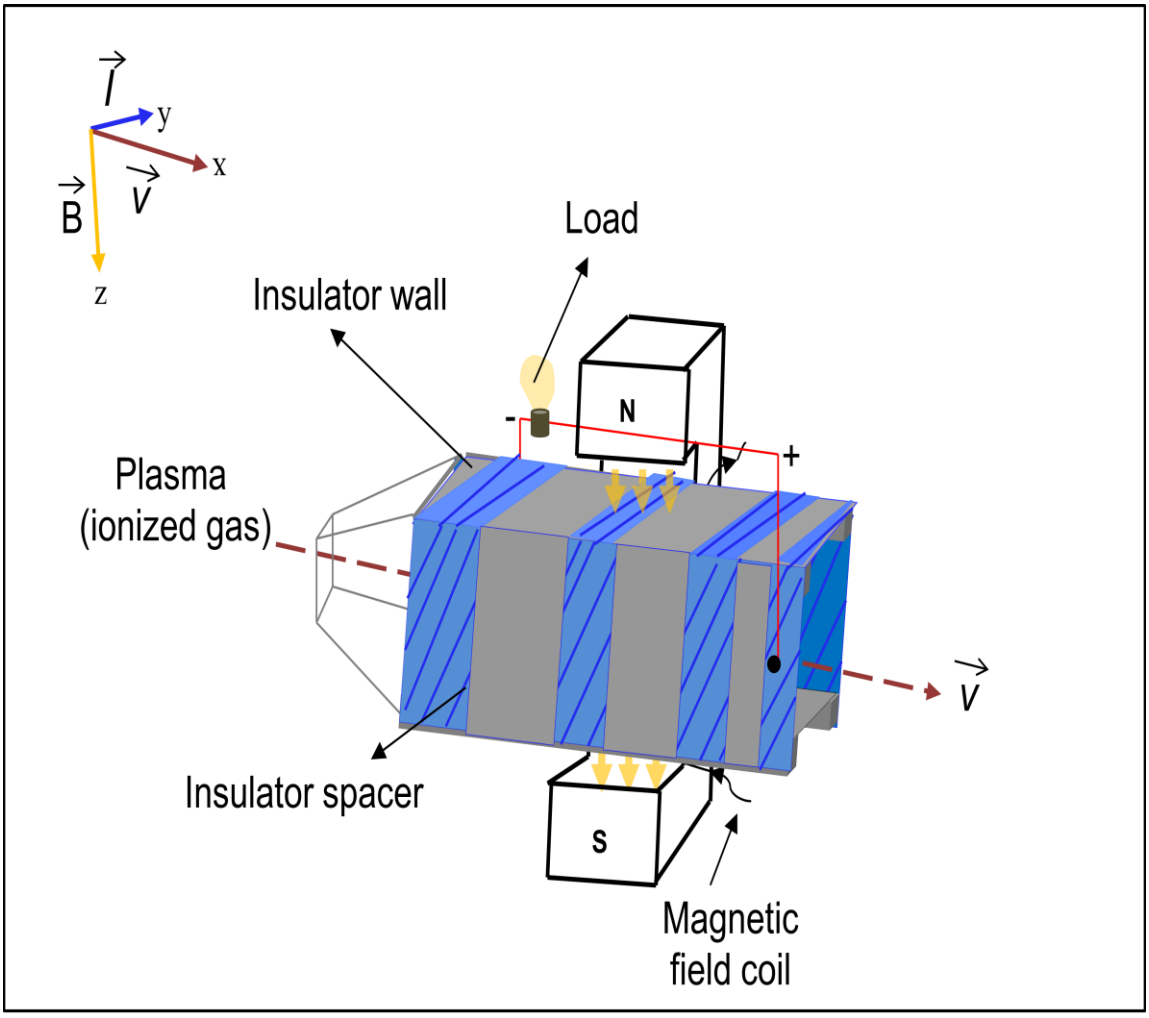

Figure 2.23: Series connected generator with discontinuous electrodes (Adapted from Sedaghati *et al*., 2013:283).

- **Disc generator**

The disc generator is shown in Figure 2.24. In this generator, the plasma flows between the centre and the edge of the disc. A circular Helmholtz coil is also placed above and under the disc to create magnetic excitations which produce Faraday's current around the edge of the disc. The advantage of this type of generator is that it is compact, and the size of the magnet is a very small (Masood *et al*., 2014:1359).

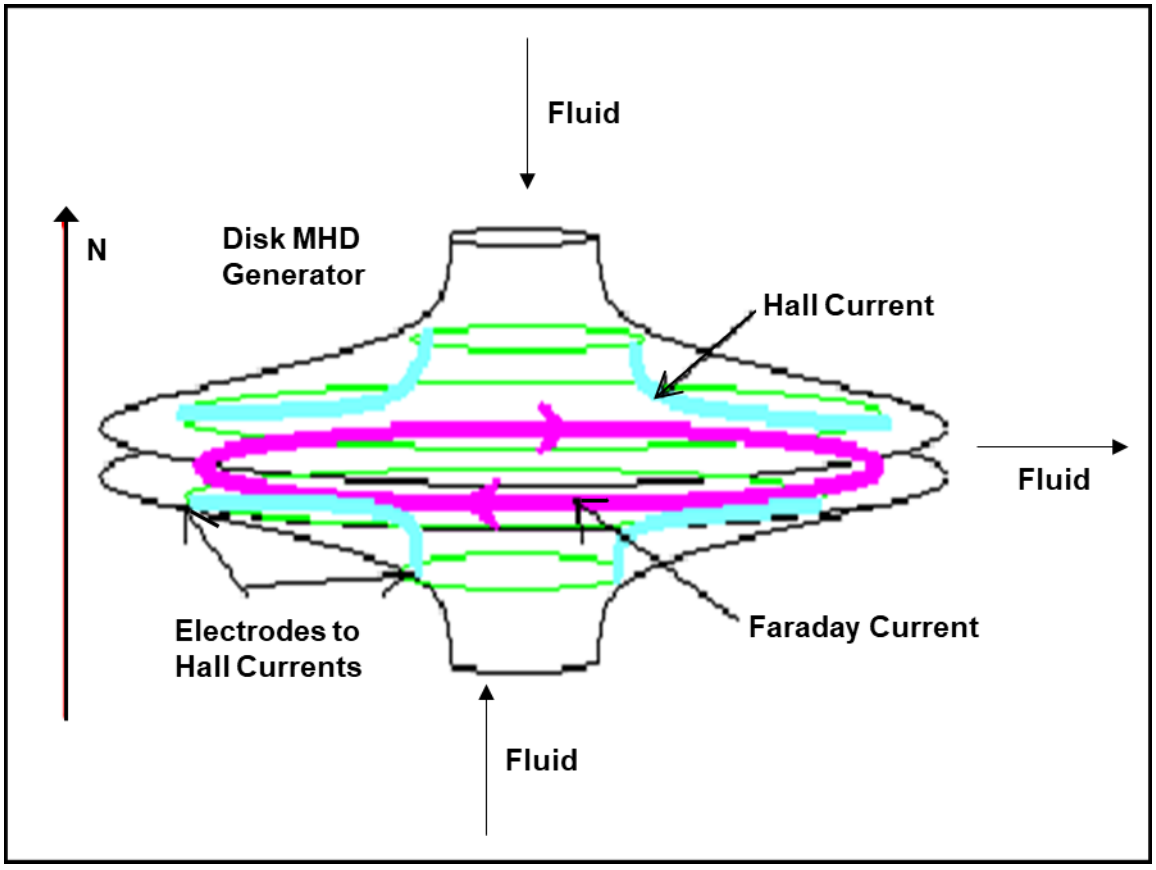

Figure 2.24: Disk generator
(From Ajith & Jinshah, 2013:4).

2.5.1.1 Fundamentals of fluid dynamics and MHD System

Fluid dynamics can be described as branch of fluid mechanics which deals with science of fluid in motion. The flow of such fluid is often guided by three different Laws: conservation of energy, conservation of mass and conservation of momentum. In addition, the fluid flow inside an MHD system can either be compressible or incompressible.

For compressible flow, there are changes in both pressure and temperature of the fluid. This causes friction effect on the fluid motion, making the flow to be viscous. Moreover, the viscous flow makes the fluid to be in an unsteady-state (turbulent flow), in which there are quick changes in the fluid pressure and velocity with respect to time. For incompressible flow, the pressure and temperature of the fluid does not change significantly with time. In this case, the fluid flow is in a steady-state (laminar flow) condition (Roman, 2014:20-22).

The tendency for an isothermal flow to become either laminar or turbulent is measured by a dimensionless quantity called the Reynolds number (R_e). This number can be described as the ratio of inertial force with respect to the viscous force inside a MHD duct (Ahsan, 2014:270-271). The Reynolds number can be determined using the diameter of the duct, fluid density and average inflow velocity of the fluid, as shown in equation 2.18 (Altintas & Ozkol, 2015:508).

$$R_e = \frac{\rho v D}{\mu}, \qquad \textbf{Equation 2.18}$$

where μ is the dynamic viscosity of the fluid, v is the fluid velocity, D is the characteristic length dimension and ρ is the fluid density.

From equation 2.18, the fluid flow can become more disordered if the inertial force is predominant over the viscous force. For a pipe duct, when the estimated R_e is below 2400, the flow is laminar. When R_e ranges between 2400 – 4000, the flow is in the transition-state (either laminar or turbulent). When R_e is above 4000, the flow becomes turbulent and it depends on many variables (Roman, 2014:22). Figure 2.25 depicts the typical parabolic shape of the flow profile for two laminar (uniform and non-uniform) and turbulent flow between two walls.

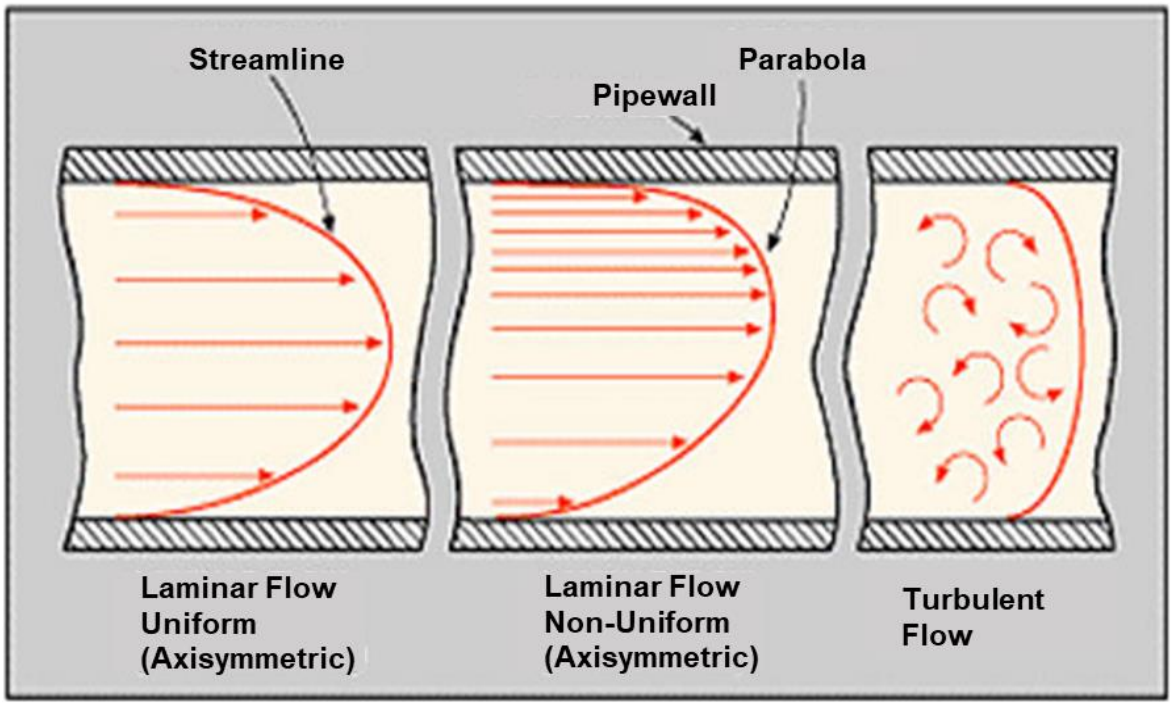

Figure 2.25: Velocity distribution of laminar and turbulent flows (From Roman, 2014:23).

2.5.1.2 MHD equations

The motion of a fluid inside an MHD system can be described using the Navier-Stokes equations (momentum and mass continuity), the Maxwell's equations and the Ohm's Law equation. The Navier-Stokes equations represent the fluid velocity with respect to time. Additionally, by applying Newton's Second Law of motion to the fluid, the resulting stress from such fluid is equal to the sum of the viscous term and proportional to the velocity and pressure gradient terms.

For an incompressible flow (Mach number > 0.3) with constant viscosity (laminar), the differential form of the Navier-Stokes momentum equation is given by equation 2.19 (Aoki *et al.,* 2012:54; Ajith & Jinshah, 2013:6; Roman, 2014:23-24),

$$\rho\left(\frac{\partial v}{\partial t}+(v\cdot\nabla)v\right)=\rho+\mu\nabla^2 v-\nabla P+j\times \mathrm{B}\ , \qquad \textbf{Equation 2.19}$$

where ρ is the fluid density, P is the fluid pressure, $j=\sigma(E+v\times \mathrm{B})$ is the current density, $j\times \mathrm{B}$ is the MHD body force, μ is the fluid dynamic viscosity, ∇ is the del operator and ∇^2 is the vector Laplacian operator.

From equation 2.19, the left term (in bracket) signifies the fluid inertia. The first term in the fluid inertia term describes the time dependent acceleration and the second term, $(v \cdot \nabla)v$, represents the convective acceleration, which gives the effect of time independent acceleration of a fluid in space. The right side of the equation 2.19 represents the summation of MHD body forces with the divergence of pressure and shear stress. The MHD body forces consist of electromagnetic and gravitational forces (Roman, 2014:24).

The Navier-Stokes momentum equation can also be used to solve a one-dimensional flow, in which equation 2.19 is simplified to linear equations. Furthermore, most non-linear problems contribute mainly to turbulent flow and can be difficult to solve unless by using a high computational fluid dynamics simulation software such as Comsol Multiphysics software (Roman, 2014:24). In any convective flow (laminar or turbulent), the mass continuity that is required to complete the flow modelling is given by equation 2.20,

$$\frac{\partial \rho}{\partial t} + \nabla \cdot \rho v = 0 \,. \qquad \textbf{Equation 2.20}$$

The Maxwell's equations can also be written as,

$$curl\ E = -\frac{\partial \mathrm{B}}{\partial t} \,, \qquad \textbf{Equation 2.21}$$

$$curl\ H = j + \frac{\partial D_e}{\partial t} \,,$$

Equation 2.22

$$div\ B = 0 \,, \qquad \textbf{Equation 2.23}$$

$$div\ D = r_v \,, \qquad \textbf{Equation 2.24}$$

where $D_e = \varepsilon_o (E + v \times \mathrm{B})$, $\mathrm{B} = \mu_o (H - v \times D_e)$ and $j = \sigma (E + v \times \mathrm{B}) + r_v v$ are the constitutive equations, ε_o is the permittivity of free space, σ is the electrical conductivity, μ_o is the magnetic permeability, D_e is the electrical flux density, E is the electrical field strength, H is the magnetic field strength, B is the magnetic flux density and r is the electric resistivity.

Considering that the fluid velocity is also included in the above constitutive equations, the field vectors that are present in these equations can lead to changes in the amount of electromagnetic quantities produced (Roman, 2014:25). Therefore, the flow of these field vectors inside an MHD system would be characterised by using the non-dimensional magnetic Reynolds number, R_{em}, given by equation 2.25.

$$R_{em} = \frac{\mu_o v D}{r}, \qquad \textbf{Equation 2.25}$$

where v is the fluid flow velocity, D is the characteristic length scale.

In addition, the flow can also be characterised by interaction parameters, N,

$$N = \frac{H_a^{\,2}}{R_e}, \qquad \textbf{Equation 2.26}$$

and Hartmann's number, H_a,

$$H_a = \mathrm{B} D \sqrt{\frac{\sigma}{\mu}}. \qquad \textbf{Equation 2.27}$$

The Hartmann's layer signifies the thickness of the viscous limit layer, δ_{H_a}, as given by equation 2.28,

$$\delta_{H_a} = \frac{1}{\mathrm{B}} \sqrt{\mu r}. \qquad \textbf{Equation 2.28}$$

In this layer, the flow is laminar and is often called viscous sublayer. Considering the velocity profile of a turbulent fluid flow near a wall (Figure 2.26), the fluid velocity reduces in radial direction before reaching the wall position. As the velocity decreases, the R_e also decreases until the flow threshold moves from turbulent to laminar flow. The region which represents the thickness of the layers between the wall and fully developed turbulent flow is known as the turbulent generation layer. This layer can either be laminar or turbulent because the flow falls between the viscous sublayer and a buffer layer. The outer layer of the flow is fully turbulent (Roman, 2014:24-26).

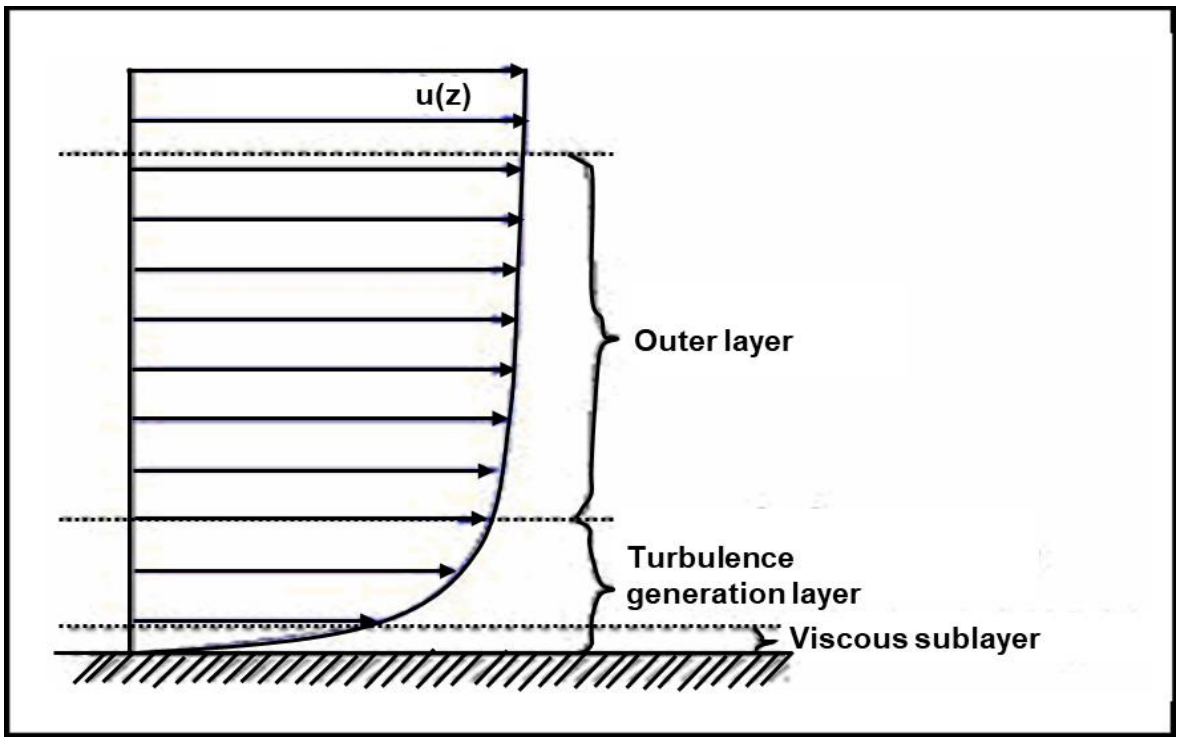

Figure 2.26: Turbulent flow profile
(From Roman, 2014:27).

2.5.1.3 Basic of MHD flow at high Hartmann's number

In a rectangular MHD duct with cartesian co-coordinate x, y and z, the fluid flow travels in x-direction while the externally applied magnetic field is aligned on the z-direction. The side of the rectangular duct wall that is aligned with the magnetic field are called side walls and the side where the walls are perpendicular to the magnetic fields are known as the Hartmann walls (Shercliff, 1953:136-140; Hunt, 1965:577–580). Considering the above mentioned flow specifications ($B = (0, 0, B_z)$ and $v = (v_x, 0, 0)$), the induced electric current flows in the negative y-direction (Figure 2.27a). When the electric current interacts with the magnetic field, a Lorentz force that opposes the pressure gradient is generated. Consequently, the velocity profiles (fields vectors and magnitudes) are flattened around the central region. Furthermore, when the H_a increases, the electromagnetic force also increases. Thus, for a given R_e, the pressure drops increase with respect to the H_a.

Another factor that has a great influence on the MHD fluid flow is the ratio between the electrical conductivity of the walls and that of the fluid. This ratio is often referred to as the wall conductivity ratio, $W_c = \sigma_w \delta_w/(\sigma_a)$, where σ is the electric conductivity, w is the duct wall, δ_w is the duct wall depth and a is the characteristic flow dimension along the magnetic field lines. Furthermore, if all the duct walls are perfectly insulated ($W_{c,side} = W_c$ and $H_a = 0$) due to charge conservation, the walls path inside the fluid domain is closed by the induced electric current stream lines (Shercliff, 1953:136-144).

The induced electric current first flow towards the side walls and, then, along the Hartmann walls (wall perpendicular to the magnetic field) up until the opposite side wall before closing the path, as shown in Figure 2.27b. Subsequently, the Lorentz force is reduced around the side walls of the duct and it is more positive near the Hartmann walls. In the region close to the side walls, the force where the side boundary layer (depth, $\delta_{side} = a/H_{a0}^{.5}$) is developed is referred to as the viscous force. In the region close to the Hartmann walls, the Lorentz force opposes the viscous force to develop Hartmann boundary layer. As the H_a increases, the Lorentz force continue to push the flow and the Hartmann boundary layer depth decreases to $\delta_{Ha} = a/H_a$. Thus, at high H_a, the boundary layers are much thinner than the side boundary layer.

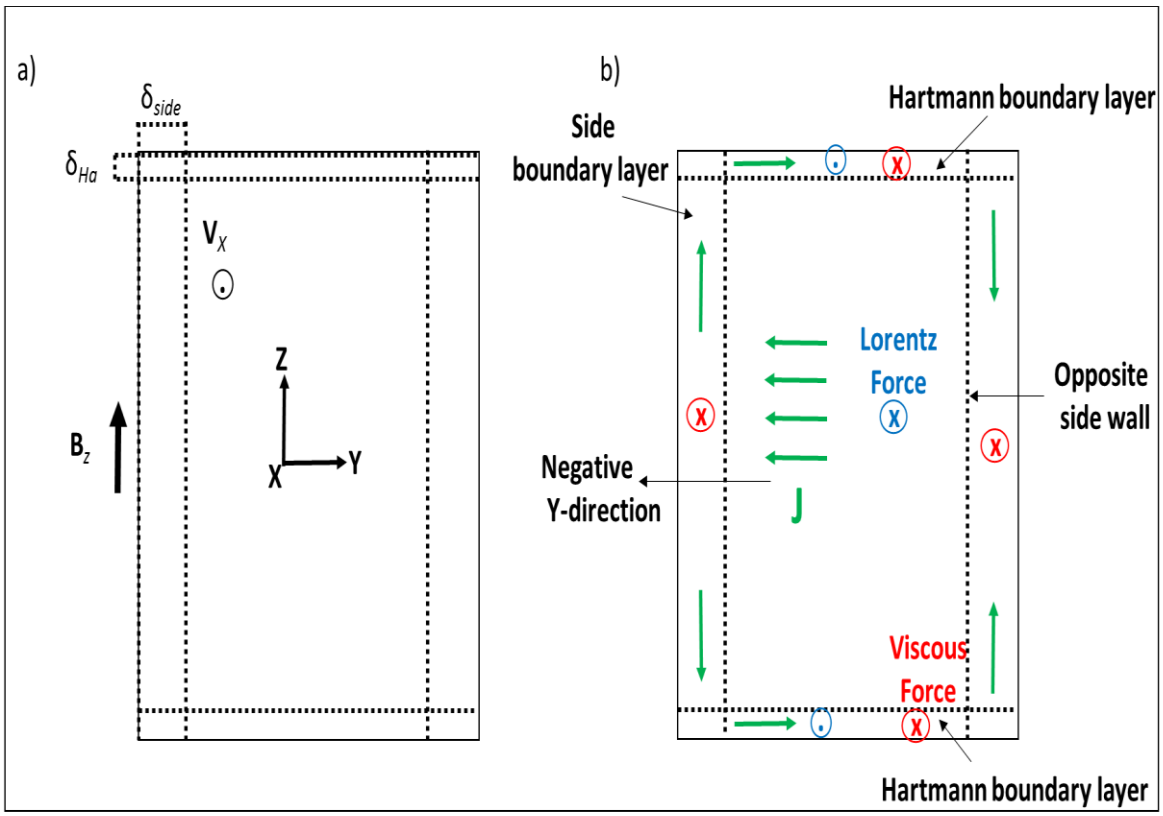

Figure 2.27: Sketch of the cross-sectional area of the MHD duct and forces acting on the fluid for $W_{c,side} = W_c$ and $H_a = 0$ (From Shercliff, 1953:136-144).

2.5.1.4 Extraction of power from an MHD generator

To perform analysis on any categories of MHD system, the following conditions are often assumed: (i) The gas should be moving at constant velocity and pressure, (ii) The operating gas should be an ideal gas, (iii) The applied magnetic field must be uniform and (iv) There should be no heat transfer to the surroundings.

When an ionised gas travels with high velocity along the MHD generator, the applied magnetic field creates an induced electromagnetic force (EMF) in the opposite direction to slows down the motion (flow) of the gas particles. Subsequently, as the particles thermal energy cuts through the magnetic force lines, an electrical energy is generated. The EMF and electric field, *E*, acting on the gas fluid is given by equation 2.29 (Ajith & Jinshah, 2013:5; Islam *et al*., 2013:746),

$$\mathrm{F} = \mathrm{Q}\left(E + v \cdot \mathrm{B}\right). \qquad \textbf{Equation 2.29}$$

In an open circuit MHD system, an electrical voltage, V, can be obtained from the gas velocity, v, the magnetic field, B, and the distance, *l*, between the electrodes, as given by equation 2.30 (Ajith & Jinshah, 2013:5; Poonthamil *et al*., 2016:145-146),

$$\mathrm{V} = v\mathrm{B}l\,. \qquad \textbf{Equation 2.30}$$

The maximum current, I_{max} flowing inside the MHD generator is given by equation 2.31 (Ajith & Jinshah, 2013:5; Poonthamil *et al*., 2016:145-146),

$$I_{max} = \frac{v\mathrm{B}A\sigma}{2}, \qquad \textbf{Equation 2.31}$$

where σ is the electrical conductivity of the fluid and *A* is the electrode surface area.

The maximum voltage, V_{max}, inside the MHD generator is given by equation 2.32 (Ajith & Jinshah, 2013:5; Poonthamil *et al*., 2016:145-146),

$$\mathrm{V}_{max} = v\mathrm{B}l - I_{max}\frac{l}{\sigma A}. \qquad \textbf{Equation 2.32}$$

Likewise, the maximum power, P_{max}, that can be extracted from the open circuit MHD generator electrodes, is given by equation 2.33 (Ajith & Jinshah, 2013:5; Sivaram *et al*., 2015:3),

$$P_{max} = \frac{\mathrm{V}^2}{4 \cdot R_l} = \frac{v^2\mathrm{B}^2l^2}{4 \cdot l/\sigma A} = \frac{v^2\mathrm{B}^2\sigma}{4} \cdot Al\,. \qquad \textbf{Equation 2.33}$$

As previously discussed by Anumaka (2014:1075), the output power, P_{out}, that can be extracted from the MHD generator electrodes with external load resistor is given by equation 2.34,

$$P_{out} = \sigma v^2 \mathrm{B}^2 Al \times k(1-k), \qquad \textbf{Equation 2.34}$$

where $k = R_L/(R_I + R_L)$, is the electrical load factor, Al is the volume of the generator, $R_I = l/\sigma A$ is the internal resistance and R_L is the external load resistance.

From equation 2.34, if the load factor ($0 \leq k \leq 1$) is approximately 0.5, the maximum output power, P_{max}, is extracted from the generator electrodes (Anumaka, 2014:1075).

The MHD system conversion efficiency can also be determined using the following equation (Ajith & Jinshah, 2013:5-6; Poonthamil *et al*., 2016:146),

$$\eta = \frac{V_{max}}{v\mathrm{B}} . \qquad \textbf{Equation 2.35}$$

2.5.1.5 The coupling of an MHD system to thermal generating plants

The generating efficiency of a typical open-cycle MHD power generator is about 62 % (Ishikawa & Itoh 2003:2111). By incorporating the MHD power generator to the conventional power plants, the overall efficiency of the combined system is increased from 40 % to about 60 %. Additionally, greater efficiency of about 65 % to 70 % can be achieved if the MHD generator, the gas turbine and the steam turbine (triple cycle) are all coupled together. Therefore, the repowering of the existing thermal power plants is possible with a significant increase in the efficiency of the plant. An MHD system can be designed as either open-cycle or closed-cycle system.

- **Open-cycle system**

In the open-cycle system, the primary fuel (coal, oil or natural gas) is first processed and burnt in the combustion chamber at high temperature of about 2273 to 2973 K (Masood *et al*., 2014:1360). To achieve such high gas temperatures, the compressed air that accompany the fuel must not be less than 1273 K. This high pressurized fluid is expanded through a convergent-divergent nozzle after leaving the combustor exit and enters the MHD duct at high velocity of about 1000 m/s, as shown in Figure 2.28 (Goel & Shukla, 2015:106). The hot gas inside the MHD duct is seeded with the injection of small amount of alkaline metals such as potassium carbonate and cesium to increase the gas electrical conductivity. The gas becomes ionised and then transversed by a uniform magnetic field to slow down the

dissociated ions and electrons. Subsequently, these particles are collected by the electrodes to produce electric current.

The hot exhaust gas exiting the duct can be recovered using a heat recovery steam generator to produce more steam that can be used for the bottom unit steam turbine (Kayukawa, 2004:38-40; Islam *et al*., 2013:747; Cicconardi & Perna, 2014:1305-1314; Masood *et al*., 2014:1360; Goel & Shukla, 2015:106; Sharma & Gambhir, 2015:5). The achievable power capacity that can be obtained from this system is about 100 MW and an efficiency of about 60 % could be realised with better heat recovery and high temperature (Dhareppagol & Saurav, 2013:102).

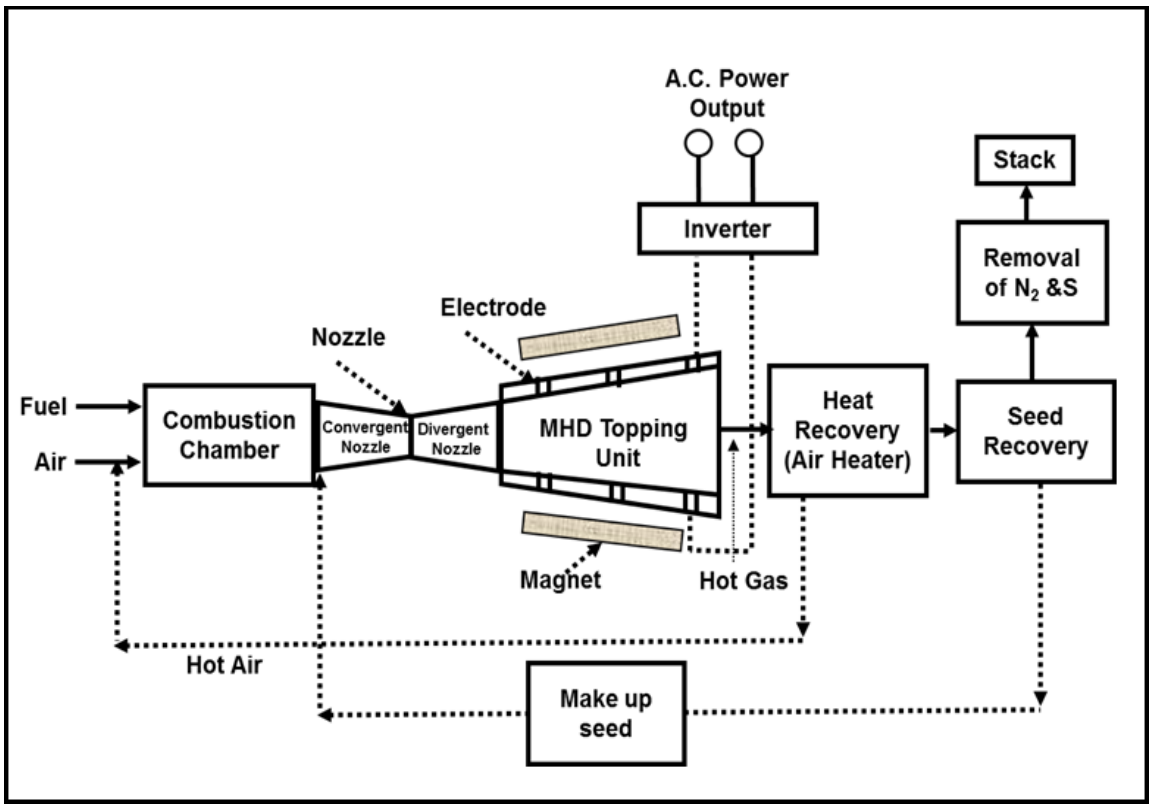

Figure 2.28: Open-cycle MHD system
(Adapted from Sharma & Gambhir, 2015:5).

Over the past years, an open-cycle Faraday type MHD power generator (pulsed MHD generator “Sakhalin”) was developed by the former Soviet Union. The length of this generator is about 4.5 m long and a continuous electrode (inlet area, 0.9 m x 1 m and outlet area, 1.6 m x 1 m) is attached to each side. The working fluid used inside this generator is solid propellant with a mass flow rate of approximately 800 kg/s. The maximum electric power output obtained from the Sakhalin generator is about 510 MW (Ishikwa *et al*., 2007:254; Dhareppagol & Saurav, 2013:102).

Other components of the Sakhalin generator are a combustion chamber with temperature of about 3800 K, a combustor pressure of about 4.0-5.6 MPa and an air-core magnet system consisting of two racetrack coils to produce a magnetic flux density of up to 2.5 T. Another open-cycle MHD power generator was developed by the USSR, with a capacity of about 25 MW and a mass flow rate of approximately 50 kg/s in 1975 (Dhareppagol & Saurav, 2013:101). Subsequently, a joint USSR effort generator was later developed with a medium capacity of 10 MW and a mass flow rate of about 50 kg/s in 1979 (Dhareppagol & Saurav, 2013:101).

In another study conducted by Avco-Everett Research Laboratory, Massachusetts, a segmented MHD power generator was successfully tested in 1959. The operating fluid used inside this generator is an argon gas seeded with powdered potassium carbonate. The operating velocity and temperature of the fluid are 240 m/s (Mach 0.7) and 2800 K, respectively. The output power obtained from this generator is about 11 kW (Kantrowitz *et al*., 1962:81; Sutton & Sherman, 1965; McClaine *et al*., 1989). Considering the high electric power generated from the open-cycle MHD system, it is clear that when this system is coupled to the South Africa thermal plants, the generating efficiency of these plants would have improved.

- **Closed-cycle system**

In the closed-cycle system, the inert gas is first heated by heat exchanger 1 at temperature of about 2273 K and then seeded with caesium vapor to get ionised. The ionised gas flows through the MHD duct to produce DC power. The hot exhaust gas leaving the duct is then recycled through another heat exchanger, as shown in Figure 2.29 (Ajith & Jinshah, 2013:8; Goel & Shukla, 2015:106). The remaining combustion products are sent to the stack after pre-heater of the air from heat exchanger 1 (Ajith & Jinshah, 2013:8; Goel & Shukla, 2015:106).

The achievable power capacity that can be obtained from the closed-cycle MHD system is about 200 MW and an efficiency of about 60% could be realised (Kayukawa, 2004:38-40; Dhareppagol & Saurav, 2013:102; Ajith & Jinshah, 2013:8; Islam *et al*., 2013:746; Goel & Shukla, 2015:106; Sharma & Gambhir, 2015:5).

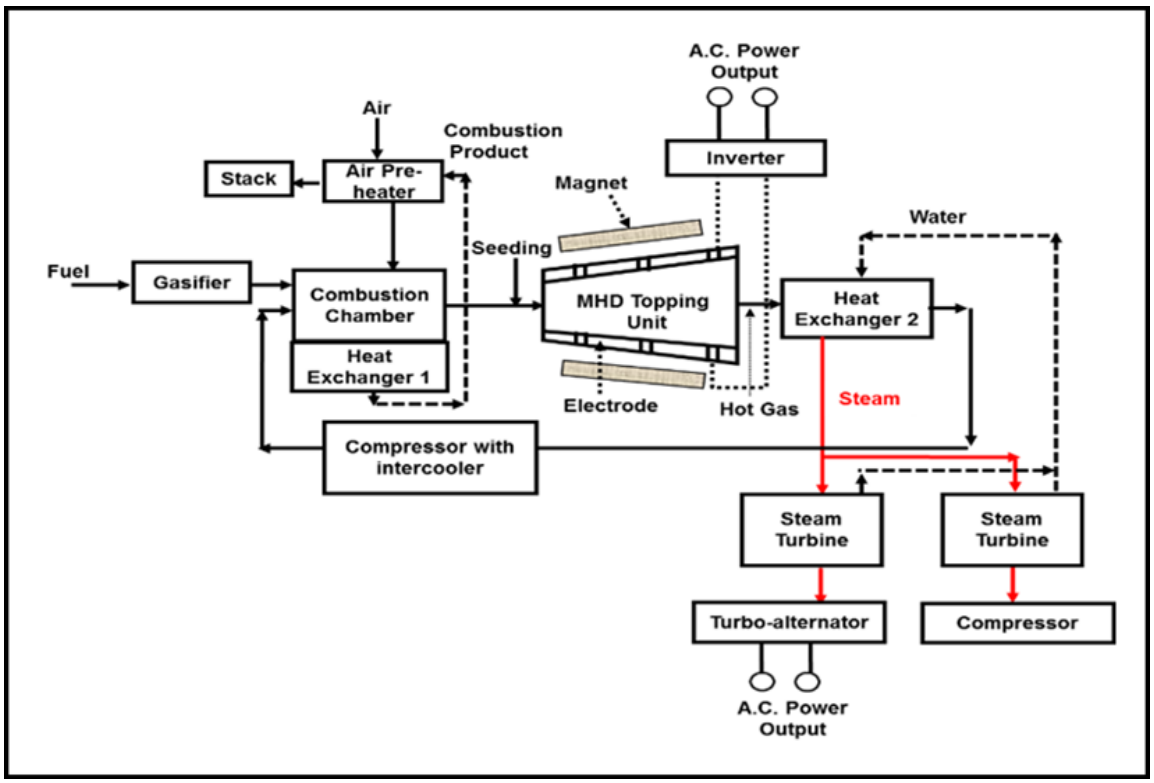

Figure 2.29: Closed-cycle MHD system (From Goel & Shukla, 2015:106).

The advantages of both open-cycle and closed-cycle MHD systems are summarised as follows (Ajith & Jinshah, 2013:3-10):

- The MHD system provides safe, efficient and reliable electric power.
- The conversion process of MHD system can significantly increase the efficiency of conventional systems to about 50-60 %.
- The MHD conversion system can be used with any heat energy source such as nuclear, solar and combustible fossil fuel.
- The MHD system reduces the amount of cooling water needed during energy conversion and it helps to reduce pollution (CO emission), which contributes to global warming.
- There are no moving parts in MHD conversion system.
- They are also cost-effective compare to the conventional systems.

2.5.2 Magnetoplasmadynamics conversion system

The magnetoplasmadynamics thruster is a powerful form of electromagnetic propulsion through which electrically charged plasma can be efficiently converted into thrust. The thruster consists of concentric electrodes: a rod-shaped cathode and a cylindrical anode. In order to operate this device, a gas is fed through the two conducting electrodes and an electric potential is applied between them. This causes electrical breakdown of the gas and a high DC arc is struck between the electrodes. Subsequently, as the cathode begins to heat up, it discharges electrons and collides with the gas to create a high temperature plasma (Nasa Facts, 2004:1-2; NPTEL, 2017:1-7). An induced magnetic field is also created at the tip of the cathodes. This field interacts with high discharge electric current lines flowing from the anode to the cathode to produce an electromagnetic force that accelerate the plasma out of the thruster in the axial direction.

Furthermore, an external magnet coil can be used to create additional magnetic fields to stabilize and accelerate the plasma discharge. The external magnetic field helps to produce a swirling motion inside the plasma jet and also direct the plasma towards the thruster axis direction. The energy created by the swirling motion is then converted into an axial energy which increases the plasma thrust. This type of device is often referred to as a self-field MPD thruster (steady-state mode), as shown in Figure 2.30 (Nasa Facts, 2004:1-2; NPTEL, 2017:1-7).

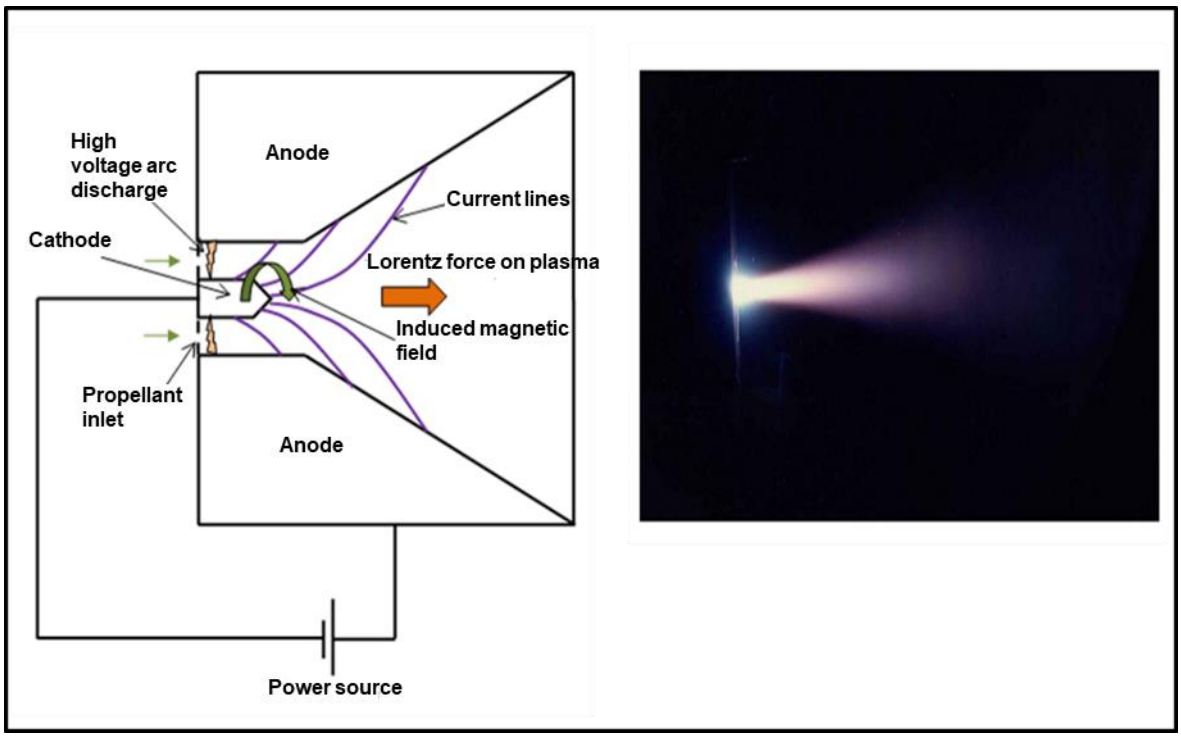

Figure 2.30: **Schematic of a self-field MPD thruster (From Nasa Facts, 2004:1-2; NPTEL, 2017:5).**

Some of the gaseous propellant used in the self-field MPD thrusters include ammonia, hydrogen, argon and lithium. Lithium MPD thrusters can produced a maximum power of about 100 kW and plasma exhaust velocity of about 50,000 m/s. An efficiency of about 45 % can be achieved from this system (Nasa Facts, 2004:1-2).

Another type of MPD device is known as the pulsed plasma thruster (Pulsed mode). This device can be used as an unsteady electromagnetic accelerator in which plasma or ionised gas is produced and accelerated in pulsed mode. In order to operate this device, a propellant gas is fed through two conducting electrodes (cathode and anode) and an electric potential is applied to the electrodes to breakdown the gas flow. This makes the gas to becomes ionised between the electrodes. The resulting current flowing across the cathode and anode electrodes also induces an electromagnetic field which create a Lorentz force acting on the ionised gas in the axial direction. Argon gas and solid such as Teflon can be used as propellants inside the pulsed plasma thruster. Figure 2.31 shows a two-dimensional schematic of a pulsed plasma thruster in parallel rail configuration.

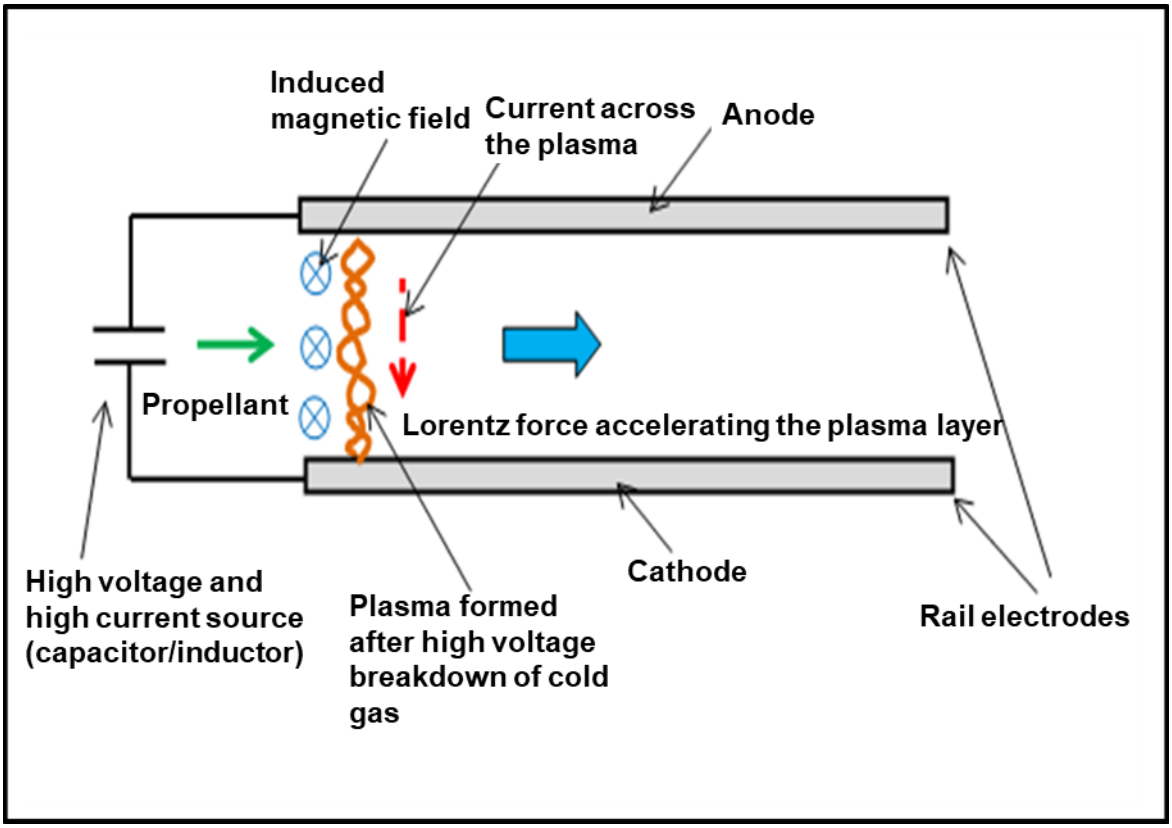

Figure 2.31: Schematic of a pulsed plasma thruster (From Nasa Facts, 2004:1-2; NPTEL, 2017:6).

Several researches on the pulsed and the steady MPD thrusters are currently being investigated by NASA to produce higher exhaust velocity and power (megawatts). The primary gas used in these thrusters is hydrogen propellant. The estimated exhaust velocity from the pulsed and the steady MPD thrusters is about 100,000 m/s, with thrust and power levels of about 100 N and 1 MW, respectively (Nasa Facts. 2004:1-2). These power and velocity could be used as thrust to drive shuttle to space unlike the ion and Hall thrusters which requires large ion thruster devices to process megawatts of power. Another advantage of using the MPD thrusters is that they are mechanically robust and can create more propulsion compared to the conventional electric propulsion systems.

2.6 Conclusion

The fundamental principle of Faraday's Law of electromagnetism and fluid dynamics have been discussed in this chapter. Several sources of plasma and categories of the MHD conversion system are presented. The chapter also presents alternative methods through which the MHD system can be coupled to thermal power stations. The concluding part of the chapter presents the theory of the MPD conversion system. Based on the MHD and MPD concepts discussed in the chapter, the next chapter focuses on the numerical simulation of an ionised gas inside a rectangular duct in which the duct is configured to act as generator and accelerator.

CHAPTER THREE: MODELLING AND SIMULATION OF MHD AND MPD CONVERSION SYSTEMS

3.1 Introduction

This chapter covers the simulations of the viscous flow of an ionised gas inside a rectangular duct based on the principle of Faraday's Law of electromagnetism and fluid dynamics. Several numerical investigations concerning the fluid flow along the MHD duct have been previously conducted: Ramos & Winowich (1990:907-910) applied a finite element method to study the fluid flow inside an MHD duct with respect to Reynolds number, electrode length and electrical conductivity. The result obtained showed that the fluid velocity profile in the axial direction under an external magnetic field was continuously distorted into M-shapes when the Reynolds number and the length of the electrode were increased (Ramos & Winowich, 1990:907-910; Daoud & Kandev, 2008:1).

Andreev *et al*. (2006:3) also reported an experimental study on the liquid metal flow inside a rectangular duct under a uniform magnetic field using Eutectic GaInSn alloy. The outcome of their experiment showed that when a Reynolds number (between 500 and 16000) and Hartmann's number (400) were applied, three regions, which include the turbulence suppression, M-shape profile and two wall jet regions were identified (Andreev *et al*.**,** 2006:10). In another study, Gedik *et al*. (2013:23-24) also carried out a numerically study on the influence of a uniform transverse magnetic field on liquid-metal flow inside a circular pipe. The operating fluid used inside the pipe was Eutectic Galinstan GaInSn alloy (Gedik *et al*.**,** 2013:24).

Aoki *et al.* (2012:53-60) also uses a rectangular micropump MHD model to couple Navier-Stokes and Maxwell equations using electrolytes as the working fluid. The aim of their study was to use a fixed magnetic field with changing electric fields to create a propulsion of the electrolyte fluid. In doing so, an interaction exists between these two fields and the levels of movement produced in terms of the fluid velocity distribution and current density. The electromagnetic forces produced when the induced current density vectors are coupled to the applied magnetic field vectors is known as the Lorentz force.

Considering these previous investigations, vast majority of the MHD studies deals mostly with laminar flows and minor works have been done on turbulence flows related to plasma thrusters. Therefore, there is a need to perform more research on MHD generators and DC MPD thrusters with high Reynolds number using propane (fluid). This fluid is considered because it is commercially available, and the combustion products are not harmful to the environment (DME, 1996).

In the present study, the fluid flow parameters such as pressure, velocity profiles and current density can be obtained through performing a three-dimensional (3-D) numerical modelling and simulation. The understanding of the flow of the fluid along the duct domain is very important in the design of MHD and MPD conversion systems. In order to represent these systems, the duct model is configured to act as generator and accelerator.

3.2 Three-dimensional modelling of an ionised gas inside an MHD/MPD duct

3.2.1 The duct geometry and design

The rectangular MHD/MPD duct is designed with Solidworks software and then imported to Comsol Multiphysics 5.1 software for simulations. The density, dynamic viscosity and electrical conductivity of the gas used for this modelling represent a propane fluid. Furthermore, the design configuration selected is a rectangular duct with segmented electrodes. The segmented electrodes are selected to alleviate the disadvantage posed by the continuous electrodes. The dimensions of the duct, the copper chrome zirconium electrodes and the two-neodymium permanent magnets can be seen in Figure 3.1.

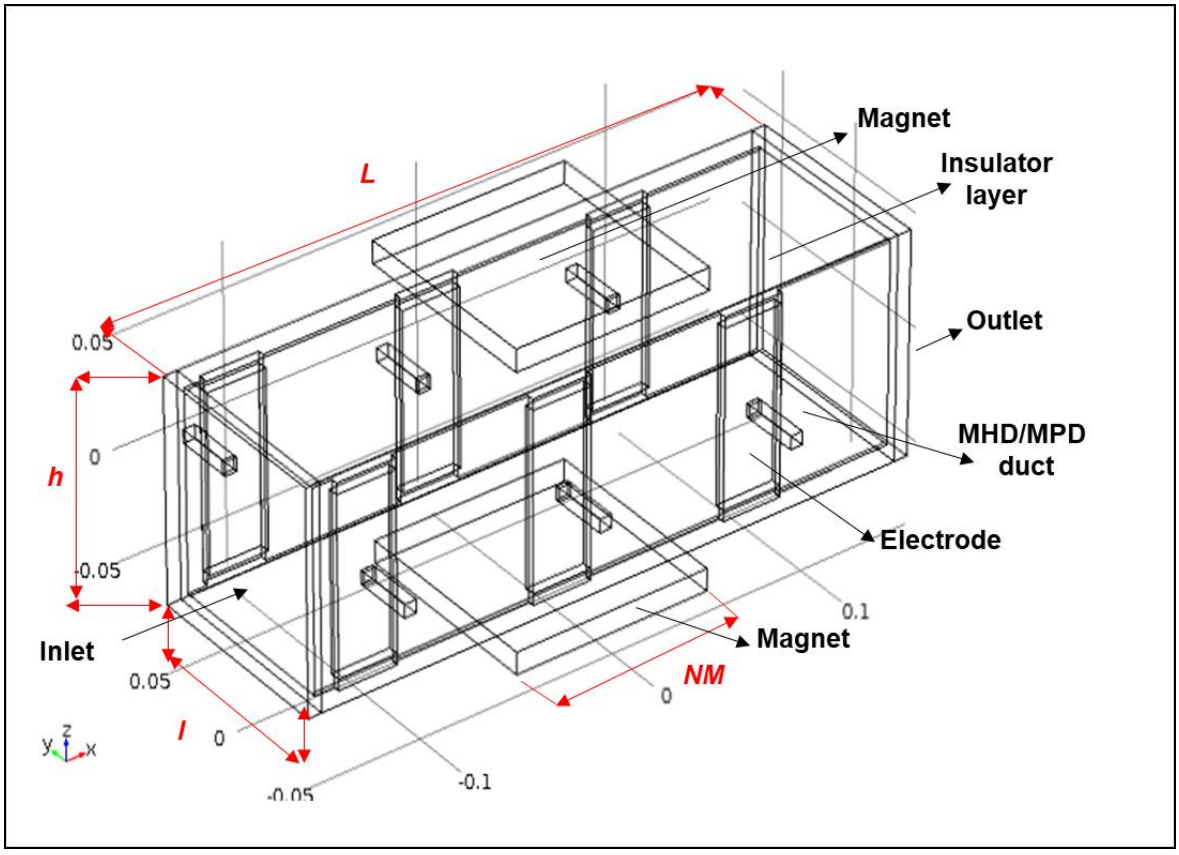

Figure 3.1: Rectangular duct with length, *L* = 0.3 m, height, *h* = 0.1 m and width, *l* =0.1 m. The neodymium magnets, *NM*, length is 0.1 m.

From Figure 3.1, the duct plane is located at the horizontal x-y plane (plane z=0). The neodymium magnets (*NM*) along the z-direction represent the applied external magnetic field and is perpendicular to the fluid direction. The remanent flux density (B) of the magnets are used to simulate the external magnetic field. The electrical conductivity of the copper chrome zirconium electrodes is 5.2e07 S/m and the relative permeability of the entire system is $\mu_r = 1$. Furthermore, an aluminium oxide insulator is placed between the duct wall and the magnets. The fluid domain is bounded by an air-cube medium, which represents the real environmental conditions. The air-cube is hidden from Figure 3.1 so as to view the duct domain properly. For this investigation, three numerical modellings (study 1, 2 and 3) are conducted.

In the first study, the fluid inflow velocity (1 m/s) is studied numerically with varying magnetic remanent flux density (0 T, 1.12 T, 1.32 T and 1.41 T) and a fixed external voltage (30 V). The aim is to examine the influence of the resulting Lorentz forces on the fluid. The electrical conductivity of the fluid is 100 S/m.

In the second study, the fluid inflow velocities (0.2 m/s, 0.5 m/s, 1 m/s, 2 m/s and 5 m/s) are studied numerically with a fixed remanent flux density (1.41 T) and a fixed external voltage (30 V). The aim is to accelerate the fluid inflow velocities and also to enhance thrust productivity. The electrical conductivity of the fluid is 20 S/m. The external electric potential is imposed to the electrodes along the y-direction to see the effect of the magnetic field on the fluid velocities. In doing so, an enhancement of the fluid propulsion (thrust) relating to the applied magnetic and electric fields is created.

In the third study, the fluid inflow velocity (2 m/s) is studied numerically with varying voltage applied to the duct electrodes (10 V, 20 V, 30 V, 40 V and 100 V) and a fixed remanent flux density (1.41 T). The aim is to accelerate the fluid velocity at a temperature of about 10000 K with the applied external electric potentials. The electrical conductivity of the fluid is 20 S/m.

3.2.2 The duct boundary conditions

In order to determine whether the fluid flow will behave as laminar or turbulence, the rectangular duct domain must be characterized based on geometry, fluctuating scales and boundary conditions. The dimensions of the duct inlet are depicted in Figure 3.2. In this figure, the width and height of the inlet are 0.1 m and 0.1 m, respectively. These dimensions are used to determine the hydraulic diameter, D_h, of the duct.

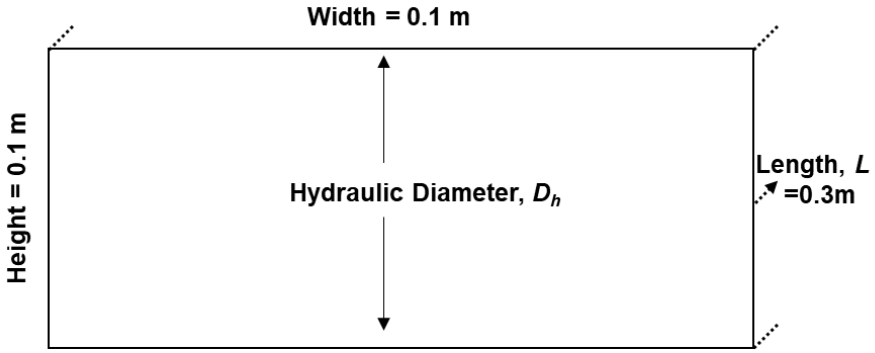

Figure 3.2: Inlet of the rectangular duct.

From Figure 3.2, the hydraulic diameter of the duct can be determined using equation 3.1 (Wang *et al.,* 2012:67),

$$D_h = \frac{2lh}{l+h} = 0.1 \text{ m}, \qquad \textbf{Equation 3.1}$$

where '*l*' and '*h*' are the width and height of the duct inlet.

Furthermore, the tendency for an isothermal fluid flow to become either laminar or turbulent is measured by the Reynolds number value. This number can be explained as the ratio of inertial forces with respect to the viscous forces inside the rectangular duct. This number can be determined using the hydraulic diameter of the duct and the average velocity (*v*) of the fluid, as given by equation 3.2 (Wang *et al.,* 2012:67),

$$R_e = \frac{\rho v D_h}{\mu}, \qquad \textbf{Equation 3.2}$$

where ρ is the fluid density and μ is the dynamic viscosity of the fluid.

- **Study 1**: The boundary conditions set for the fluid domain in this study consist of no-slip velocity at the duct wall. A fixed fluid velocity is imposed as the boundary condition at the inlet of the rectangular duct while at the duct outlet, a zero-pressure condition is imposed. From equation 3.2, a propane fluid velocity of 1 m/s, density of about 1.83 kg/m3 and dynamic viscosity of about 8.01e-06 pa.s, produce a Reynolds number of about 22846. Since this Reynolds number is greater than the critical Reynolds number for turbulent flow (i.e. > 4000), a viscous k-ε turbulent flow simulation is considered for this study. In addition, the inlet velocity value chosen ensured that the fluid flow inside the duct is turbulence.

Furthermore, the effect of the fluid flow inside the duct can be determined using the interaction parameters in equation 2.26 and the Hartmann's number in equation 2.27 (Daoud & Kandev, 2008:1-2; Kandev, 2012:3-4). Table 3.1 shows the Hartmann's numbers and the interaction parameters for the selected remanent flux densities, fluid velocity (1 m/s), Reynolds number and electrical conductivity.

Table 3.1: Hartmann's numbers and interaction parameters for the selected remanent flux densities, fluid velocity, Reynolds number and electrical conductivity.

Remanent flux density [T]	σ [S/m]	R_e	H_a	N
0	100	22846	0	0
1.12	100	22846	395.73	6.9
1.32	100	22846	466.40	9.5
1.41	100	22846	498.20	10.9

- **Study 2**: The boundary conditions set for the fluid domain in this study consist of no-slip velocity at the duct wall. Several fluid velocities (0.2 m/s, 0.5 m/s, 1 m/s, 2 m/s and 5 m/s) are imposed as the boundary condition at the duct inlet while at the duct outlet, a zero-pressure boundary condition is imposed.

Table 3.2 shows the Hartmann's number and the interaction parameters for the selected fluid velocities, Reynolds numbers, remanent flux density and electrical conductivity.

Table 3.2: Hartmann's number and interaction parameters for the selected fluid velocities, Reynolds numbers, remanent flux density and electrical conductivity.

Fluid inflow velocity, V_{inlet} [m/s]	σ [S/m]	B [T]	R_e	H_a	N
0.2	20	1.41	4569	222.8	10.86
0.5	20	1.41	11423	222.8	4.346
1	20	1.41	22846	222.8	2.173
2	20	1.41	45693	222.8	1.086
5	20	1.41	114232	222.8	0.435

From Table 3.2, when the fluid inflow velocities and Reynolds number are decreased, the interaction parameters are increased. However, at higher velocity, a higher magnetic obstacle is required to achieve strong magnetic interaction within the flow structure.

- **Study 3**: The boundary conditions set for the fluid domain in this study consist of no-slip velocity at the duct wall. Several voltages (10 V, 20 V, 30 V, 40 V and 100 V) are applied to the duct electrodes while a fixed fluid velocity (2 m/s) with electrical conductivity of about 20 S/m is imposed as the boundary condition at the duct inlet (Table 3.2). A fixed remanent flux density of about 1.41 T is also imposed at the center of the duct while a zero-pressure is imposed as the boundary condition at the duct outlet.

3.2.3 Optimized MHD/MPD equations in Comsol Multiphysics software

An ionised gas can be modelled as fluid because their field vectors behave as a single charged fluid (Ayeleso *et al*., 2015:206-208). This fluid moves with the same velocity and its behaviour can be studied using the electromagnetic field and fluid dynamics terms of Maxwell and Reynolds-Average Navier-Stokes (RANS) equations. These equations have been optimised and adapted into Comsol Multiphysics software for numeric computational studies. For electromagnetic field equations, the Gauss Law is given by equation 3.3 (Aoki *et al*., 2012:54),

$$\nabla . E = \frac{\rho_e}{\varepsilon_0} \quad . \qquad \textbf{Equation 3.3}$$

The Faraday's Law can be written as,

$$\nabla \times E = -\frac{\partial \mathrm{B}}{\partial \mathrm{t}} \quad . \qquad \textbf{Equation 3.4}$$

The non-magnetic monopole can be written as,

$$\nabla \cdot \mathrm{B} = 0 \quad . \qquad \textbf{Equation 3.5}$$

The Ampere's Law can be written as,

$$\nabla \times \mathrm{B} = \mu_0 j + \mu_0 \varepsilon_0 \frac{\partial E}{\partial t} \quad . \qquad \textbf{Equation 3.6}$$

The convenient form of Ohm's Law in MHD and MPD systems can be written as,

$$j = \sigma \left(E_m + v \times \nabla \times A_m \right) \quad , \qquad \textbf{Equation 3.7}$$

where j is the total current density, A_m is the magnetic vector potential, $E_m = -\nabla \varphi$ is the electric field intensity and φ is the electrical potential.

For fluid dynamics, the equation of the incompressible viscous k-ε turbulent flow and the solver algorithms have been optimized in Comsol Multiphysics. The model coefficients of these equations have also been fine-tuned by computer optimization with real experimental data (Daoud & Kandev, 2008:1-2; Kandev, 2012:5).

The *k*-omega (*k*-ω) turbulence flow model is not used because it is sensitivity to free stream values of the ω and it is also numerically less robust than the *k*-ε model (Comsol Multiphysics, 2015). The *k*-ε turbulence model for fluid dynamics can be grouped into two categories: The first category is the fluid velocity and pressure components while the second category is the turbulence components (*k* and ε).

$$\nabla \cdot v = 0 \ , \qquad \textbf{Equation 3.8}$$

$$\rho(v \cdot \nabla)v = \nabla \cdot \left[-p\mathrm{I} + (\mu + \mu_{\mathrm{T}})\left(\nabla_v + (\nabla_v)^{\mathrm{T}}\right)\right] + \mathrm{F} \ , \qquad \textbf{Equation 3.9}$$

$$\rho \nabla \cdot (v) = 0 \, , \qquad \textbf{Equation 3.10}$$

$$\rho(v \cdot \nabla)k = \nabla \cdot \left[\left(\mu + \frac{\mu_T}{\sigma_k} \right) \nabla k \right] + P_k - \rho\varepsilon \ , \qquad \textbf{Equation 3.11}$$

$$\rho(v \cdot \nabla)\varepsilon = \nabla \cdot \left[\left(\mu + \frac{\mu_T}{\sigma_\varepsilon} \right) \nabla \varepsilon \right] + C_{\varepsilon 1} \frac{\varepsilon}{k} P_k - C_{\varepsilon 2} \rho \frac{\varepsilon^2}{k} \ , \qquad \textbf{Equation 3.12}$$

where

$$P_k = \mu_T \left[\nabla v : \left(\nabla v + (\nabla v)^T \right) \right], \qquad \textbf{Equation 3.13}$$

$$\mu_T = \rho C_\mu \frac{k^2}{\varepsilon} . \qquad \varepsilon_o = ep . \qquad \textbf{Equation 3.14}$$

Equations 3.8, 3.9, 3.11 and 3.12 represent the mass conservation, momentum, turbulence kinetic energy, *k*, and dissipation rate, ε, of a gas fluid in motion. In these equations, p is the pressure, F, is the volumetric Lorentz force, ρ is the fluid density and μ_T is the turbulent viscosity. The terms $C_\mu = 0.09$, $C_{\varepsilon 1} = 1.44$, $C_{\varepsilon 2} = 1.92$, $\sigma_k = 1$ and $\sigma_\varepsilon = 1.3$ are the constants of the turbulence model (Comsol Multiphysics, 2015). The coupling of electromagnetic field and fluid dynamics equations can be achieved through the current density in equation 3.7 and the Lorentz force ($\mathrm{F} = \mathrm{J} \times \mathrm{B}$) in equation 3.9.

For the simulation parameters, a free tetrahedral shaped mesh is used for all the calculations. The mesh sizes are chosen to achieve sufficient accuracy within a reasonable computational time. The fluid domain is uniformly meshed with a high mesh density (fine) in the surrounding area of the neodymium magnets and near the duct wall due to high magnetic field and velocity gradients.

All simulations are carried out using the Comsol Multiphysics commercial software, which is used to solve iteratively, the partial differential equations (3-dimensional) of the fluid dynamics and electromagnetic field in conditions typical of the MHD and MPD systems.

3.2.4 Simulation results of a propane fluid flow with a fixed velocity, a fixed external voltage and varying magnetic field (Study 1)

In this section, the simulation results of the flow of a propane fluid with a fixed velocity, a fixed external voltage and varying magnetic remanent flux density are discussed.

- **Magnetic flux densities**

The magnetic flux density distributions along the rectangular duct relating to the selected magnetic remanent flux densities (0 T, 1.12 T, 1.32 T and 1.41 T) are shown in Figure 3.3. In this figure, the maximum magnetic flux densities of 0.09449 T, 0.1116 T and 0.1191 T are obtained at the center of the duct.

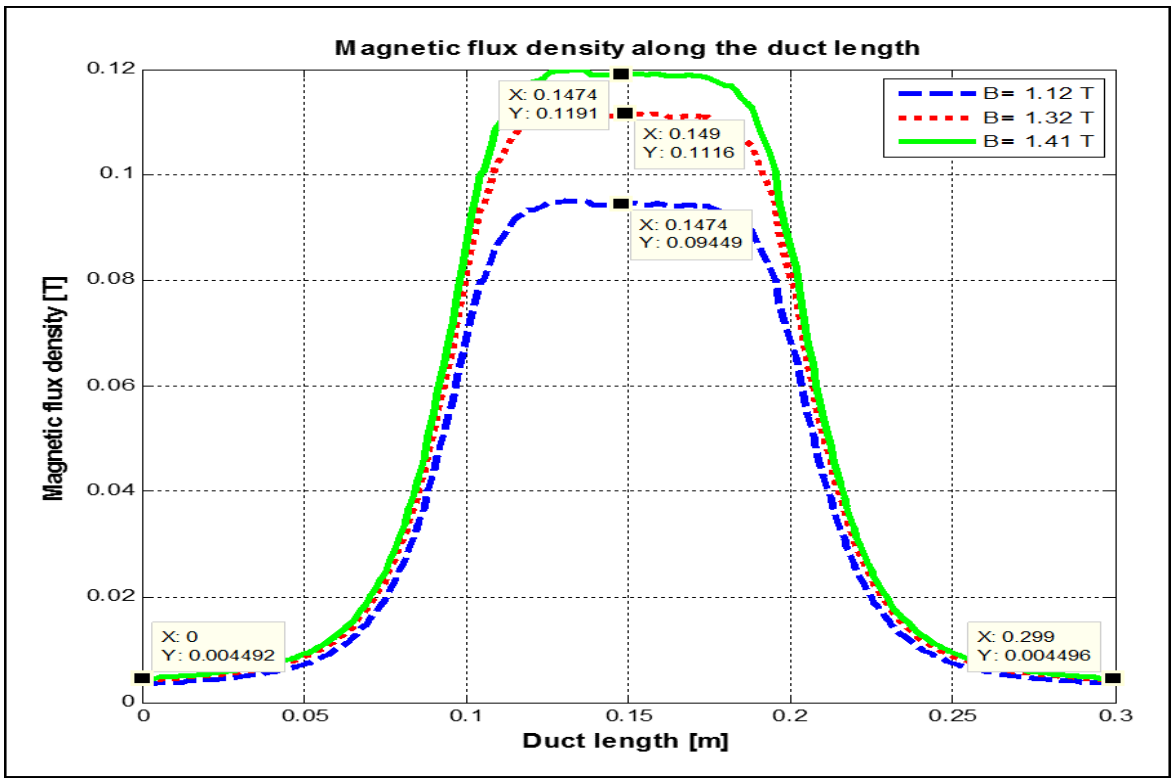

Figure 3.3: **Magnetic flux densities along the duct length.**

- **Lorentz forces due to the applied magnet remanent flux densities**

The Lorentz forces acting on the fluid are more intense at the center of the duct due to the applied magnet remanent flux densities, as shown in Figure 3.4.

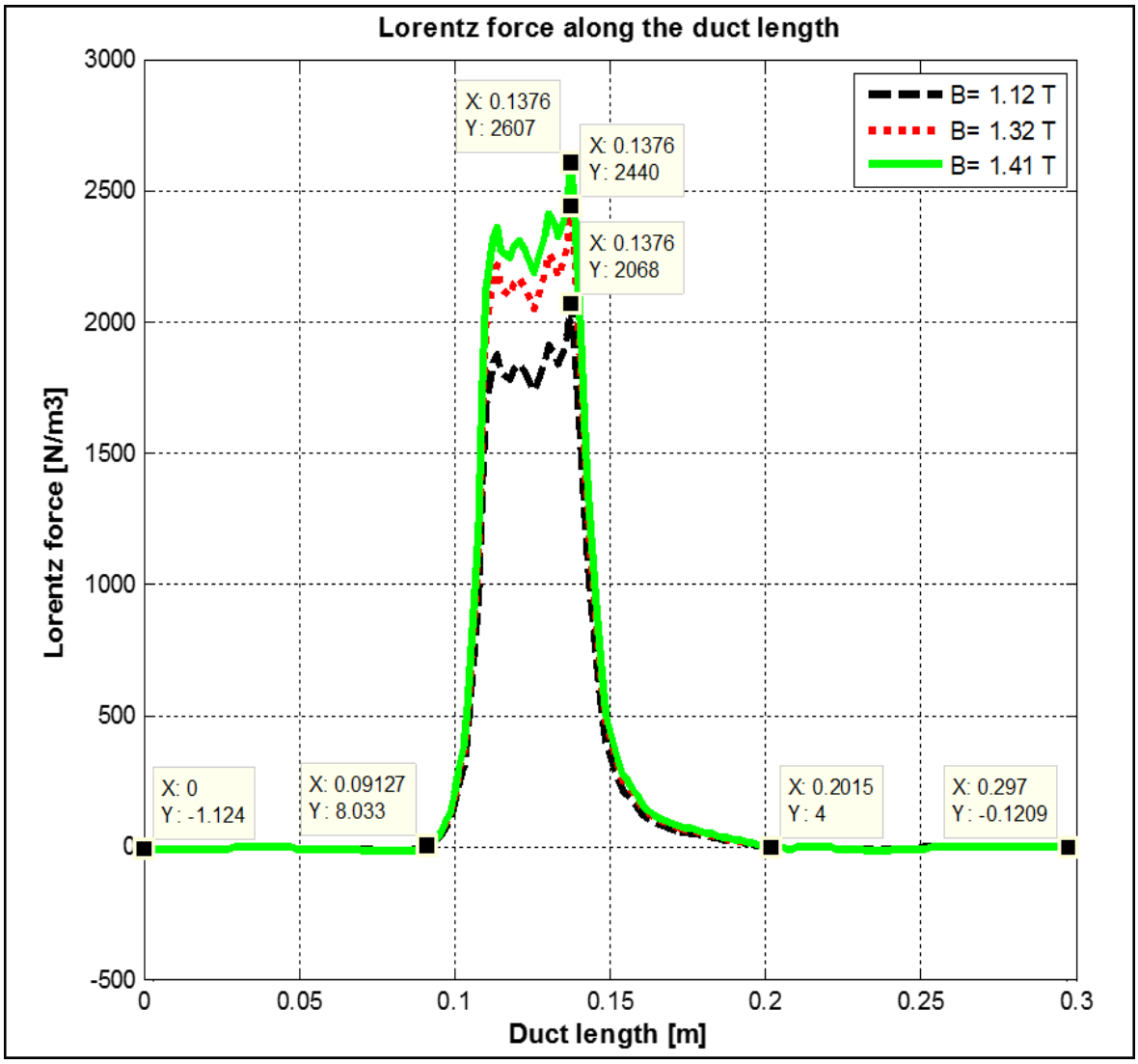

Figure 3.4: **Lorentz forces due to the applied magnet remanent flux densities.**

From the Lorentz force distributions, the fluid field vectors decelerate to lower values at the middle region between x = 0.1 m and 0.2 m, as shown in Figure 3.5. Additionally, the field vectors continue to decelerate when the applied magnetic fields are increased from 0 T to 1.41 T, particularly at positions where there are higher Lorentz forces. Figure 3.5 shows the M-shaped velocity profiles of the fluid, which are formed due to the interaction between the magnetic fields and the fluid, especially in the areas where the electrodes are positioned. Similar patterns have been reported by (Aoki *et al*., 2012:57-59).

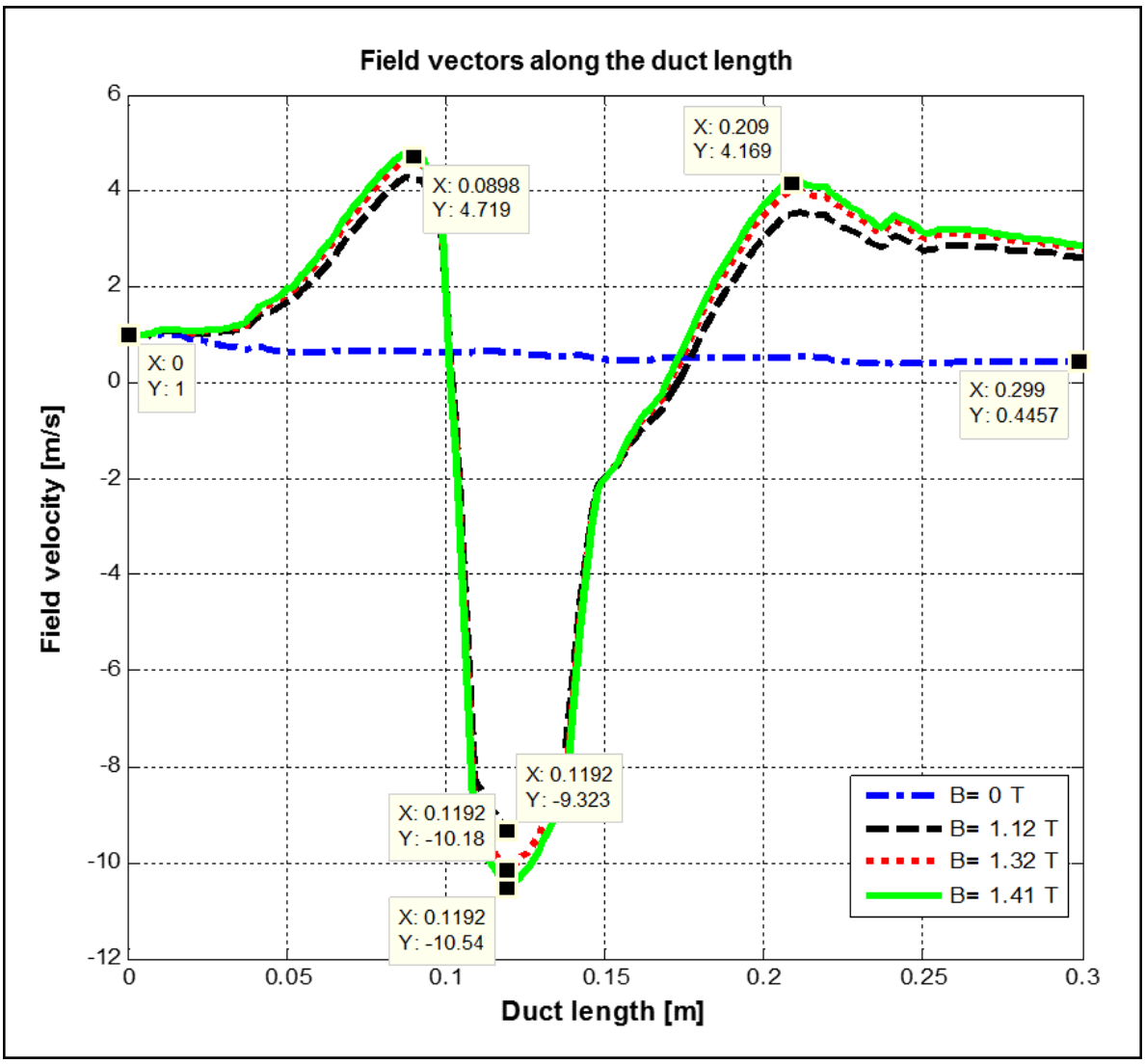

Figure 3.5: **The velocity of the fluid field vectors due to the Lorentz forces.**

- **Pressure distributions of the fluid for each applied remanent flux density**

The pressure distributions of the fluid for each applied remanent flux density along the duct length are shown in Figure 3.6. These pressures are low at the duct inlet and gradually increases at the center of the duct due to the intensity of the applied magnetic fields and then decreases to zero at the duct outlet, as indicated in the boundary condition.

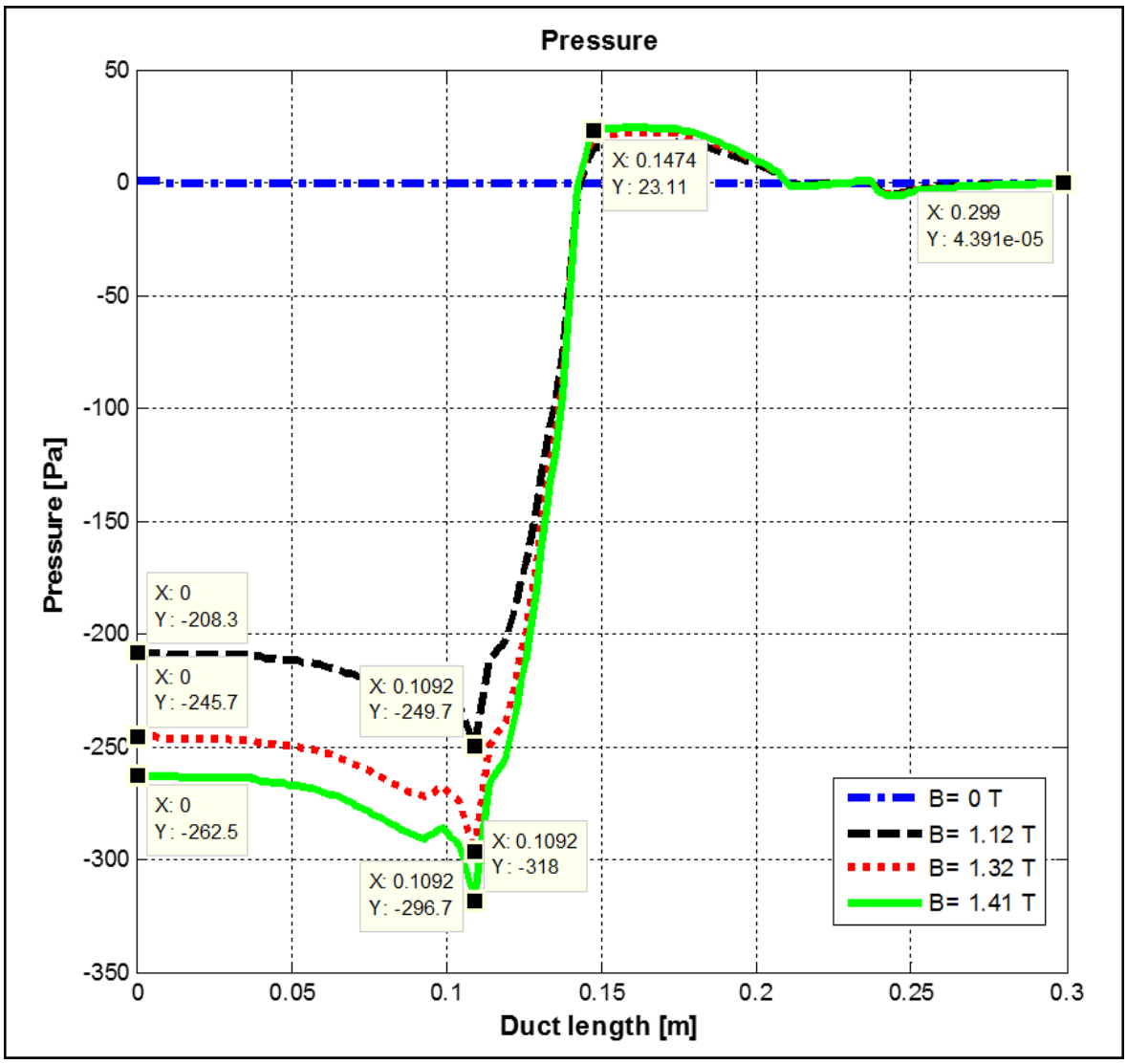

Figure 3.6: Pressure distributions of the fluid for each applied remanent flux density along the duct length.

- **Fluid velocity magnitudes for each applied remanent flux density**

The velocity magnitudes (speed per seconds) of the fluid along the duct length for each applied remanent flux density are depicted in Figure 3.7. In this figure, the field vectors of the fluid accelerate towards the electrodes walls at the center of the duct (MPD mode). By applying an external load resistor to the duct electrodes, this field vectors can be captured (MHD mode). One of the reasons for high velocity magnitude is that when the field vectors are slowed down by the applied magnetic field, they are also attracted to the electric potential (30 V) imposed to the electrodes. Therefore, these field vectors are accelerated in the direction of the electrodes, and result to the increase of the fluid velocity magnitudes, as shown in Figure 3.7. When the magnetic field of 1.41 T is applied, the field vectors are most accelerated (10.92 m/s). Conversely, when the magnetic field of 1.12 T is applied, the field vectors are least accelerated (9.517 m/s).

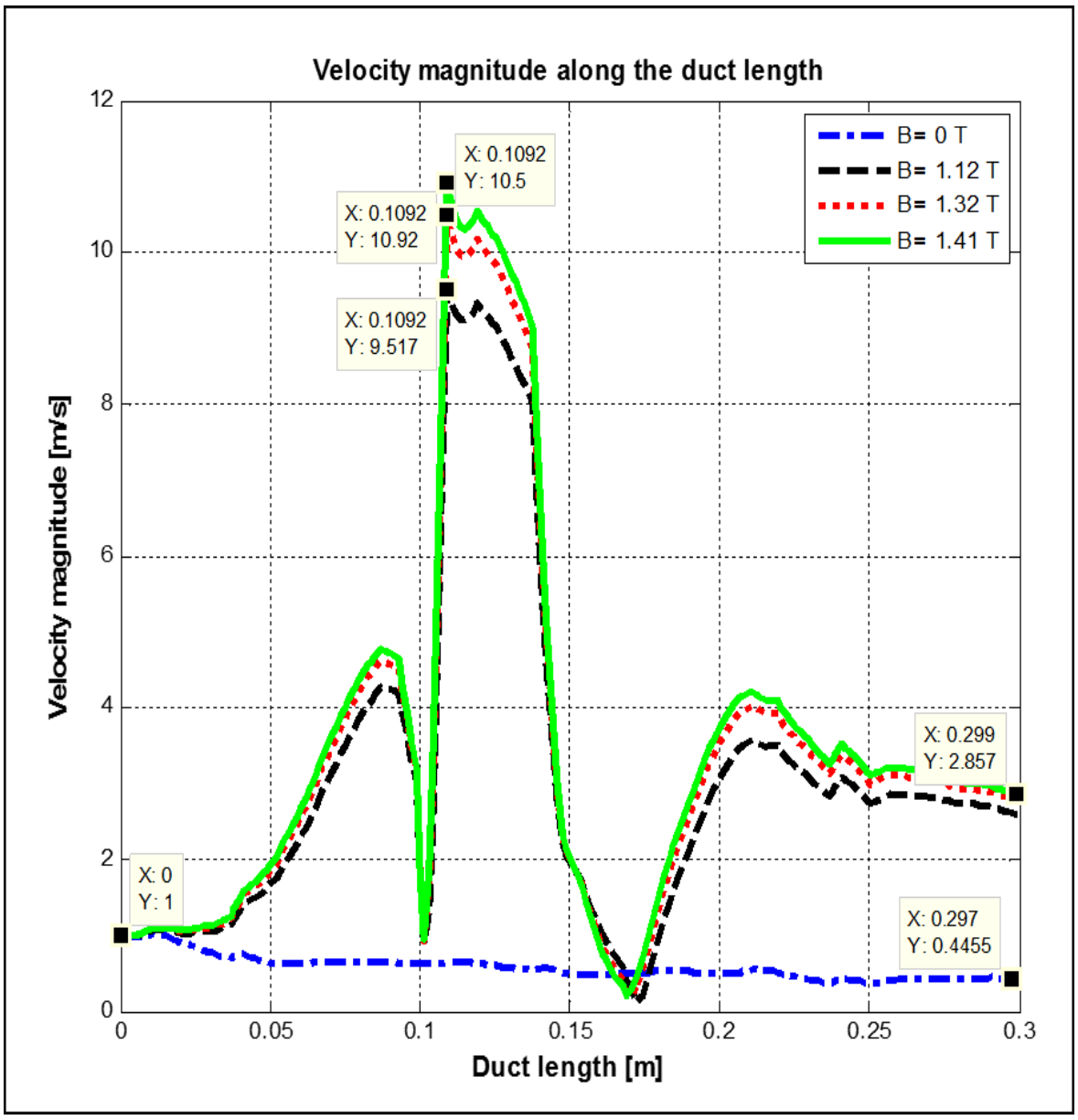

Figure 3.7: Fluid velocity magnitudes for each applied remanent flux density.

- **Patterns of the fluid velocity magnitudes for each applied remanent flux density**

The patterns of the fluid velocity magnitudes along the duct length relating to the applied remanent flux densities are depicted in Figure 3.8. In this figure, the velocity magnitudes are higher at the electrode walls when the remanent flux densities of 1.12 T, 1.32 T and 1.41 T are applied. In the absence of magnetic field, the velocity magnitudes are low at the electrode walls and the field vectors are more populated at the center of the duct.

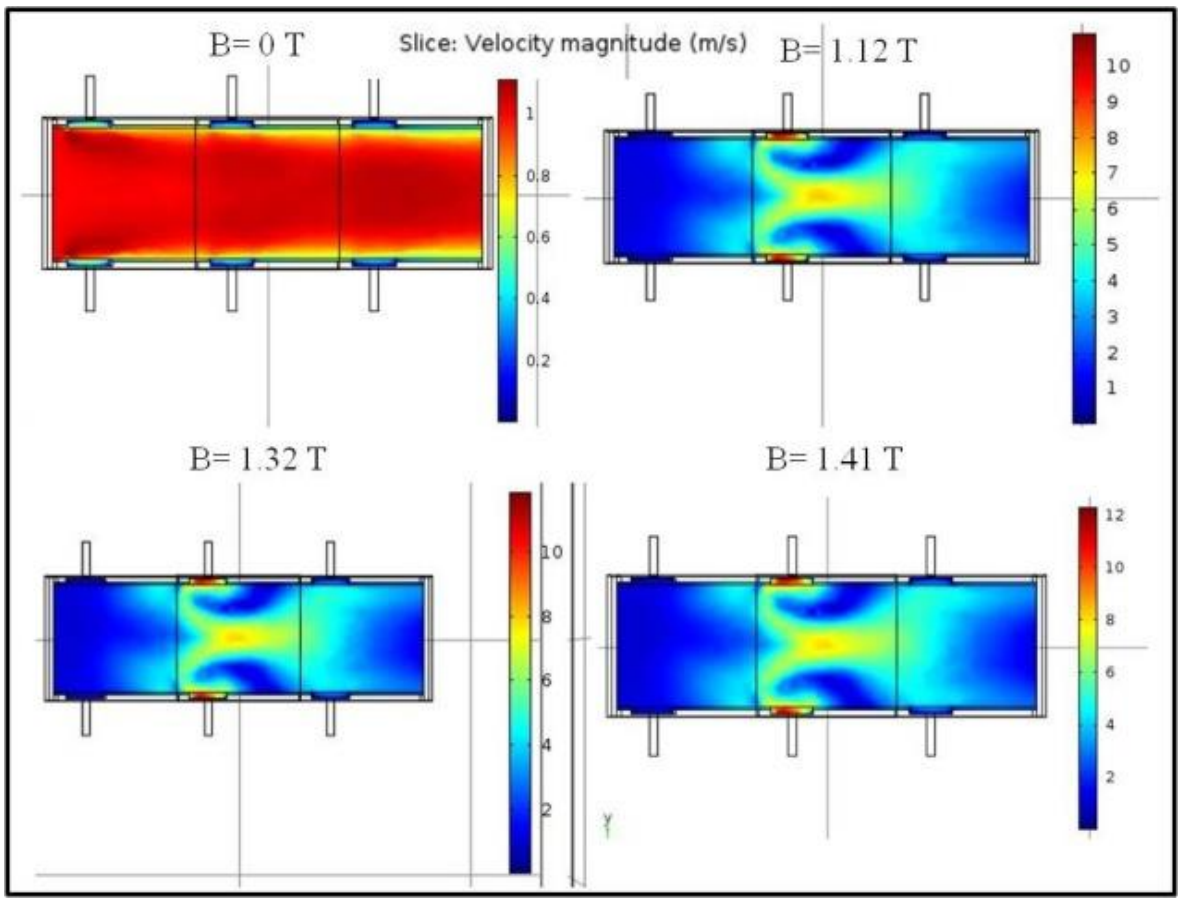

Figure 3.8: Patterns of the fluid velocity magnitudes for each applied remanent flux density.

3.2.5 Simulation results of a propane fluid flow with varying velocity, a fixed external voltage and a fixed magnetic field (Study 2)

In this section, the simulation results of the flow of a propane fluid with varying velocity, a fixed external voltage and a fixed magnetic remanent flux density are discussed.

- **Magnetic flux density**

The highest remanent flux density (B=1.41 T), which produces the highest magnetic obstacle in study 1 is used to decelerate the motion of the fluid in study 2. The resulting magnetic flux density distribution along the duct length is shown in Figure 3.9. In this figure, the maximum magnetic flux density (0.1193 T) is obtained at the center of the duct.

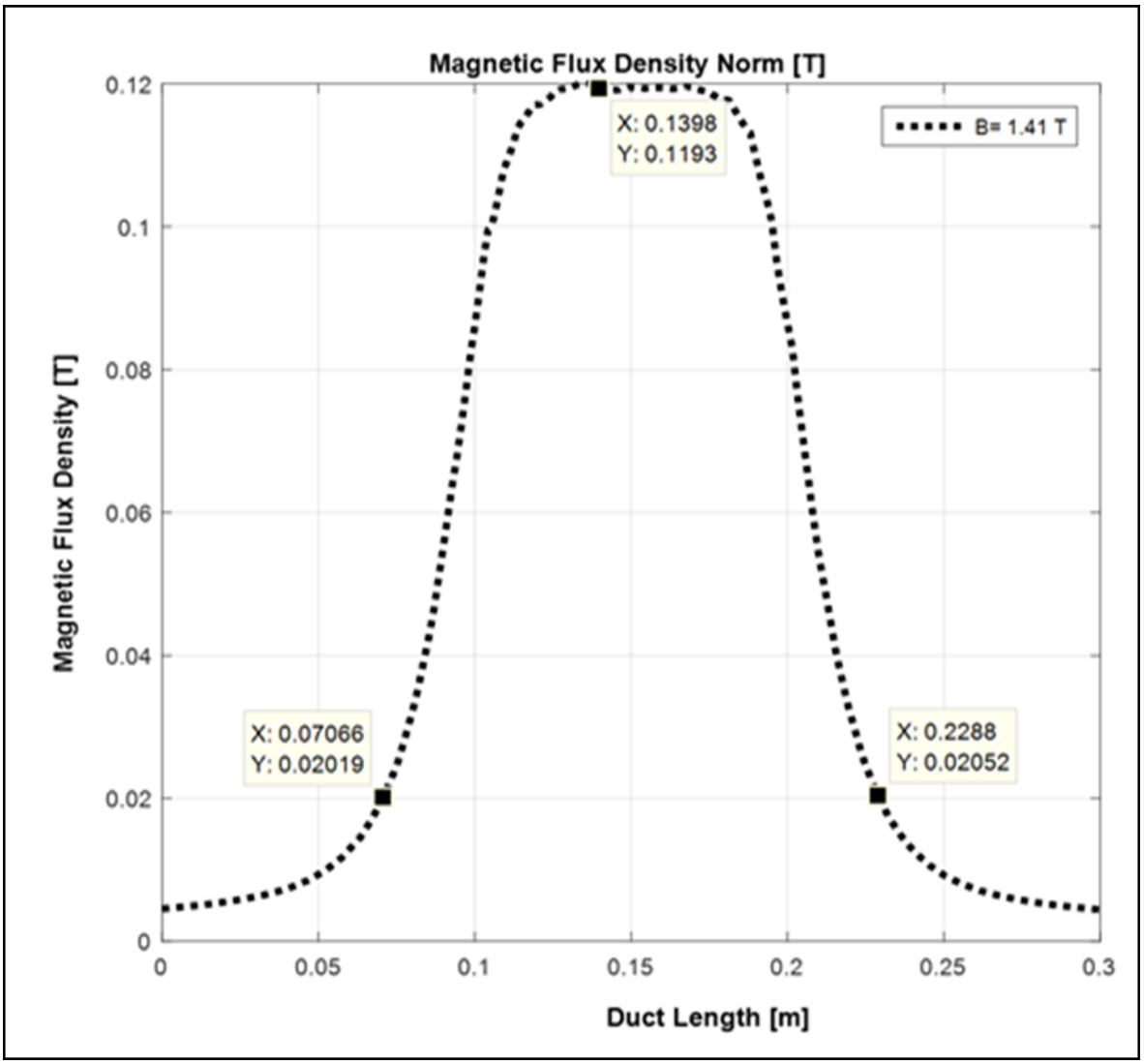

Figure 3.9: Magnetic flux density along the duct length.

- **Lorentz force due to the applied magnetic remanent flux density**

The Lorentz force acting on each fluid inflow velocities (0.2 m/s, 0.5 m/s, 1 m/s, 2 m/s and 5 m/s) is more intense (560.9 N/m^3) at the center of the duct, as shown in Figure 3.10. However, at higher fluid velocities, a higher magnetic field is required to create a higher Lorentz force that could decelerate the motion of such fluid.

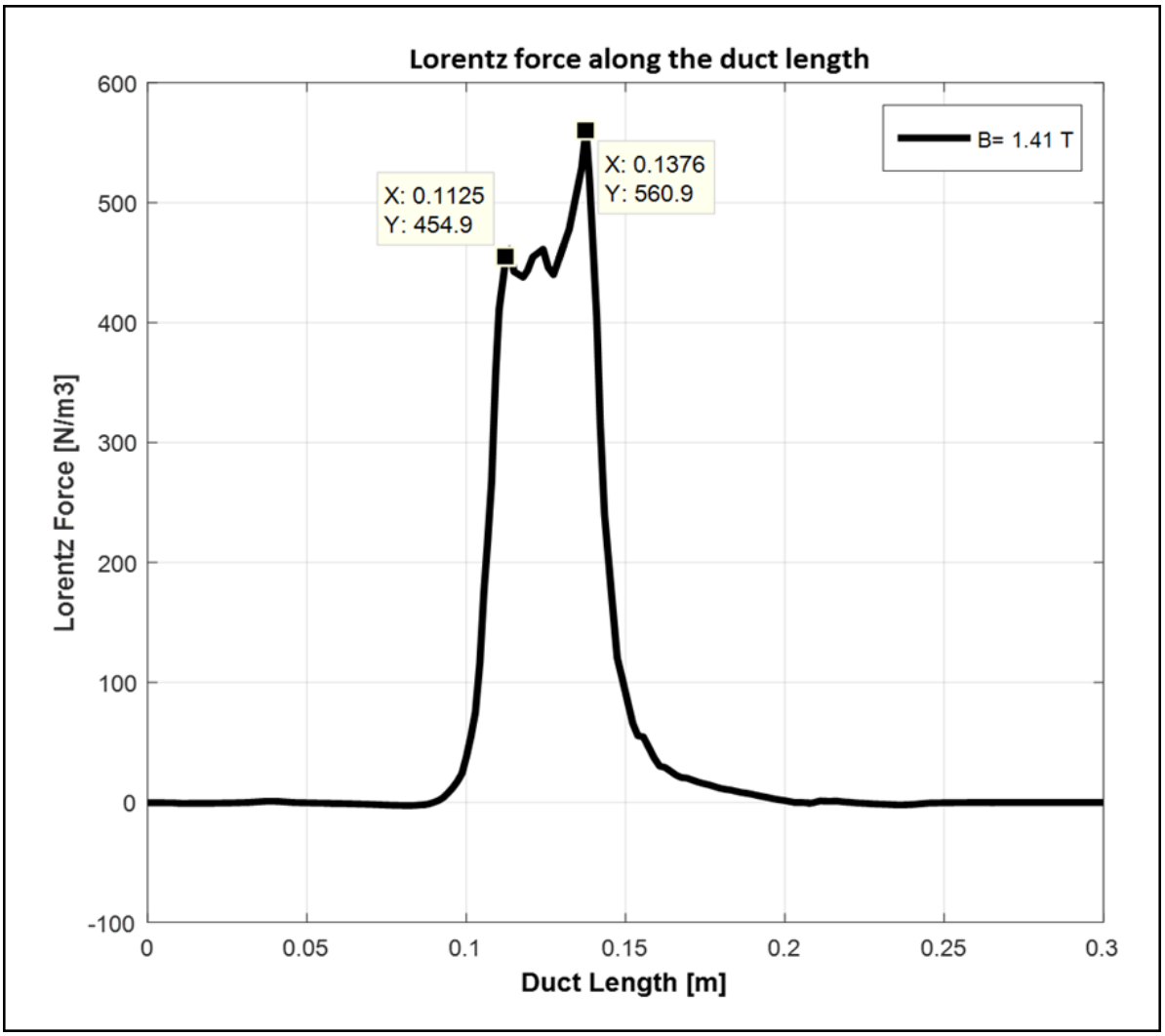

Figure 3.10: Lorentz force due to the applied magnetic remanent flux density.

Considering Figure 3.10, the electromagnetic force is used to slow down the fluid motion along the duct length. When the fluid attempts to avoid areas of high magnetic field, an M-shaped velocity profile is created in the span-wise direction within the stagnant region created at the center of the magnetic gap.

Figure 3.11 shows the influence of the magnetic obstacle on the fluid velocities. In this figure, the higher the interaction parameter, the stronger the Lorentz force traversing the movement of each fluid inflow velocity. Furthermore, the field vectors of each fluid inflow velocity continue to decelerate to lower values at the center (x = 0.1 m and 0.2 m) of the duct. When the fluid velocity of 2 m/s is applied at the duct inlet, the field vectors are most decelerated (-5.007 m/s) with the remanent flux density of 1.41 T. Conversely, when the fluid velocity of 5 m/s is applied, the field vectors are least decelerated (-4.226 m/s) with the same remanent flux density. One reason why the highest fluid inflow velocity (5 m/s) decelerated less than the rest of the fluid inflow velocities (0.2 m/s, 0.5 m/s, 1 m/s and 2 m/s) is because the ratio of the Lorentz force to the inertial force is very small to create a strong retarding effect for fluid at higher velocity (i.e. v = 5 m/s). Thus, the retarding effect due to the Lorentz force is weak in such case.

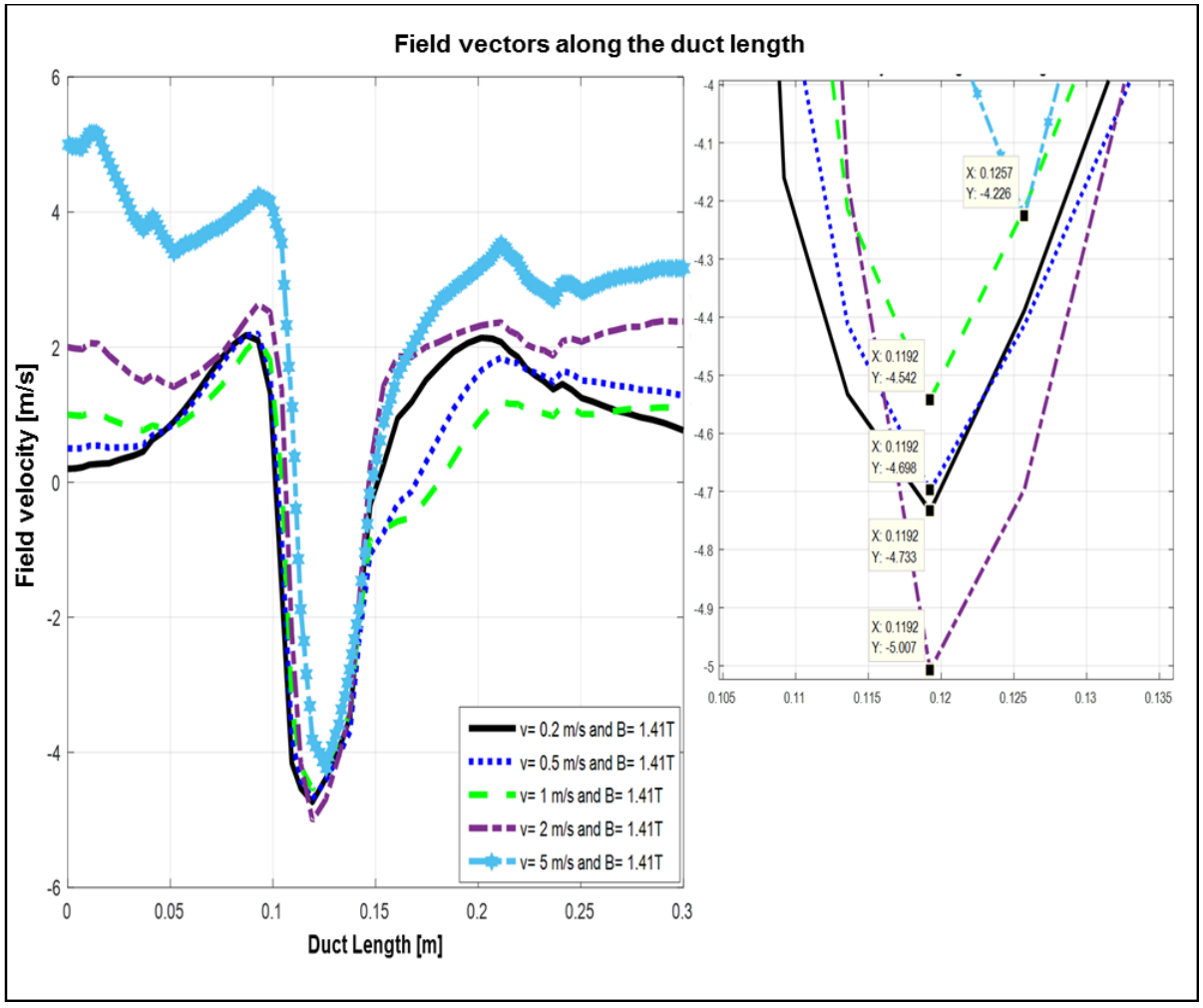

Figure 3.11: Field vectors of each fluid inflow velocity due to the Lorentz force.

- **Pressure distributions of the fluid for each inflow velocity**

The pressure distributions of the fluid for each inflow velocity along the duct length are depicted in Figure 3.12. These pressures are low at the inlet of the duct and gradually increases at the center of the duct due to the intensity of the applied magnetic field and then decreases to zero at the outlet of the duct as indicated in the boundary condition.

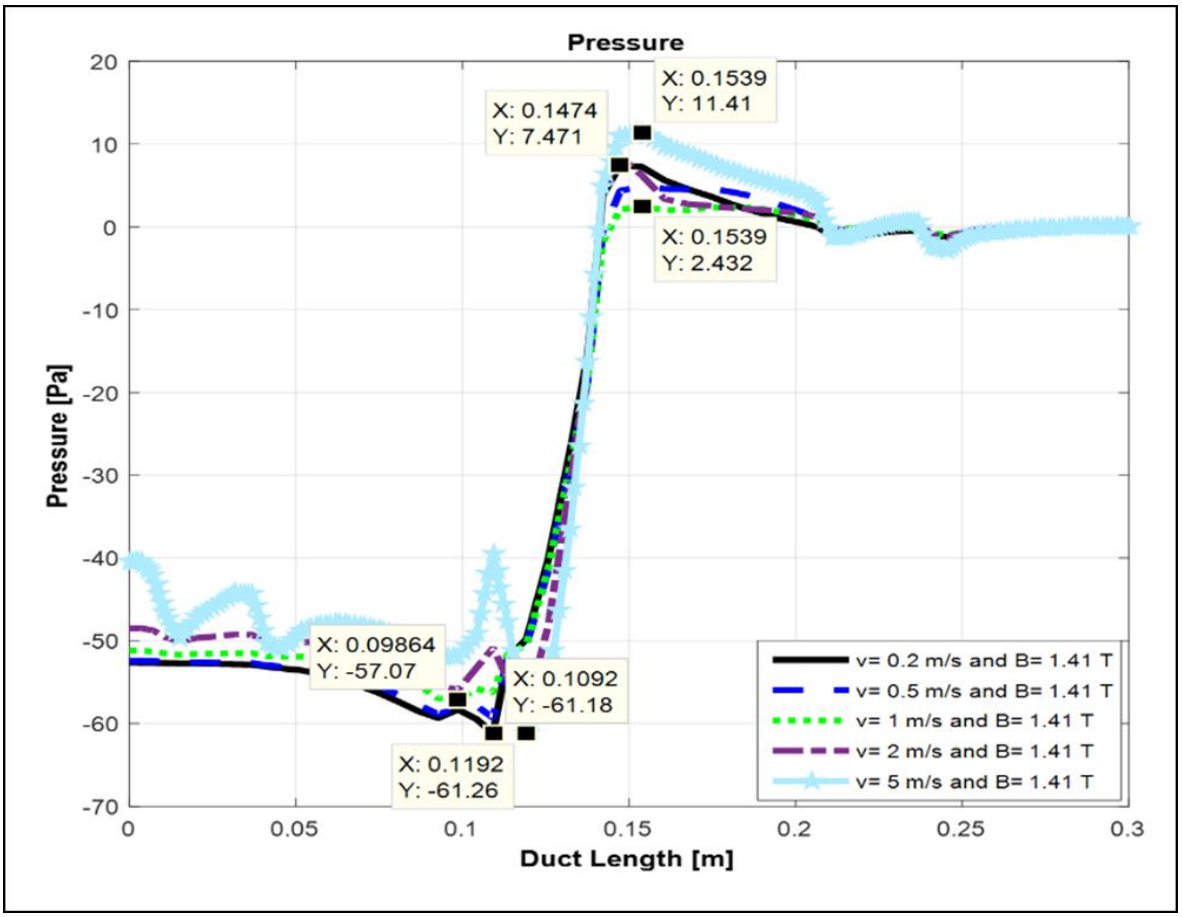

Figure 3.12: Pressure distributions of the fluid for each inflow velocity along the duct length.

- **Magnitudes of each fluid inflow velocity with respect to the applied remanent flux density**

The magnitudes of the fluid inflow velocities along the duct length are depicted in Figure 3.13. In this figure, the field vectors of each fluid inflow accelerate towards the electrodes walls at the center of the duct (MPD mode). By applying an external load resistor to the duct electrodes, these field vectors can be captured (MHD mode). When the fluid velocity of 2 m/s is applied at the duct inlet, the field vectors are most accelerated (5.011 m/s) under a remanent flux density of 1.41 T. Conversely, when the fluid velocity of 5 m/s is applied, the field vectors are least accelerated (4.241 m/s) under the same remanent flux density. One of the reasons for high velocity magnitudes in Figure 3.13 is that when the field vectors are slowed down by the magnetic force fields, they are also attracted by the electric potential (30

V) imposed to the duct electrodes. Thus, these field vectors are accelerated in the direction of the electrodes, resulting to high velocity magnitudes.

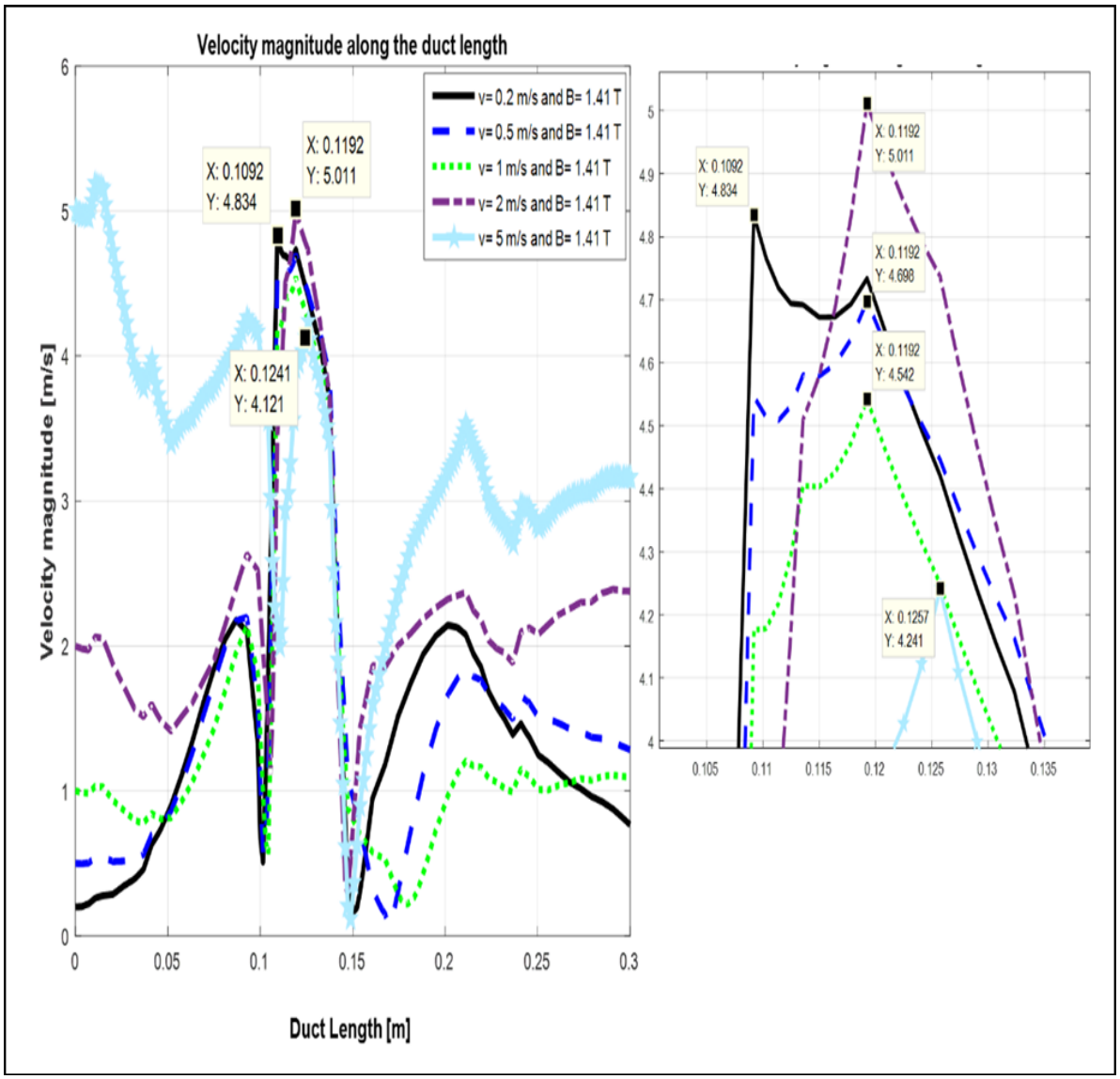

Figure 3.13: Magnitudes of each fluid inflow velocity with respect to the applied remanent flux density.

- **Patterns of the magnitudes of each fluid inflow velocity with respect to the applied remanent flux density**

The patterns of the fluid velocity magnitudes along the duct length are shown in Figure 3.14. In this figure, the fluid velocity magnitudes are higher at the electrode walls when the fluid velocities of 0.2 m/s, 0.5 m/s, 1 m/s and 2 m/s are applied. In contrast, when the fluid velocity of 5 m/s is applied, the fluid velocity magnitude is more populated at the center of the duct.

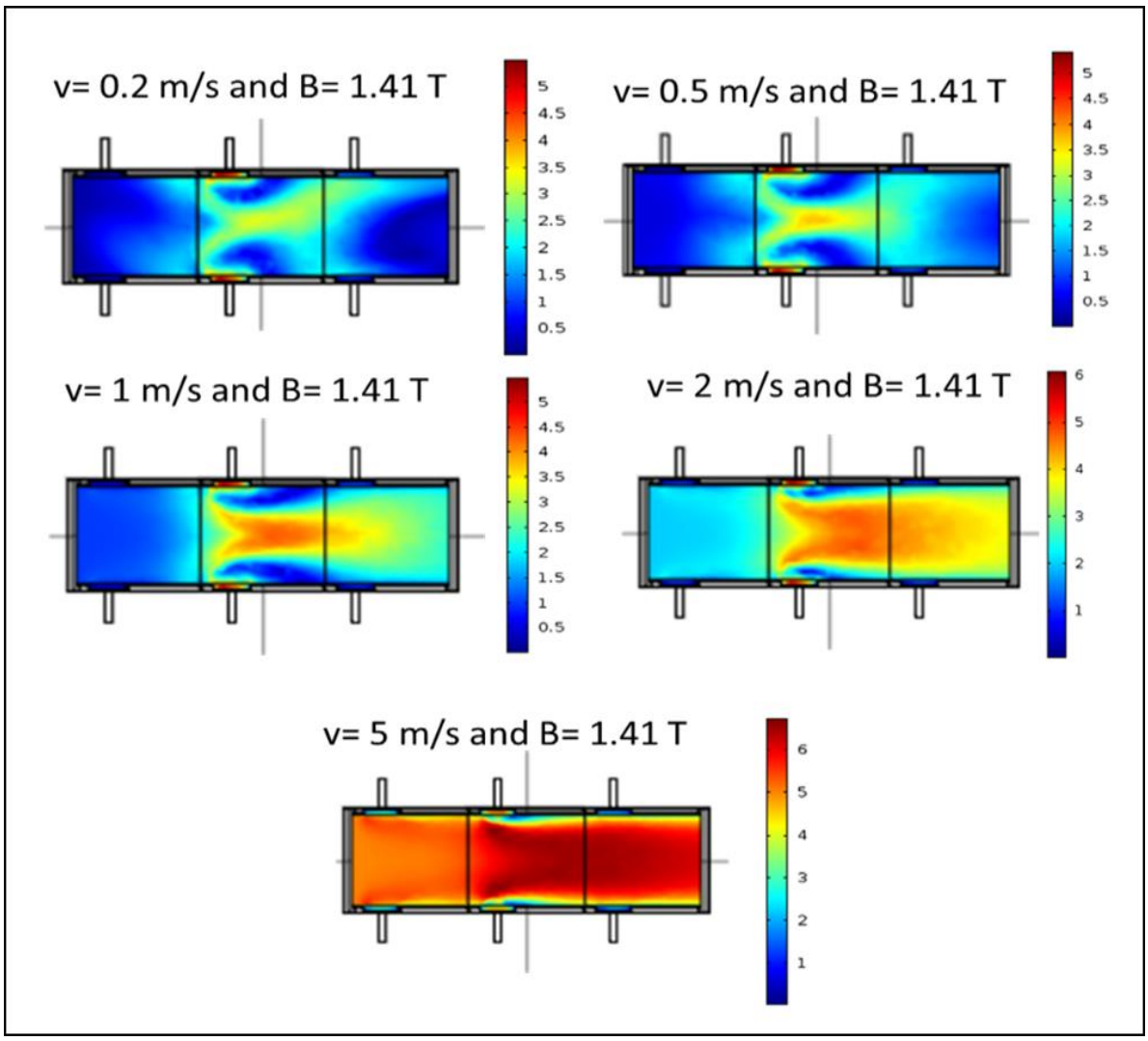

Figure 3.14: Patterns of the magnitudes of each fluid inflow velocity with respect to the applied remanent flux density.

3.2.6 Simulation results of an ionised propane fluid flow with a fixed velocity, varying external voltage and a fixed magnetic field (Study 3)

In this section, the simulation results of the flow of an ionised propane fluid with a fixed velocity, varying external voltage and a fixed magnetic remanent flux density are discussed.

- **Lorentz forces due to the applied magnetic remanent flux density for each applied external voltage**

The Lorentz forces due to the applied magnetic remanent flux density (1.41 T) for each applied external voltage are more intense at the center of the duct, as shown in Figure 3.15. In this figure, the maximum Lorentz forces of 1864 N/m^3, 747 N/m^3, 560.4 N/m^3, 373.7 N/m^3 and 186.9 N/m^3 are obtained at the center of the duct.

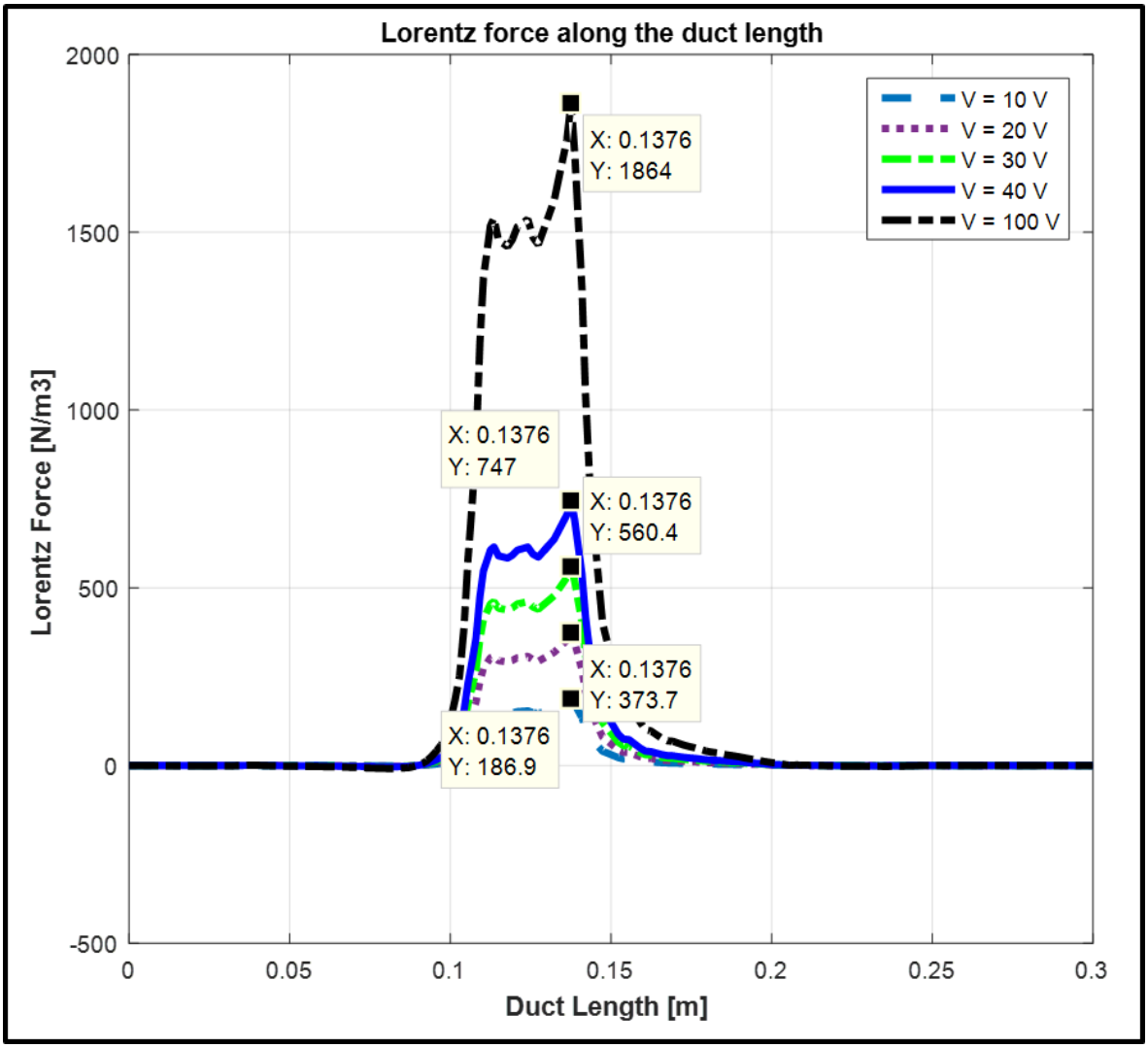

Figure 3.15: Lorentz forces due to the applied magnetic remanent flux density for each applied external voltage.

- **Fluid velocity magnitudes for each applied external voltage**

The velocity magnitudes of the fluid along the duct length relating to the external voltages are depicted in Figure 3.16. In this figure, the field vectors of the fluid for each applied voltage accelerate towards the electrodes walls at the center of the duct (MPD mode). By applying an external load resistor to the duct electrodes, this field vectors can be captured (MHD mode). One of the reasons for high velocity magnitude is that when the field vectors are slowed down by the applied magnetic field, they are also attracted to the applied voltages (10 V, 20 V, 30 V, 40 V and 100 V) imposed to the electrodes. Therefore, these field vectors (ions and electrons) are accelerated in the direction of the electrodes, and result to the increase of the fluid velocity magnitudes, as shown in Figure 3.16. When a voltage of about 100 V is applied to the duct electrodes, the field vectors are most accelerated (49.13 m/s) under a remanent flux density of 1.41 T. Conversely, when a voltage of about 10 V is applied, the field vectors are least accelerated (13.98 m/s) under the same remanent flux density.

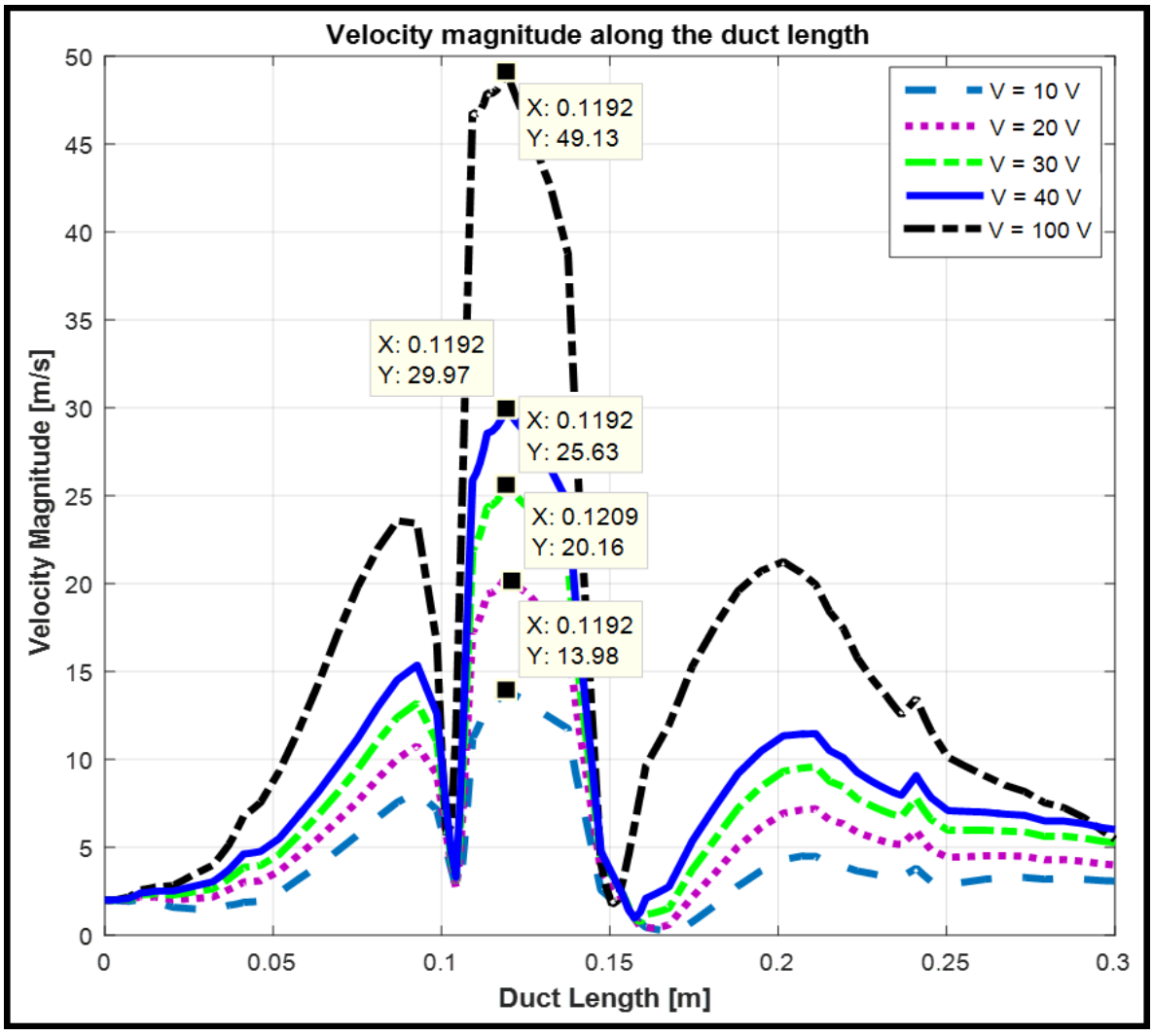

Figure 3.16: Fluid velocity magnitudes for each applied external voltage.

- **Current densities for each applied external voltage**

The current density distributions along the duct length are shown in Figure 3.17. Due to the applied potentials, the current densities are low at the duct inlet and gradually increases at the center of the duct and then decreases to zero at the duct outlet. When a voltage of 100 V is applied to the duct electrodes, the maximum current density of about 7.397e4 is obtained. Conversely, when a voltage of 10 V is applied, the minimum current density of about 7397 is obtained.

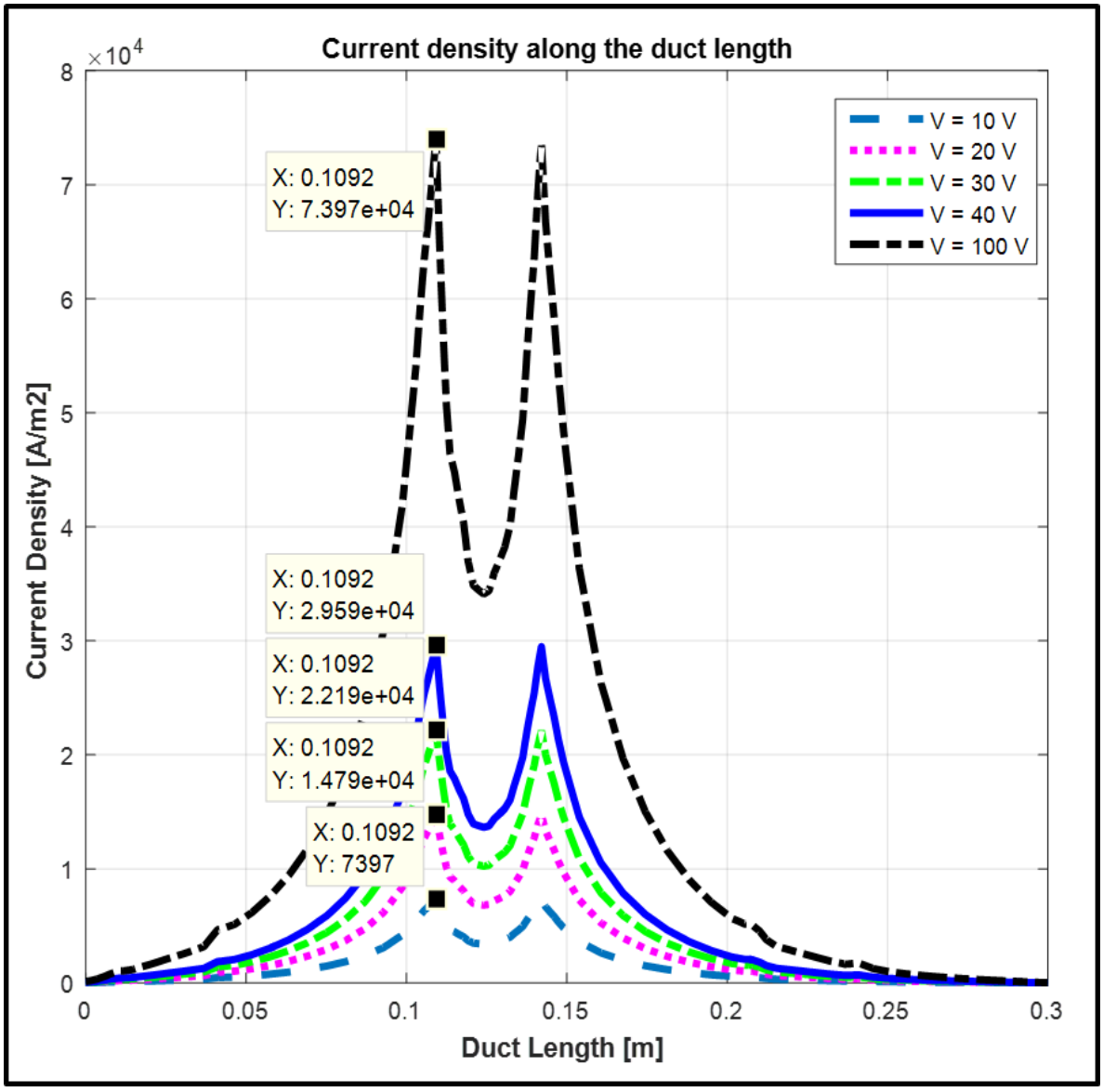

Figure 3.17: Current densities for each applied external voltage.

- **Patterns of the fluid velocity magnitudes for each applied external voltage**

The patterns of the fluid velocity magnitudes relating to the external voltages at the duct electrodes are depicted in Figure 3.18. In this figure, the fluid velocity magnitudes are higher at the electrode walls when the applied voltage of 10 V, 20 V, 30 V, 40 V and 100 V are applied. At the inlet and outlet of the duct (areas which are not covered by the applied magnetic field), the fluid velocity magnitudes and the field vectors are low.

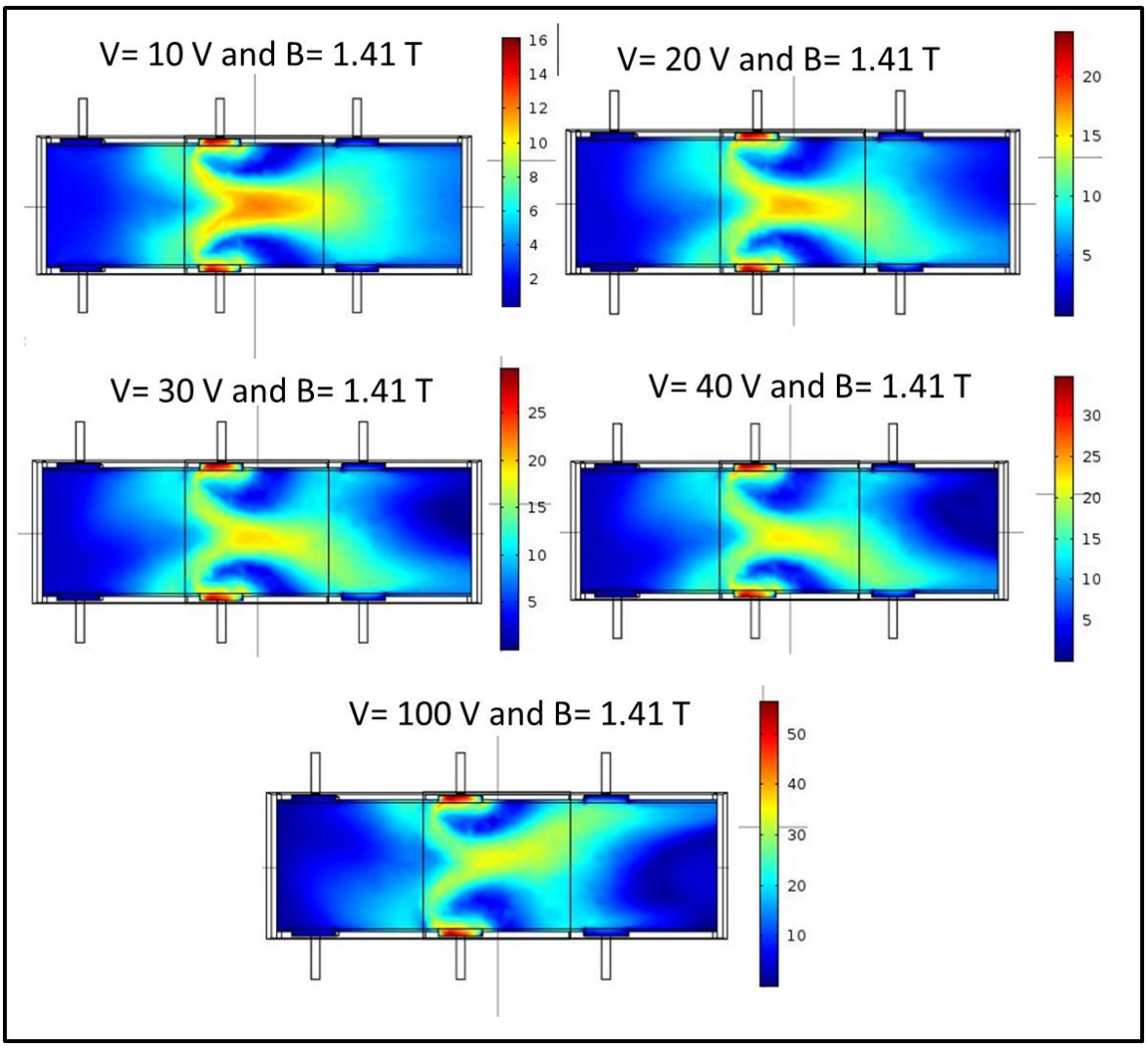

Figure 3.18: Patterns of the fluid velocity magnitudes for each applied external voltage.

3.3 Conclusion

In this chapter, three-dimensional simulations of the viscous flow of an ionised propane fluid inside a rectangular duct have been conducted based on the principle of Faraday's Law of electromagnetism and fluid dynamics. In these modelling, the fluid flow is studied numerically at different high Reynolds number and the duct is configured to act as generator and accelerator.

In the first study, the fluid flow is studied numerically with a fixed velocity, a fixed external voltage applied to the duct electrodes and varying remanent flux density (0 T, 1.12 T, 1.32 T and 1.41 T). In the second study, the fluid flow is studied numerically with varying velocity (0.2 m/s, 0.5 m/s, 1 m/s, 2 m/s and 5 m/s) applied to the duct inlet, a fixed external voltage and a fixed remanent flux density. In the third study, the fluid flow is studied numerically with a fixed velocity, varying external voltage (10 V, 20 V, 30 V, 40 V and 100 V) applied to the duct electrodes and a fixed remanent flux density. Numerical results such as the Lorentz force distributions, velocity profiles (field vectors and magnitudes), magnetic flux densities and pressure gradients along the duct length are presented and discussed.

The results obtained from the first study showed that when the intensities of the applied magnetic fields (Lorentz force) are increased, the Hartmann's number and the interaction parameter are increased, which ultimately slowed down the field vectors of the fluid to lower values at the center of the duct (x = 0.1 m and 0.2 m). This also creates M-shaped velocity profiles in the center of the magnetic gap (stagnant region). Imposing an electrical potential to the duct electrodes led to increase in the magnitudes of the field vectors accelerating towards the middle-electrode walls (MPD mode). Applying an external load resistor to the duct electrodes, these field vectors can be captured to generate electric power (MHD mode).

The results obtained from the second study showed that when the fluid inflow velocities are increased at the duct inlet, the Reynolds number are increased while the interaction parameters are decreased. The fixed applied magnetic field (1.41 T) decelerate the field vectors of each applied fluid inflow to lower values at the center of the duct. Moreover, imposing an electrical potential to the electrodes led to increase in the magnitudes of each field vectors (applied fluid inflow) arriving at the middle-electrode walls (MPD mode). Applying an external load resistor to the duct electrodes, these field vectors can be captured to generate electric power (MHD mode).

The results obtained from the third study showed that when the temperature of the fluid is increased and the applied voltages to the duct electrodes are varied, the magnitudes of the field vectors arriving at the middle-electrode walls are increased (MPD mode) under a remanent flux density of about 1.41 T. Applying an external load resistor to the duct electrodes, these field vectors can be captured to generate electric power (MHD mode).

Considering the above simulation results, the interaction between the magnetic field strength and bulk of the fluid produce an optimum magnitude of the flow velocity. Additionally, the magnetic flux density results are relevant for this study and serve as a guide towards the selection of a suitable remanent flux density value to be used in the MHD experiments. The simulation results could also be used in the design and development of MHD and MPD systems for aerospace propulsion, sea-water thruster's productivity, space-ship propulsion performance.

CHAPTER FOUR: MHD CONVERSION SYSTEM COUPLED TO THERMAL POWER PLANTS IN SOUTH AFRICA

4.1 Introduction

This chapter covers the coupling of an MHD topping unit to the South Africa Ankerlig and Gourikwa power stations. In addition, the modelling and simulation of a convergent-divergent nozzle is discussed.

4.2 Integration of MHD system to the South African thermal power plants

As previously discussed in section 2.5.1.5, the MHD system can be designed as an open-cycle system. Many researchers around the world have been thinking of different ways through which the MHD system (generators) can be developed and be integrated into the existing conventional power plants as a topping unit. Therefore, in this study, the MHD system is coupled to the South African Ankerlig and Gourikwa Open-cycle gas turbines (OCGT) to improve their total nominal capacity.

In the Ankerlig power station, the electricity generating units are grouped into two phases, with phase one comprising of 4 units and phase two comprising of 5 units. Each unit consist of a gas turbine, GT, (148.2 or 149.2 MW). The combined capacity of all the nine units is about 1338 MW (Phase-1: 149.2 MW x 4 units + Phase-2: 148.2 MW x 5 units) (Spalding-Fecher, 2011:11; Eskom, 2014; Pollet *et al.,* 2015:16698).

In the Gourikwa power station, there are five electricity generating units and each unit also consisting of a gas turbine. The combined capacity of all the five units is about 746 MW (149.2 MW x 5 units) (Spalding-Fecher, 2011:11; Pollet *et al.,* 2015:16698). As reported by Silinga & Gauché (2014:1545), primary fuel like coals, natural gas (propane) and petroleum derivative (kerosene or diesel) are presently used in these stations. The operation of these two OCGT plants begins when an atmospheric air is compressed and mixed with the fuel inside a combustion chamber (1303 K – 1473 K). The fuel-air mixture is burnt, and the resulting high velocity gas is used to turn the turbine shaft connected to the generator rotor. As the rotor spins inside the stator, electricity is generated and distributed via a high voltage transmission system (Figure 4.1). The Ankerlig and Gourikwa OCGT can also be converted into a more efficient combined-cycle gas-steam turbines (CCGST), as shown in Figure 4.1.

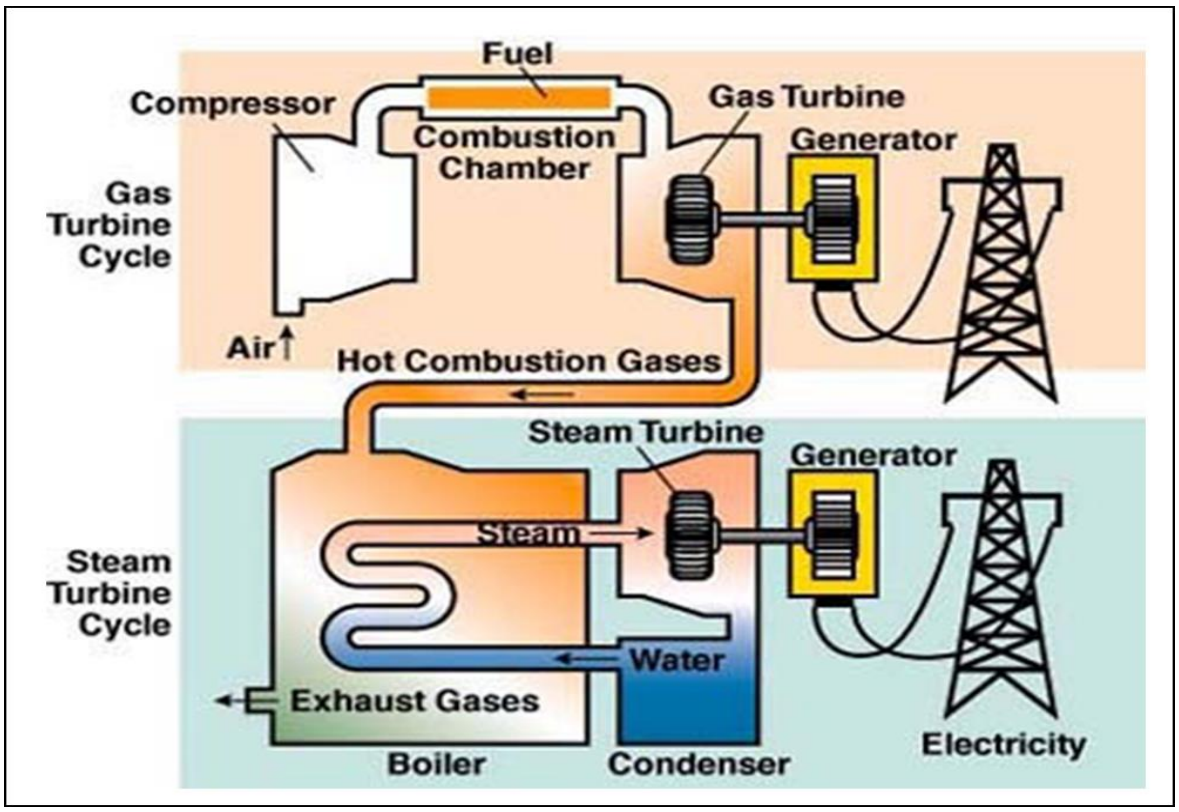

Figure 4.1: Combined-cycle gas-steam turbine system (Energy without Carbon, 2015).

The combined-cycle is often referred to as the combination of a Brayton cycle (gas turbine) and a Rankine cycle (steam turbine). The idea of converting the OCGT to a CCGST is to utilize the hot exhaust gas (about 873 K) energy leaving the gas turbine to create steam (water vapour) in a heat recovery steam generator (HRSG). This steam is used to drive the bottom unit steam turbine. The mechanical energy that is produced by the steam turbine is then converted to electrical energy using the generator. Subsequently, a condenser converts the exhaust steam from the steam turbine back into the HRSG through a cooling process (Eskom, 2014; Energy without Carbon, 2015).

Taking Gourikwa power station as a case study, it has been estimated that each converted CCGST unit will generates an additional 80 MW capacity, with a total nominal capacity of approximately 1146 MW (80 MW x 5 units + 746 MW) (Eskom, 2014). While in the Ankerlig power station, each converted CCGST unit will also generates an additional 80 MW capacity, with a total nominal capacity of approximately 2058 MW (80 MW x 9 units + 1338 MW). Considering the increasing electricity demands and usage in South Africa, these total nominal capacities can be substantially improved by combining to each unit of the CCGST, an MHD system topping unit. The coupling of an MHD unit to the Ankerlig and Gourikwa CCGST can be used to produce optimum cyclic thermal plants efficiency.

To achieve this, two open circuit MHD systems are designed and studied using numerical and theoretical modellings. In the first study, two MHD models (1 and 2) are incorporated into the Ankerlig and Gourikwa CCGST to form a combined-cycle MHD gas-steam turbine (CCMGST) system, as shown in Figure 4.2. The maximum power inside the MHD generator is solved using equation 2.33.

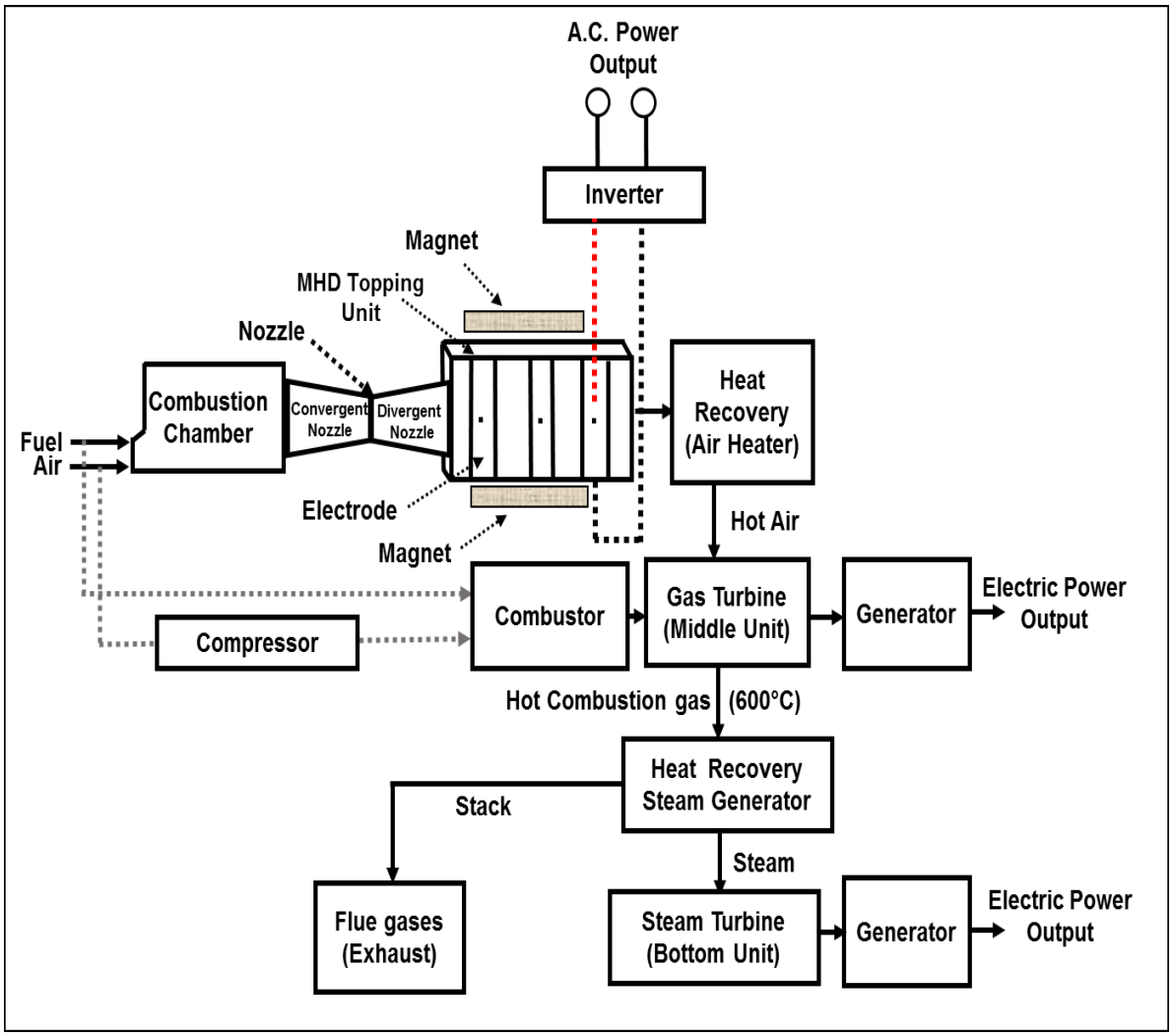

Figure 4.2: CCMGST system.

In the second study, another two MHD models (3 and 4) with varying external load resistor, are incorporated into the Ankerlig and Gourikwa CCGST to form the CCMGST system, as shown in Figure 4.3. The energy balance inside the MHD generator is solved using the maximum power in equation 2.34.

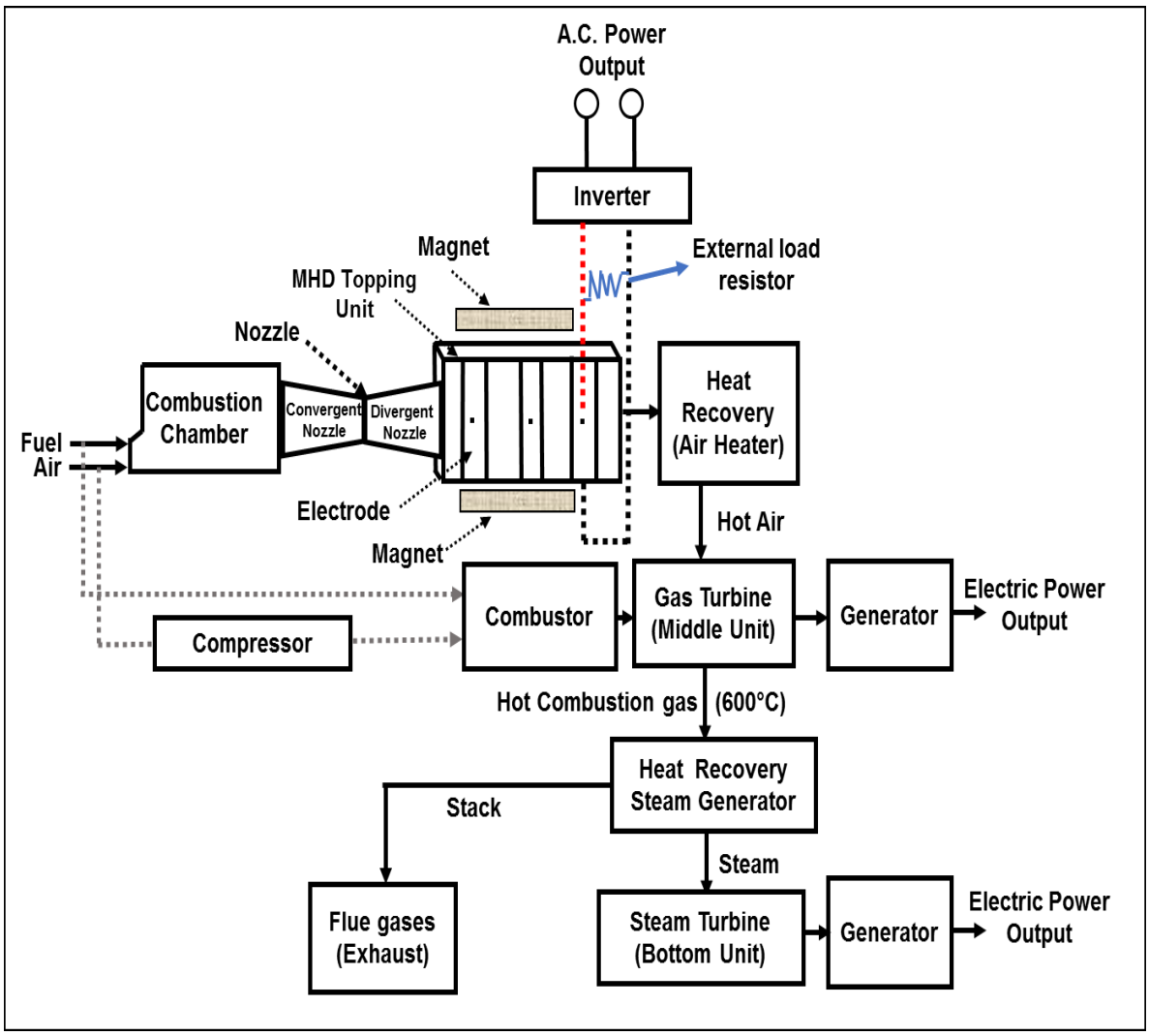

Figure 4.3: CCMGST system with external load resistor.

4.3 Two-dimensional modelling of a combustible fluid flow through a convergent-divergent nozzle

Several computational investigations involving the optimization of combustion chamber geometry, injection timing and duration of an ionised fluid flowing to an MHD generator have been conducted. In 2015, a study led by Martinas and co-workers modelled the combustion in a direct injection natural gas engine using non-premixed combustion (Martinas *et al.,* 2015:72-77). Thereafter, another study was conducted to improve significantly the quantity of power that can be generated in coal fired plants using the MHD system (Poonthamil *et al.,* 2016:143-146).

Considering that most MHD generators require high velocity gas and temperature, the fuel-air (fluid) exhaust exiting the combustion chamber (CCMGST plants) in Figures 4.2 and 4.3 is forced to flow through a convergent and divergent nozzle. Therefore, the fluid flow inside the nozzle is first modelled in this study. The purpose of the nozzle is to accelerate the fluid velocity up to the required Mach number before entering the inlet of the MHD generator. In the Ankerlig and Gourikwa thermal plants, the commonly used fluid is diesel fuel. Thus, this fuel is selected for the present nozzle modelling, as shown Figure 4.4.

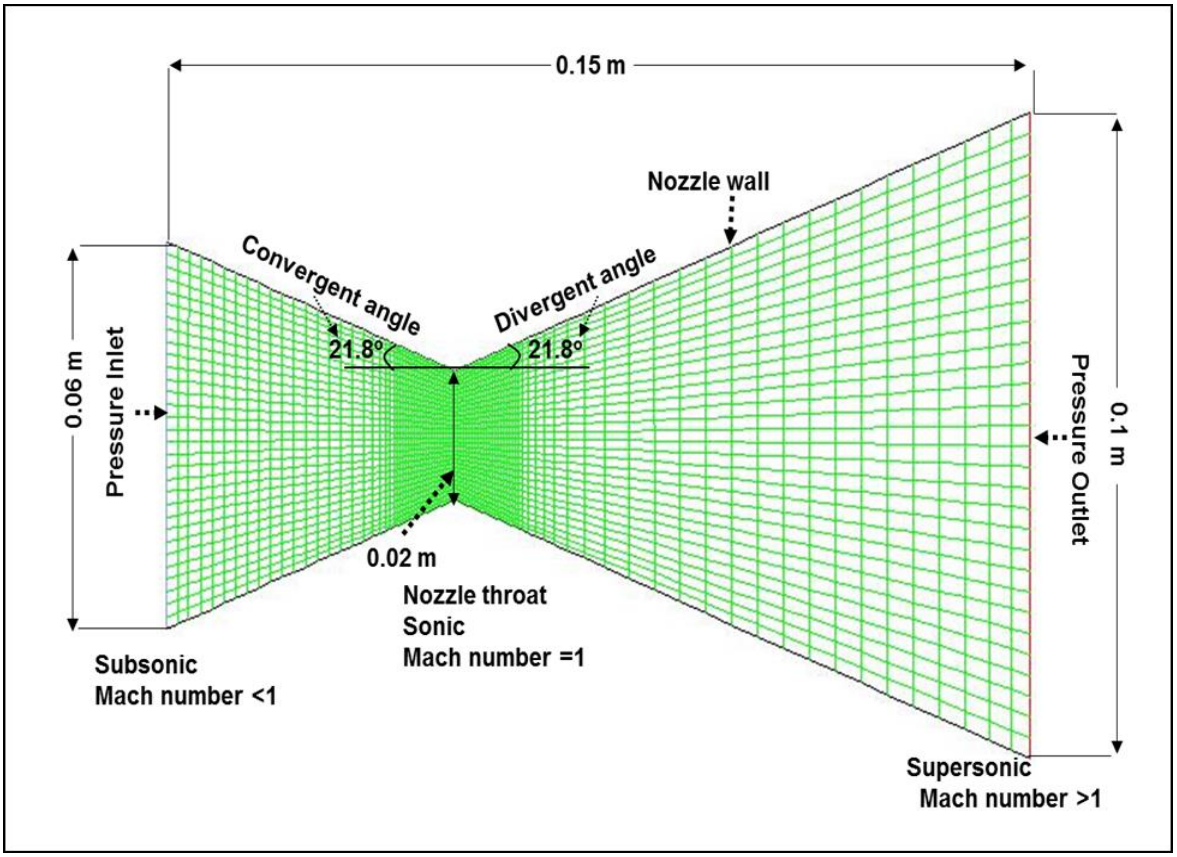

Figure 4.4: Nozzle mesh and geometry.

The supersonic propelling nozzle (Figure 4.4) uses the heat energy of the combustor exhaust to accelerate the fluid to a very high speed (Surya Narayana & Sadhashiva Reddy, 2016:58). The nozzle geometry and the flow analysis are performed using Ansys Fluent 16.2 software. The nozzle boundary conditions are set in such a way that when the fluid pressure increases at the inlet, their velocity should be very low (Subsonic). As the fluid flows through the nozzle throat, the pressure begins to decrease (Sonic) and the fluid velocity distribution increases toward the nozzle outlet (Supersonic).

For the simulation parameters, a quadrilateral shaped mesh is applied for all calculations. The mesh sizes are chosen to achieve sufficient accuracy within a reasonable computational time and no critical error is discovered. The complete mesh results consist of 2912 nodes and 2790 elements. The nozzle design setup and boundary conditions are listed in Table 4.1 (Velikhov, *et al.,* 1999:389; Hardianto, *et al.,* 2008:1118-1119; Deshpande *et al.,* 2014:34; ANSYS Inc, 2015; Butt & Arshad, 2015:105-106).

Table 4.1: Nozzle design setup and boundary conditions.

General setup	Solver Type: Density-Based, 2D Space: Planar, Time: Steady Velocity formulation: Absolute.
Models	Energy equation: On Viscous model: Standard k-epsilon model, Standard Wall Function.
Materials	Fluid: Diesel and air mixture, Density: ideal-gas, Viscosity = 1.72e-05 Kg/m-s, Thermal conductivity = 0.0454 W/m-K, Mass diffusivity = 2.88e-05 m^2/s.
Cell zone boundary condition	Fluid Domain
Boundary conditions	Inlet: Pressure-Inlet, Gauge Total Pressure = 3e5 Pa = 3 bar, Outlet: Pressure-Outlet, Gauge Total Pressure = 0 Pa, Inlet Temperature = 2000 K, Outlet Temperature = 300 K (For initialization purpose only).

- **Simulation results of the Convergent-Divergent Nozzle**

From the contour of velocity distribution result (Figure 4.5), the fluid (diesel-air) velocity is minimum at the inlet (68 m/s) and increases along the nozzle throat up till the nozzle outlet (1088 m/s). The velocity magnitude of the fluid is Mach 1 at the nozzle throat section, which means that the nozzle is at choked flow condition state. When the fluid reaches the nozzle outlet, the Mach number is approximately 2.35 (Figure 4.5).

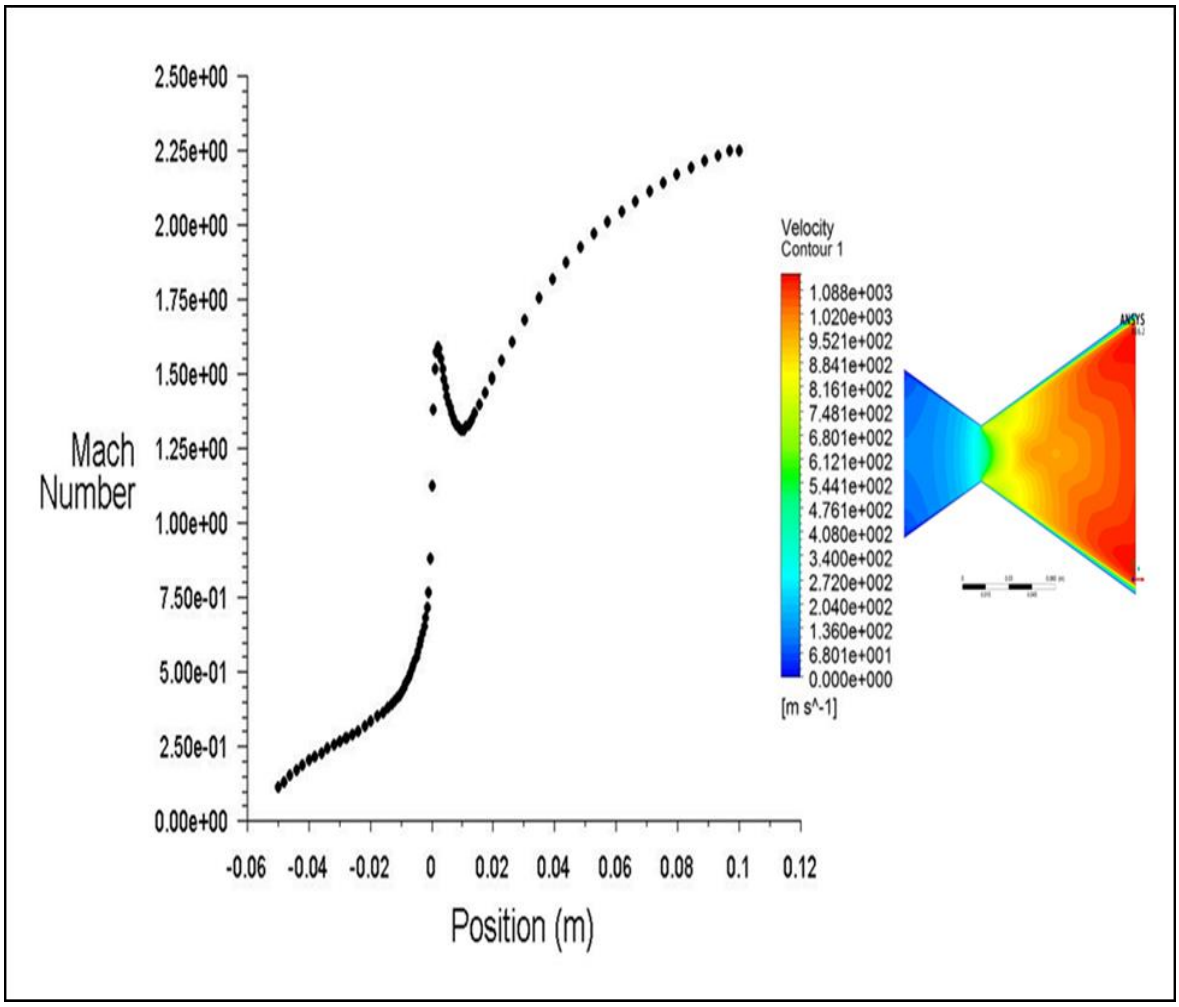

Figure 4.5: Contour of velocity and plot of Mach number along the nozzle wall position.

Figure 4.6 depicts the contour of the nozzle temperature distributions. In this figure, the temperature of the fluid is maximum at the inlet (1991 K) and decreases along the nozzle throat up till the nozzle outlet. When the fluid reaches the nozzle outlet, the magnitude of temperature at the outlet is 1782 K (Figure 4.6).

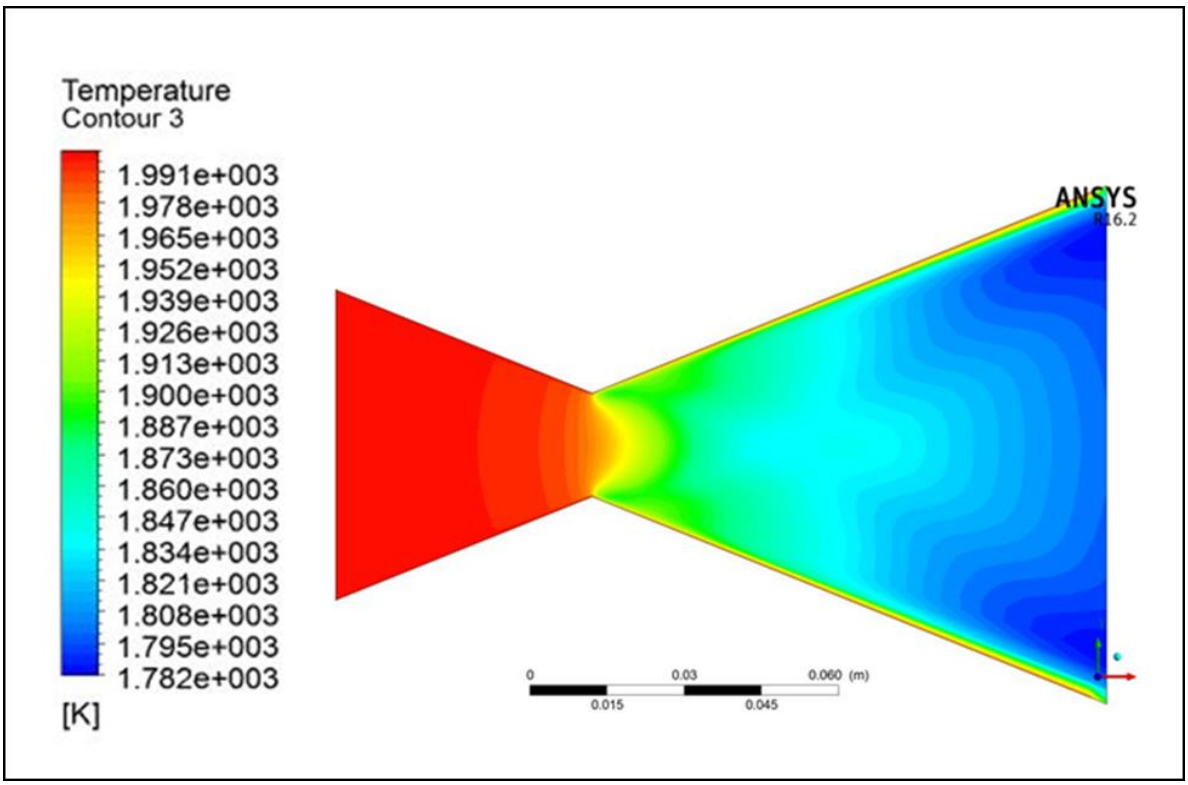

Figure 4.6: Contour of nozzle temperature.

Figure 4.7 depicts the contour of the nozzle pressure distributions. In this figure, the fluid pressure is maximum at the inlet (2.823 Pa) and decreases along the nozzle throat up till the nozzle outlet. When the fluid leaves the nozzle throat, there is a sudden reduction of pressure due to shock waves just after the throat section.

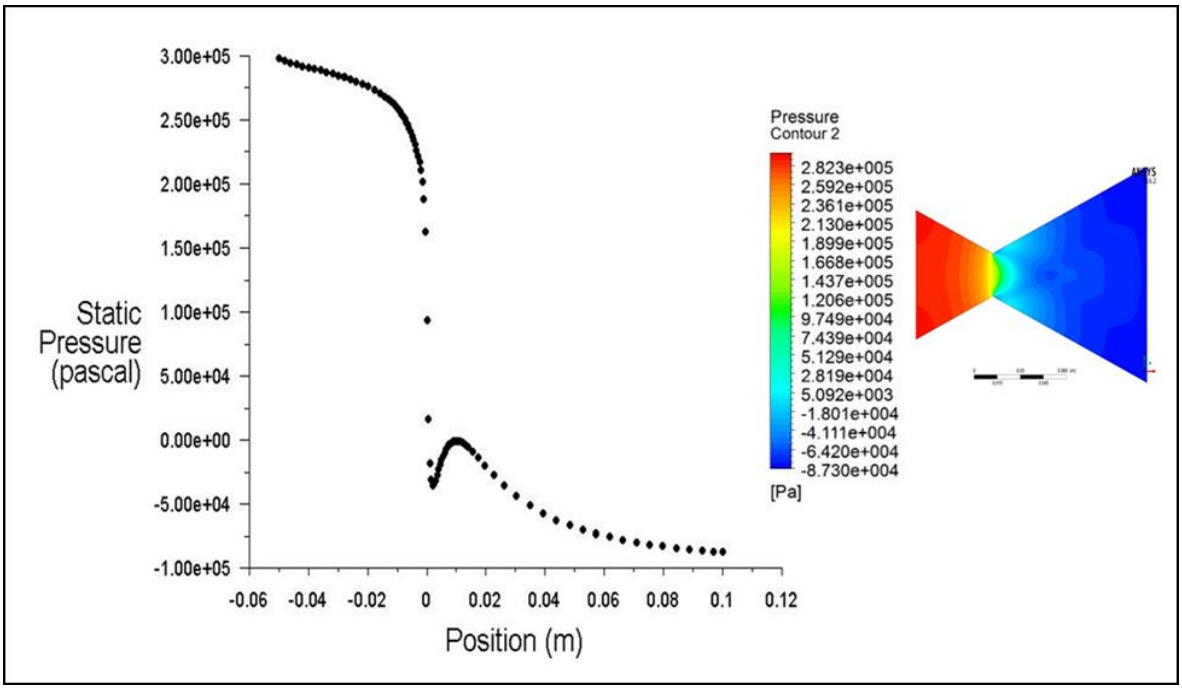

Figure 4.7: Contour and plot of pressure along the nozzle wall position.

4.4 Theoretical modelling of MHD conversion system incorporated into Ankerlig and Gourikwa CCGST

After performing the modelling of the fluid flow along the convergent and divergent nozzle, the supersonic fluid velocity (Figure 4.5) flowing out of the nozzle outlet can be used as input data for the modelling of the MHD topping unit in Figure 4.2. Table 4.2 illustrates the parameters of MHD models 1 and 2. These parameters are modelled theoretically using equations 2.32 and 2.33 to determine the optimum power that can be obtained from the CCMGST plant (Sawhney & Verma, 1988:137-141; Sawhney & Verma, 1995:343-346; Velikhov, *et al.,* 1999:389; Hardianto, *et al.,* 2008:1118-1119).

Table 4.2: MHD models 1 and 2.

Parameters	Model 1	Model 2
Simulated Diesel exhaust velocity (v)	1088 m/s	1088 m/s
Magnetic field (B)	2 Tesla	2.5 Tesla
Diesel exhaust conductivity (σ)	15 mho/m	20 mho/m
Electrode surface area (A)	1 m^2	1.6 m^2
Distance between the electrode (*l*)	1 m	1.6 m

- **Theoretical results**

The maximum voltage and power that can be obtained from the MHD topping unit are given by equations 2.32 and 2.33 (Ajith & Jinshah, 2013:5; Poonthamil *et al.,* 2016:145-146),

Model 1:

$$V_{max} = 2176 - 1088 = 1088\ \text{V},$$

$$P_{max} = \frac{(1088)^2 \cdot (2)^2 \cdot (15) \cdot (1) \cdot (1)}{4} = 17.76\ \text{MW}. \qquad \text{(1 unit)}$$

Model 2:

$$V_{max} = 4352 - 2176 = 2176\ \text{V},$$

$$P_{max} = \frac{(1088)^2 \cdot (2.5)^2 \cdot (20) \cdot (1.6) \cdot (1.6)}{4} = 94.7\ \text{MW}. \qquad \text{(1 unit)}$$

Based on the above calculation, the MHD generator units with Model 1 parameters, produce a total power capacity of 160 MW (17.76 MW x 9 units) and 89 MW (17.76 MW x 5 units), respectively, for all the gas turbine units in Ankerlig and Gourikwa CCGST stations. Similarly, a total power capacity of 852.3 MW (94.7 MW x 9 units) and 473.5 MW (94.7 MW x 5 units) are produced with both stations using model 2 parameters (Table 4.3).

Furthermore, an increase in the electrical conductivity of the fluid, magnetic field and electrical load factor can positively influence the gross output power from the MHD generator and the overall generating efficiency of the Ankerlig and Gourikwa power stations. The conversion efficiency of each MHD generator unit using models 1 and 2 can be determined as follows (Ajith & Jinshah, 2013:5; Poonthamil *et al*., 2016:146):

Model 1: $$\eta = \frac{V_{max}}{v\mathrm{B}} = \frac{1088}{1088 \times 2} \times 100 = 50\% .$$

Model 2: $$\eta = \frac{V_{max}}{v\mathrm{B}} = \frac{2176}{1088 \times 2.5} \times 100 = 80\% .$$

From the conversion of OCGT to CCGST (section 4.2), the power capacity of Ankerlig station is increased from 1338 MW (Phase-1: 149.2 MW x 4 units + Phase-2: 148.2 MW x 5 units) to 2058 MW (80 MW x 9 units + 1338 MW), while in the Gourikwa station, the power capacity is increased from 746 MW (149.2 MW x 5 units) to 1146 MW (80 MW x 5 units + 746 MW) (Table 4.3). This conversion gives an overall generating cycle efficiency of about 65%.

The coupling of model 1 MHD unit to each of the nine-electricity generating unit in the Ankerlig CCGST station produces a total nominal capacity of approximately 2218 MW, for the CCMGST plant, as shown in Table 4.3. Likewise, the coupling of model 1 MHD unit to each of the five-electricity generating unit in the Gourikwa CCGST station produces a total nominal capacity of approximately 1235 MW, for the CCMGST plant.

The coupling of model 2 MHD unit to each of the nine-electricity generating unit in the Ankerlig CCGST station produces a total nominal capacity of approximately 2910 MW, for the CCMGST plant (Table 4.3). Likewise, the coupling of model 2 MHD unit to each of the five-electricity generating unit in the Gourikwa CCGST station produces a total nominal capacity of approximately 1620 MW, for the CCMGST plant. Thus, the overall generating efficiency of these power plants has increased significantly.

Table 4.3: Summary of the CCMGST output power calculations for models 1 and 2.

	Model 1 Parameters	GT Units	OCGT (MW)	OCGT to CCGST Increments (MW)	CCGST (OCGT+ Increment), (MW)	MHD (MW)	CCMGST Total Capacity(MW)
Ankerlig Station	Phase-1	4	597 [a]	320 [d]	917	71 [g]	988
	Phase-2	5	741 [b]	400 [e]	1141	89 [h]	1230
	Gross Output Power [Phase 1 & 2]	9	**1338**	720	**2058**	160	**≈ 2218**
Gourikwa Station	Gross Output Power	5	**746** [c]	400 [f]	**1146**	89 [i]	**≈ 1235**

	Model 2 Parameters	GT Units	OCGT (MW)	OCGT to CCGST Increments (MW)	CCGST (OCGT+ Increment), (MW)	MHD (MW)	CCMGST Total Capacity (MW)
Ankerlig Station	Phase-1	4	597 [a]	320 [d]	917	378.8 [j]	1295.8
	Phase-2	5	741[b]	400 [e]	1141	473.5 [k]	1614.5
	Gross Output Power [Phase 1 & 2]	9	**1338**	720	**2058**	852.3	**≈ 2910**
Gourikwa Station	Gross Output Power	5	**746** [c]	400 [f]	**1146**	473.5 [l]	**≈ 1620**

Table 4.3 Note:

Model 1 & 2 OCGT: [a] 149.2 MW (Ankerlig Phase-1 gas turbine unit) x 4, [b] 148.2 MW (Ankerlig Phase-2 gas turbine unit) x 5, [c] 149.2 MW (Gourikwa gas turbine unit) x 5;

Model 1 & 2 OCGT to CCGST increments: [d] 80 MW (1 unit of increment) x 4, [e] 80 MW (1 unit of increment) x 5, [f] 80 MW (1 unit of increment) x 5;

Model 1 MHD: [g] 17.76 MW (Ankerlig Phase-1 MHD unit) x 4; [h] 17.76 MW (Ankerlig Phase-2 MHD unit) x 5; [i] 17.76 MW (Gourikwa MHD unit) x 5;

Model 2 MHD: [j] 94.7 MW (Ankerlig Phase-1 MHD unit) x 4; [k] 94.7 MW (Ankerlig Phase-2 MHD unit) x 5; [l] 94.7 MW (Gourikwa MHD unit) x 5.

4.5 Theoretical modelling of MHD conversion system coupled with external load resistors and incorporated into Ankerlig and Gourikwa CCGST

As previously discussed in section 4.2, the supersonic fluid velocity exiting the nozzle outlet (Figure 4.5) can also be used as input data for the modelling of the MHD topping unit in Figure 4.3. Table 4.4 illustrates the parameters of MHD models 3 and 4 with varying electrical load factor (Anumaka, 2014:1075; Banerjee, 2015:6516). These parameters are modelled theoretically using equation 2.34 to determine the optimum power that can be obtained from the CCMGST plant.

Table 4.4: MHD models 3 and 4 with varying electrical load factor.

Parameters	Model 3	Model 4
Simulated Diesel exhaust velocity (v)	1088 m/s	1088 m/s
Magnetic field (B)	2 Tesla	2.5 Tesla
Diesel exhaust conductivity (σ)	15 mho/m	20 mho/m
Electrode surface area (A)	1 m^2	1.6 m^2
Distance between the electrode (*l*)	2 m	2 m
Internal resistance (R_i)	0.13 ohm	0.06 ohm
External load resistance (R_L)	0.1 ohm	0.1 ohm
Electrical Load factor (*k*)	0.43	0.62

- **Theoretical results**

The output power that can be obtained from the MHD topping unit are given by equation 2.34 (Takayanagi *et al*., 2014:1),

Model 3:

$$P_{out} = 15 \times (1088)^2 \times (2)^2 \times 1 \times 2 \times 0.43 \times (1 - 0.43),$$

$$P_{out} = 34.79\,\text{MW} \quad . \qquad \text{(1 unit)}$$

Model 4:

$$P_{out} = 20 \times (1088)^2 \times (2.5)^2 \times 1.6 \times 2 \times 0.62 \times (1 - 0.62),$$

$$P_{out} = 112.1\ \text{MW} \quad . \qquad \text{(1 unit)}$$

Based on the above calculation, the MHD generator units with model 3 parameters, produce a total power capacity of 313 MW (34.79 MW x 9 units) and 173.9 MW (34.79 MW x 5 units), respectively, for the Ankerlig and Gourikwa CCGST stations. Similarly, the total power capacity of 1008.9 MW (112.1 MW x 9 units) and 560.5 MW (112.1 MW x 5 units) are produced with both stations using model 4 parameters (Table 4.5). From the conversion of OCGT to CCGST (section 4.2), the power capacity of the Ankerlig station is increased from 1338 MW (Phase-1: 149.2 MW x 4 units + Phase-2: 148.2 MW x 5 units) to 2058 MW (80 MW x 9 units + 1338 MW), while in the Gourikwa station, the power capacity is increased from 746 MW (149.2 MW x 5 units) to 1146 MW (80 MW x 5 units + 746 MW) (Table 4.5).

The coupling of model 3 MHD unit to each of the nine-electricity generating unit in the Ankerlig CCGST station produces a total nominal capacity of approximately 2371 MW, for the CCMGST plant (Table 4.5). Likewise, the coupling of model 3 MHD unit to each of the five-electricity generating unit in the Gourikwa CCGST station produces a total nominal capacity of approximately 1320 MW, for the CCMGST plant.

The coupling of model 4 MHD unit to each of the nine-electricity generating unit in the Ankerlig CCGST station produces a total nominal capacity of approximately 3067 MW, for the CCMGST plant (Table 4.5). Likewise, the coupling of model 4 MHD unit to each of the five-electricity generating unit in the Gourikwa CCGST station produces a total nominal capacity of approximately 1707 MW, for the CCMGST plant. These results show that the overall generating efficiency of the Ankerlig and Gourikwa CCGST stations using models 3 and 4 is higher when compared to models 1 and 2.

Table 4.5: Summary of the CCMGST output power calculations for models 3 and 4 with external load resistors.

	Model 3 Parameters	GT Units	OCGT (MW)	OCGT to CCGST Increments (MW)	CCGST (OCGT+ Increment), (MW)	MHD (MW)	CCMGST Total Capacity(MW)
Ankerlig Station	Phase-1	4	597 [a]	320 [d]	917	139.2 [g]	1056.2
	Phase-2	5	741 [b]	400 [e]	1141	173.9 [h]	1314.9
	Gross Output Power [Phase 1 & 2]	9	**1338**	720	**2058**	313	**≈ 2371**
Gourikwa Station	Gross Output Power	5	**746** [c]	400 [f]	**1146**	173.9 [i]	**≈ 1320**

	Model 4 Parameters	GT Units	OCGT (MW)	OCGT to CCGST Increments (MW)	CCGST (OCGT+ Increment), (MW)	MHD (MW)	CCMGST Total Capacity (MW)
Ankerlig Station	Phase-1	4	597 [a]	320 [d]	917	448.4 [j]	1365.4
	Phase-2	5	741 [b]	400 [e]	1141	560.5 [k]	1701.5
	Gross Output Power [Phase 1 & 2]	9	**1338**	720	**2058**	1008.9	**≈ 3067**
Gourikwa Station	Gross Output Power	5	**746** [c]	400 [f]	**1146**	560.5 [l]	**≈ 1707**

Table 4.5 Note:

Model 3 & 4 OCGT: [a] 149.2 MW (Ankerlig Phase-1 gas turbine unit) x 4, [b] 148.2 MW (Ankerlig Phase-2 gas turbine unit) x 5, [c] 149.2 MW (Gourikwa gas turbine unit) x 5;

Model 3 & 4 OCGT to CCGST increments: [d] 80 MW (1 unit of increment) x 4, [e] 80 MW (1 unit of increment) x 5, [f] 80 MW (1 unit of increment) x 5;

Model 3 MHD: [g] 34.79 MW (Ankerlig Phase-1 MHD unit) x 4; [h] 34.79 MW (Ankerlig Phase-2 MHD unit) x 5; [i] 34.79 MW (Gourikwa MHD unit) x 5;

Model 4 MHD: [j] 112.1 MW (Ankerlig Phase-1 MHD unit) x 4; [k] 112.1 MW (Ankerlig Phase-2 MHD unit) x 5; [l] 112.1 MW (Gourikwa MHD unit) x 5.

Table 4.6: Summary of the CCMGST output power for models 1, 2, 3 and 4.

	Model Parameters	1	2	3	4
		Without Load Resistor		With Load Resistor	
		CCMGST Total Capacity (MW)	CCMGST Total Capacity (MW)	CCMGST Total Capacity(MW)	CCMGST Total Capacity (MW)
Ankerlig Station	Phase-1	988	1295.8	1056.2	1365.4
	Phase-2	1230	1614.5	1314.9	1701.5
	Gross Output Power [Phase 1 & 2]	**≈ 2218**	**≈ 2910**	**≈ 2371**	**≈ 3067**
Gourikwa Station	Gross Output Power	**≈ 1235**	**≈ 1620**	**≈ 1320**	**≈ 1707**

4.6 Conclusion

In this chapter, two separate studies have been conducted to investigate the possibility of coupling an MHD system into the South African power stations, namely Ankerlig and Gourikwa (CCGST). In order to achieve this, a 2-D numerical modelling of a combustible fluid through a convergent-divergent nozzle was first performed. Thereafter, the fluid velocity obtained at the exit of this nozzle and several MHD parameters (models 1, 2, 3 and 4) coupled to the power stations were modelled theoretically.

In the first study, two open circuit MHD models (1 and 2) are modelled theoretically to the CCGST stations to form the Ankerlig and Gourikwa CCMGST stations. This is done in order to produce an output power with optimum generating efficiency. The results showed that when models 1 and 2 parameters are applied to a single MHD generator unit, the maximum output powers obtained are 17.76 MW and 94.7 MW, respectively. When model 1 MHD unit is incorporated into the CCMGST stations, the optimum powers obtained are 2218 MW and 1235 MW, respectively. Likewise, when model 2 MHD unit is incorporated into the CCMGST stations, the optimum powers obtained are 2910 MW and 1620 MW, respectively.

In the second study, another two-open circuit MHD models (3 and 4) with external load resistors are modelled theoretically to both CCGST stations to form the Ankerlig and Gourikwa CCMGST stations. The results showed that when models 3 and 4 parameters are applied to a single MHD generator unit, the maximum output powers obtained are 34.79 MW and 112.1 MW, respectively. When model 3 MHD unit is incorporated into the CCMGST stations, the optimum powers obtained are 2371 MW and 1320 MW, respectively. Likewise, when model 4 MHD unit is incorporated into the CCMGST stations, the optimum powers obtained are 3067 MW and 1707 MW, respectively. These results showed that by increasing the distance between the MHD duct electrodes in models 3 and 4, the generating efficiency of the CCMGST stations is higher when compared to models 1 and 2.

CHAPTER FIVE: MODELLING AND SIMULATION OF THERMAL PLASMA TORCH

5.1 Introduction

This chapter covers the modelling and simulation of thermal plasma torches such as the inductively coupled plasma and the direct current arc plasma.

For the inductively coupled plasma torch, the gas discharge is usually sustained by coupling plasma energy with induction coil current produced through time varying magnetic field. The operation of ICP begins when an HF current is fed into the induction coils placed around the quartz tubes of the system. Consequently, a strong oscillating magnetic field is formed in the centerline direction of the quartz tubes and creates azimuthal electric field within the tubes. The free electrons emanating from the main gas source are accelerated by this electric field and when their kinetic energies exceed the gas atoms ionization energy, a plasma is formed. The plasma formation is due to the collision (chain reaction) between the gas atoms and the naturally occurring free electrons (Herdrich & Petkow, 2008:391-400). Due to the high electrical conductivity of the generated plasma, an electric current is produced from the collision to provide heat that sustains the plasma.

Moreover, when the plasma current flows in the direction opposite to the induction coil current and the magnetic field is also flowing in the direction opposite to the field caused by the coil current, a skin effect occurred. The ICP (ring-shaped) is mostly formed around the inner wall regions of the tubes that are not affected by magnetic field damping produced along the centerline of the tubes (Herdrich & Petkow, 2008: 391-400). Tong *et al.* (2016:1199-1202) conducted a study to investigate the plasma flow field and temperature distribution of TiAl based alloy powder using the ICP method. Their results showed that a plasma temperature of about 9873 K and a velocity magnitude of about 26.7 m/s were obtained at the outlet of the torch.

For the direct current arc plasma torch, an electric arc is flamed by applying a DC between the cathode and anode of the torch. This arc serves as an energy source which helps to accelerate the working gas velocity and also to increase the gas temperature. The plasma generated is sustained through heating and ionisation of the gas along the upstream region of the torch cathode. The torch cathode is then water/air cooled in order to constrict the plasma (Chine, 2015:1).

5.1 Two-dimensional simulation of an Inductively Coupled Plasma system

5.1.1 Description of an ICP torch model

The modelling and simulation of an ICP system is performed using the equilibrium inductively coupled discharge interface (Plasma and AC/DC Modules) in Comsol Multiphysics 5.1 software. The density, dynamic viscosity and electrical conductivity of the main gas used for this modelling represent an ionised argon fluid. The ICP torch model consists of copper coils (C), electrodes and the three concentric quartz tubes: carrier tube (cat), central tube (cet) and sheath tube (st). Figure 5.1 and Table 5.1 depict the geometrical parameters and the boundary conditions used for the ICP torch model.

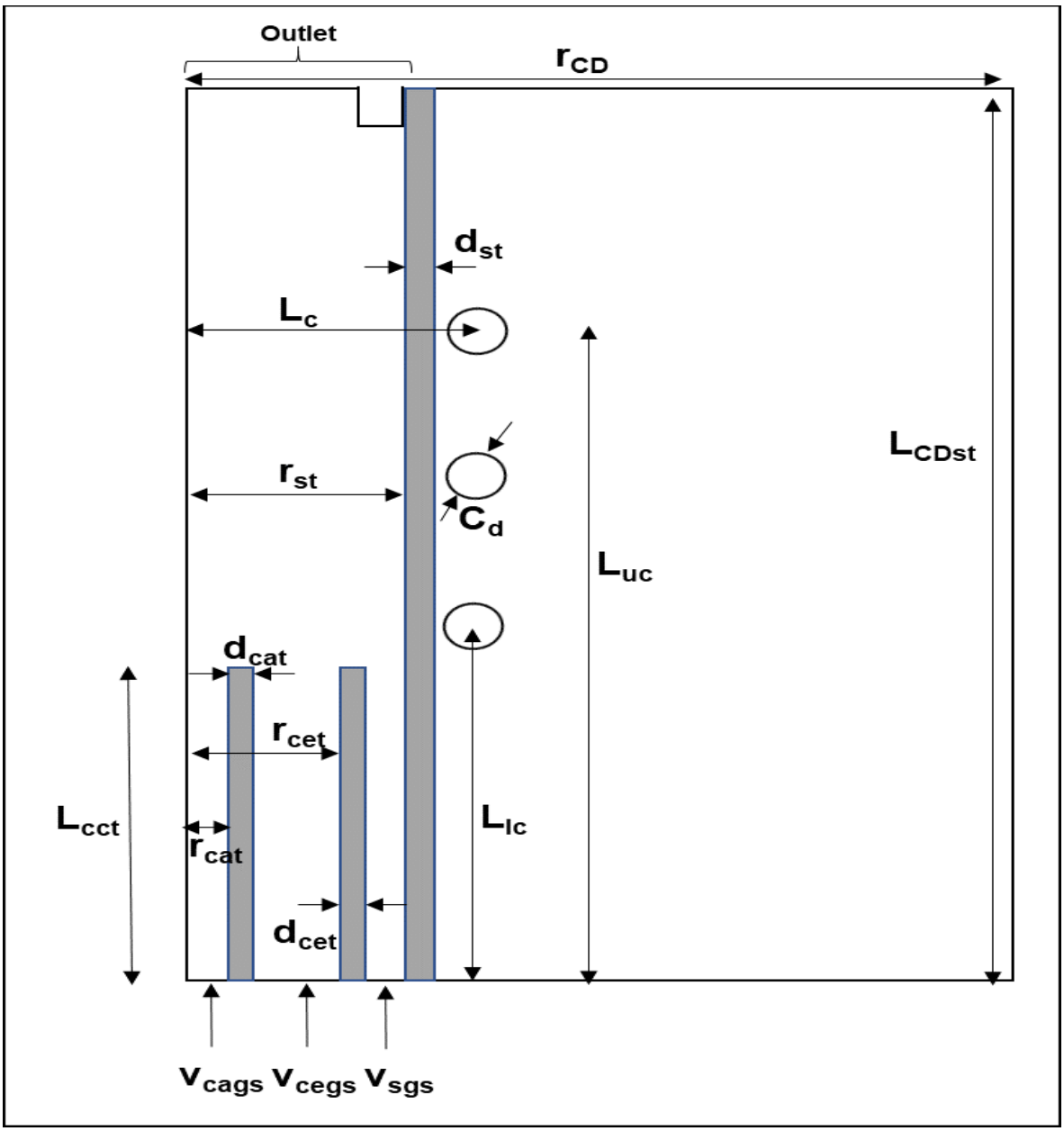

Figure 5.1: Schematic representation of the ICP torch model.

Table 5.1: Geometrical parameters and boundary conditions used for the ICP torch model.

T	300 [K]	Ambient temperature
P_{ext}	20 [kW]	Coil excitation power
f	3 [MHz]	Coil excitation frequency
r_{CD}	125 [mm]	Axial length of the computational domain
L_{CDst}	180 [mm]	Height of the computational domain and sheath tube
d_{cat}	2.3 [mm]	Thickness of the carrier tube
L_{cct}	46 [mm] and 50 [mm]	Height of the carrier tube and central tube
r_{cat}	3.7 [mm]	Inner radius of the carrier tube
d_{cet}	2.2 [mm]	Thickness: Central tube
r_{cet}	18.8 [mm]	Inner radius of the central tube
d_{st}	3.5[mm]	Thickness of the sheath tube
r_{st}	25[mm]	Inner radius of the sheath tube
C_d	9 [mm]	Diameter of the coils
L_c	34 [mm]	Axial length of the center of the coils
L_{lc}	63 [mm]	Height of the center of the lower coil
L_{uc}	130 [mm]	Height of the center of the upper coil
G_{scat}	1 [l/min] or 1.6667e-05 m^3/s	Gas stream of the carrier tube
G_{scet}	1 [l/min] or 1.6667e-05 m^3/s	Gas stream of the central tube
G_{sst}	31 [l/min] or 5.1667e-04 m^3/s	Gas stream of the sheath tube
M	0.04 [kg/mole]	Molar mass of the argon
$M_{v\text{-}stp}$	22.4 [l/mole]	Molar volume at stp
m_{cat}	$M*G1/M_{v\text{-}stp}$ = 2.9762e-05 kg/s	Mass flow rate of the carrier tube
m_{cet}	$M*G2/M_{v\text{-}stp}$ = 2.9762e-05 kg/s	Mass flow rate of the central tube
m_{st}	$M*G3/M_{v\text{-}stp}$ = 9.2262e-04 kg/s	Mass flow rate of the sheath tube
ρ	1.91 [kg/m^3]	Density of argon at stp
A_{cags}	$pi*(r_{cat})^2$ = 4.3008e-05 m^2	Cross section of the carrier gas stream
A_{cegs}	$pi*(r_{cet}^2-(r_{cat}+d_{cat})^2)$ = 9.9727e-04 m^2	Cross section of the central gas stream
A_{sgs}	$pi*(r_{st}\text{^}2-(r_{cet}+d_{cet})\text{^}2)$ = 5.7805e-04 m^2	Cross section of the sheath gas stream
v_{cags}	$m_{cat}/ρ/A_{cags}$ = 0.3623 m/s	Velocity of the carrier gas stream
v_{cegs}	$m_{cet}/ρ/A_{cegs}$ = 0.015625 m/s	Velocity of the central gas stream
v_{sgs}	$m_{st}/ρ/A_{sgs}$ = 0.83564 m/s	Velocity of the sheath gas stream

From Figure 5.1, the height of the computational domain and sheath tube, L_{CDst}, is 180 mm while the coil diameter, C_d, is 9 mm. Each coil has three turns covering 34 mm in the axial length direction with a spacing of about 33.5 mm. In order to perform the simulation of the present ICP torch model, the following assumptions are considered (Bhuyan *&* Goswami, 2007:1781):

- The flow of the gas is steady and laminar at atmospheric pressure
- The ICP torch is modelled with fully two dimensional axi-symmetric coordinates system.
- The plasma is optically thin at the outside of the electrode boundary layer and the pattern of the plasma species obeys LTE conditions.
- The induction coil is made up of parallel current carrying circular rings (9 mm in diameter) and the axial component of the coil current is neglected.
- Gravitational force and heat dissipation due to viscosity are negligible (i.e. viscous dissipation and pressure variables in the energy equation are neglected).

Considering the above assumption, the argon gas (velocity of the carrier gas, Vcags, velocity of the central gas, Vcegs and velocity of the sheath gas, Vsgs) is injected from the inlet (bottom) of the torch and exit from the outlet (top) of the torch. Additionally, a fixed excitation power of 20 kW is transferred to the argon plasma using the three-turn coils operating at about 3 MHz. Subsequently, the argon gas is ionized by Joule heating.

5.1.2 Governing equations and boundary conditions

- **Laminar Flow**

For this simulation, laminar time and frequency dependent compressible argon gas flow is solved using the Navier-Stokes equations. These equations are solved for the entire computational domain to obtain a steady state solution with respect to the time (0.1 s). (Comsol Multiphysics, 2015).

$$\rho(v\cdot\nabla)v = \nabla\cdot\left[-p\mathrm{I} + v\cdot\left(\nabla_v + (\nabla_v)^{\mathrm{T}}\right) - \frac{2}{3}\cdot\mu\cdot(\nabla\cdot v)\cdot\mathrm{I}\right] + \mathrm{F}, \qquad \textbf{Equation 5.1}$$

$$\nabla\cdot(\rho v) = 0\ , \qquad \textbf{Equation 5.2}$$

where v is the plasma velocity, ρ is the fluid density, p is the pressure, μ is the viscosity and F is the volumetric Lorentz force.

- **Magnetic field**

The magnetic field boundary conditions are applied to the exterior and the symmetry axis of the ICP torch model. In the exterior boundary region, a magnetic insulation is applied so that the magnetic vector potential is zero at the model boundary, with zero magnetic flux. In the symmetry axis boundary, the magnetic potential is continuous across the interior boundary between the copper coils and the air domain. The magnetic vector potential (A_m) used for this study obeys the following relations (Comsol Multiphysics, 2015),

$$\left(jw\sigma - w^2\varepsilon_0\varepsilon_r\right)A_m + \nabla \times \mathrm{H} = \mathrm{J_e} \ , \qquad \textbf{Equation 5.3}$$

$$\mathrm{B} = \nabla \times A_m \ , \qquad \textbf{Equation 5.4}$$

where w is the angular frequency, σ is the electrical conductivity, ε_0 is the permittivity of free space, ε_r is the medium relative permittivity, H is the magnetic field strength and B is the magnetic field.

- **Heat Transfer in Fluid**

In order to model the heat transfer (conduction and convection) of the argon fluid inside the ICP torch, the following equations are used (Comsol Multiphysics, 2015),

$$\rho C_p \frac{\partial T}{\partial t} + \rho C_p v + \nabla \times \mathrm{q} = \mathrm{Q} + \mathrm{Q}_p + \mathrm{Q_{vd}} \ , \qquad \textbf{Equation 5.5}$$

$$\mathrm{q} = -k_t \nabla T \ , \qquad \textbf{Equation 5.6}$$

where C_p is the specific heat capacity, q is the heat flow, Q is the heat flow rate, k_t is the thermal conductivity, t is the time and T is the temperature.

Equations 5.1 to 5.6 are the magnetohydrodynamics (MHD) equations used for the modelling of the ICP torch. For the simulation parameters, a free triangular shaped mesh is used for all the calculations. Moreover, to achieve sufficient accuracy within a reasonable computational time, the fluid domain is uniformly meshed with extra-fine option (Figure 5.2).

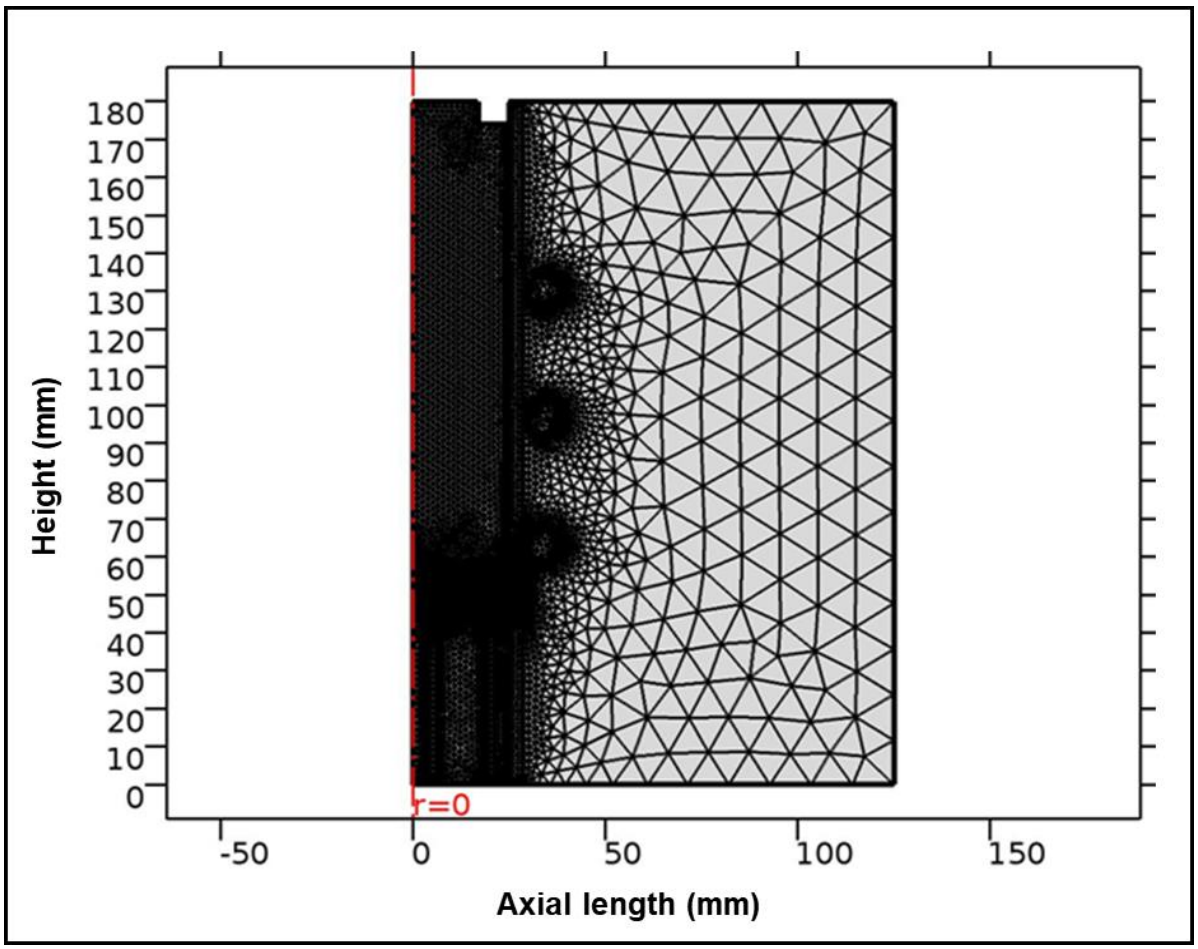

Figure 5.2: The mesh for the ICP torch model.

From Figure 5.2, the complete mesh results consist of 405 number of domain elements, 215 boundary elements, and 31 vertex elements. This generates 27331 degrees of freedom (plus 728 internal DOFs). A frequency-transient study using the single turn coil parameter is used to obtain the simulation convergence. The supply excitation power is fixed to ensure that the electric potential and the current is varied inside the induction coil as the plasma begins to build-up. An electrical conductivity of about 1 S/m is also set to initialise the plasma formation. Subsequently, the simulation converges when the coil current reaches its nominal value (steady condition).

5.1.3 The simulation results of the ICP torch model.

- **Magnetic flux density norm**

The surface plot of the magnetic flux density distribution along the ICP computational domain is shown in Figure 5.3. In this figure, the maximum magnetic flux of about 0.02 T is obtained at a normalise steady state of about 0.1 s. In addition, the electrical conductivity of the plasma screens the magnetic flux due to the skin effect.

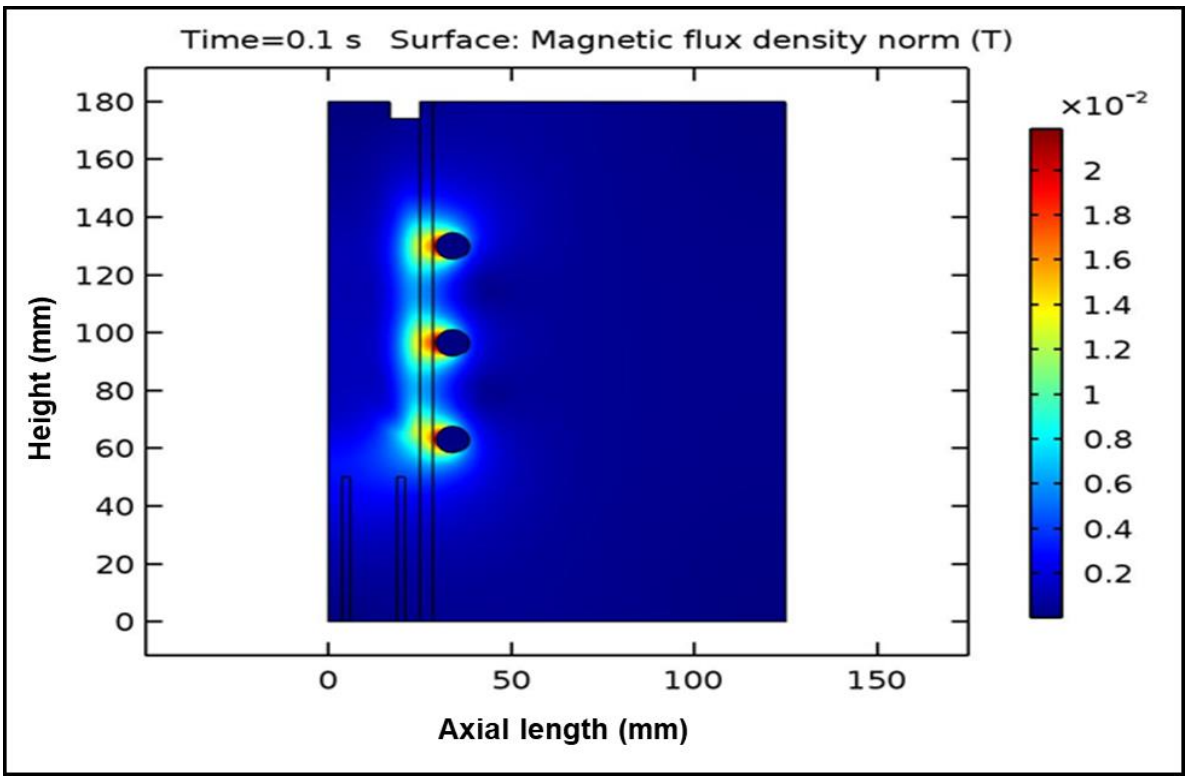

Figure 5.3: Surface plot of the magnetic flux density.

Figures 5.4 and 5.5 show the surface plot of the resulting coil current and the plasma electrical conductivity under a constant excitation power (20 kW) with respect to the simulation time. A steady state is attained when the current normalises at about 0.1 s.

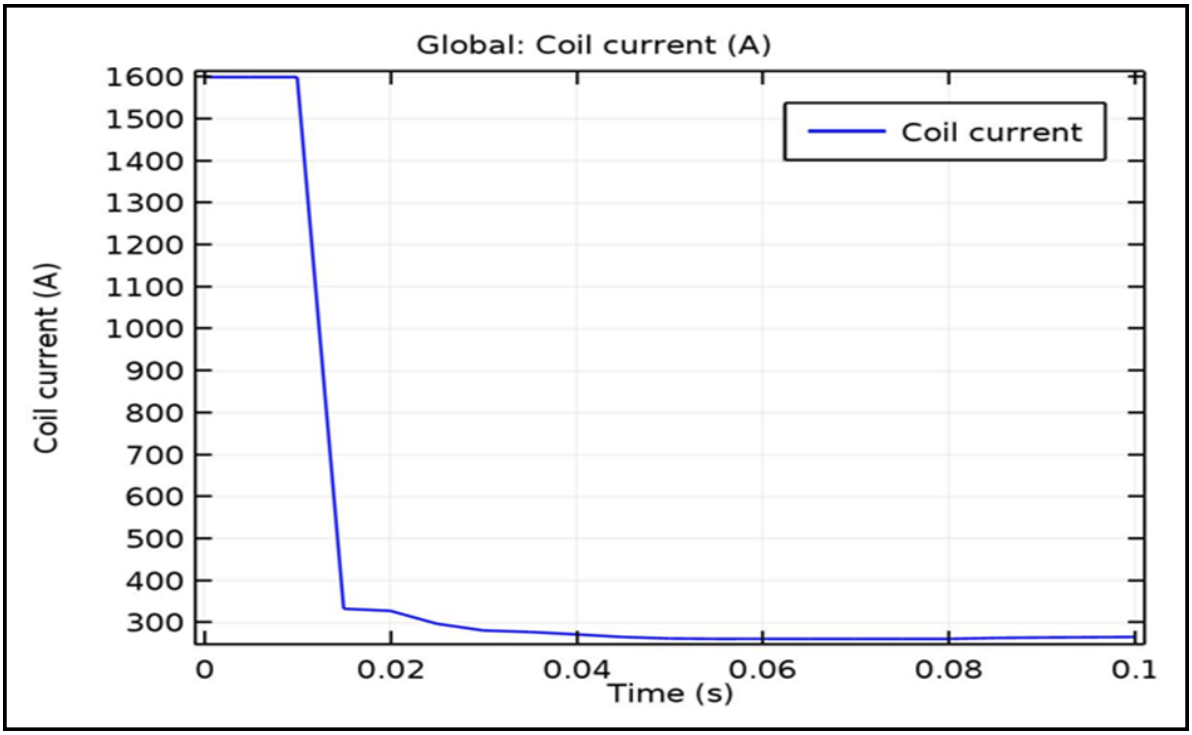

Figure 5.4: Surface plot of the coil current with respect to time.

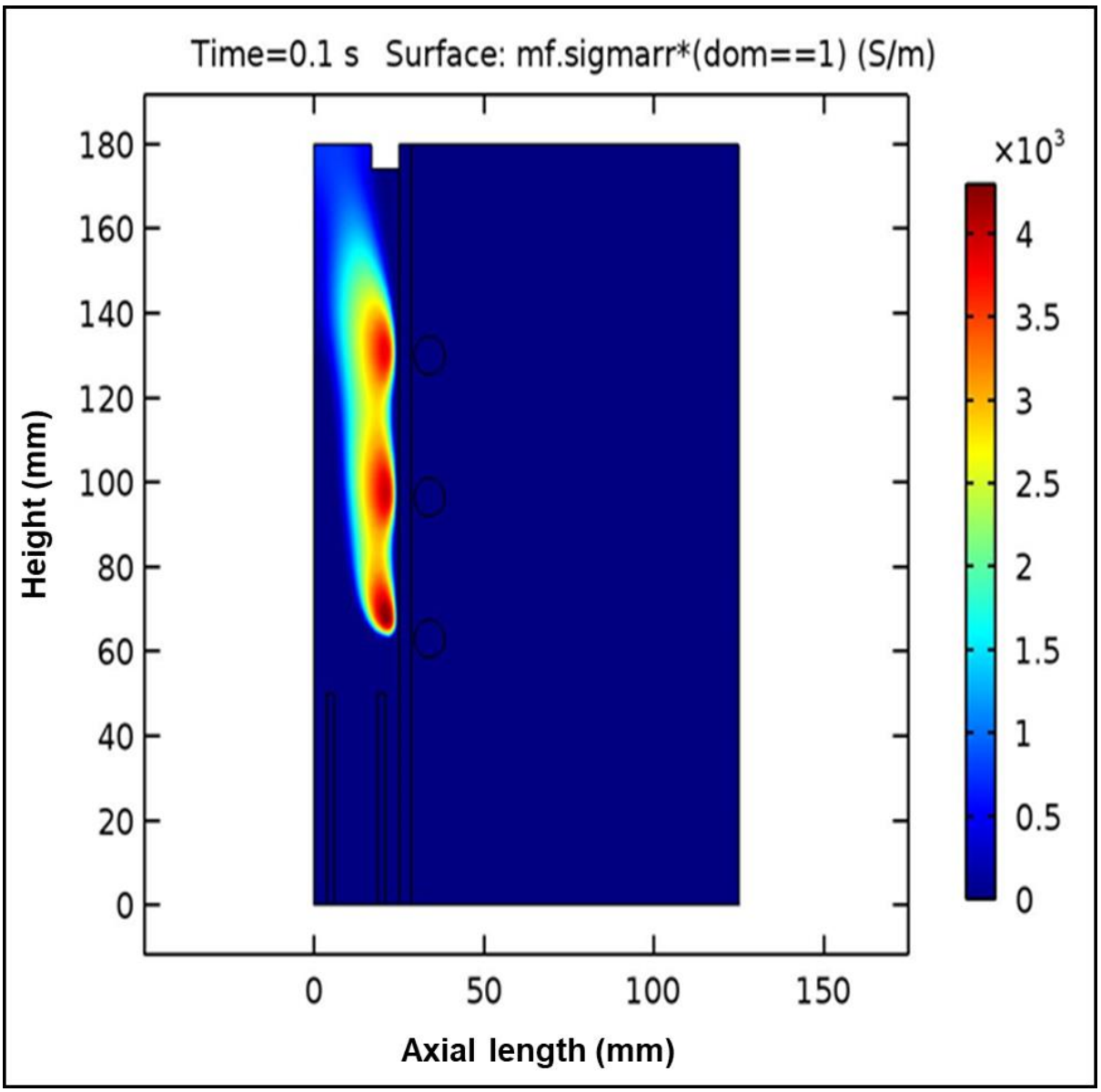

Figure 5.5: Surface plot of the argon plasma electrical conductivity.

- **Temperature distribution**

The surface plot of the argon plasma temperature as a function of time is shown in Figure 5.6. In this figure, the maximum temperature (11000 K) is obtained at the center of the torch. This temperature exhibit significant drop toward the torch outlet. The temperature of the plasma reaching the ICP torch outlet is about 9000 K.

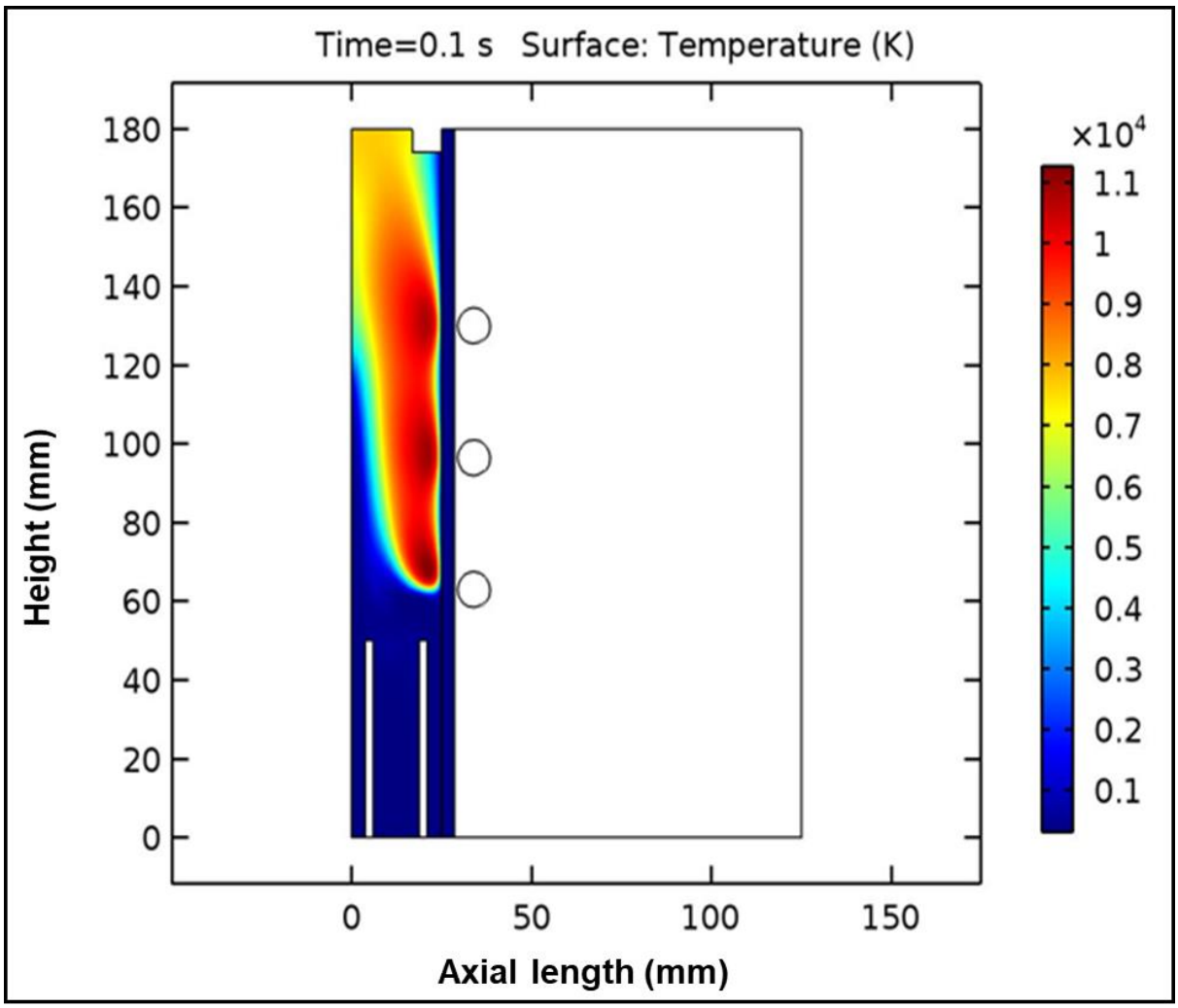

Figure 5.6: The surface plot of the argon plasma temperature.

- **Velocity magnitude**

From the temperature distribution, the maximum velocity magnitude (6 m/s) of the argon plasma is obtained after 0.1 s. The increase in the velocity magnitude is due to the excitation power applied to the induction coil at the center of the torch (from z = 63 mm to 130 mm), as shown in Figure 5.7.

Figure 5.8 depicts the plot of revolution 2D and the line graph for the velocity distribution inside the torch. In this figure, the velocity distribution is symmetrical at the center of the torch. The maximum velocity of the plasma is generated mainly because of the 31 l/min gas stream applied around the sheath quartz tube. In addition, the magnetic flux density in the centreline direction creates electric field within the quartz tube and electrons are accelerated toward the torch outlet.

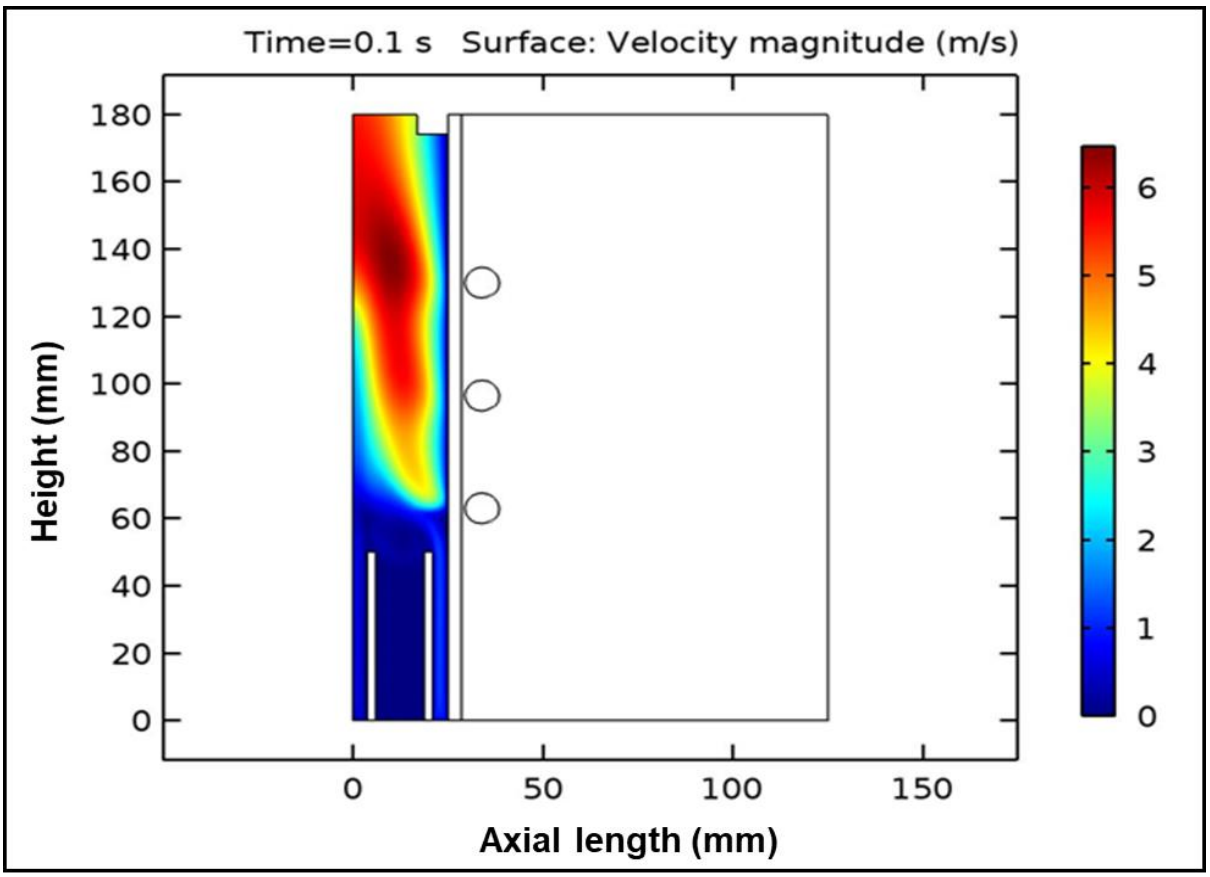

Figure 5.7: Surface plot of the velocity magnitude.

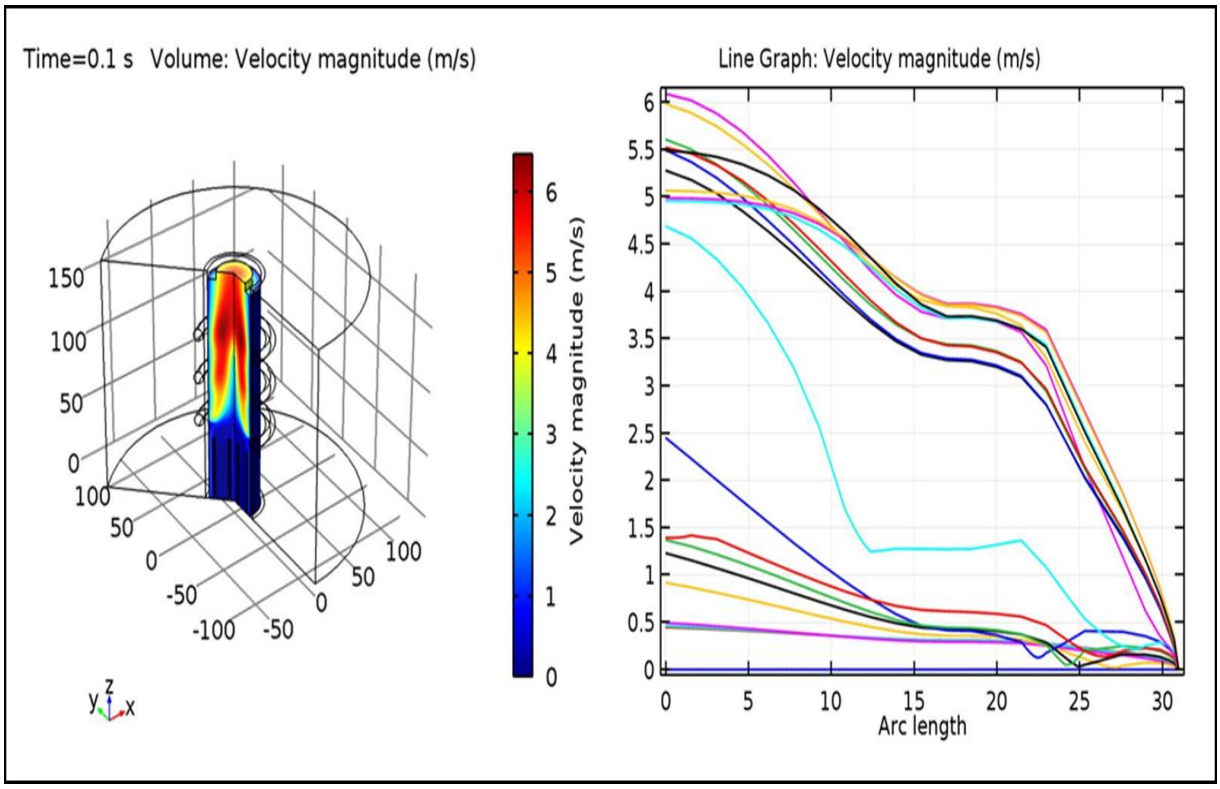

Figure 5.8: Revolution 2D plot and line graph for the velocity magnitude.

5.2 Modelling of DC arc plasma torch system

The DC arc plasma is a system which results from the coupling of strong interaction between thermal gas flow and magnetic fields inside a torch. Over the past years, numerical investigations concerning the modelling of DC arc plasma torch has been reported in the literature. Huang *et al.* (2011:1974-1982) conducted a study on the conventional LTE DC plasma, in which both anode and cathode electrodes were placed inside a torch. This was done in order to determine the plasma torch temperature and the velocity distributions. Additionally, a nominal electron temperature derived from the plasma gas temperature was used to determine the electrical conductivity of the gas. The results obtained showed that a temperature of about 13000 K and velocity magnitude of about 1000 m/s were found at the outlet of the torch (Table 5.2).

Jing *et al.* (2011:201) also use the MHD equations to simulate the fluid flow, heat transfer and electromagnetic field inside a DC arc plasma torch under laminar and turbulent conditions. During their study, a fluid-solid coupled technique was used so as to ensure that there was continuous flow of electric current and heat transfer within the plasma-electrode (cathode and anode) interfaces. Mendoza Gonzalez *et al*. (2009:1) also modelled a DC arc plasma torch based on the MHD equations proposed by (Jing *et al.,* 2011:201). In this case, a three-dimensional study was conducted to study the azimuthally asymmetric flow pattern from the gas velocity distribution and the downstream of the localized arc root attachment on the anode wall. In another study, Chine (2015:1-7) conducted a steady state two-dimensional simulation of a DC non-transferred arc plasma torch based on the assumption of LTE plasma. The results obtained showed that a plasma temperature of about 12000 K and velocity magnitude of about 500 m/s were found at the outlet of the torch. Table 5.2 shows the summary of the previous modelling in relation to the non-transferred DC arc plasma torches.

Table 5.2: Summary of the previous modelling in relation to the DC arc plasma torches.

Literature	**Plasma gas**	**Applied Current [A]**	**Current density [A/m^2]**	**Temperature [K]**	**Velocity magnitude [m/s]**
Huang *et al.,* 2011:1974-1982.	Argon	600	2.5 x 10^8	13000	1000
Chine, 2015:1-7.	Argon	n/a	-1 x 10^7	12000	500
Davis, 2004:54-76.	Argon, Air & Nitrogen	> 600	n/a	25000	500-3000
Yin *et al.,* 2007:391.	Argon	100	4 x 10^8	30000	317
Chau *et al.,* 2016:3117-3126.	Air	100	>5 x 10^6	7900	346
Chau *&* Hsu, 2011:109-115.	Air	432	6.4 x 10^3	12000	200
Chau *&* Hsu, 2011:115.	Air	901	12 x 10^3	15000	400
Chau *et al.,* 2011:152-154.	Steam	180	3 x 10^7	24000	1500

5.3 Determination of optimum power from the MHD generator using ICP and DC arc plasma sources

Considering the previous studies on ICP and the DC arc plasma sources reported in the literature, the obtained plasma velocities and temperatures (Figure 5.8 and Table 5.2) are modelled theoretically to the MHD power generator with external load resistors (1 Ω, 100 Ω and 470 Ω using equation 2.34. In this case, the width (*l*), height (*h*) and length (*L*) of the MHD duct are 0.1 m, 0.1 m and 0.3 m, respectively, while the magnet remanent flux density, B, is 1.17 T. Additionally, the surface area of the duct is about 0.00327 m^2, as shown in Appendix C. The optimum powers obtained are given in Table 5.3. These powers are calculated using the Matlab code described in Appendix A.1.

Table 5.3: Summary of the power generated from the MHD generator using ICP and DC arc plasma sources.

Thermal plasma torches	**Gas**	**Velocity magnitude [m/s]**	**Electrical conductivity [S/m]**	**MHD power [W]**		
				External load resistors		
				1 Ω	**100 Ω**	**470 Ω**
Inductively coupled plasma (ICP):						
1. Simulated inductively couple plasma	Argon	6	4000	0.490	0.005	0.001
2. Tong *et al.*, 2016:1199-1202.	TiAl alloy powder	26.7	2000	9.467	0.098	0.021
Non-transferred DC arc plasma:						
1. Huang *et al.,* 2011:1974-1982.	Argon	1000	6000	13551	137.876	29.125
2. Chine, 2015:1-7; Murphy *&* Arundell, 1994:465.	Argon	500	5500	3384.5	34.219	7.281
3. Yin *et al.,* 2007:391; Murphy *&* Arundell, 1994:465.	Argon	317	11000	1368.0	13.755	2.927
4. Kagoné *et al.,* 2012:8-11; Kohio, *et al*., 2014:714; Chau *et al.,* 2016:1.	Air	346	1000	1543.0	16.378	3.486
5. Chau *&* Hsu, 2011:109-115; Murphy, 1995:292	Air	200	5000	540.923	5.475	1.165
6. Chau *&* Hsu, 2011:115; Murphy, 1995:292.	Air	400	7000	2171.2	21.901	4.660

5.4 Conclusion

From the inductively coupled plasma simulations, the temperature of the plasma at the ICP torch outlet is about 9000 K. In addition, the maximum velocity magnitude at the torch outlet is about 6 m/s. The increase of velocity inside the torch is due to the applied induction coil excitation power (20 kW) and the applied argon flow rate (31 l/min).

From the DC arc plasma simulation results obtained from literature, the plasma temperature at the outlet of the selected torches ranged from 7900 K to 30000 K. Likewise, the plasma velocity magnitude at the outlet of these torches ranged from 317 m/s to 3000 m/s. These temperatures and velocities are modelled theoretically to the MHD generator and the optimum power is obtained when 1 Ω load resistor is used.

CHAPTER SIX: EXPERIMENT DESIGN, IMPLEMENTATION AND MEASUREMENT

6.1 Introduction

In this chapter, the design and fabrication of the MHD power generator prototype are discussed. For the experimental design, two different generator configurations are considered: continuous and segmented electrodes. Subsequently, the generator is tested with a DC arc plasma source.

6.2 Fabrication of the MHD power generator prototype

The prototype is made of a rectangular mild steel duct, round copper electrodes and neodymium N35 permanent magnet. The typical remanent flux density of this magnet is 1.17 T. This value falls within the remanent flux densities used in sections 3.24 and 3.25, The duct plane is located at the horizontal x-y plane (plane z=0). In addition, the neodymium magnets are position along the z-direction to produce external magnetic fields and Lorentz force acting on the plasma gas. Pictures and dimensions of the duct, the copper electrodes and the neodymium permanent magnets can be seen in Figures 6.1 and 6.2.

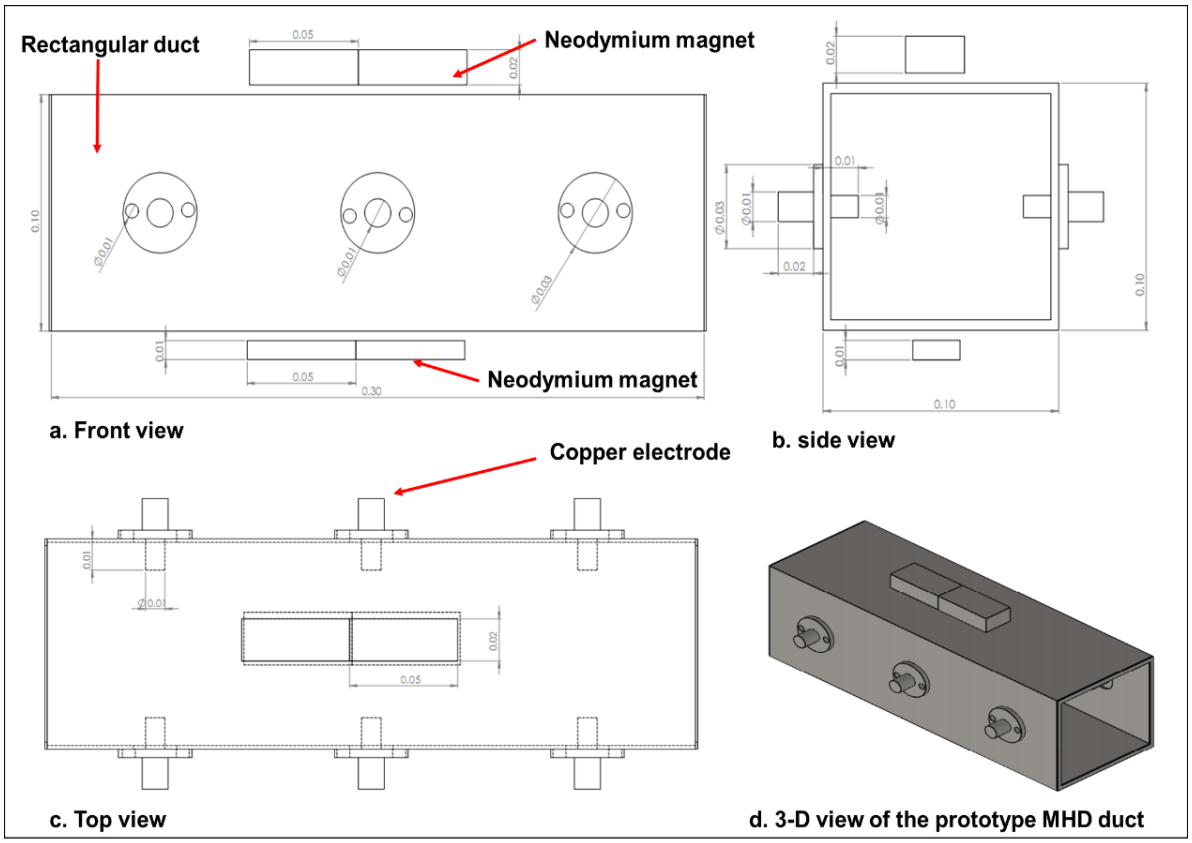

Figure 6.1: The dimensions of the rectangular duct.

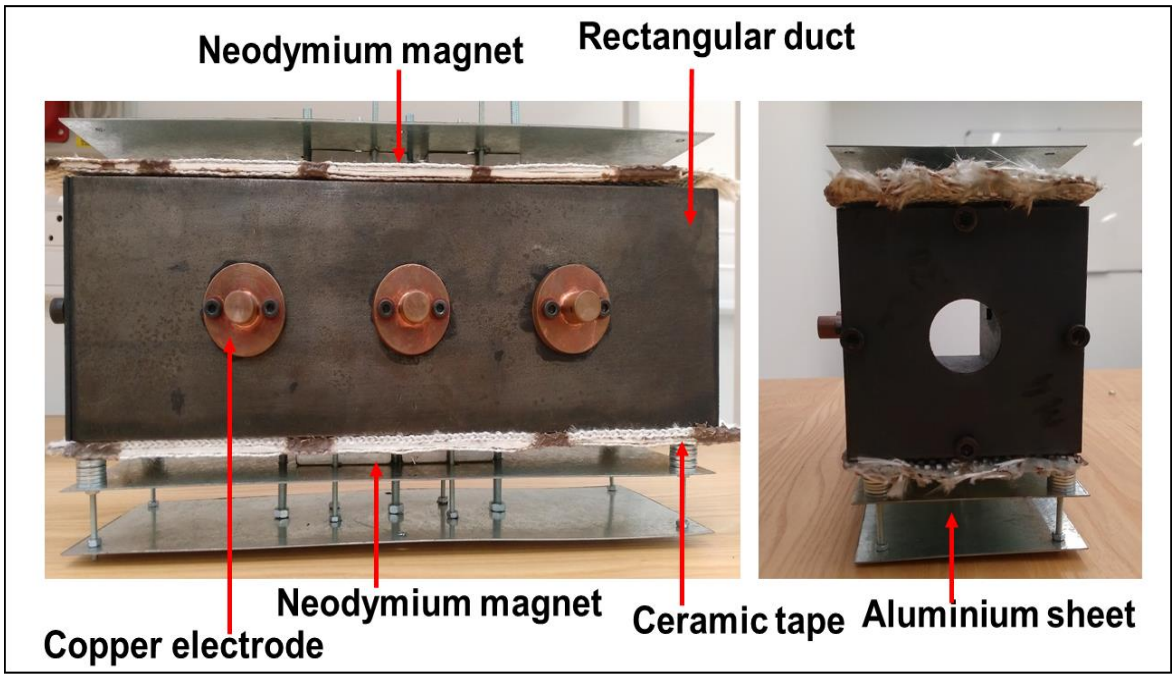

Figure 6.2: Photo of the rectangular duct.

As seen from Figure 6.2, the duct and the magnets are insulated from one another using ceramic materials while the round electrodes are insulated from the duct using tufnol materials. The round segmented electrode has been selected to minimise experimental uncertainty that could arise from complex designs and structures. Additionally, this configuration is an innovative concept which can be used to improve the efficiency of the generator. Copper is used for the construction of the electrodes due to its good work function and high conductivity. Materials like titanium and nickel can also be used but are not considered due to cost and availability.

6.3 The DC arc plasma source and experimental procedure

In order to generate plasma for the experiment, a transferred DC arc source is used to create an actual plasma environment, which flows into the MHD power generator prototype. The experiments are conducted at the Department of Electrical, Electronic and Computer Engineering, Cape Peninsula University of Technology, Cape Town (South Africa).

6.3.1 Setup of the DC arc plasma source

The DC arc plasma device consists of a power supply, an arc starting circuit which ignite the torch and an air compressor, with a tank capacity of about 24 Litres (Figure 6.3). This HF device has a maximum operating current of about 40 amps and an operating voltage of about 220 V. In the experiment, the maximum DC arc current of 25 A is used. The main arc and pilot arc of the air plasma device are shown in Figure 6.3.

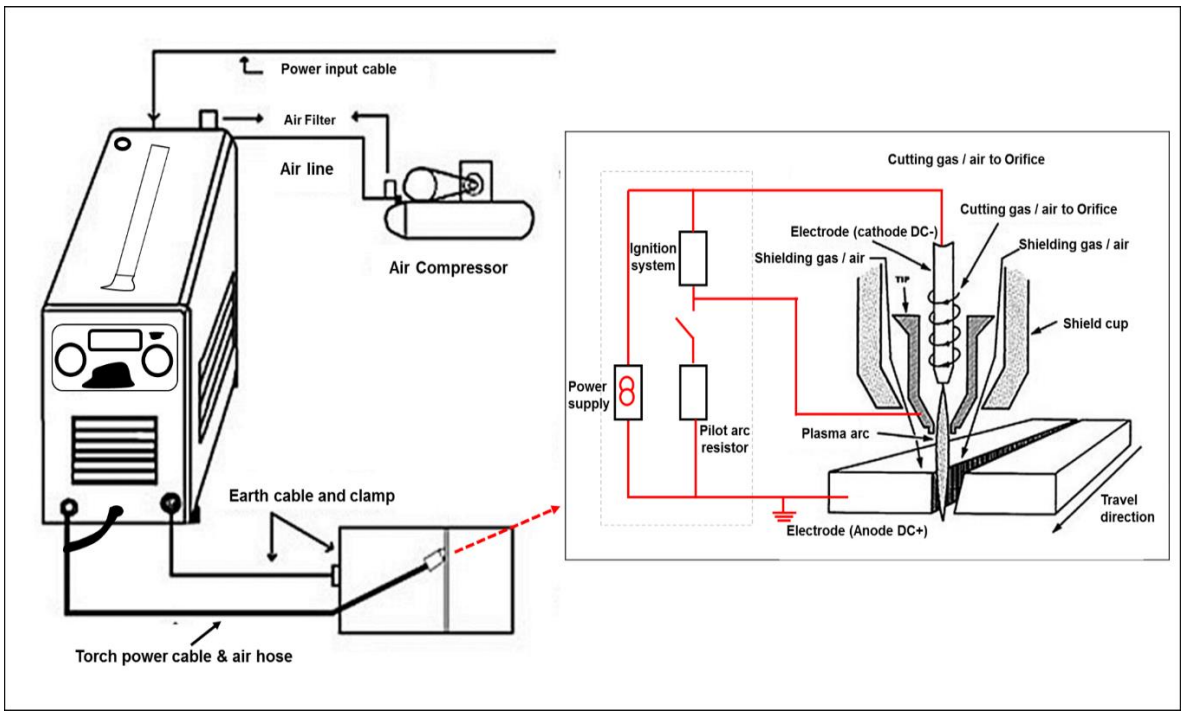

Figure 6.3: The main and pilot arc of the DC plasma device (Adapted from Robot Industrial Supplies, 2018).

From Figure 6.3, the power unit consists of a pilot arc ignition system which is responsible for lighting and sustenance of the plasma. Ignition of pilot arc can be done in two ways: retract starting mode and short HF pulse mode.

In the retract starting mode, the pressure of the air supplied to the torch is used to drive back a piston connected to the electrode. When the electrode and nozzle come in contact with the applied electric current, the electrode are retracted. As the electrode retracts, a pilot arc is created, and the main gas blow out of the nozzle. Once the anode is within 5–15 mm from the end of the nozzle, heat is transferred to the workpiece and current is established within the electrode and workpiece gap (Nemchinsky, 1998:3102–3104).

In the short HF pulse mode, a pulse is applied along the gap between the copper electrode (cathode) and the nozzle to ignite the pilot arc. Once the pilot arc is ignited, it creates an arc discharge between the electrode and the nozzle. Subsequently, ionisation occurs in the space between the nozzle and the workpiece (anode). As the electric arc burn towards the workpiece, the main plasma gas flows through the narrow orifice of the nozzle (2 mm in diameter), where they are heated and ionised. When the arc plasma jet reaches the workpiece, heat is transferred, and the workpiece is melted by the plasma gas. The cathode electrode is then cooled down with secondary air from a constricting nozzle inside the torch head. The components of the DC arc plasma device used in the present study is depicted in Figure 6.4.

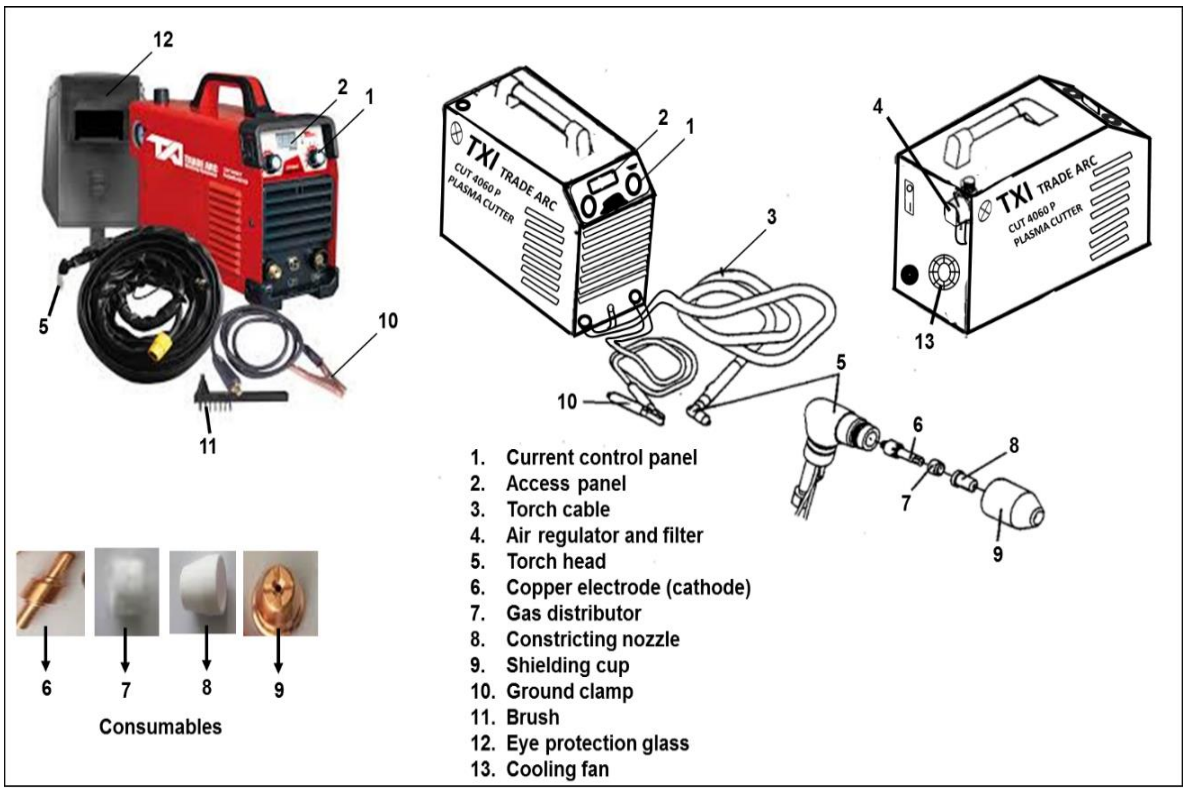

Figure 6.4: Components of the DC arc plasma device (Adapted from Grill, 2018).

From Figure 6.4, the plasma torch consists of special consumable materials such as copper electrode, shielding cup, hafnium or zirconium copper nozzle and retaining cup (Xue *et al.,* 2005:44-49).

6.3.2 Experimental setup and the description of the circuit model

For the experimental setup, atmospheric air is first compressed and filtered at a pressure of about 3.5 bar to 4 bar (50 psi to 58 psi) inside the DC arc plasma device. Thereafter, the torch anode (workpiece) is placed within few millimeters to the torch cathode before the start of each experiment. This is to ensure that a high temperature non-transferred arc plasma jet flows out of the torch nozzle before entering the inlet of the MHD power generator (Appendix E). In doing so, a high ionization capability and strong plasma energy is produced during the experiment.

The output voltage from the MHD generator is then measured and recorded using a personal computer (PC) with National Instrument (NI) Labview and data acquisition (DAQ) software packages installed. The measurement procedure used during the DC arc plasma experiment is shown in Figures 6.5 and 6.6.

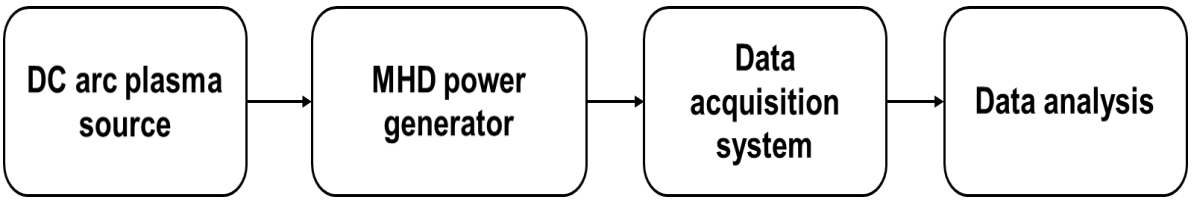

Figure 6.5: Flow chart of the experimental setup.

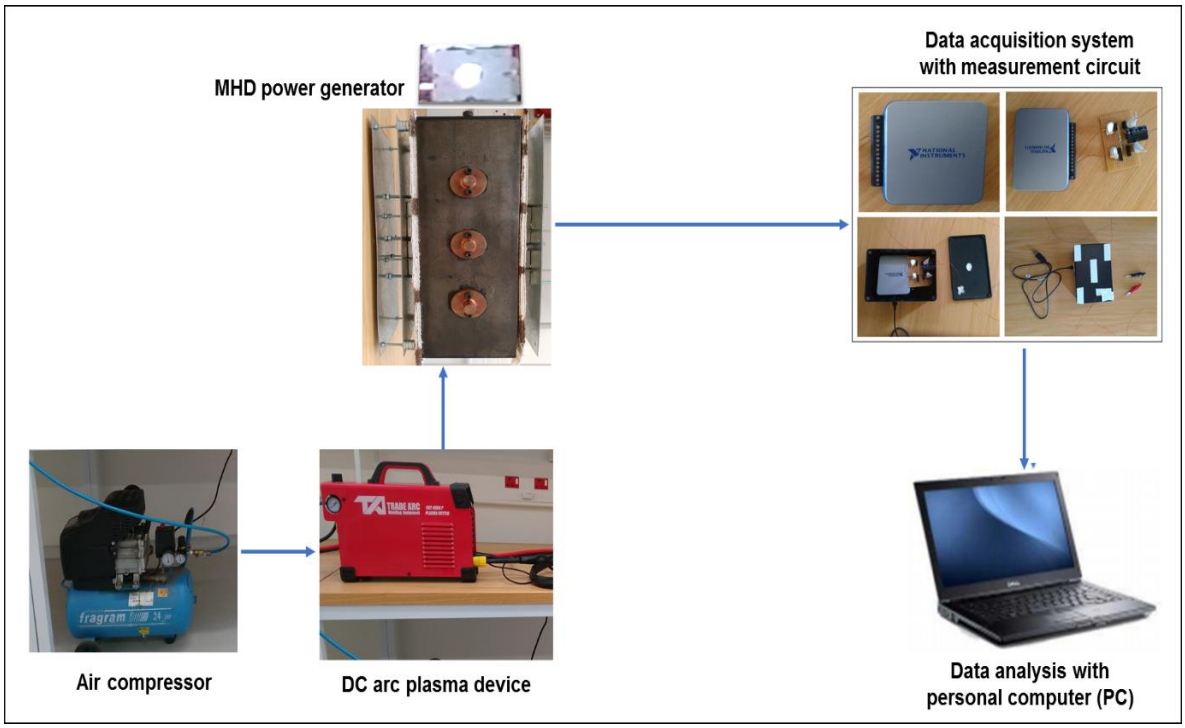

Figure 6.6: The setup of the DC arc plasma experiment.

The aim of the experiment is to measure the terminal voltage across the MHD power generator electrodes when exposed to a plasma generated from the DC arc device. The first experiment conducted served as a control experiment. In this experiment, no arcing with plasma is performed.

In the second experiment, arcing with plasma occurs, and the three electrodes on each side of the duct are connected together in continuous mode. Additionally, three load resistors, 1 Ω, 100 Ω and 470 Ω, are connected to the continuous electrodes one after the other (Figure 6.9 & Appendix E).

In the third experiment, arcing with plasma occurs, and only the middle electrodes are connected in segmented mode (where the neodymium magnets are positioned). The load resistors are also connected to the middle-segmented electrodes one after the other (Figure 6.9 & Appendix E).

- **Important note**

The experiment outcomes were initially captured with a digital multimeter and an “Agilent” oscilloscope. However, due to the high level of noise interference from the surrounding environment, the actual voltage signal magnitude was not captured by the oscilloscope. Therefore, the oscilloscope was not used in the subsequent experiments. To reduce these high noise levels, the measurement circuit is connected to the NI USB-6001/6002/6003 DAQ device which has a differential terminal configuration. In this mode, the measurement circuit behave as a virtual channel and the voltage signal difference across the electrodes is measured. This process provides good rejection of common mode voltage and noise. The measurement circuit and the DAQ device are kept inside a container to further reduce the surrounding noise (Appendix D and Figures D.1 to D.5).

6.4 Data acquisition system

6.4.1 NI USB-6001/6002/6003 DAQ

The NI USB-6001/6002/6003 is a data acquisition instrumentation device that can be used to measure or capture electrical parameters such as voltage, current, temperature and pressure. In the present study, the device is used to log, and record voltage data measured across the electrodes. This data is then stored inside the PC for post-analysis. The NI USB-6001/6002/6003 DAQ consists of 2 analog output (AO) channels, four differential channels, 13 digital input/output (DIO) channels, 32-bit counter and a full-speed USB device which provides 8 single-ended analog input (AI) channels. All these functional components are combined on a single device unit, as shown in Figure 6.7.

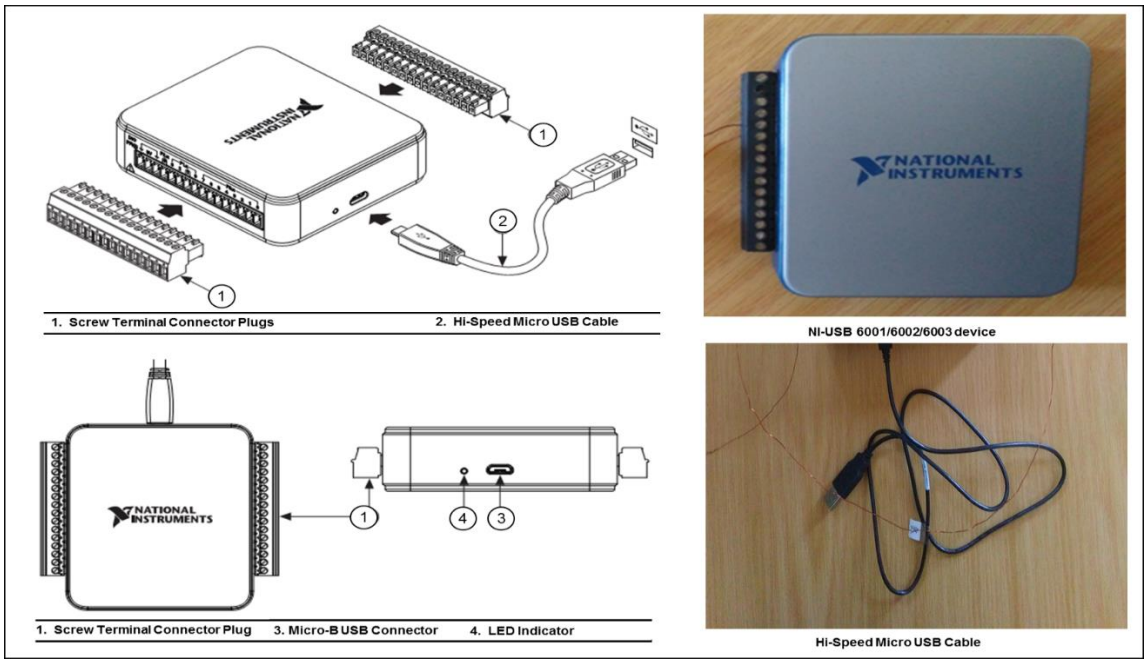

Figure 6.7: Hardware Setup for NI USB-6001/6002/6003 DAQ.

From Figure 6.7, the DAQ communicates with the PC through a Signal Express interface, which is often used to acquire, create, generate, analyse, process, load and save signals. The DAQ also uses the data logging interface from the Labview National Instruments software to log data continuously in real time. The log and read mode option is selected before the start of the experiment. The DAQ device is known to produce instant interactive measurements which does not require programming. Figure 6.8 depicts the internal circuitry of the NI USB-6001/6002/6003 DAQ device.

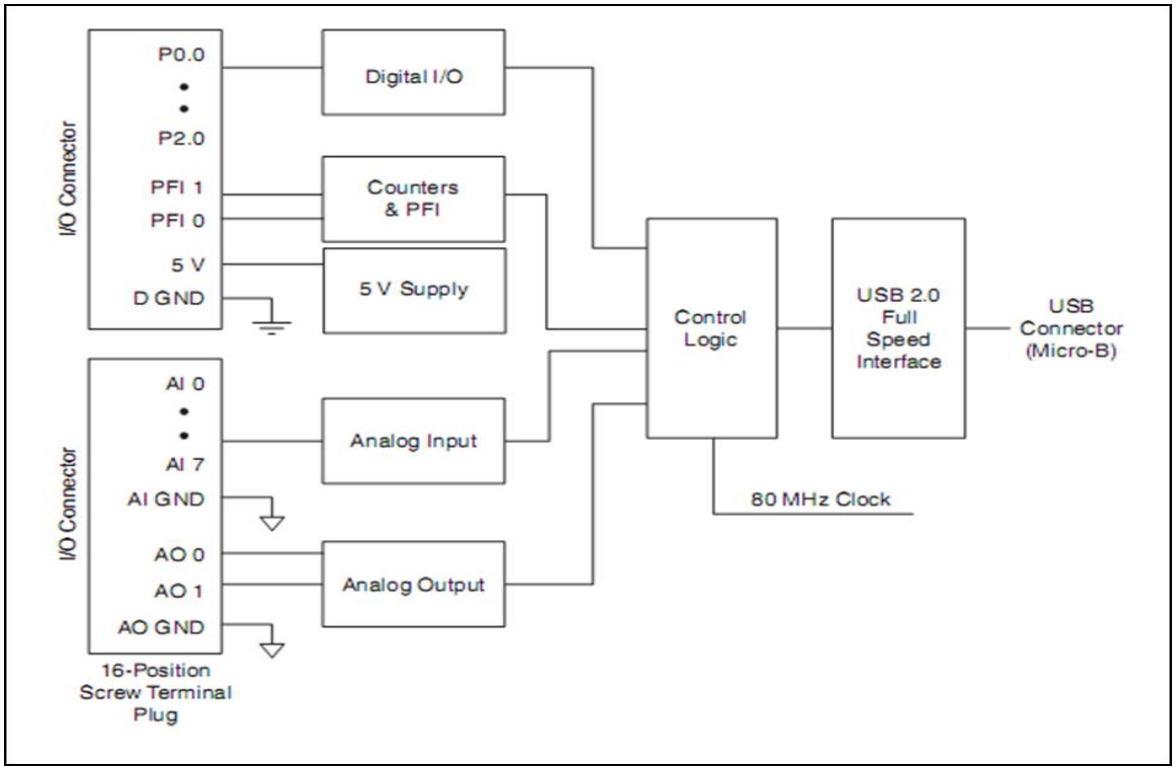

Figure 6.8: Internal circuitry of NI USB-6001/6002/6003 DAQ (National Instruments, 2014).

The NI USB-6001/6002/6003 data acquisition device specifications are:

- Maximum sample rate: **6001**: 20 kS/s; **6002**: 50 kS/s; **6003**: 100 kS/s.
- Maximum voltage: +/- 10 VDC
- Resolution: **6001**: 14 bits; **6002**: 14 bits; **6003**: 100 14 bits.
- Analog input: 4 differential channels and 8 single-ended analog input (AI) channels.
- 12 bits analog outputs (0-5 Volts, 150 updates/sec maximum)
- 13 digital Input / Output channel lines

6.4.2 Analog signal acquisition using the NI USB-6002 DAQ device

In order to log and read voltage data from the experiments, an NI-DAQmx icon is selected from the LabView measurement input/output interface. Subsequently, from the NI-DAQmx drop-down list, the DAQ Assistant interface, which is often used for analog signal acquisition is selected.

During the experiment, the NI USB-6002 DAQ and the differential measurement mode options are selected for capturing the voltage signal. In the differential mode, the NI USB-6002 DAQ interface is configured to measure and store the voltage difference between the two analog signals (AI+, and AI-), placed across the external load, which is connected to the electrodes, as shown in Figure 6.9. Data samples are taken at continuous time intervals, 1000 samples over a period of 0.5 ms. The NI USB-6002 DAQ has more than one analog input channel (Dev1/ai0 to ai7). The physical channel selected to read and acquire the signal is Dev1/ai1.

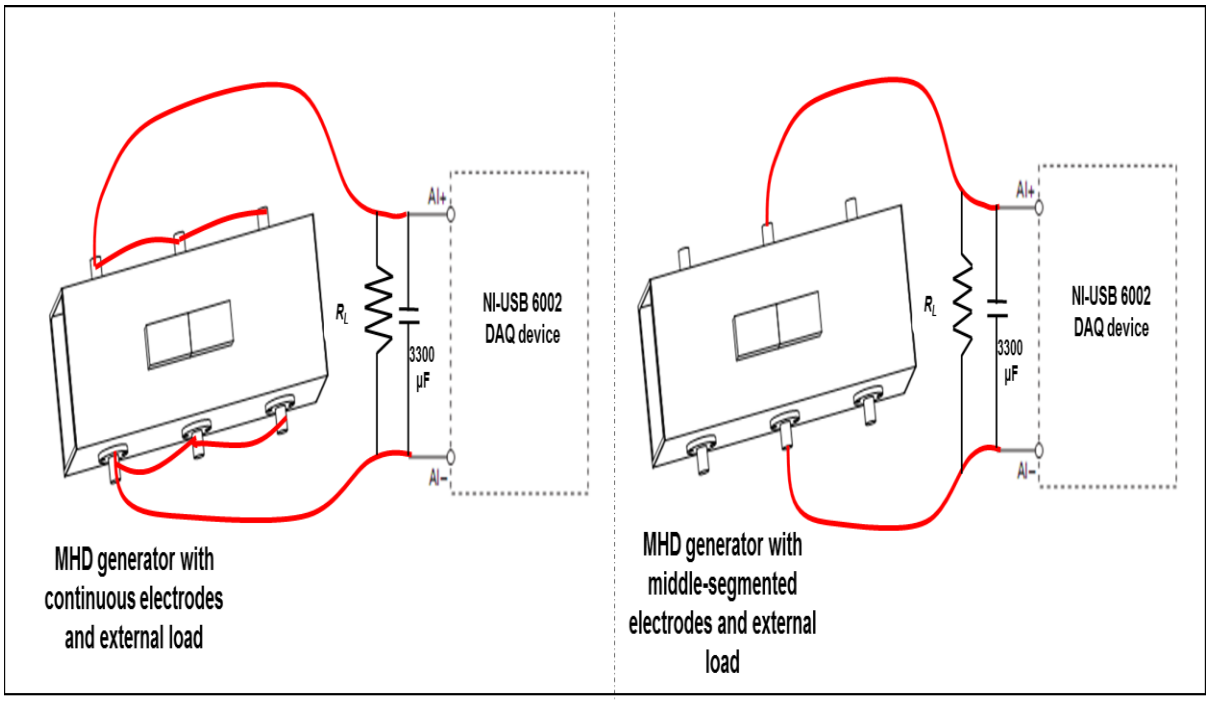

Figure 6.9: Representation of the measurement circuit in continuous and segmented electrodes modes.

From Figure 6.9, the capacitor is used during the experiment to stabilise the voltage signal, which is further filtered with a Butterworth Filter (Figure 6.10) for greater accuracy and noise reduction. This is done because the signal leads (greater than 2 m) travel through noisy environment. The picture of the measurement circuit without the DAQ device is shown in Figure D.1.

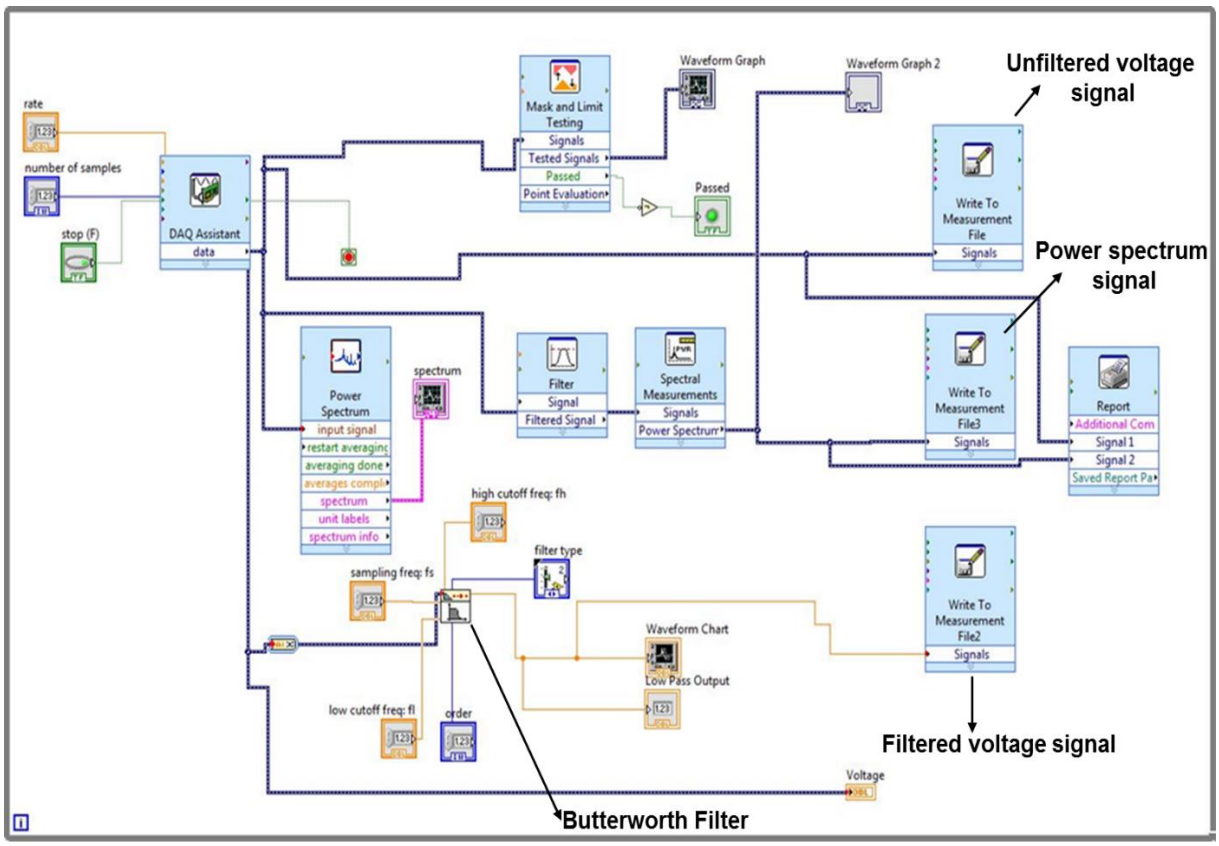

Figure 6.10: Labview software block diagram for NI USB-6002 DAQ.

6.5 Outcomes of the MHD power generator under DC arc plasma experiments

This section presents the measurement results of the DC arc plasma experiment. The current flowing through the electrodes is determined by measuring the terminal voltage signals across the external load resistors. The equipment used during the experimental setup includes a multimeter, an Agilent oscilloscope and the NI USB-6001/6002/6003 DAQ. For the limited time available to carry out the experiments, the measurement circuit through the differential terminal configuration of the NI USB-6002 DAQ device has been used to capture the experiment results and also to reduce the high noise levels from the surrounding environment.

- **Control experiment**

The first experiment (without arc plasma) is used as the control experiment since there is no generation of electrons and ions. The voltage measured is assumed to be a systemic offset voltage (Figure 6.11). Moreover, the calculated absolute offset voltage is 0.965 mV (Appendixes A.5 & B). The spectrogram of the measured voltage without arc plasma is shown in Figure 6.12 (Appendix A.3). In this figure, the offset voltage signal is decomposed into its frequency components through the use of a mathematical algorithm described in Appendix A.2. This algorithm is called the Fast Fourier Transform (FFT).

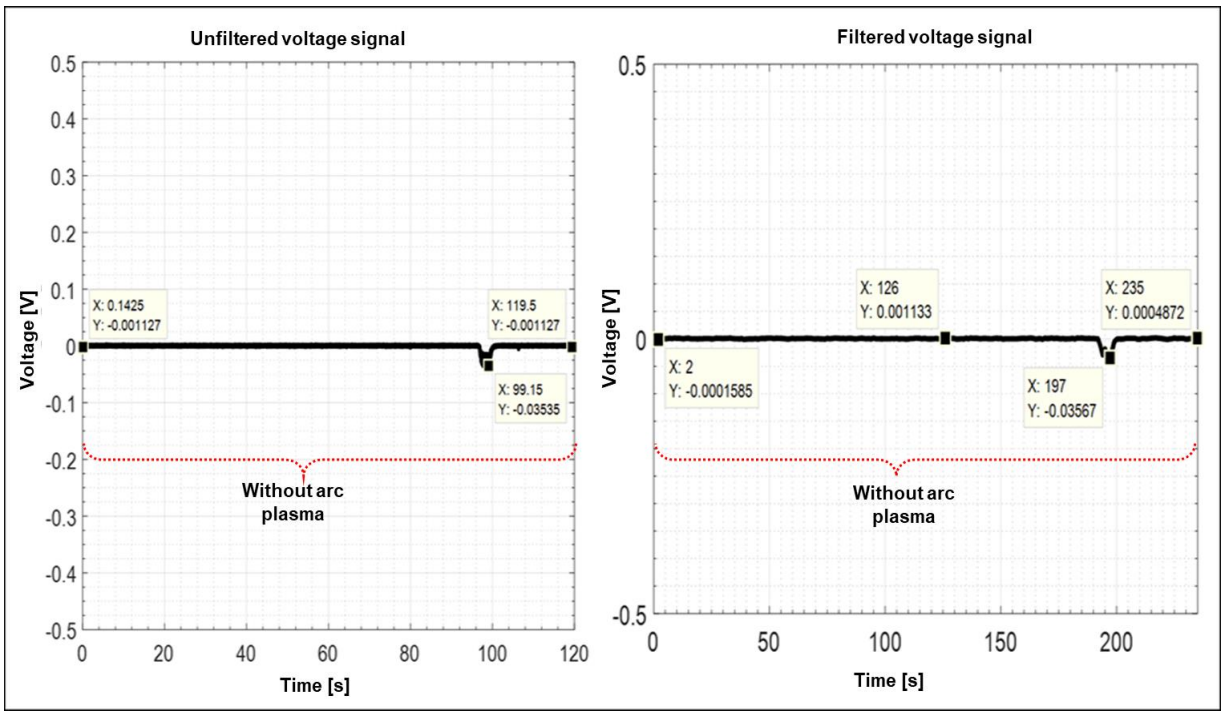

Figure 6.11: Measured voltage without arc plasma.

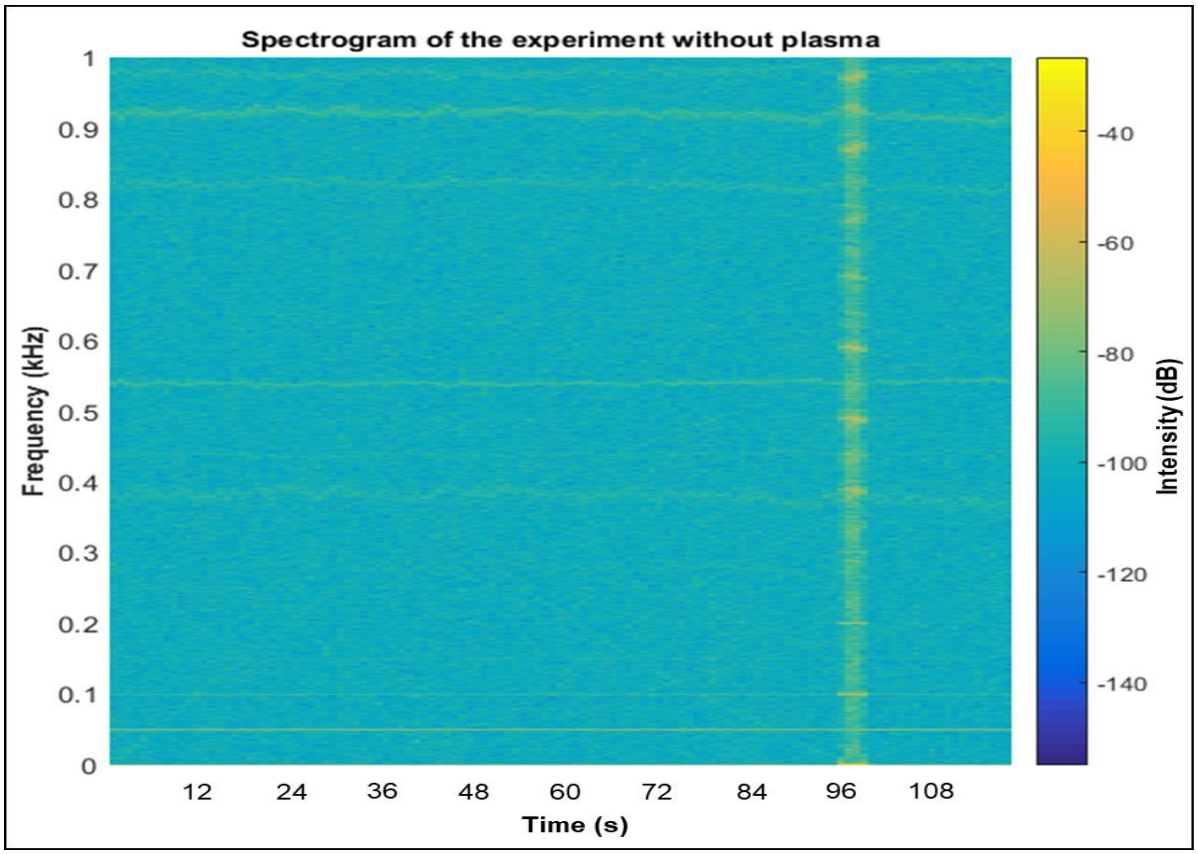

Figure 6.12: Spectrogram of the measured voltage without arc plasma.

- **Experiment 2 results**

In the second experiment during which arcing with plasma occurred, three electrodes on each side of the duct are connected together in continuous mode. The terminal voltage signals obtained using 1 Ω, 100 Ω and 470 Ω resistors change significantly under different arcing experiments and conditions. The graphical representation of the acquired voltage data helps to observe the overall signal magnitude, significant peaks, and typical frequency patterns. The voltage signals are shown in Figures 6.13 to 6.24, in which the horizontal axis signifies the time domain and the vertical axis represents the signal magnitude.

The terminal voltage measured across the continuous electrodes in experiment 2 using 1-ohm resistor is very low and consistent before the arc occurred. When the arc plasma is applied, the amplitude of the voltage signal increases and gradually decreases to lower levels when the arc plasma is not applied. The increase in the voltage signal at the time interval ranging from 25 s to 65 s indicates the presence of arc plasma, as shown in Figure 6.13.

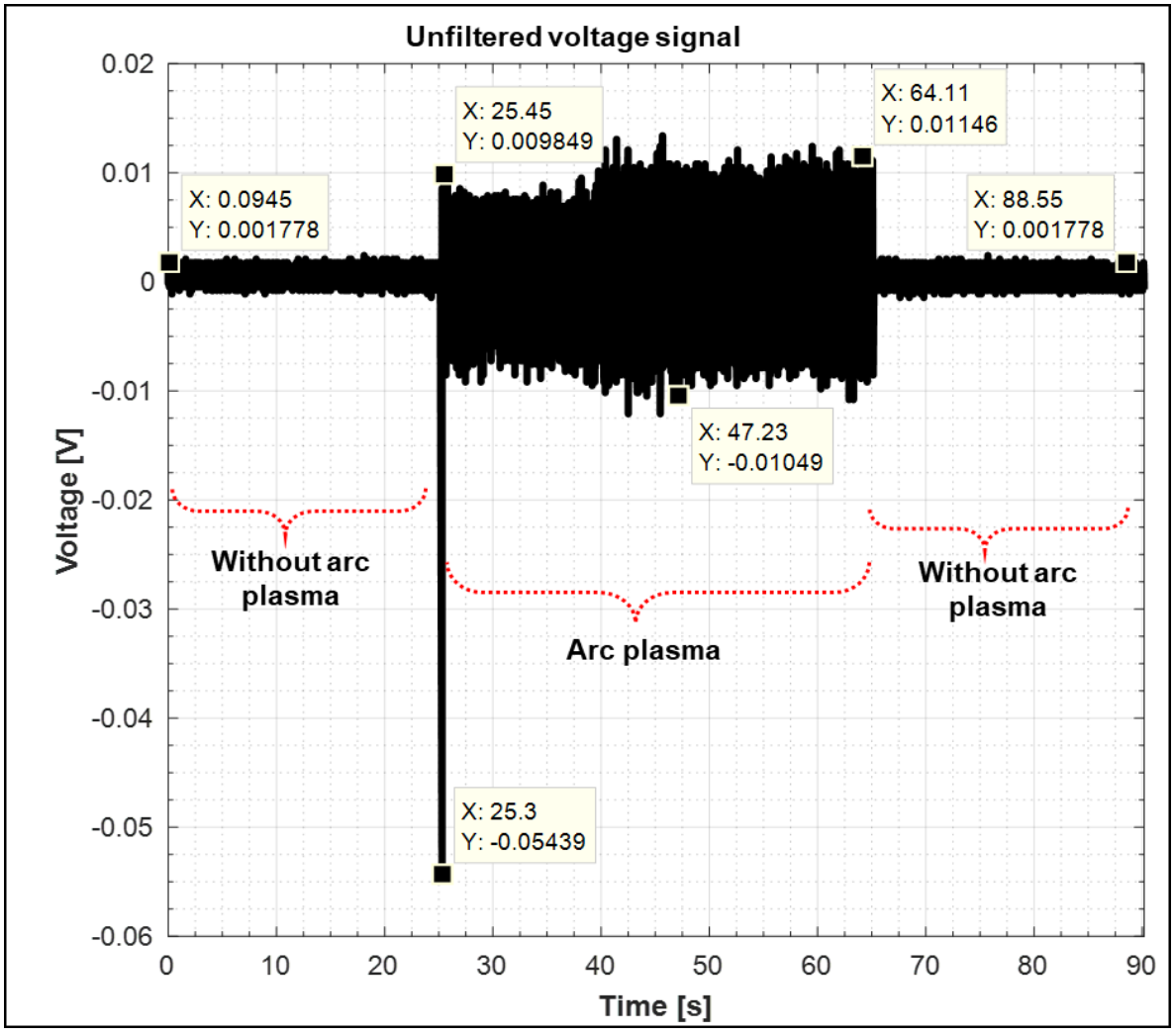

Figure 6.13: Terminal voltage measured across the continuous electrodes using 1-ohm resistor.

From Figure 6.13, the unwanted low frequency and high frequency noise are minimised using the Butterworth low-pass filter, with cut-off frequency of about 500 Hz. This filtering method helps to minimise the surrounding noise and also give insight into the frequency characteristics of the voltage signal, as shown in Figure 6.14. In this figure, a clear signal difference is observed between the arc plasma state (from 53 s to 129 s) and non-arc plasma state.

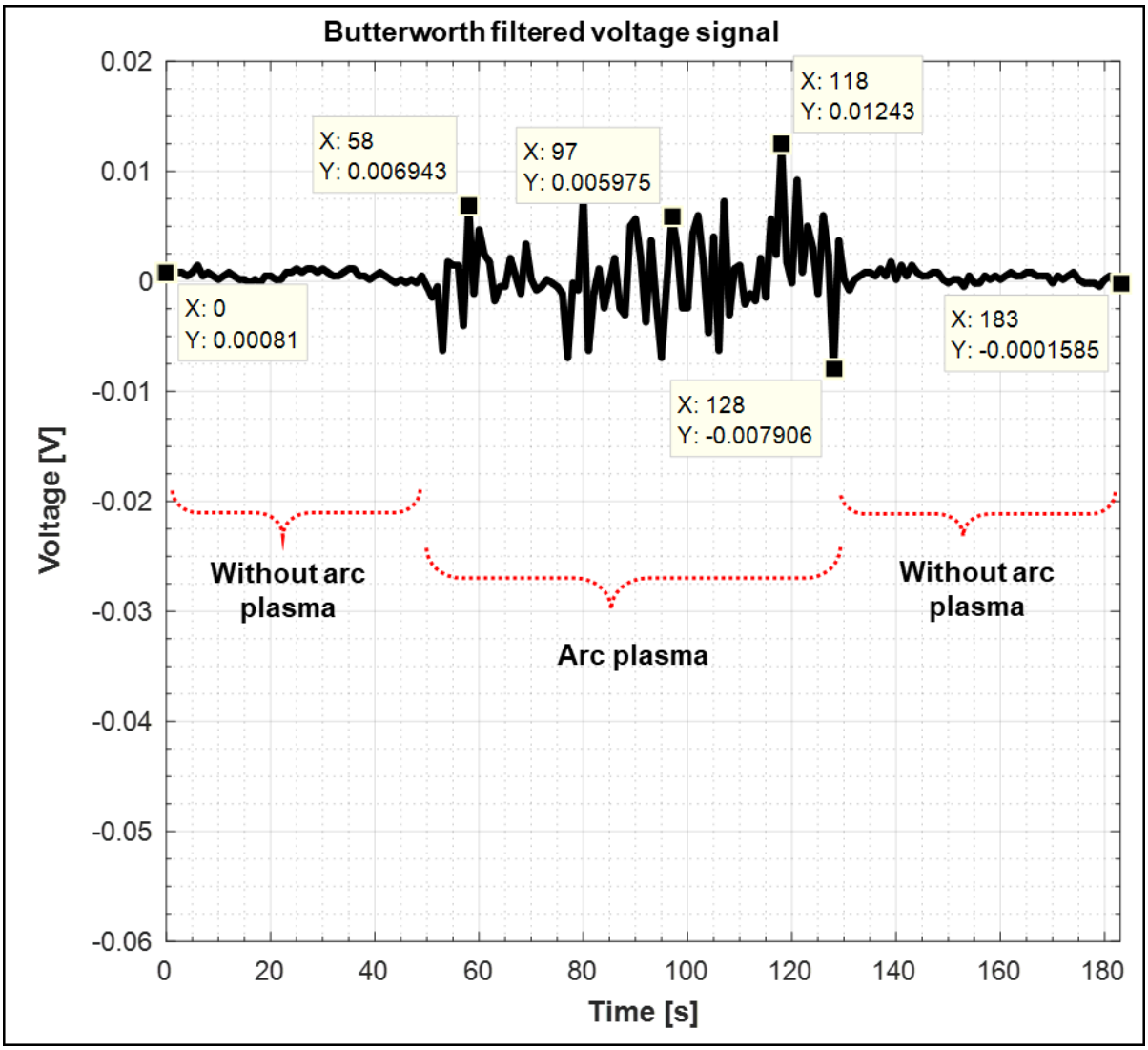

Figure 6.14: Butterworth filtered voltage measured across the continuous electrodes using 1-ohm resistor.

The challenges faced in relation to the time domain measurements can be reduced using the frequency domain analysis, which is expected to have a characteristic spectrum. This is done by performing an FFT on the time signal using the Matlab code described in Appendix A.2. The frequencies of the measured voltage in experiment 2 using 1-ohm resistor, with and without arc plasma, are shown in Figure 6.15. In this figure, significant harmonics are observed in the experiment. These frequencies exhibit consistent behaviour which can be directly related to the time domain voltage signal.

Furthermore, the FFT of the voltage (original) data in experiment 2 using 1-ohm resistor has some high frequency noise which supresses the low periodic frequencies (50 Hz, 100 Hz and 200 Hz) present in the signal. The amplitude of this high frequency noise gets bigger with time, making the low frequency signals invisible to be captured. To reduce this noise, the FFT of the absolute value of the voltage data is calculated. Thereafter, the amplitudes (0.125, 0.062 and 0.021) of the low frequency signals are captured, as shown in Figure 6.15.

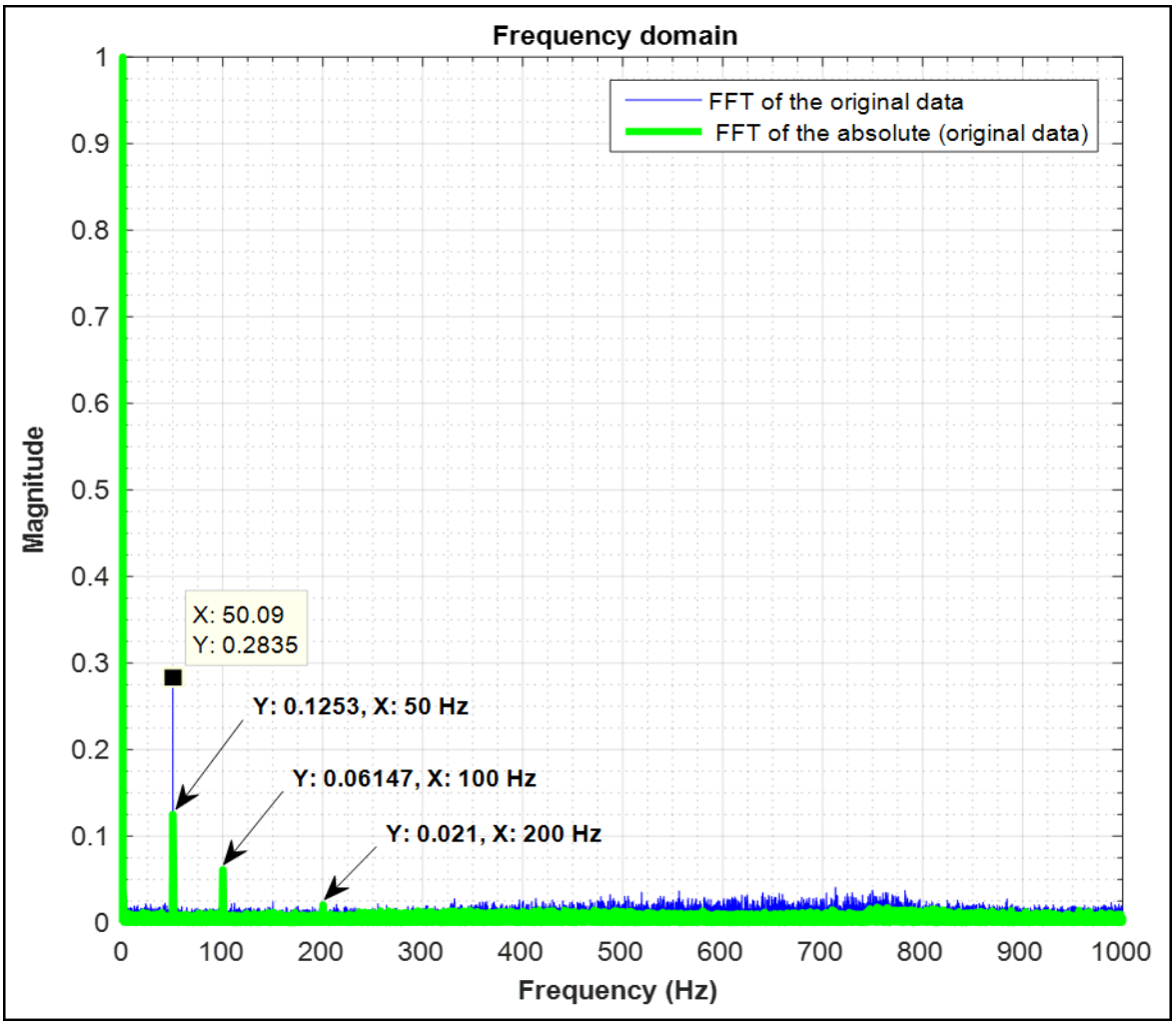

Figure 6.15: Frequency spectra of the terminal voltage measured across the continuous electrodes using 1-ohm resistor.

The spectrogram (time-frequency analysis) of the terminal voltage measured across the continuous electrodes in experiment 2 using 1-ohm resistor is shown in Figure 6.16. In this figure, the time signal is represented along the horizontal axis while the frequency of the signal is represented along the vertical axis.

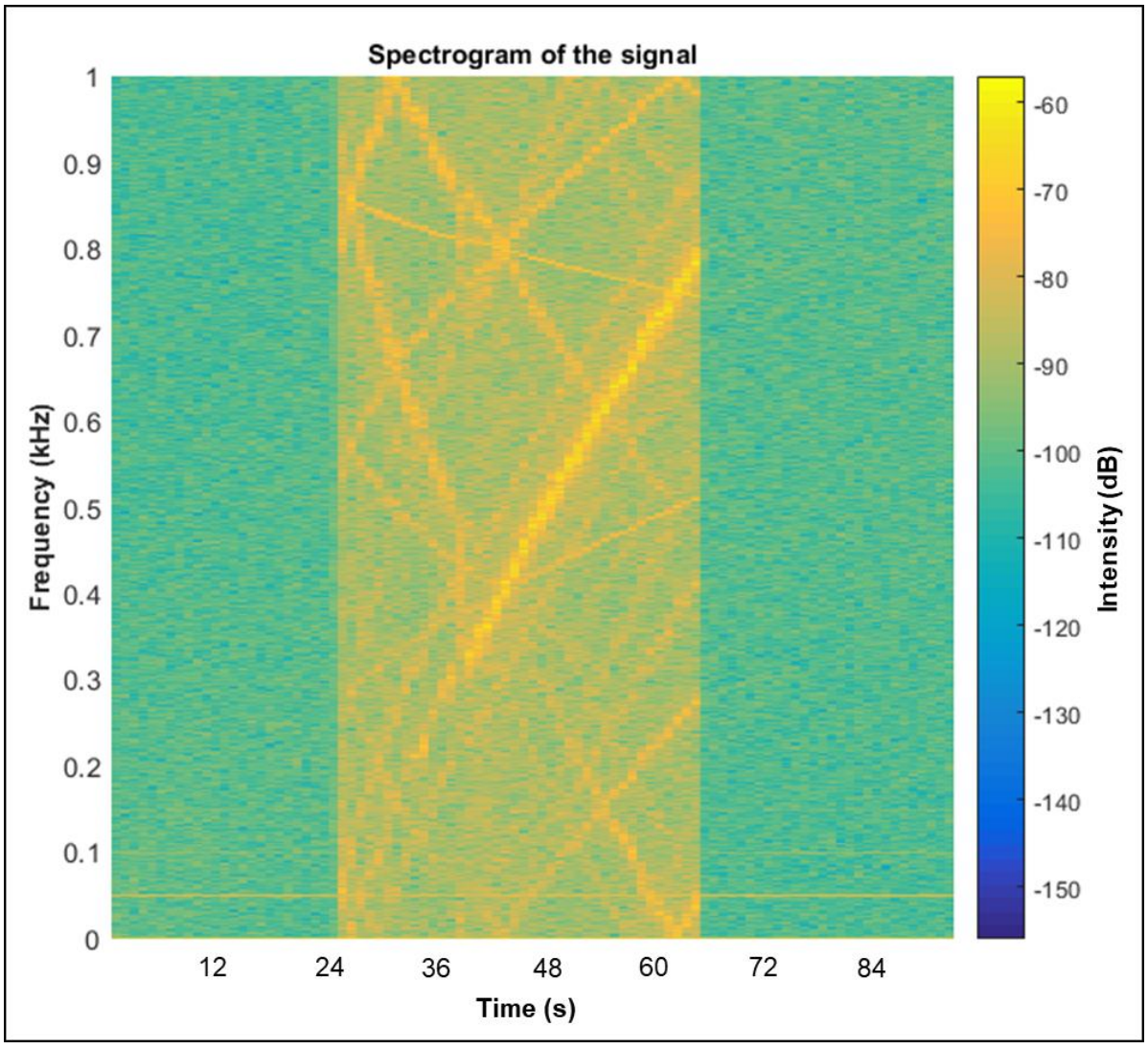

Figure 6.16: Spectrogram of the terminal voltage measured across the continuous electrodes using 1-ohm resistor.

From Figure 6.16, the intensity of each frequency is represented by a coloured spectrum, which gives a visual representation of how the spectral densities of the measured voltage changes with respect to time. Furthermore, at the time interval ranging from 25 s to 65 s, the increase in the intensity levels indicate the presence of arc plasma. A normalised Hanning window has been used to display the frequencies that are involved in the signal. For the window settings, the number of FFT (NFFT) points is 50000, the window length is 3000 and the overlap is 1000. The window length is useful for the resolution of the time and frequency signals.

The terminal voltage measured across the continuous electrodes in experiment 2 using 100-ohm resistor is also very low and consistent before the arc occurred. When the arc plasma is applied, the amplitude of the voltage signal increases (from 41 s to 125 s) and gradually decreases to lower levels when the arc plasma is not applied, as shown in Figure 6.17.

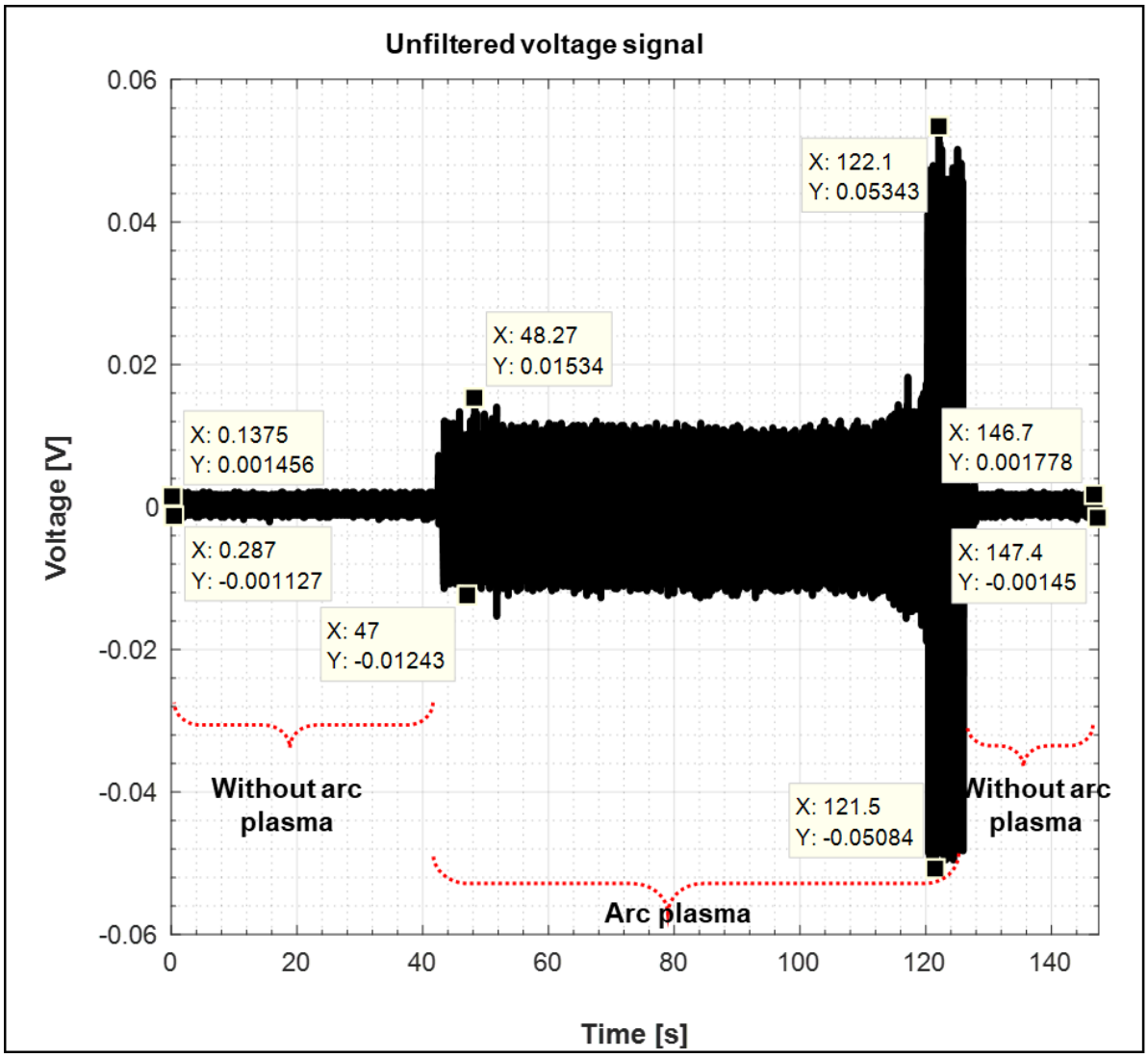

Figure 6.17: Terminal voltage measured across the continuous electrodes using 100-ohm resistor.

Figure 6.18 depicts the Butterworth filtered voltage measured across the continuous electrodes in experiment 2 using 100-ohm resistor. In this figure, the unwanted low frequency and high frequency noise of the measured voltage signal are also minimised. Additionally, at the time interval ranging from 85 s to 250 s, a clear signal difference is observed when the arc plasma is applied.

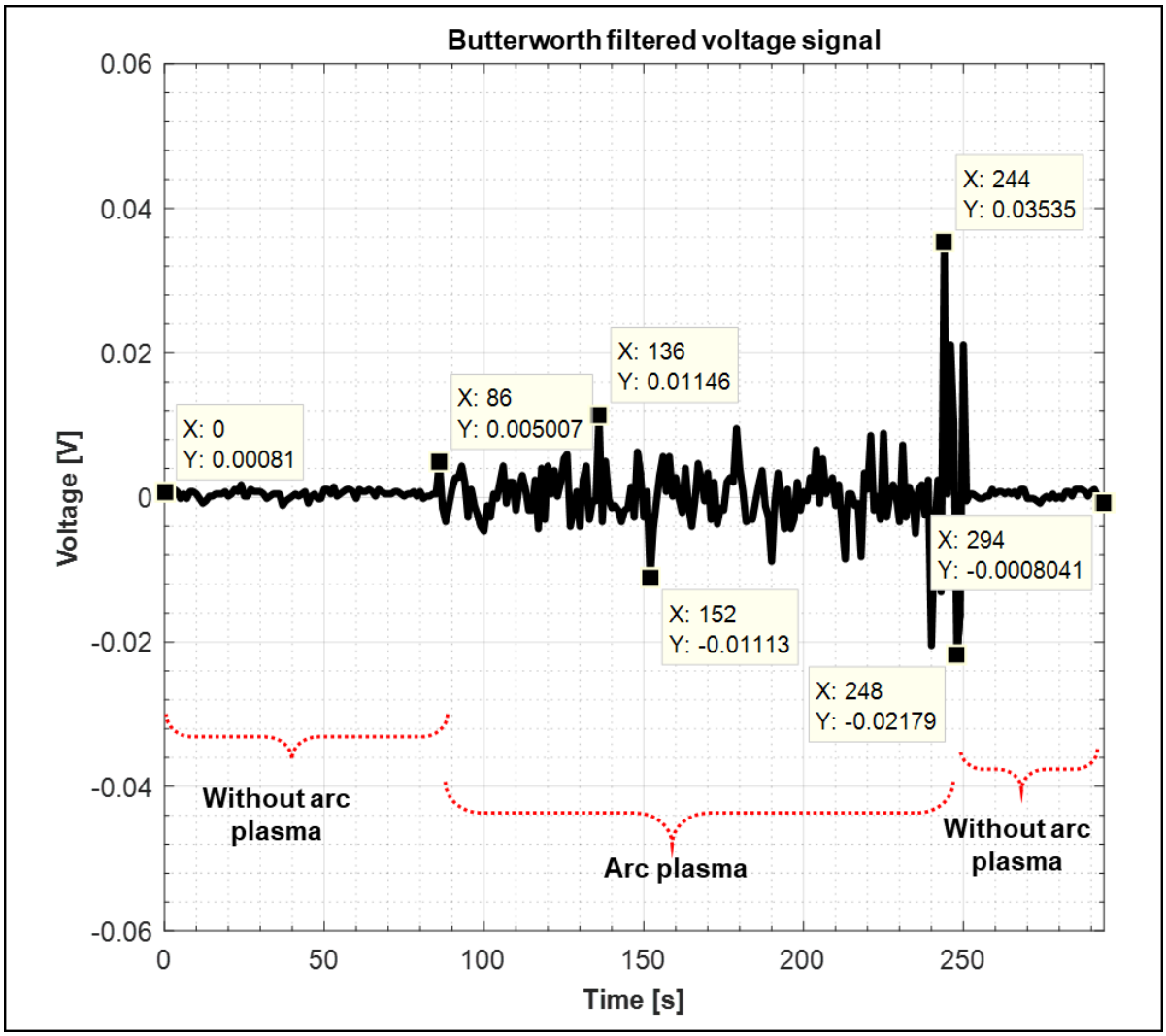

Figure 6.18: Butterworth filtered voltage measured across the continuous electrodes using 100-ohm resistor.

The frequency of the measured voltage in experiment 2 using 100-ohm resistor, with and without arc plasma, is shown in Figure 6.19. In this figure, the frequencies exhibit consistent behaviour that is comparable to the time domain voltage signal.

The FFT of the voltage (original) data in experiment 2 using 100-ohm resistor also contains some high frequency noise which supresses the low periodic frequencies (50 Hz, 100 Hz and 655.7 Hz) present in the signal. To decrease this noise, the FFT of the absolute value of the voltage data is calculated. Afterward, the amplitudes (0.041, 0.046 and 0.041) of the low frequency signals are captured, as shown in Figure 6.19.

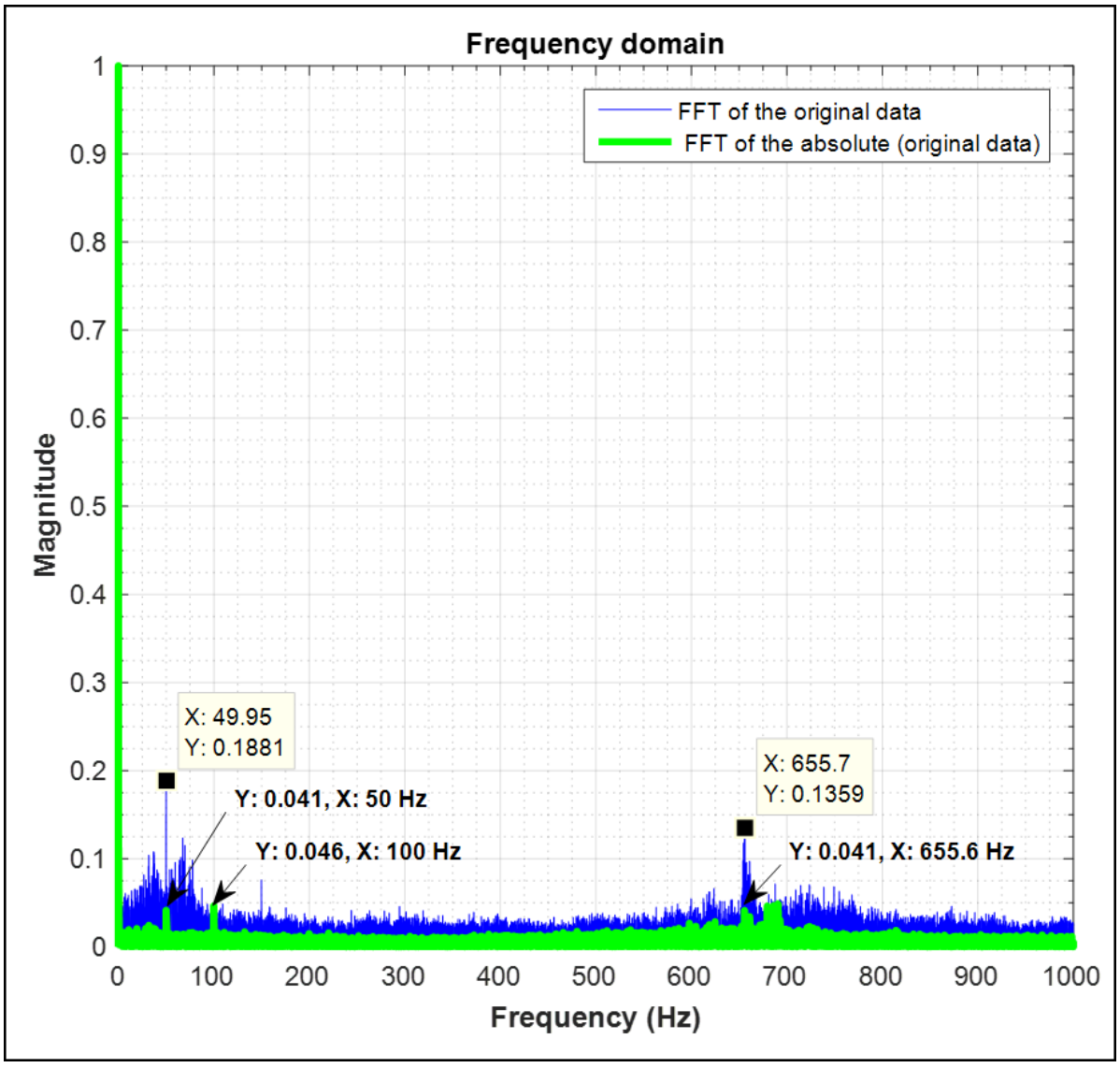

Figure 6.19: Frequency spectra of the terminal voltage measured across the continuous electrodes using 100-ohm resistor.

The spectrogram of the terminal voltage measured across the continuous electrodes in experiment 2 using 100-ohm resistor is shown in Figure 6.20. In this figure, the frequency of the signal is represented along the vertical axis while the time signal is represented along the horizontal axis.

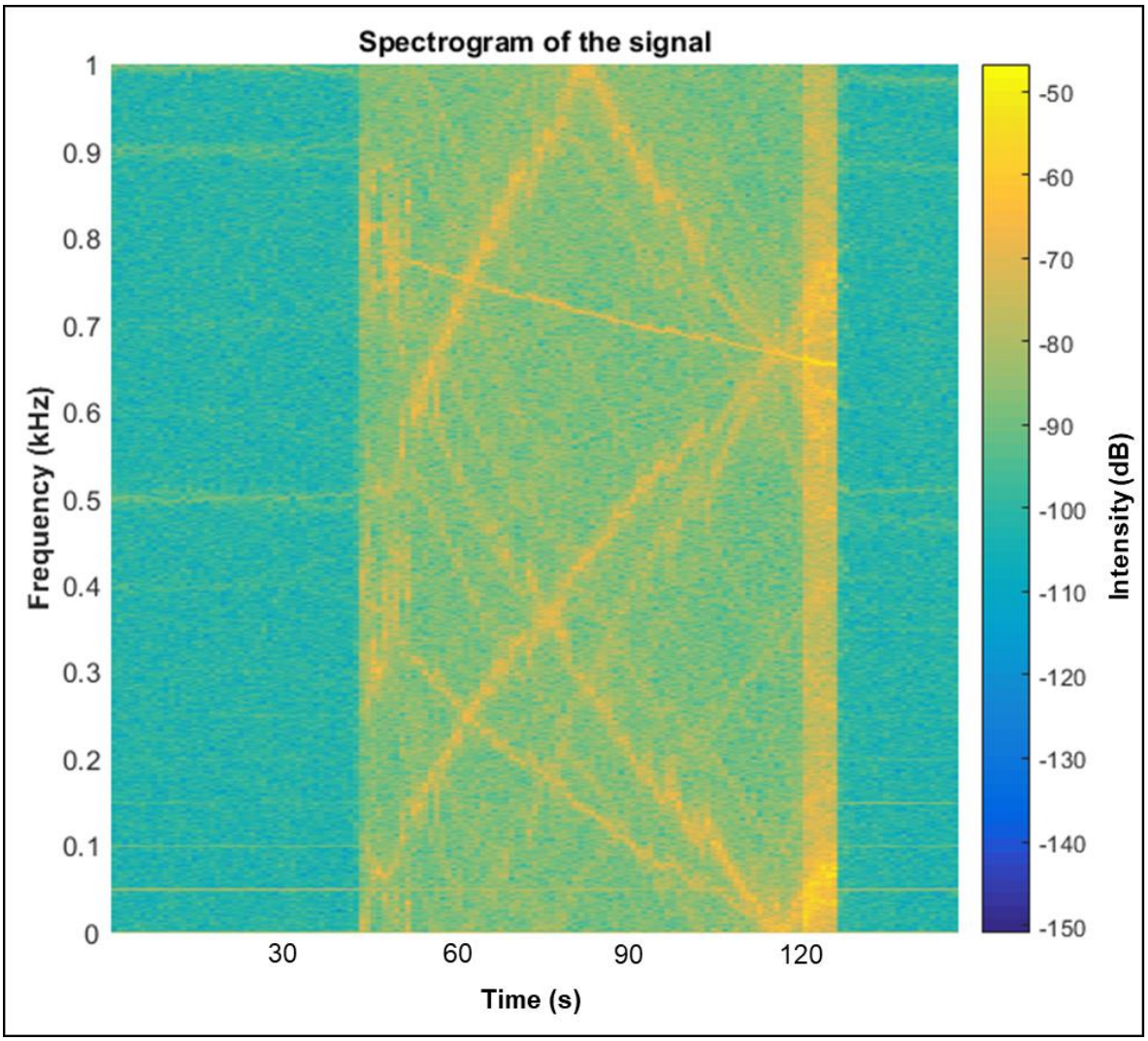

Figure 6.20: Spectrogram of the terminal voltage measured across the continuous electrodes using 100-ohm resistor.

From Figure 6.20, the coloured spectrum represents the intensity of the frequency components of the signal. This gives a visual representation of how the spectral densities of the measured voltage changes with respect to time. Furthermore, at the time interval ranging from 41 s to 125 s, the increase in the intensity levels indicate the presence of arc plasma. As previously explained, a normalised Hanning window is used to display the frequencies that are involved in the signal. For the window settings, the number of FFT (NFFT) points is 50000, the window length is 3000 and the overlap is 1000. The window length is useful for the resolution of the frequency and time signals.

The terminal voltage measured across the continuous electrodes in experiment 2 using 470-ohm resistor is also very low and consistent before the arc occurred, as shown in Figure 6.21. When the arc plasma is applied, the amplitude of the voltage signal increases (from 25 s to 57 s) and gradually decreases to lower levels when the arc plasma is not applied.

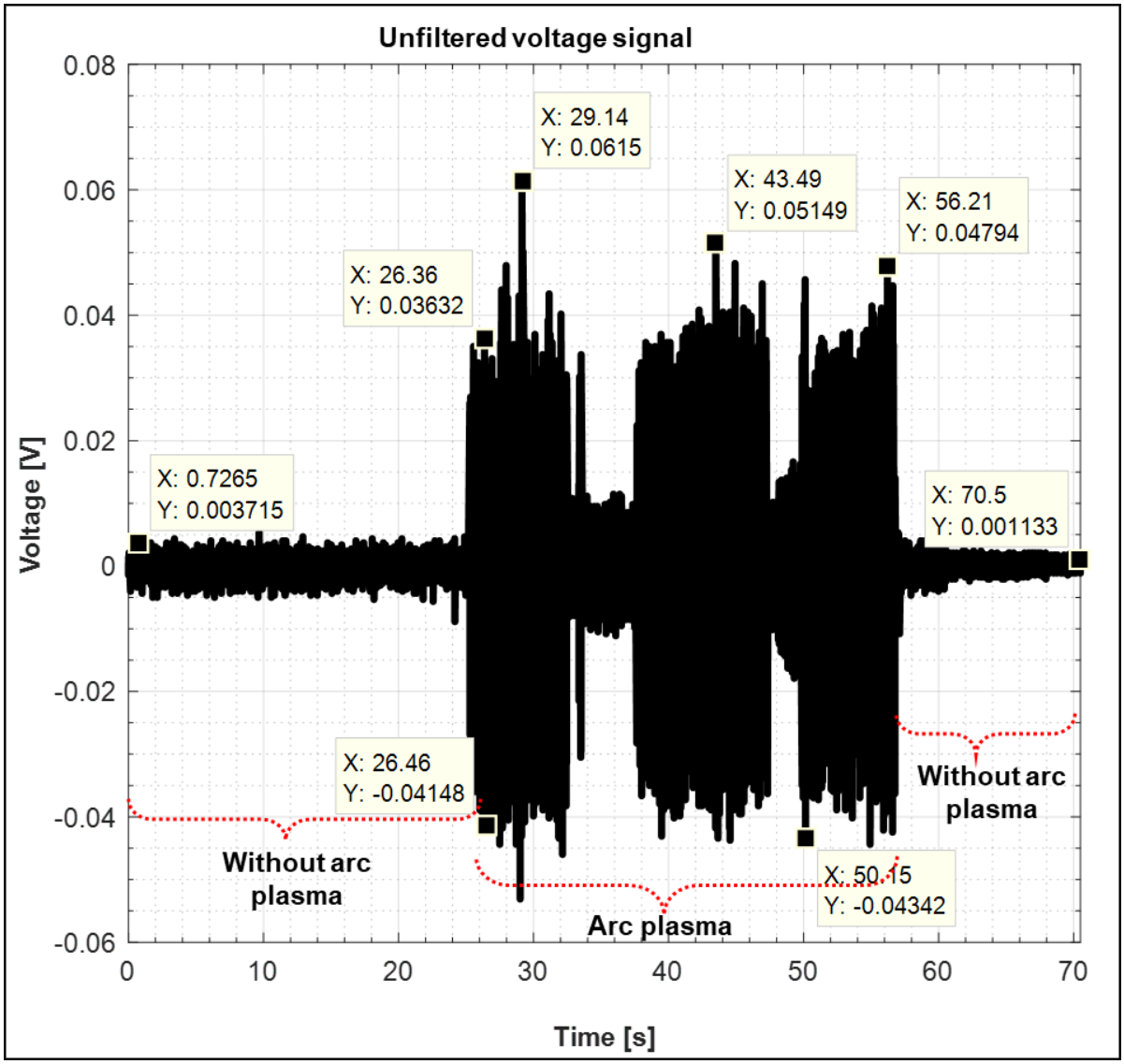

Figure 6.21: Terminal voltage measured across the continuous electrodes using 470-ohm resistor.

Figure 6.22 depicts the Butterworth filtered voltage measured across the continuous electrodes in experiment 2 using 470-ohm resistor. In this figure, the unwanted low frequency and high frequency noise of the measured voltage signal are also minimised. Moreover, a clear signal difference is observed between the arc plasma state (from 50 s to 115 s) and non-arc plasma state.

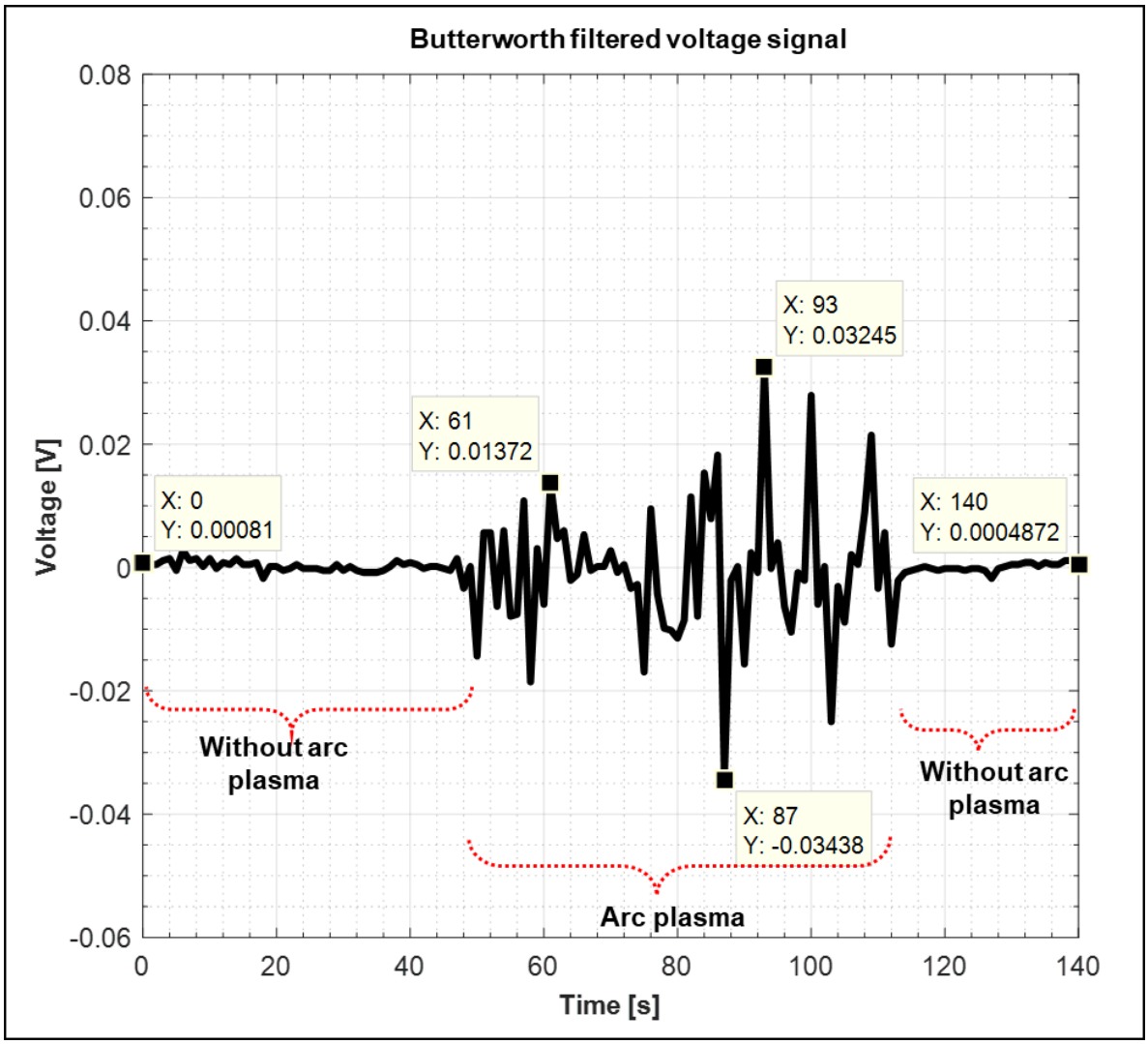

Figure 6.22: **Butterworth filtered voltage measured across the continuous electrodes using 470-ohm resistor.**

The frequency of the measured voltage in experiment 2 using 470-ohm resistor, with and without arc plasma, is shown in Figure 6.23. In this figure, the frequencies exhibit consistent behaviour that is comparable to the time domain voltage signal.

Furthermore, the FFT of the voltage (original) data in experiment 2 using 470-ohm resistor also contains some high frequency noise which supresses the low periodic frequencies (50 Hz and 100 Hz) present in the signal. To reduce this noise, the FFT of the absolute value of the voltage data is calculated. Subsequently, the amplitudes (0.019 and 0.038) of the low frequency signals are captured, as shown in Figure 6.23.

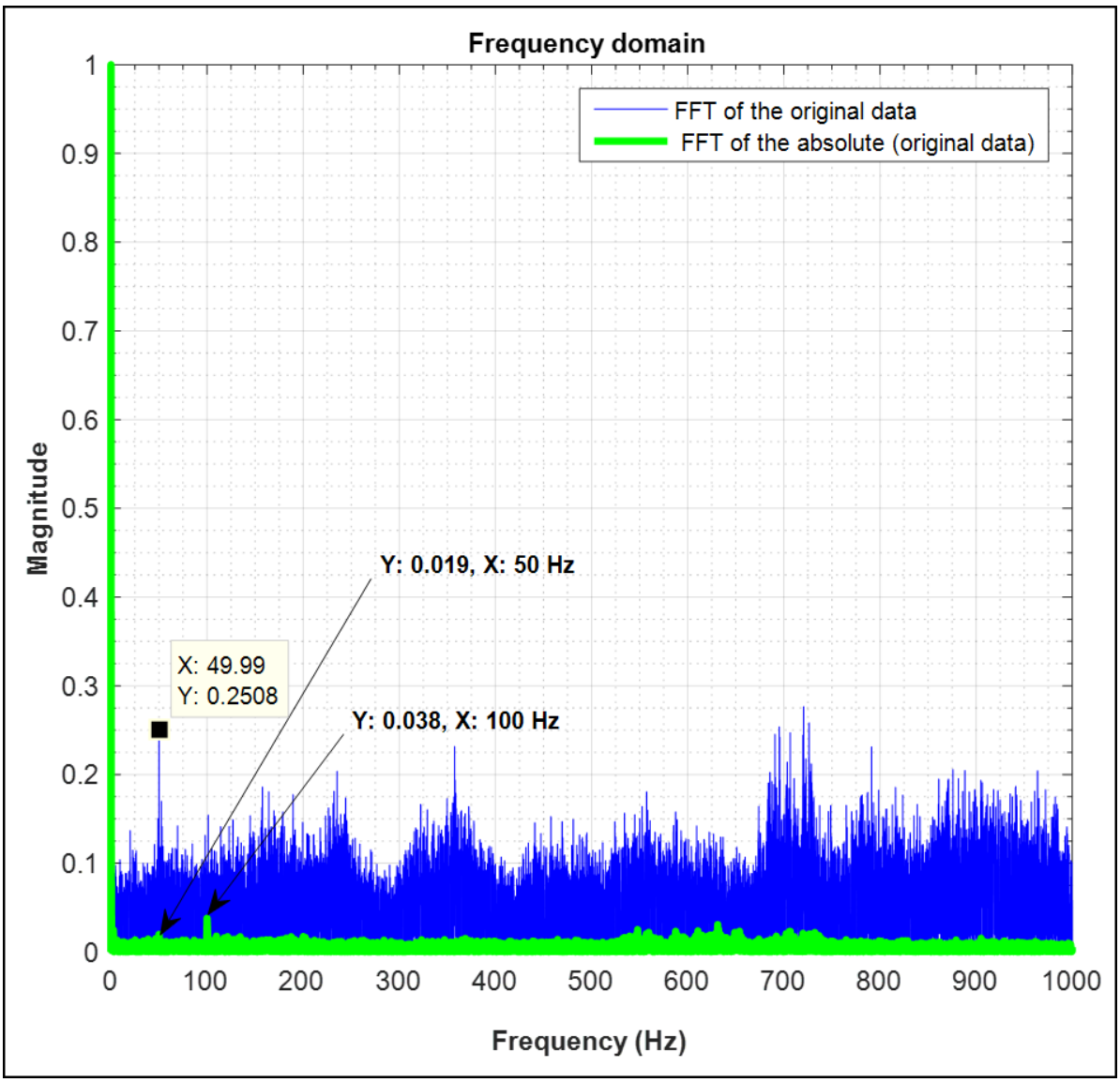

Figure 6.23: Frequency spectra of the terminal voltage measured across the continuous electrodes using 470-ohm resistor.

The spectrogram of the terminal voltage measured across the continuous electrodes in experiment 2 using 470-ohm resistor is shown in Figure 6.24. In this figure, the time signal is represented along the horizontal axis while the frequency of the signal is represented along the vertical axis.

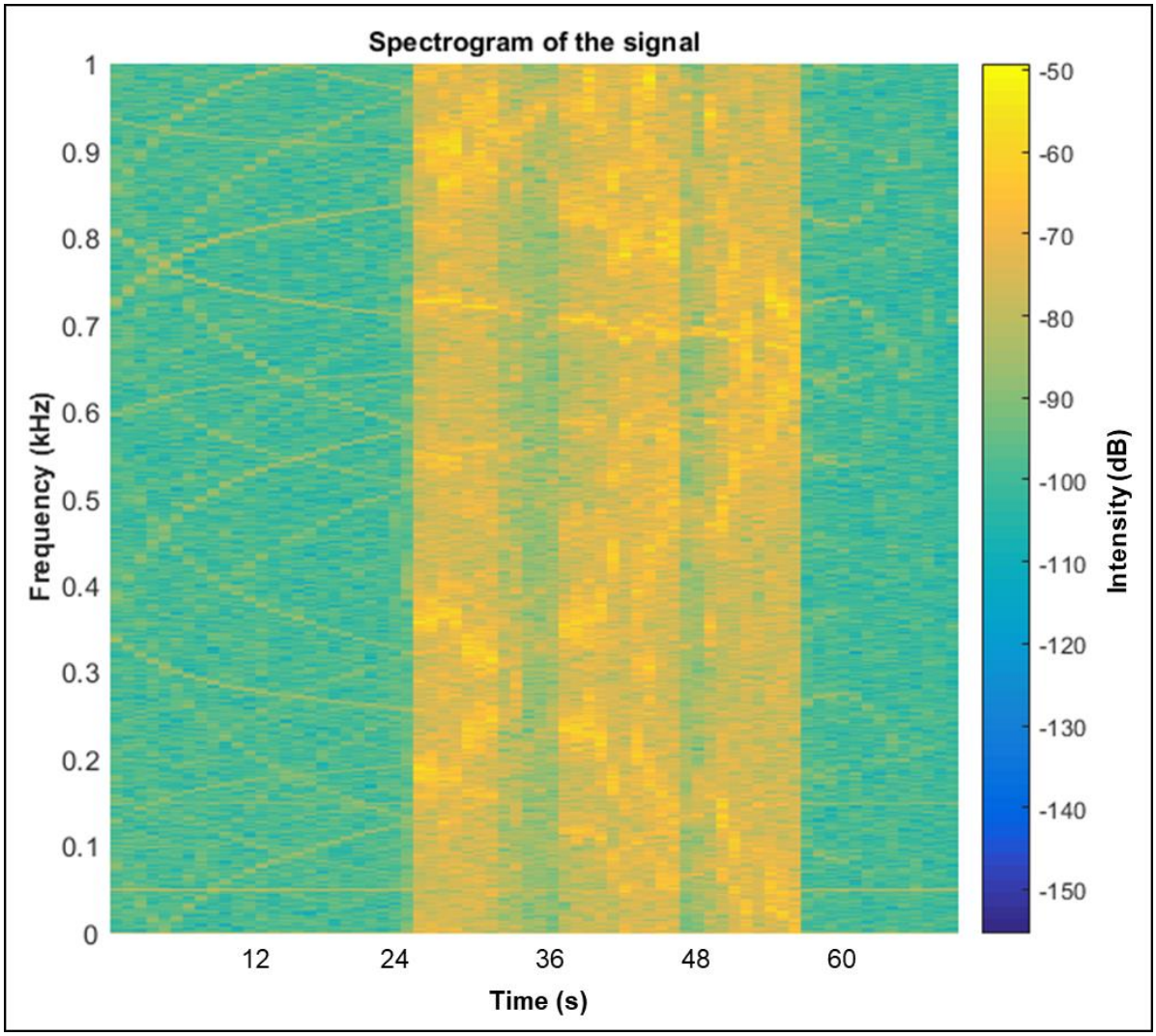

Figure 6.24: Spectrogram of the terminal voltage measured across the continuous electrodes using 470-ohm resistor.

From Figure 6.24, the intensity of each frequency is represented by a coloured spectrum, which gives a visual representation of how the spectral densities of the measured voltage changes with respect to time. Moreover, at the time interval ranging from 25 s to 57 s, the increase in the intensity levels indicate the presence of arc plasma. These frequency signals have been displayed using the normalised Hanning window. For the window settings, the number of FFT (NFFT) points is 50000, the window length is 3000 and the overlap is 1000. The window length is useful for the resolution of the time and frequency signals.

- **Experiment 3 results**

In the third experiment, arcing with plasma occurred with only the middle electrodes connected in segmented mode. The terminal voltage signals obtained using 1 Ω, 100 Ω and 470 Ω resistors change significantly under different arcing experiments and conditions (Figures 6.25 to 6.36). The terminal voltage measured across the middle-segmented electrodes in experiment 3 using 1-ohm resistor is very low and consistent before the arc occurred. When the arc plasma is applied, the amplitude of the measured voltage signal increases and gradually decreases to lower levels when the arc plasma is not applied. The increase in the voltage signal at the time interval ranging from 30 s to 78 s indicates the presence of arc plasma, as shown in Figure 6.25.

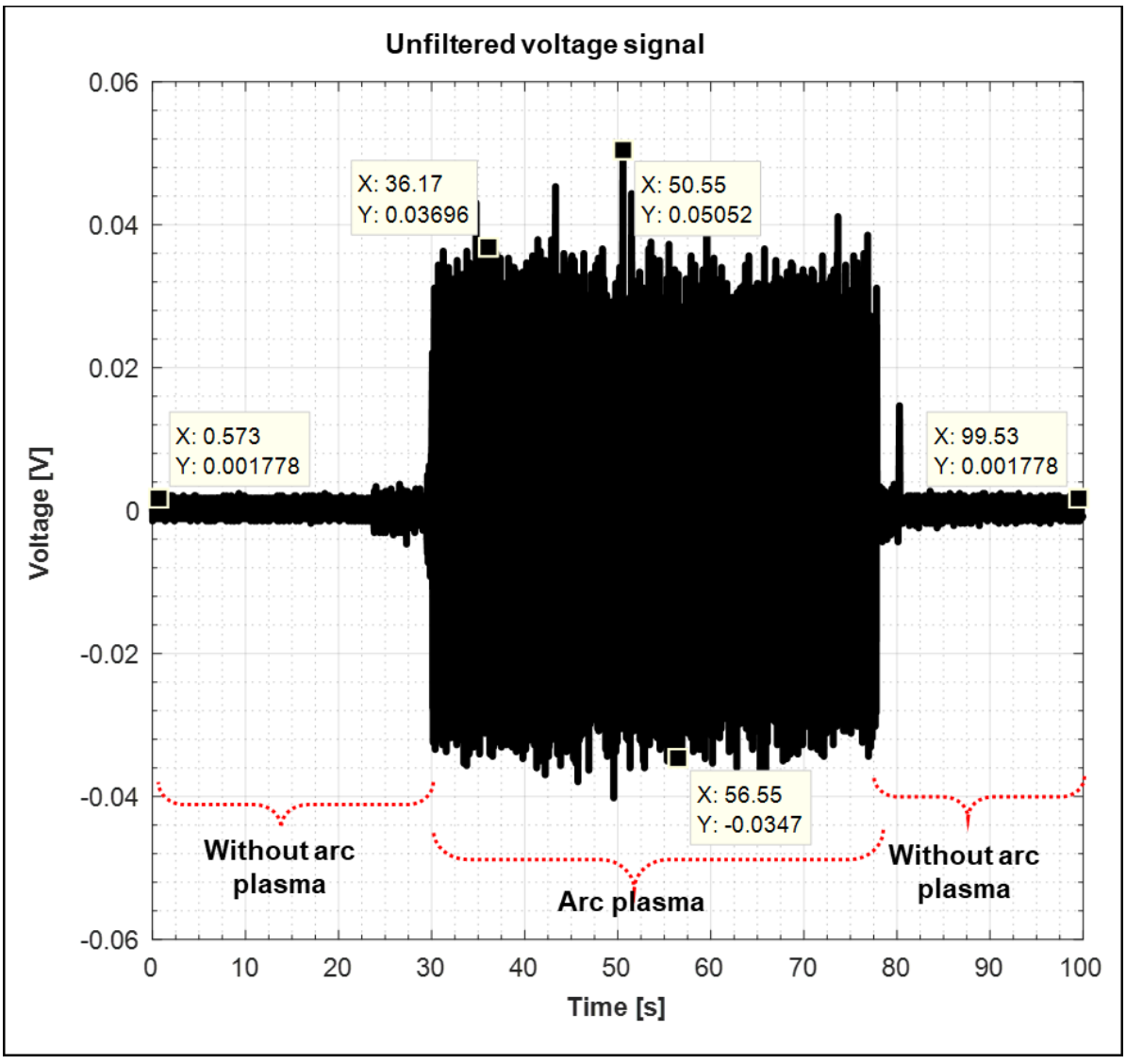

Figure 6.25: Terminal voltage measured across the middle-segmented electrodes using 1-ohm resistor.

Figure 6.26 depicts the Butterworth filtered voltage measured across the middle-segmented electrodes in experiment 3 using 1-ohm resistor. In this figure, the unwanted low frequency and high frequency noise of the measured voltage signal are minimised. Additionally, at the time interval ranging from 60 s to 154 s, a clear signal difference is observed when the arc plasma is applied.

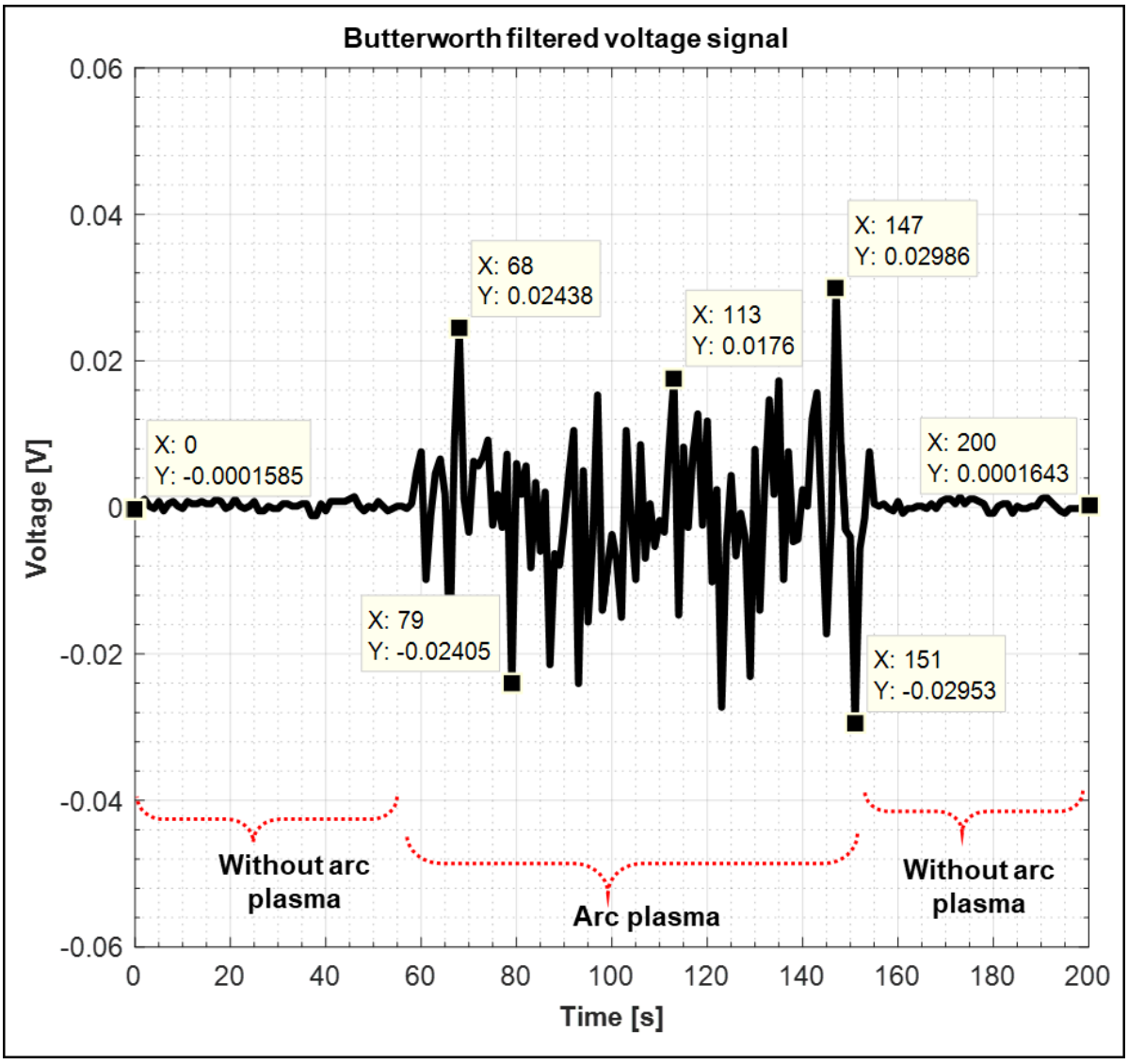

Figure 6.26: Butterworth filtered voltage measured across the middle-segmented electrodes using 1-ohm resistor.

The frequency of the measured voltage in experiment 3 using 1-ohm resistor, with and without arc plasma, is shown in Figure 6.27. In this figure, the frequencies exhibit consistent behaviour that is comparable to the time domain voltage signal.

Furthermore, the FFT of the voltage (original) data in experiment 3 using 1-ohm resistor has some high frequency noise which supresses the low periodic frequencies (50 Hz and 100 Hz) present in the signal. To decrease this noise, the FFT of the absolute value of the voltage data is calculated. Thereafter, the amplitudes (0.015 and 0.038) of the low frequency signals are captured, as shown in Figure 6.27.

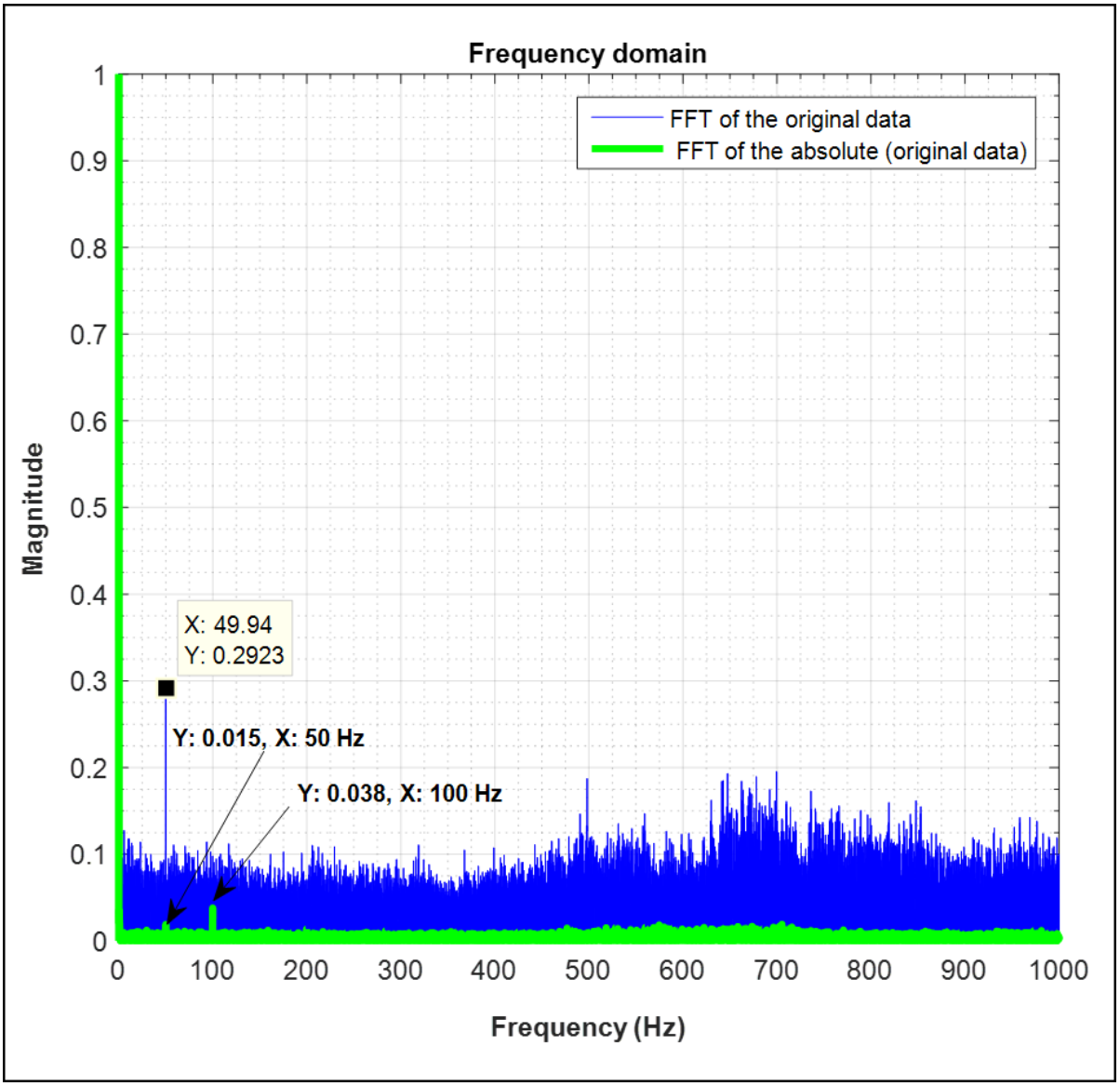

Figure 6.27: Frequency spectra of the terminal voltage measured across the middle-segmented electrodes using 1-ohm resistor.

The spectrogram of the terminal voltage measured across the middle-segmented electrodes in experiment 3 using 1-ohm resistor is shown in Figure 6.28. In this figure, the frequency of the signal is represented along the vertical axis while the time signal is represented along the horizontal axis.

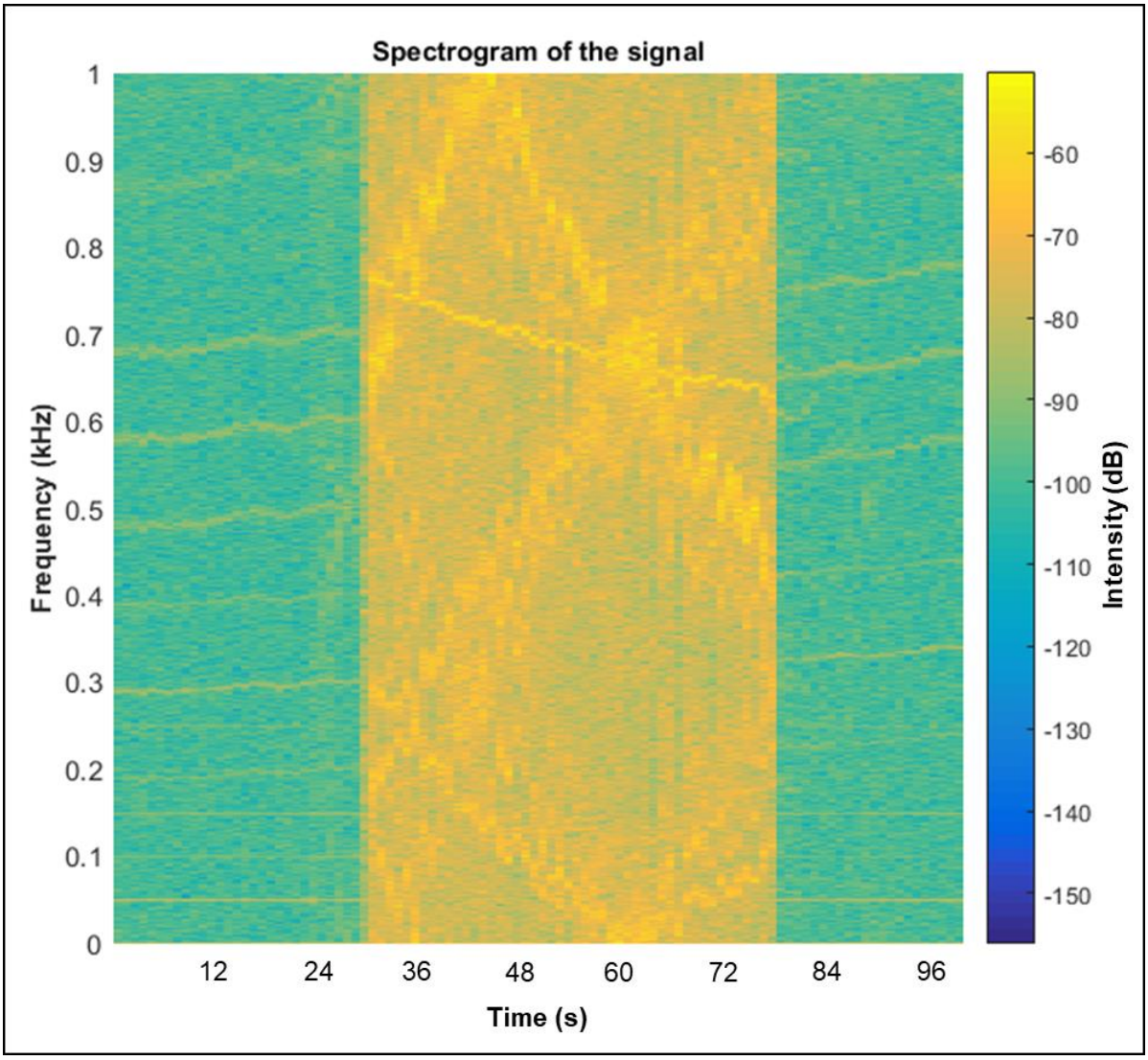

Figure 6.28: Spectrogram of the terminal voltage measured across the middle-segmented electrodes using 1-ohm resistor.

From Figure 6.28, the coloured spectrum represents the intensity of the frequency components of the signal. This gives a visual representation of how the spectral densities of the measured voltage changes with respect to time. Furthermore, at the time interval ranging from 30 s to 78 s, the increase in the intensity levels indicate the presence of arc plasma. These frequency signals have also been displayed using the normalised Hanning window. For the window settings, the number of FFT (NFFT) points is 50000, the window length is 3000 and the overlap is 1000. The window length is useful for the resolution of the frequency and time signals.

The terminal voltage measured across the middle-segmented electrodes in experiment 3 using 100-ohm resistor is also very low and consistent before the arc occurred. When the arc plasma is applied, the amplitude of the voltage signal increases (from 48 s to 77 s and 96 s to 117 s) and gradually decreases to lower levels when the arc plasma is not applied, as shown in Figure 6.29.

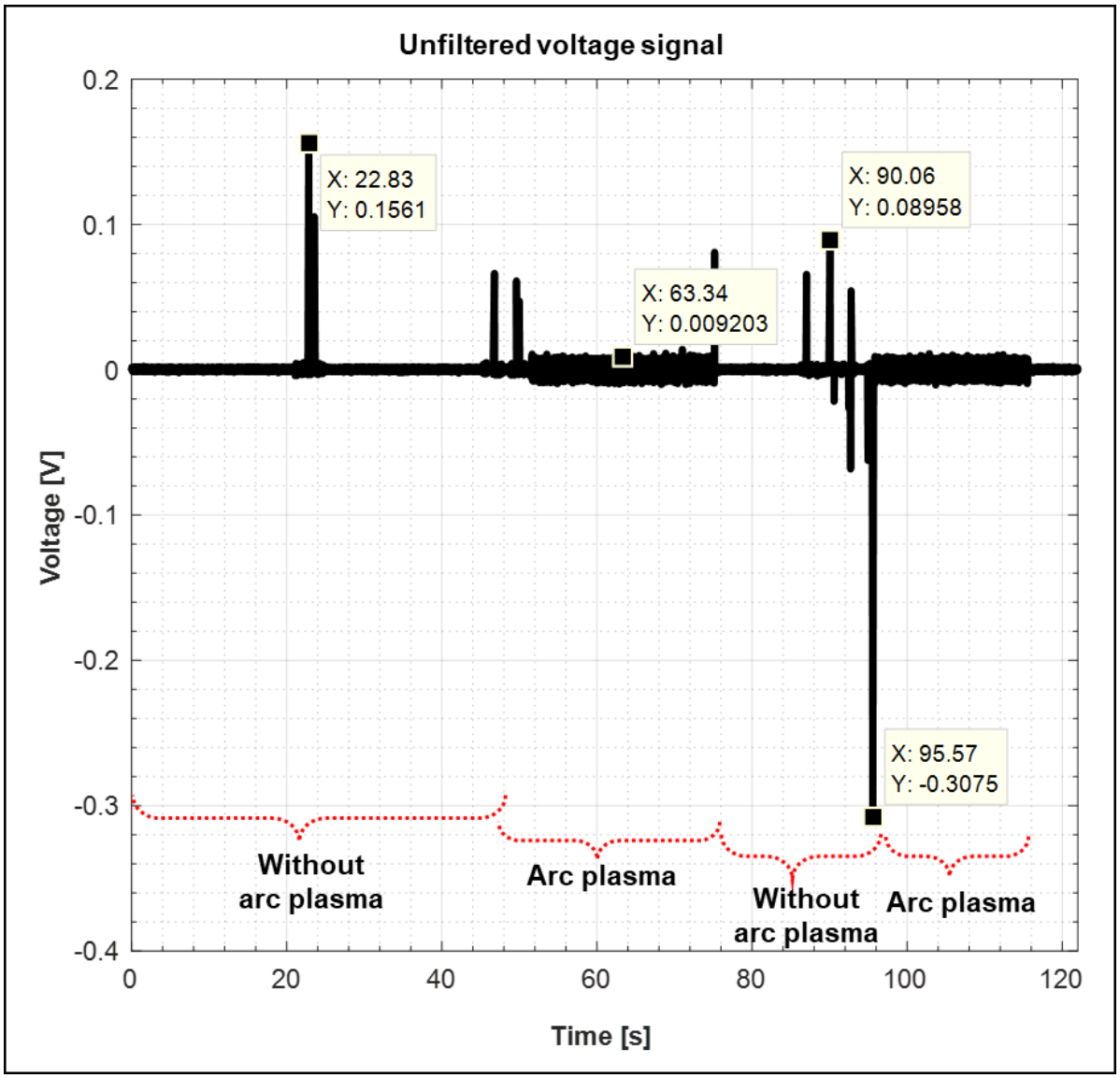

Figure 6.29: Terminal voltage measured across the middle-segmented electrodes using 100-ohm resistor.

Figure 6.30 depicts the Butterworth filtered voltage measured across the middle-segmented electrodes in experiment 3 using 100-ohm resistor. In this figure, the unwanted low frequency and high frequency noise of the measured voltage signal are also minimised. Moreover, a clear signal difference is observed between the arc plasma state (from 105 s to 150 s and 195 s to 240 s) and non-arc plasma state.

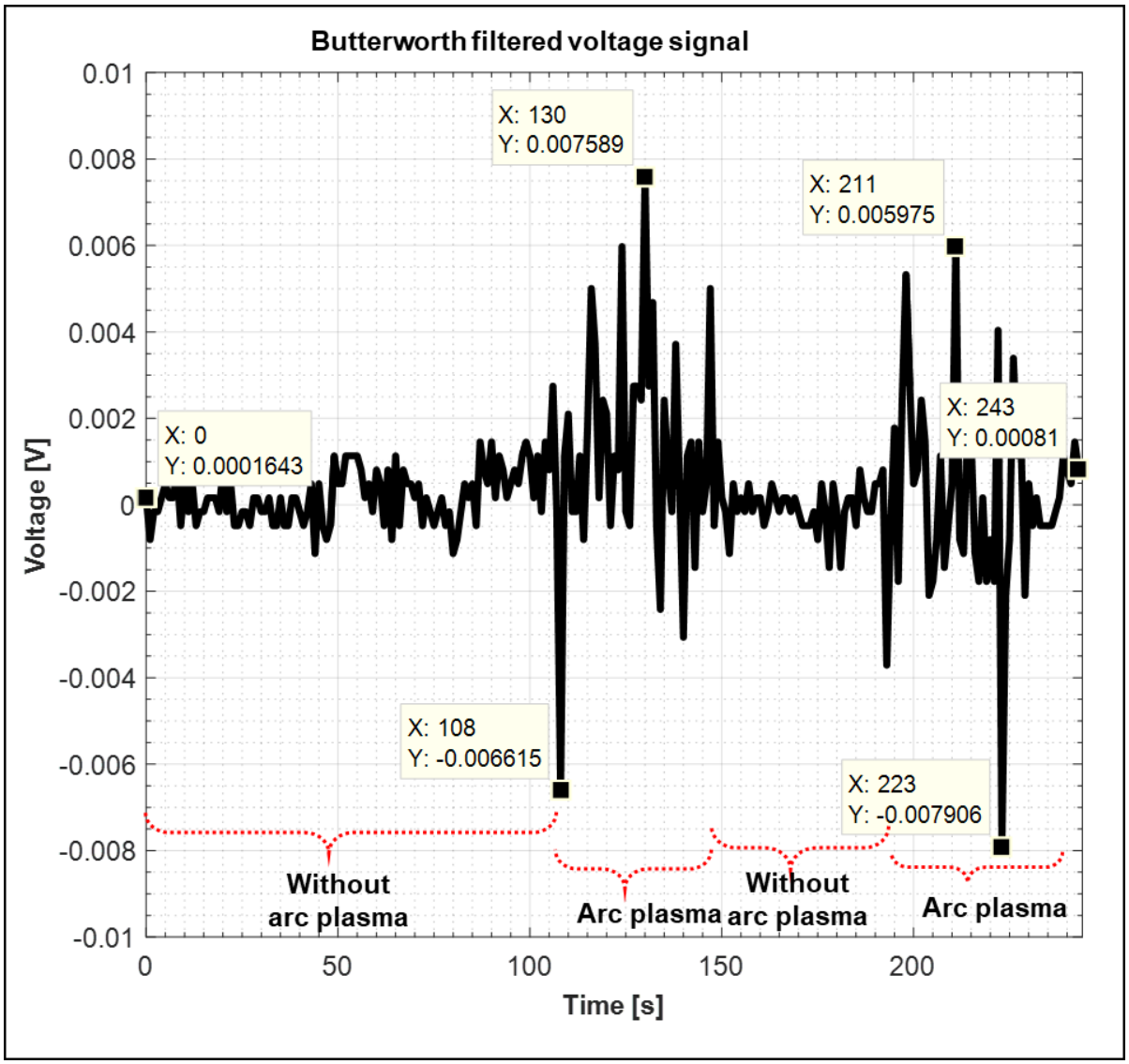

Figure 6.30: Butterworth filtered voltage measured across the middle-segmented electrodes using 100-ohm resistor.

The frequency of the measured voltage in experiment 3 using 100-ohm resistor, with and without arc plasma, is shown in Figure 6.31. In this figure, the frequencies exhibit consistent behaviour that is comparable to the time domain voltage signal.

The FFT of the voltage (original) data in experiment 3 using 100-ohm resistor also contains some high frequency noise which supresses the low periodic frequencies (50 Hz, 100 Hz and 149.8 Hz) present in the signal. To reduce this noise, the FFT of the absolute value of the voltage data is calculated. Afterward, the amplitudes (0.023, 0.042 and 0.029) of the low frequency signals are captured, as shown in Figure 6.31.

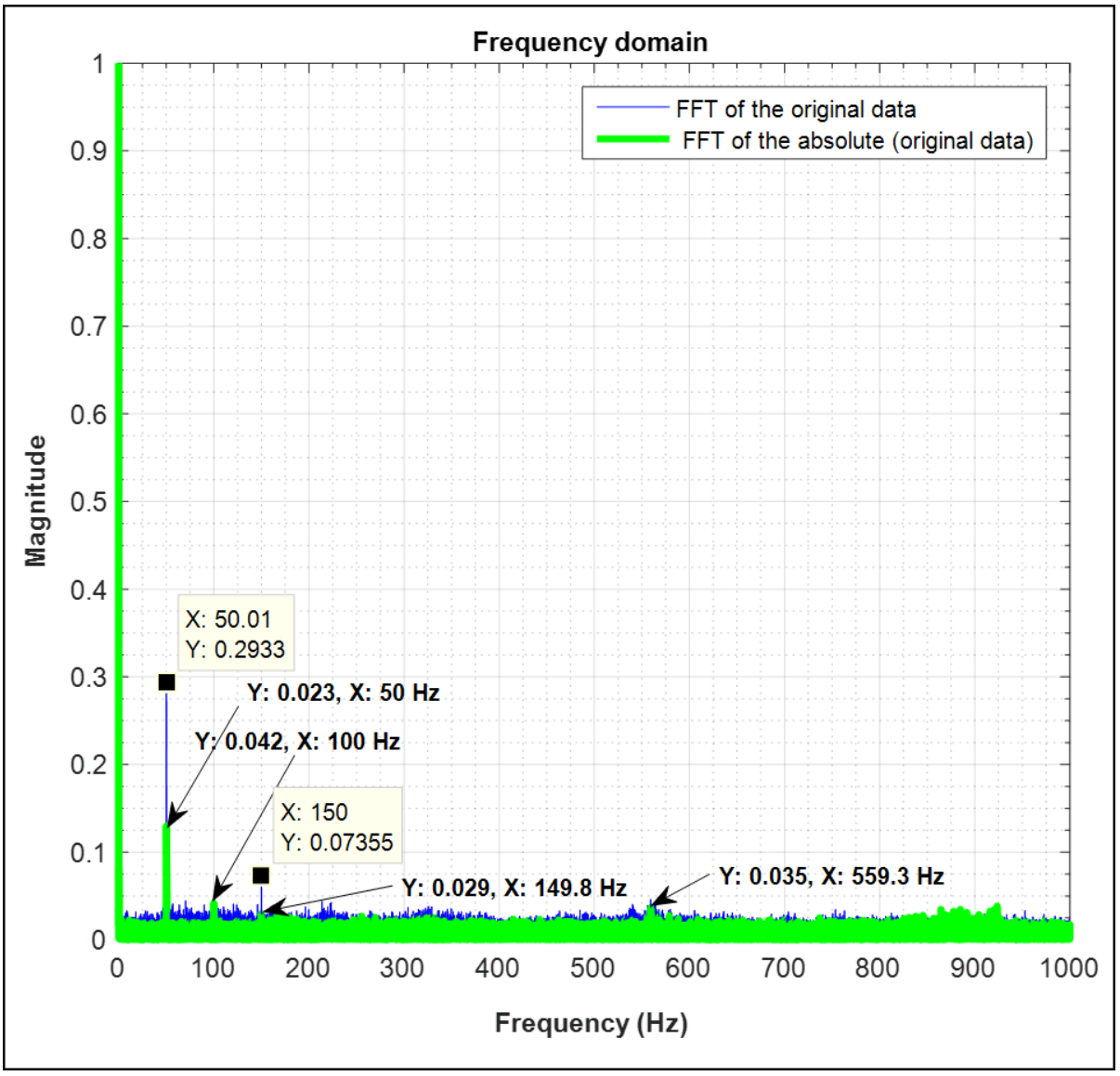

Figure 6.31: Frequency spectra of the terminal voltage measured across the middle-segmented electrodes using 100-ohm resistor.

The spectrogram of the terminal voltage measured across the middle-segmented electrodes in experiment 3 using 100-ohm resistor is shown in Figure 6.32. In this figure, the time signal is represented along the horizontal axis while the frequency of the signal is represented along the vertical axis.

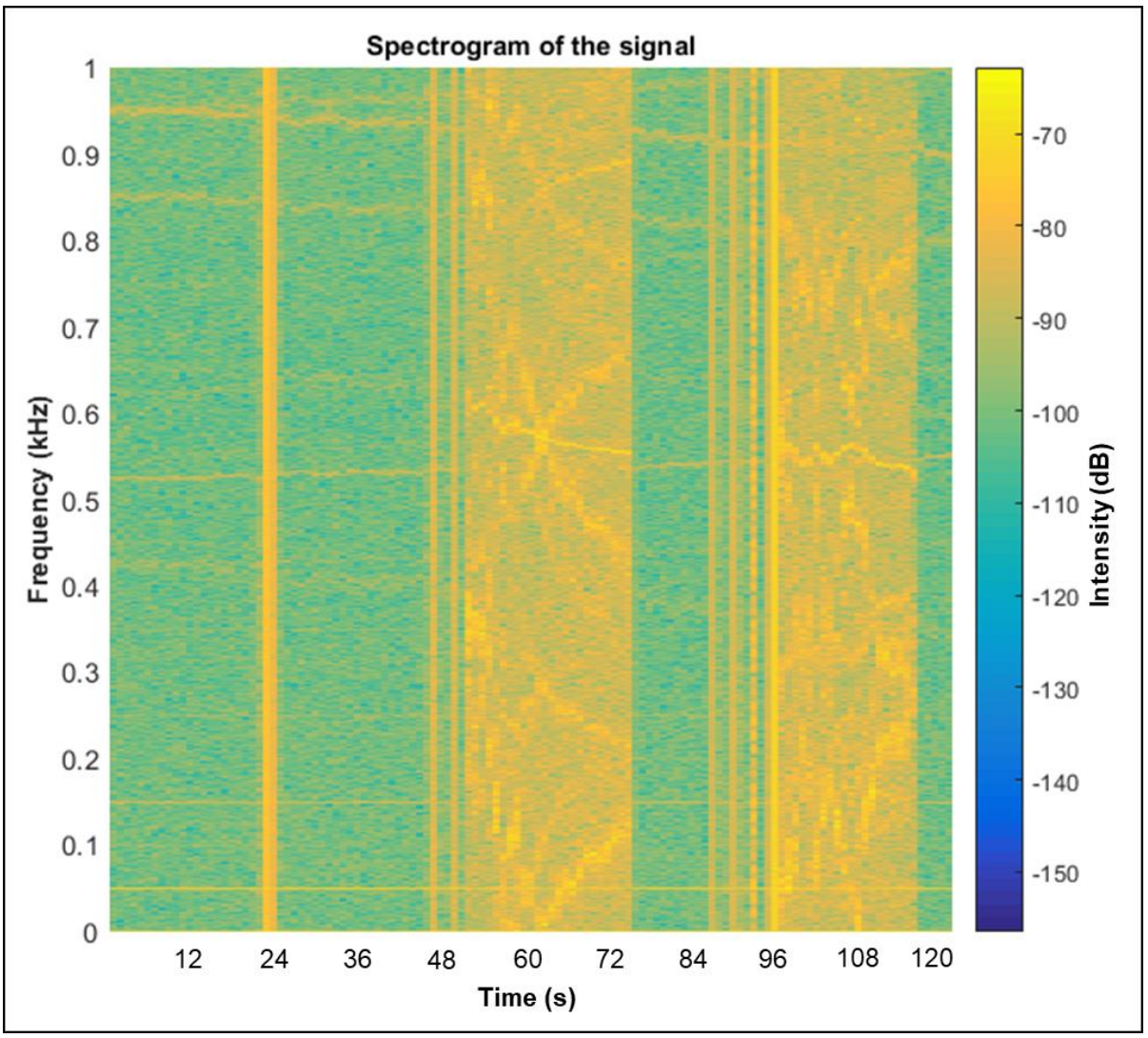

Figure 6.32: Spectrogram of the terminal voltage measured across the middle-segmented electrodes using 100-ohm resistor.

From Figure 6.32, the intensity of each frequency is represented by a coloured spectrum, which gives a visual representation of how the spectral densities of the measured voltage changes with respect to time. Moreover, at the time interval ranging from 48 s to 77 s and 96 s to 117 s, the increase in the intensity levels indicate the presence of arc plasma. As previously explained, these frequency signals have been displayed using the normalised Hanning window. For the window settings, the number of FFT (NFFT) points is 50000, the window length is 3000 and the overlap is 1000. The window length is useful for the resolution of the time and frequency signals.

The terminal voltage measured across the middle-segmented electrodes in experiment 3 using 470-ohm resistor is also very low and consistent before the arc occurred. When the arc plasma is applied, the amplitude of the voltage signal increases (from 65 s to 106 s) and gradually decreases to lower levels when the arc plasma is not applied, as shown in Figure 6.33.

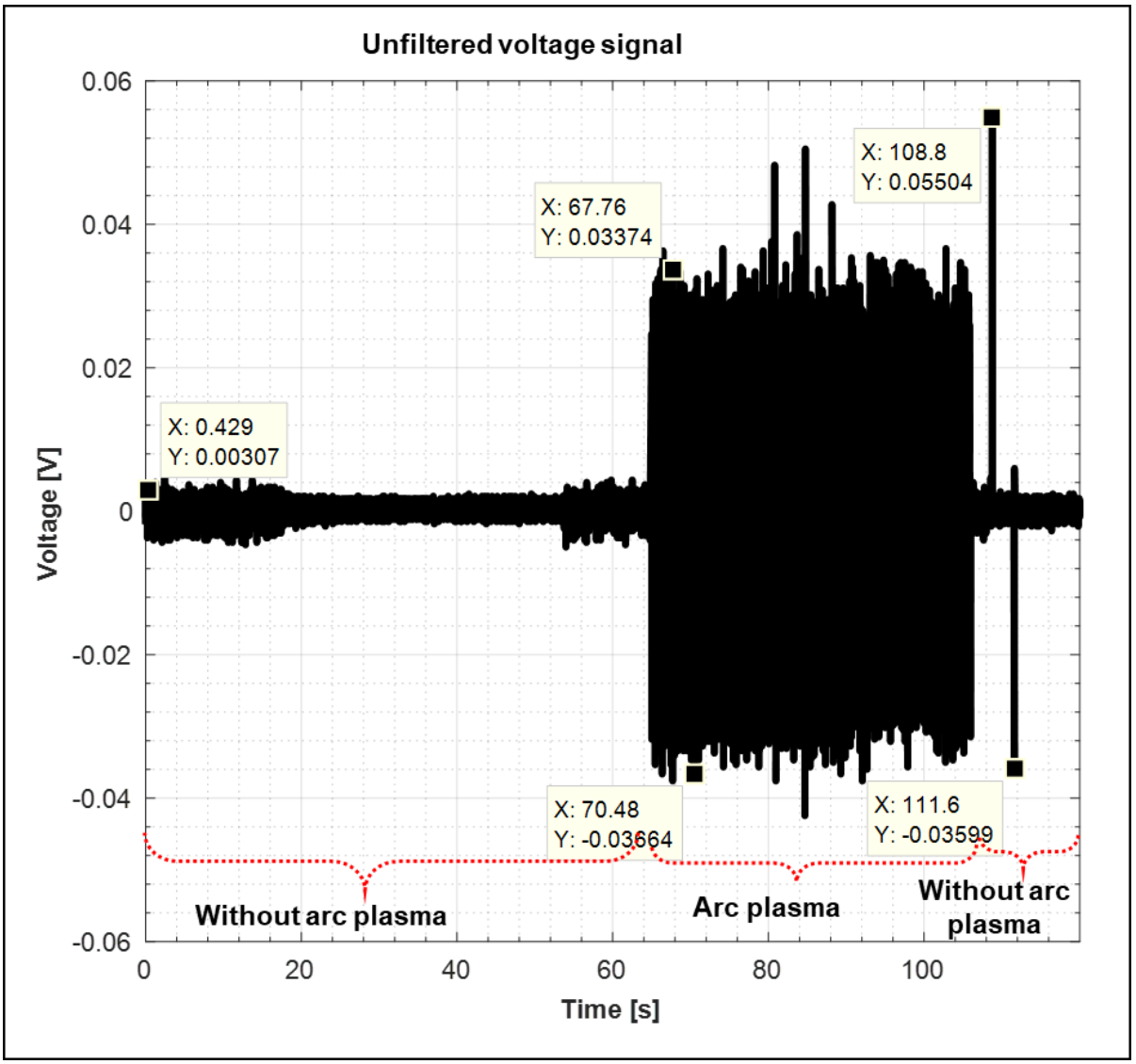

Figure 6.33: Terminal voltage measured across the middle-segmented electrodes using 470-ohm resistor.

Figure 6.34 depicts the Butterworth filtered voltage measured across the middle-segmented electrodes in experiment 3 using 470-ohm resistor. In this figure, the unwanted low frequency and high frequency noise of the measured voltage signal are also minimised. Additionally, at the time interval ranging from 139 s to 209 s, a clear signal difference is observed when the arc plasma is applied.

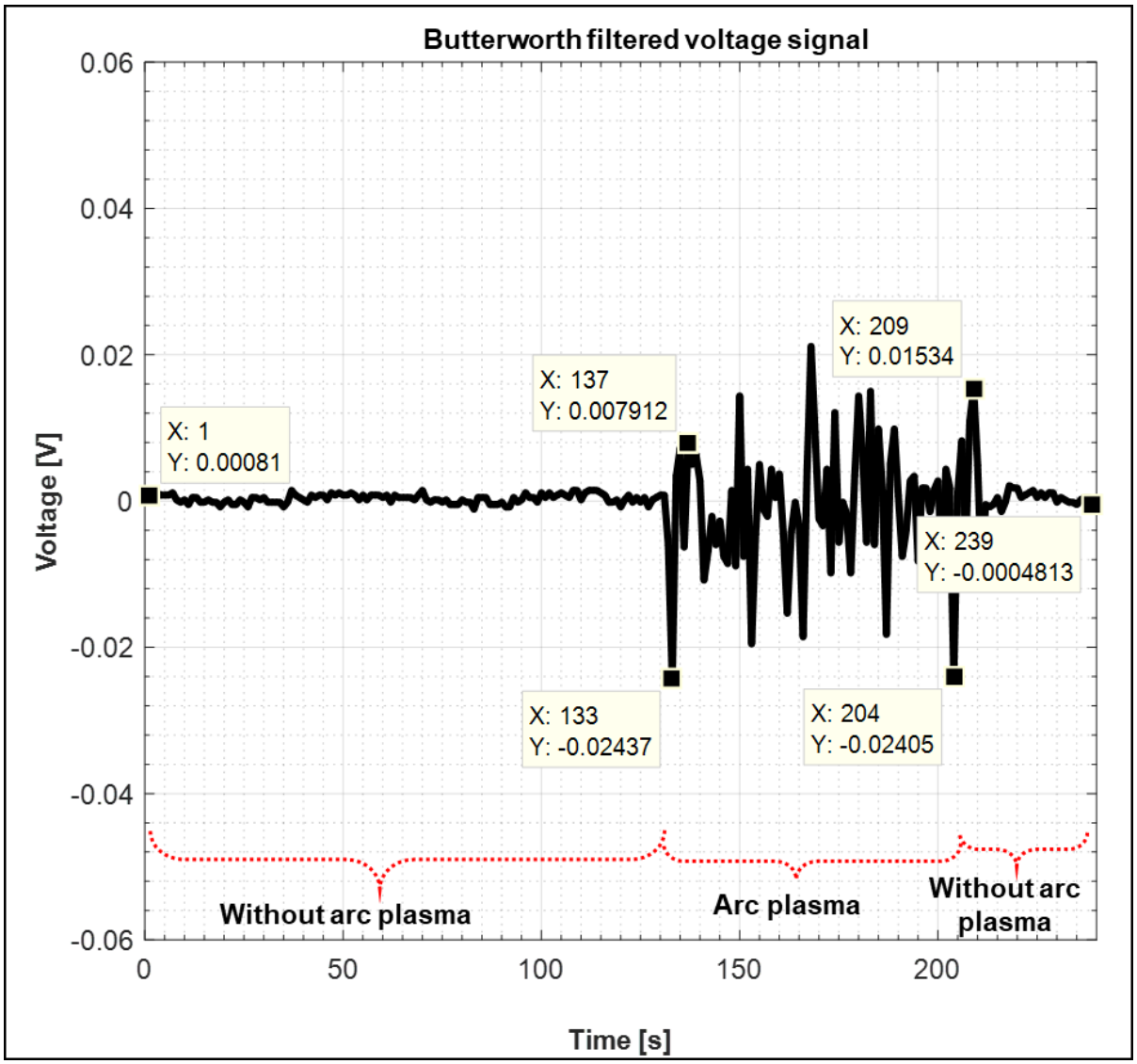

Figure 6.34: Butterworth filtered voltage measured across the middle-segmented electrodes using 470-ohm resistor.

The frequency of the measured voltage in experiment 3 using 470-ohm resistor, with and without arc plasma, is shown in Figure 6.35. In this figure, the frequencies exhibit consistent behaviour that is comparable to the time domain voltage signal.

Furthermore, the FFT of the voltage (original) data in experiment 3, using 470-ohm resistor, also contains some high frequency noise which supresses the low periodic frequencies (50 Hz, 100 Hz and 583.6 Hz) present in the signal. To decrease this noise, the FFT of the absolute value of the voltage data is calculated. Subsequently, the amplitudes (0.023, 0.029 and 0.027) of the low frequency signals are captured, as shown in Figure 6.35.

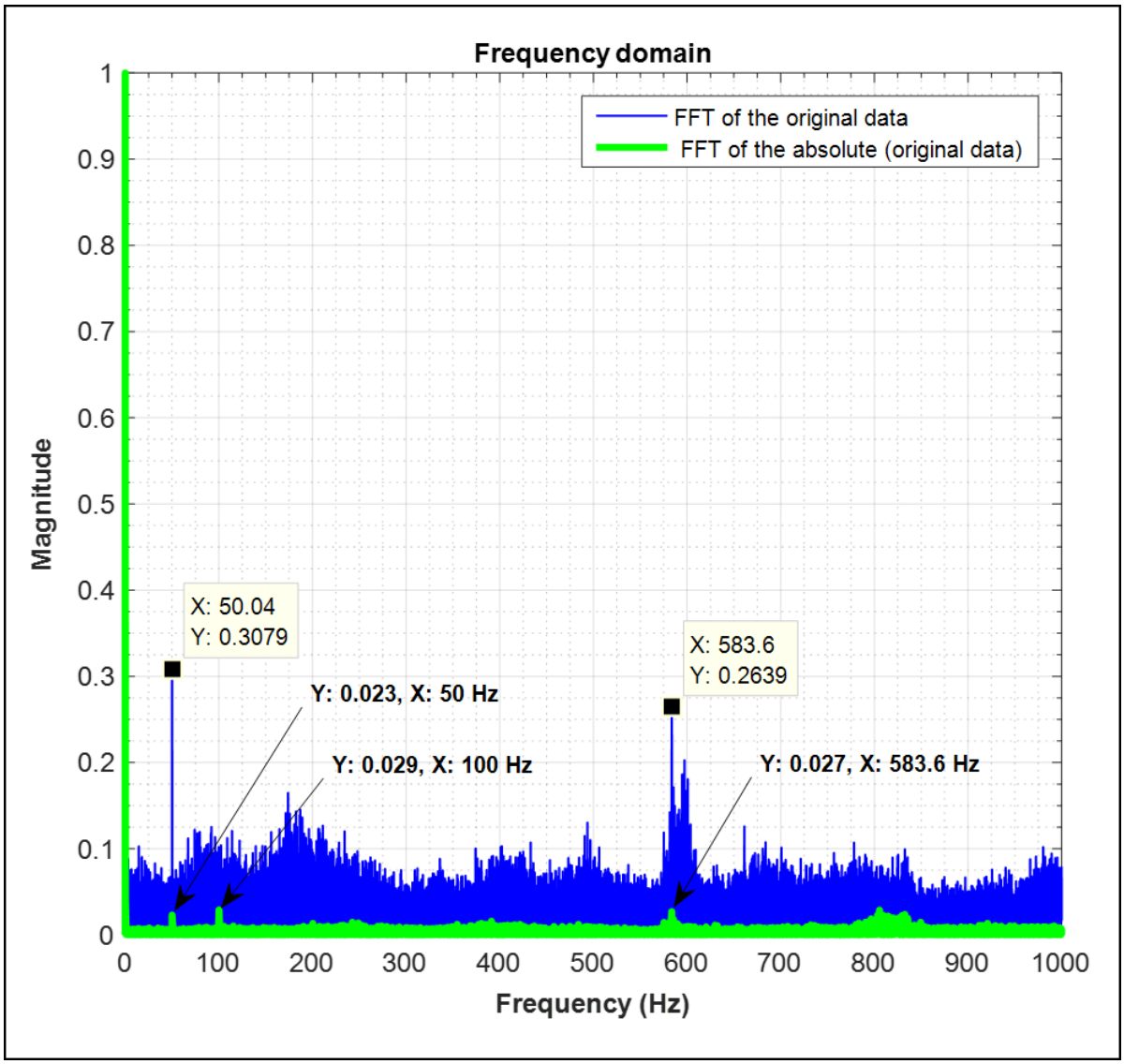

Figure 6.35: Frequency spectra of the terminal voltage measured across the middle-segmented electrodes using 470-ohm resistor.

The spectrogram of the terminal voltage measured across the middle-segmented electrodes in experiment 3 using 470-ohm resistor is shown in Figure 6.36. In this figure, the frequency of the signal is represented along the vertical axis while the time signal is represented along the horizontal axis.

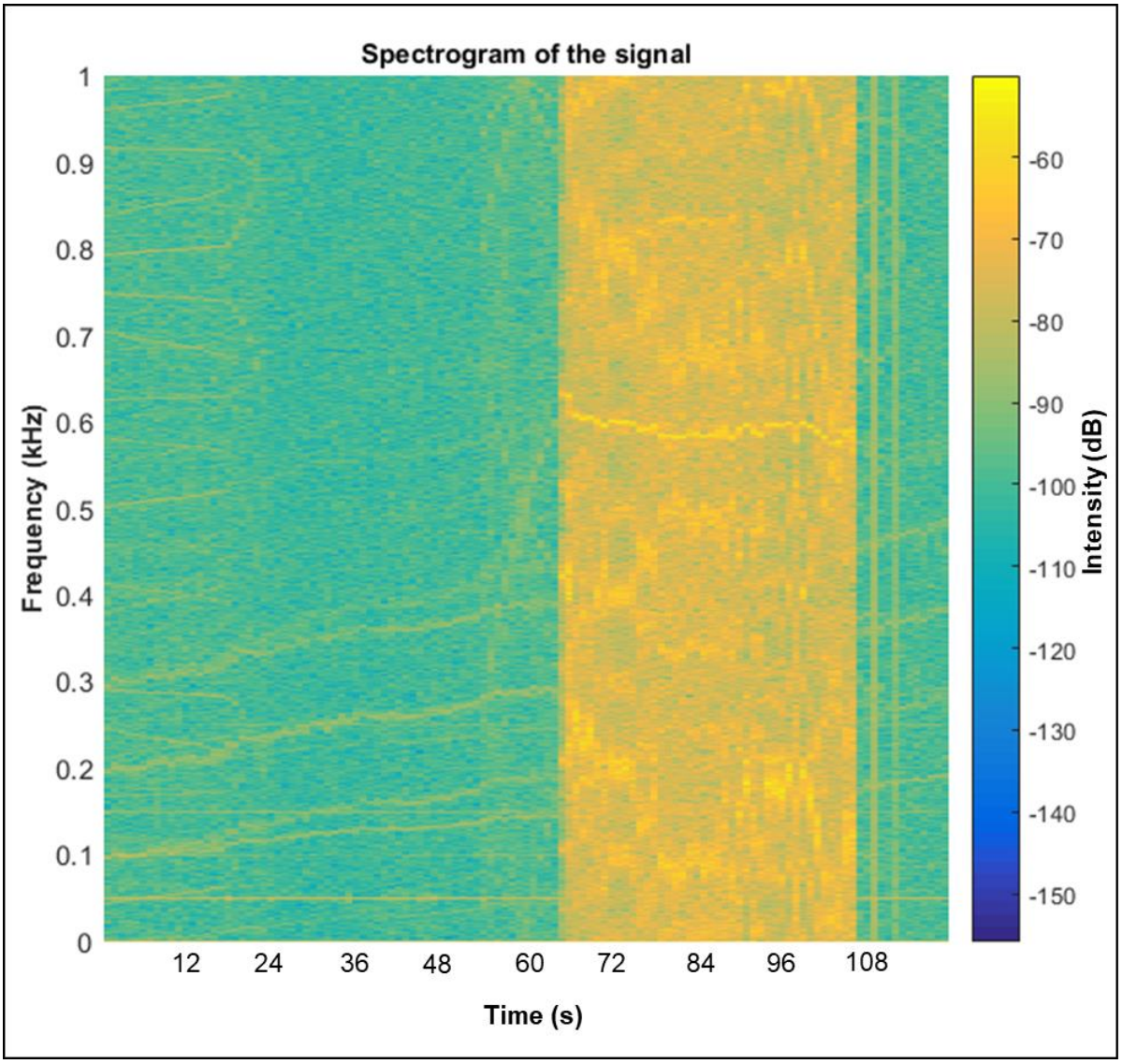

Figure 6.36: Spectrogram of the terminal voltage measured across the middle-segmented electrodes using 470-ohm resistor.

From Figure 6.36, the coloured spectrum represents the intensity of the frequency components of the signal. This gives a visual representation of how the spectral densities of the measured voltage changes with respect to time. Furthermore, at the time interval ranging from 65 s to 106 s, the increase in the intensity levels indicate the presence of arc plasma. These frequency signals have also been displayed using the normalised Hanning window. For the window settings, the number of FFT (NFFT) points is 50000, the window length is 3000 and the overlap is 1000. The window length is useful for the resolution of the frequency and time signals.

From the Butterworth filtered voltage signals (Figures 6.14, 6.18, 6.22, 6.26, 6.30 and 6.34), the average voltage value of each experiment can be determined by taking the absolute of the measured voltage signals for time intervals when plasma arcing occurred, as shown in Figures 6.37, 6.38, 6.39, 6.40, 6.41 and 6.42. In these figures, the negative voltage of the original waveform has been converted into positive voltage with the same amplitude. The average voltage is determined using the Matlab code described in Appendix A.4.

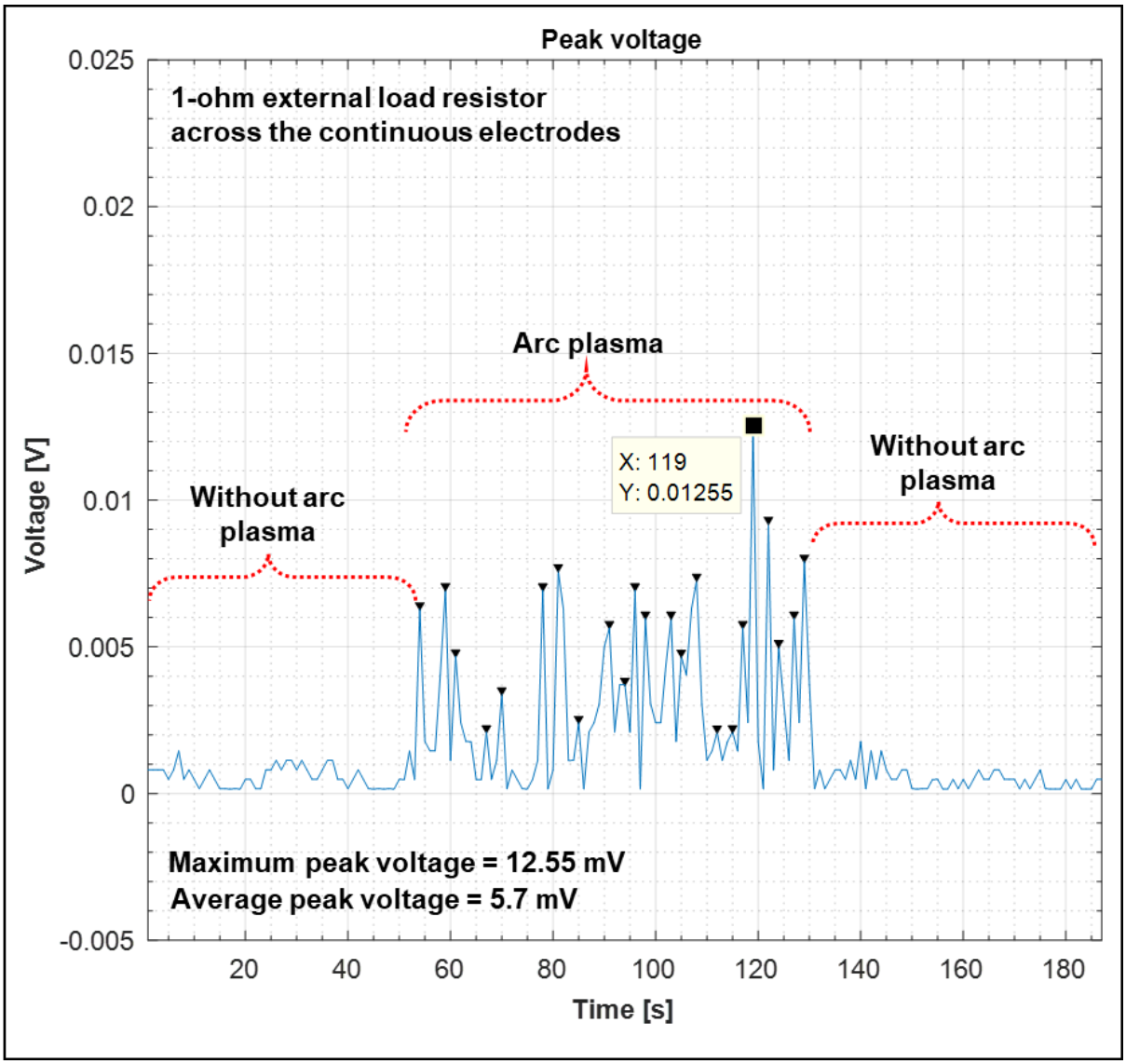

Figure 6.37: Average voltage measured across the continuous electrodes in experiment 2 using 1-ohm resistor.

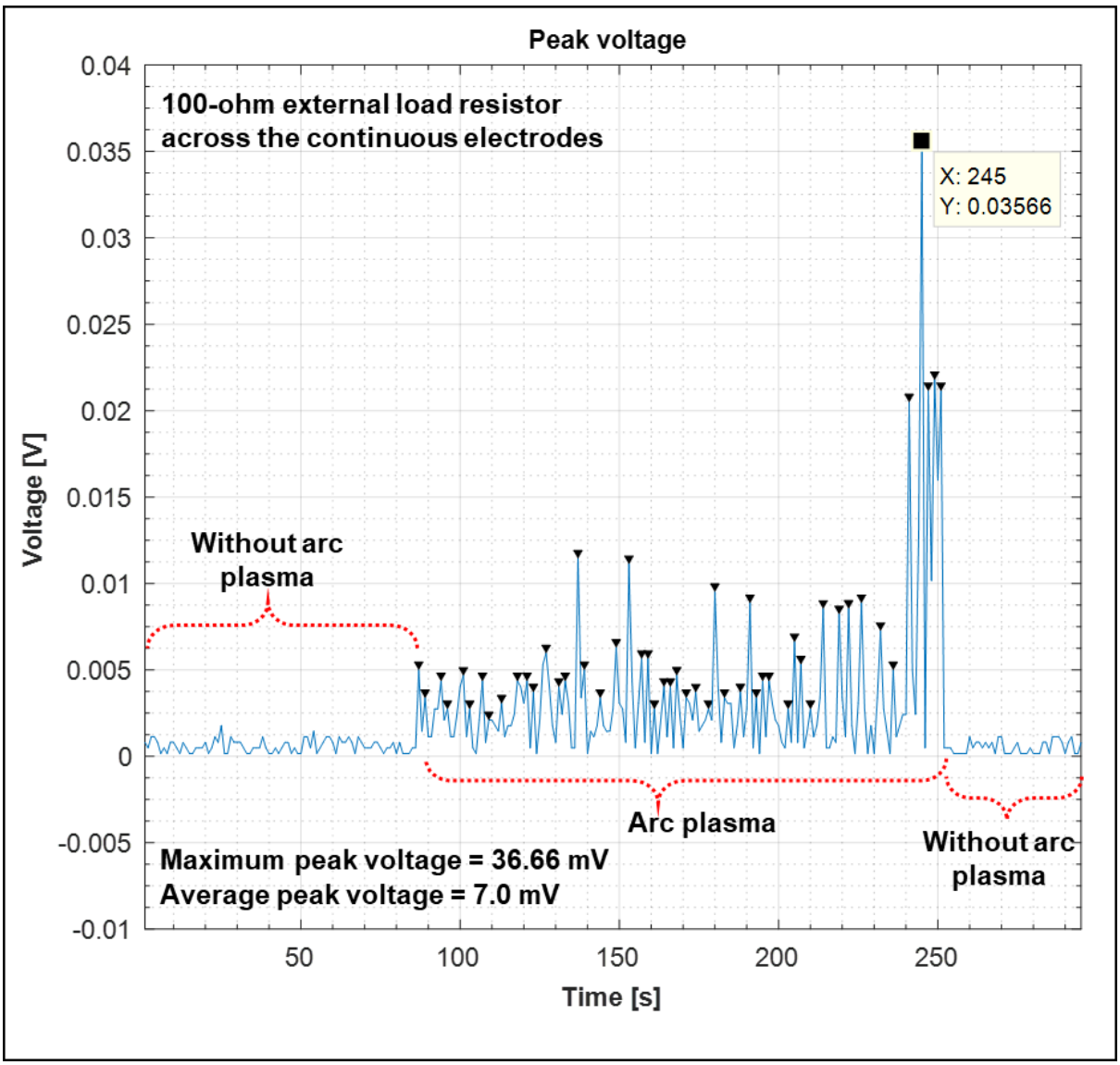

Figure 6.38: Average voltage measured across the continuous electrodes in experiment 2 using 100-ohm resistor.

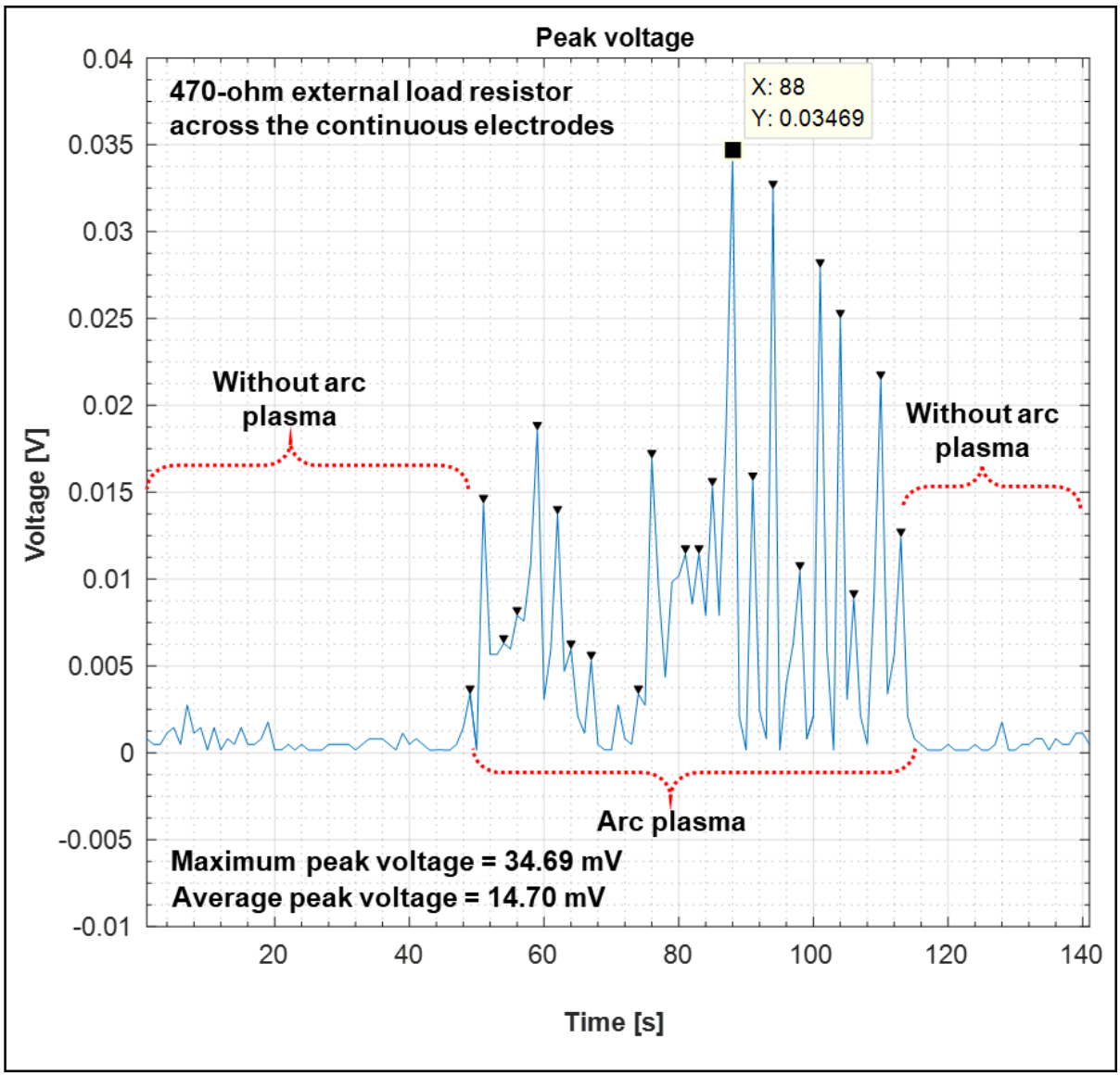

Figure 6.39: Average voltage measured across the continuous electrodes in experiment 2 using 470-ohm resistor.

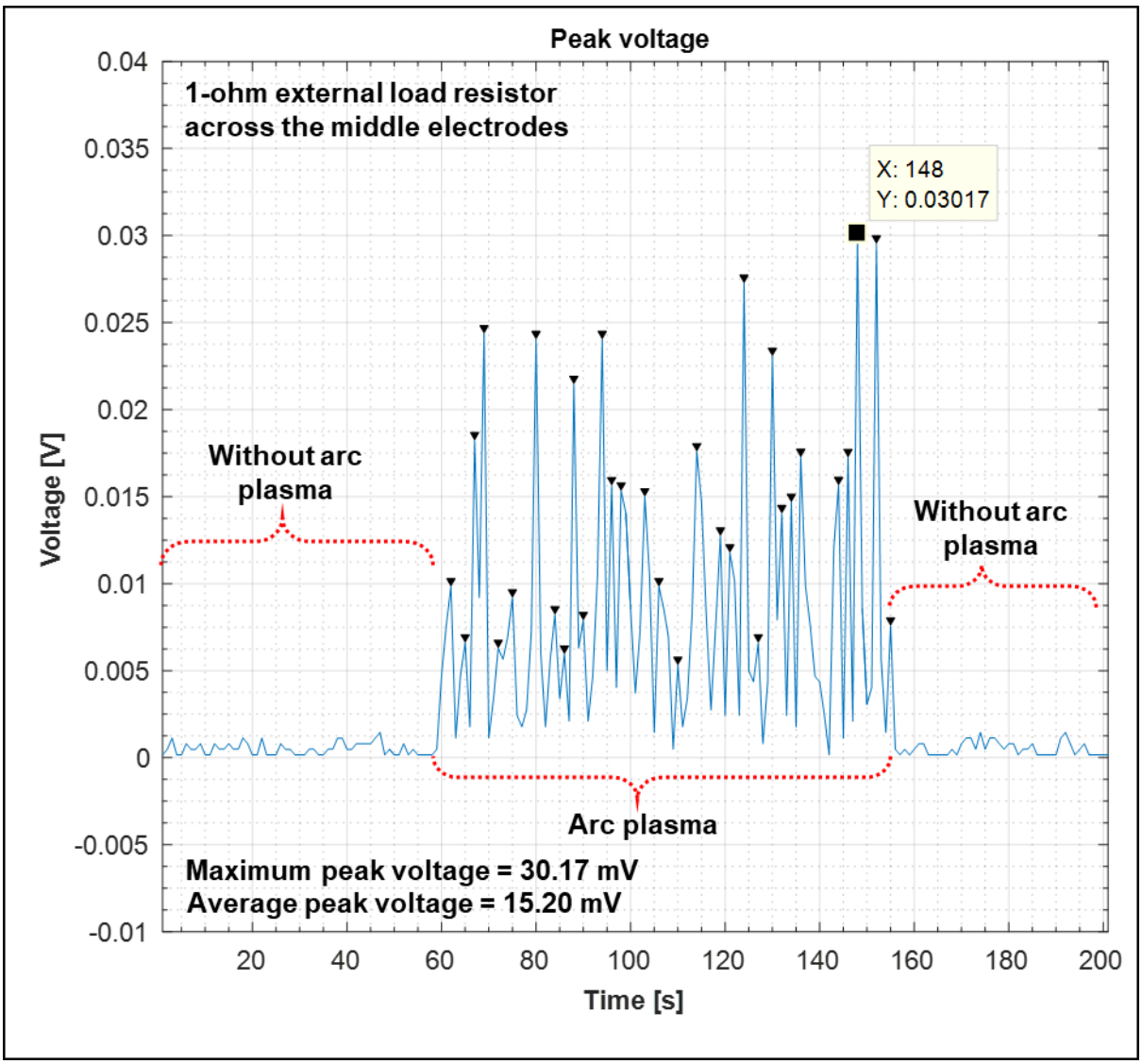

Figure 6.40: Average voltage measured across the middle-segmented electrodes in experiment 3 using 1-ohm resistor.

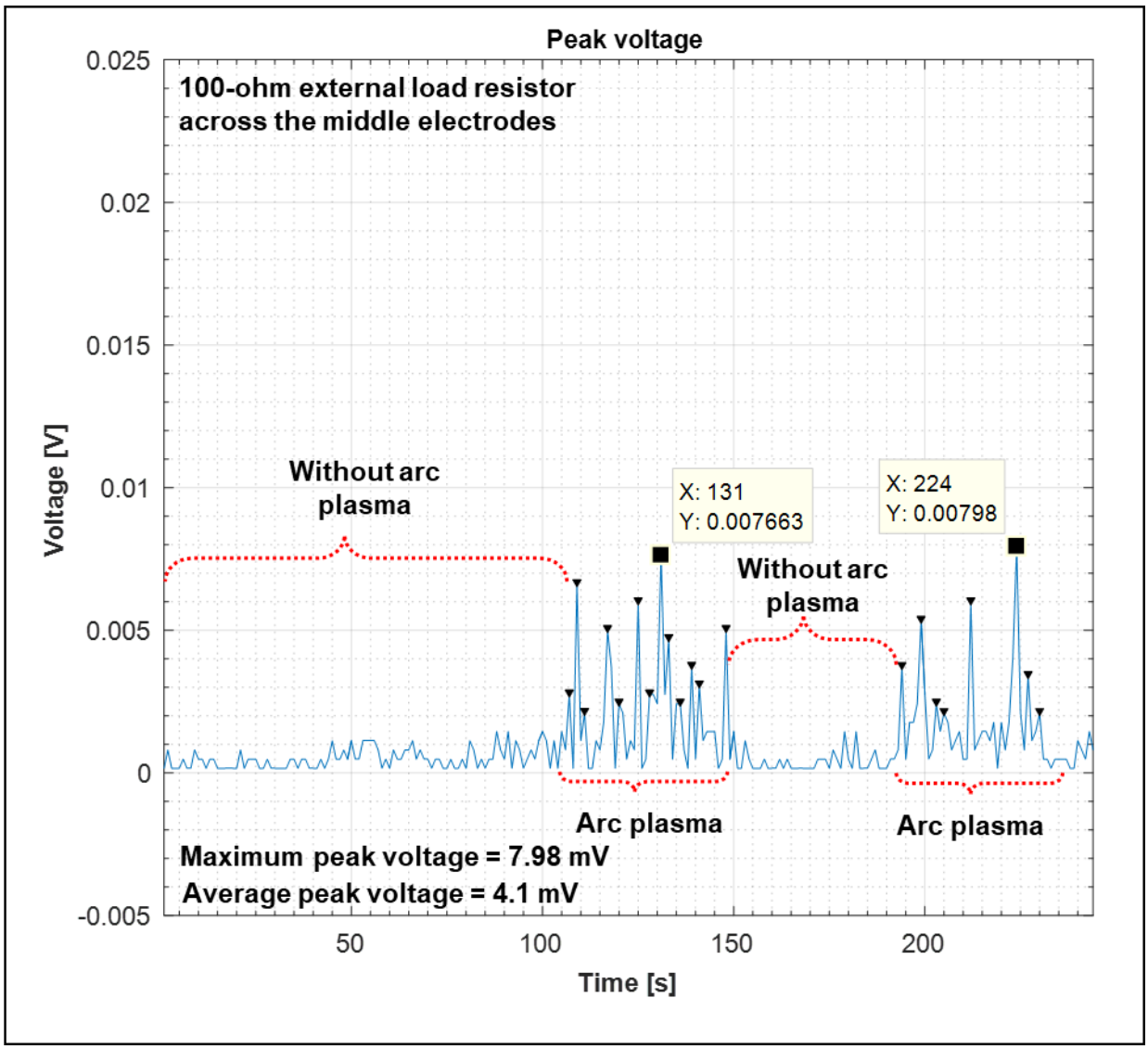

Figure 6.41: Average voltage measured across the middle-segmented electrodes in experiment 3 using 100-ohm resistor.

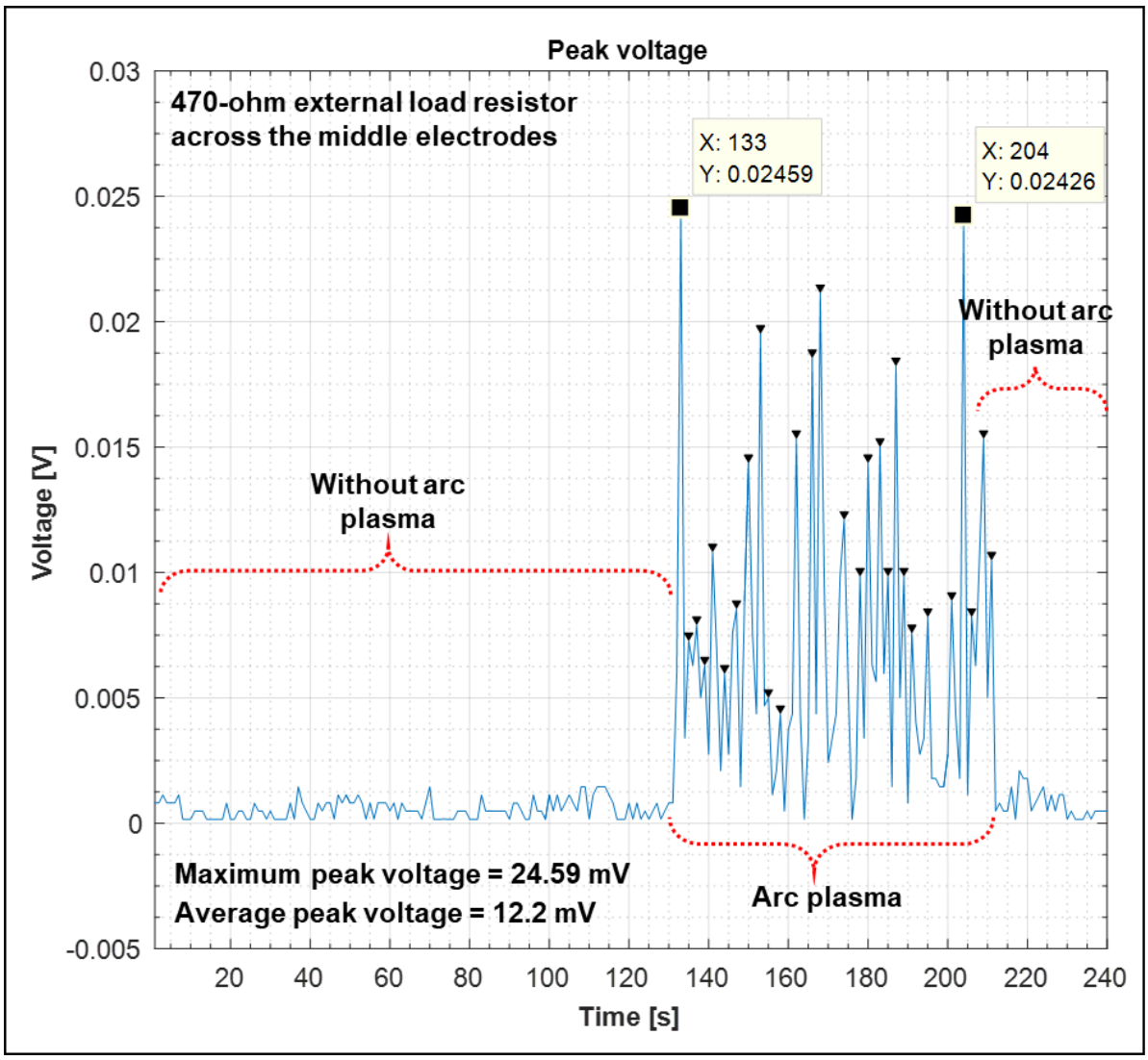

Figure 6.42: Average voltage measured across the middle-segmented electrodes in experiment 3 using 470-ohm resistor.

From Figures 6.37, 6.38, 6.39, 6.40, 6.41 and 6.42, the average voltages can be used to determine the maximum current, I_{mhd}, from the MHD generator using equation 6.1,

$$I_{mhd} = \frac{V_{actual}}{R_L} \; . \qquad \textbf{Equation 6.1}$$

In all experiments, the actual voltage, V_{actual}, is the voltage measured across the 1 Ω, 100 Ω and 470 Ω load resistors, after subtracting the offset voltage (0.965 mV) from the average voltage. From the experimental results, the maximum actual voltage of about 14.235 mV and maximum current of about 14.235 mA are obtained when 1 Ω load resistor is applied to the middle-segmented electrodes. The estimated velocity of the plasma can also be derived from the following generating circuit, as given by equation 6.2.

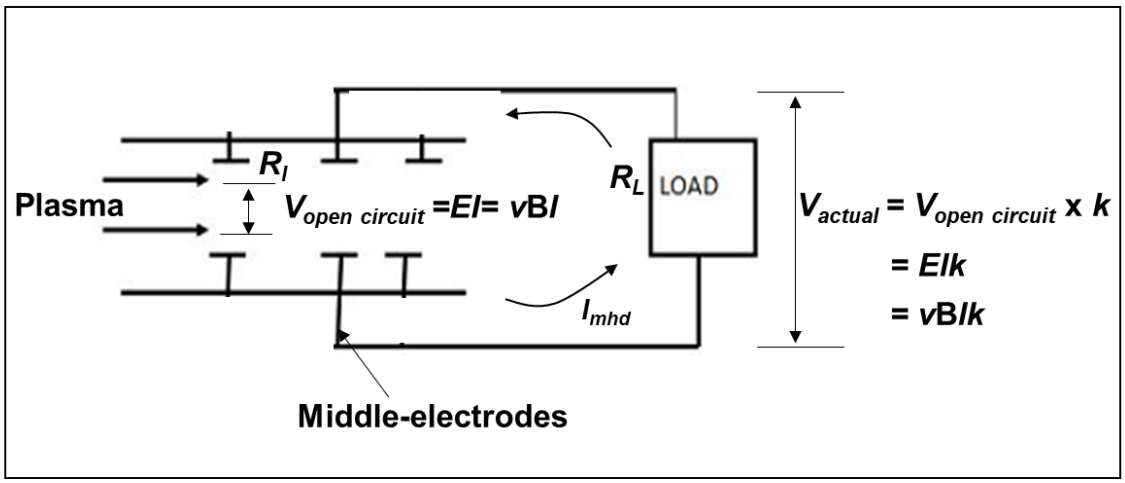

Figure 6.43: MHD power generating circuit.

$$v = \frac{V_{actual}}{\mathrm{B} \times l \times k} = 0.1303\,\mathrm{m/s} \; . \qquad \textbf{Equation 6.2}$$

Considering the above results and the dimension (0.3 m x 0.1 m x 0.1 m) of the MHD generator prototype used in this study, the optimum power can be determined using equation 2.34, with the Matlab code described in Appendix A.1,

$$P_{out} = I_{mhd} \cdot V_{actual} = \sigma v^2 \mathrm{B}^2 Al \times k\left(1 - k\right) = 0.2026\,\mathrm{mW} \;\; ,$$

where $V_{actual} = 14.235\,\mathrm{mV}$ is the measured voltage, $I_{mhd} = 14.235\,\mathrm{mA}$ is the measured current, $\mathrm{B} = 1.17\ \mathrm{T}$ is the neodymium magnet remanent flux density, $E = vB$ is the electric field, $A = 0.00327\,\mathrm{m}^2$ is the electrode surface area, $k = R_L/(R_I + R_L) = 0.9339$ is the calculated electrical load factor for 1 Ω external load resistor and $\sigma = 432\,\mathrm{S/m}$ (= 6400 K) is the

electrical conductivity of air plasma (section 2.4.1.1 & Appendix F) (Zhukov & Zasypkin, 2007:211; Ducharme & Themelis, 2010:1-2; Boulos *et al*., 2013:11).

Table 6.1 shows the summary of the experimental results.

Table 6.1: Measured power from the MHD generator under DC arc plasma experiment.

	Experiment 2 With plasma			**Experiment 3 With plasma**		
	Continuous electrodes			**Middle-segmented electrodes**		
External load resistor	1 Ω	100 Ω	470 Ω	1 Ω	100 Ω	470 Ω
Plasma velocity [m/s]	0.0433	0.0516	0.1174	0.1303	0.0268	0.0960
Average voltage [mV]	5.7	7.0	14.7	15.2	4.1	12.2
Measurement offset voltage [mV]	0.965	0.965	0.965	0.965	0.965	0.965
V_{actual} = Average – offset voltage [mV]	4.735	6.035	13.735	14.235	3.135	11.235
Current, I_{mhd}, [mA]	4.735	0.060	0.029	14.235	0.031	0.024
MHD Power [mW]	0.0224	0.0004	0.0004	0.2026	0.0001	0.0003

From Table 6.1, the results show that the estimated plasma velocity has a significant influence on the measured output power from the MHD generator. By using a plasma source with high velocity such as the ones used in large thermal plants, more power can be generated, as estimated in Figures 6.44 and 6.45.

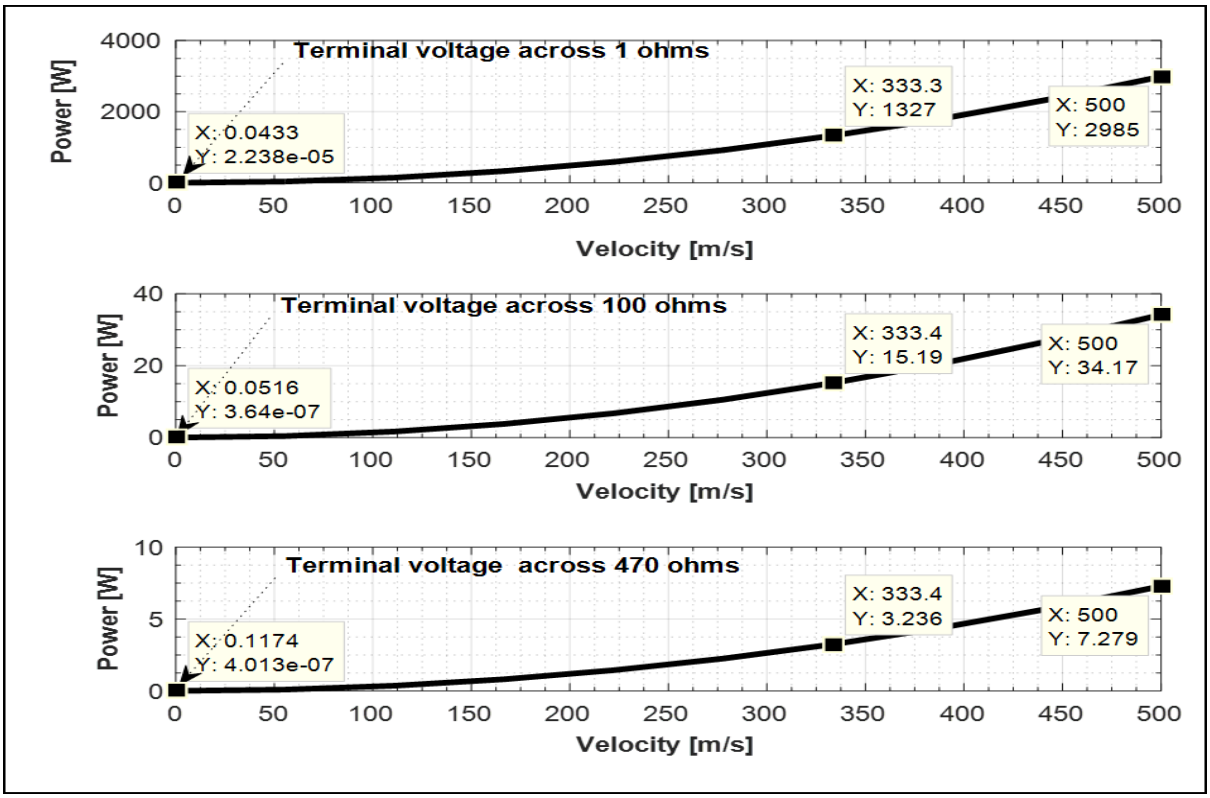

Figure 6.44: Power against velocity using the continuous electrodes.

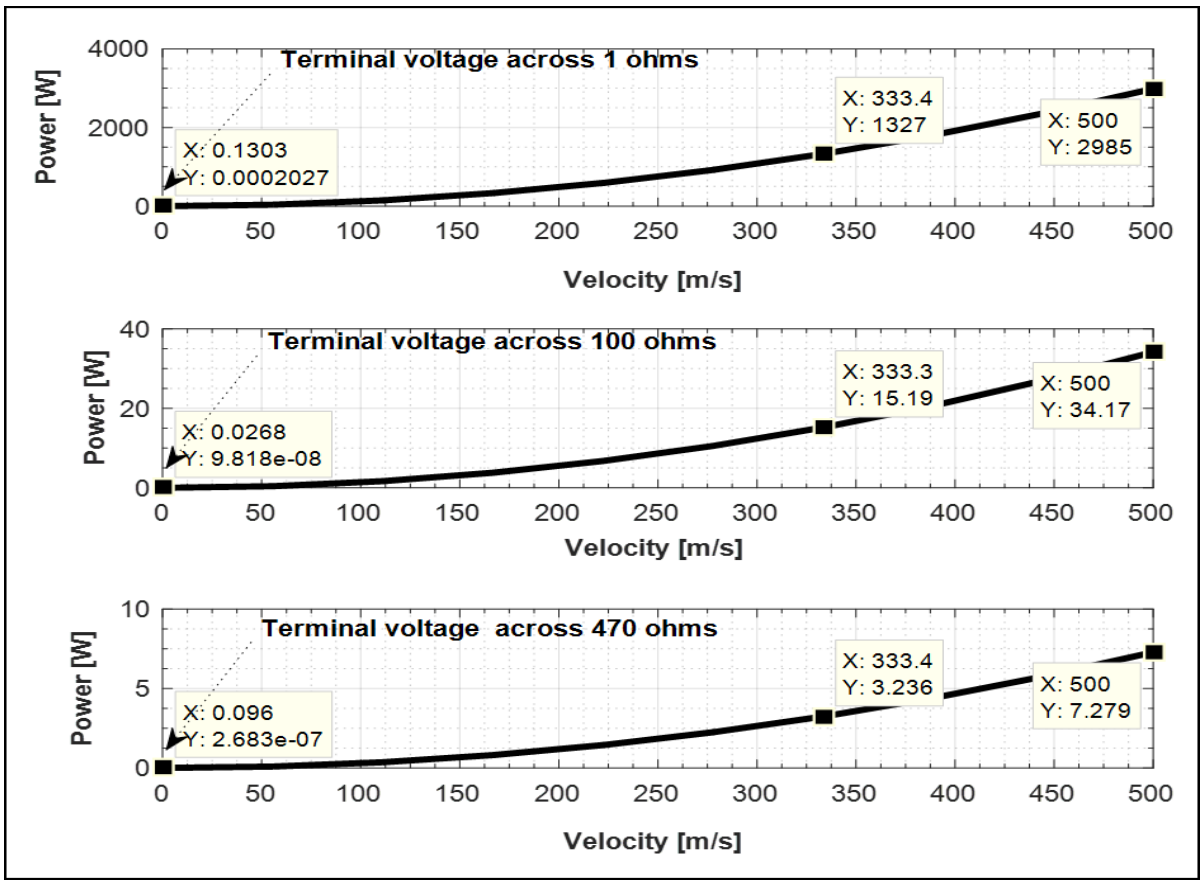

Figure 6.45: Power against velocity using the middle-segmented electrodes.

Comparing the results of experiments 2 and 3, the terminal voltage signals measured from the continuous-three electrodes and the selected middle-segmented electrodes are of the same order, that is, the flux of particles are similar. Additionally, the increase in the intensity levels of these voltage signals indicate the presence of arc plasma. In both experiments, there is a difference in the values of the measured voltages when varying the load resistors (Table 6.1). One possible reason may be due to the high resistance of the loads. Moreover, it is also possible that some consumable components of the plasma device might have been affected by heat and corrosion which could in long time influence the plasma flow and can cause fluctuations inside the generator.

A frequency analysis is also performed to determine which frequencies are involved in the voltage signals. From experiment 2, the frequency spectra of the absolute voltage when using 470 Ω differs from the frequency spectra observed when using 1 Ω and 100 Ω. From experiment 3, the frequency spectra of the absolute voltage when using 100 Ω differs from the frequency spectra observed when using 1 Ω and 470 Ω. From both experiments, the magnitude of the frequency observed when using 470 Ω in experiment 2 is comparable to the magnitude of the frequency observed when using 1 Ω and 470 Ω in experiment 3 (Figures 6.23, 6.27 and 6.35). The actual measured voltages (Table 6.1) observed in these experiments are high.

Likewise, the magnitude of the frequency observed when 100 Ω is used in experiment 3 is similar to the magnitude of the frequency observed when 1 Ω and 100 Ω are used in experiment 2 (Figures 6.15, 6.19 and 6.31). The actual measured voltages (Table 6.1) observed in these experiments are low.

In all the experiments conducted, the maximum power (0.203 mW) is obtained when 1 Ω resistor is connected to the middle-segmented electrodes. This result can be compared to the calculated MHD powers in Table 5.3 (section 5.3), in which 1 Ω load resistor produces the optimum power. The magnet remanent flux density value (1.17 T) chosen based on the simulations in chapter three has also helped in the realisation of this power. Moreover, the output power obtained from this study and literature show that the effect of Hall current and joule heating is negligible when the MHD power generator electrodes are connected in segmented mode.

6.6 Conclusion

This chapter reported on the development of an MHD power generator prototype and the experimental test setup. In this setup, two different generator configurations, namely the continuous and the segmented electrodes have been tested and analysed. The focus of the experiment was to measure the terminal voltage across the MHD power generator electrodes after exposure to plasma generated from the DC arc device. Consistent measurements have been observed in the DC arc plasma experiments.

CHAPTER SEVEN: CONCLUSION AND RECOMMENDATIONS

7.1 Introduction

The shortage supply of electricity due to the lack of fossil fuel and other conventional resources that are currently being used in Africa has motivated the present study to develop an alternative power generating system using plasma. Through theoretical modelling, this objective was achieved by coupling an MHD generator to existing conventional plants such as those in Ankerlig and Gourikwa. In doing so, the thermal cycle efficiency of both plants was improved. Furthermore, an MHD power generator prototype that can convert plasma energy directly to electric power has been built based on the principle of Faraday's Law of electromagnetism and fluid dynamics. The testing procedures of the device have been analysed using the facility available in the Western Cape region (South Africa).

7.2 Addressing the research questions

- **Direct energy conversion system**

The focus of this study was to design, build and test an MHD power generator prototype that can convert plasma energy into electricity. This device was chosen because of its high power generating efficiency.

- **Couplings of MHD power generator to the existing thermal plants**

Another focus of this study was to investigate alternative methods through which the MHD power generator can be developed and be integrated into the existing conventional power plants as a topping unit. To achieve this, two separate studies were conducted to investigate the possibility of coupling an MHD system to the South African power stations, namely Ankerlig and Gourikwa (CCGST).

- **Gases and seeded substances used for creating plasma**

A low temperature plasma can be created inside a combustion chamber if an inert gas is seeded with small amount of alkaline metals such as potassium carbonate and cesium. Several plasmas can also be created in the laboratory. Among these plasmas are the reactive ion etcher plasma, the flame discharge plasma, the inductively coupled plasma, the electron cyclotron resonance plasma, the radio frequency inductive plasma, the helicon wave plasma and the microwave induced plasma. For this study, air plasma was created using a DC arc thermal device.

- **Material used to develop the MHD power generator prototype**

Any metallic material could be used in the fabrication of the MHD power generator prototype. However, for this study, the material of preference selected for the MHD duct was mild steel because of its hardness and wide-spread availability. Materials like titanium and nickel were not considered due to high cost and unavailability. The round electrodes were selected to minimise experimental uncertainty that could arise from complex designs and structures. Additionally, the material selected for these electrodes was copper because of its high electrical conductivity, wide-spread availability and work function (4.7 eV). The magnetic and insulating materials used during the experiment were Neodymium permanent magnet, ceramic insulator and tufnol insulator.

- **Experimental measurement of plasma**

The MHD power generator prototype was tested in the laboratory through the use of a DC arc plasma source which mimic the actual plasma environment. Due to the limited plasma facilities in the Western Cape region, these experiments were carried out at the Department of Electrical, Electronic and Computer Engineering, Cape Peninsula University of Technology, Cape Town (South Africa). From the obtained results, the electric response of the generator to the plasma was determined and a significant correlation exists with literature. The main contributions and findings of this thesis are elaborated in the following sections.

7.3 Summary of the results obtained in the thesis

7.3.1 Simulation and modelling results

In the course of this research, 3-D simulations of the viscous flow of an ionised propane fluid inside a rectangular duct were performed based on the principle of Faraday's Law of electromagnetism and fluid dynamics. In these modellings, the fluid flow was studied numerically at high Reynolds number and the duct was configured to act as generator and accelerator.

In the first study, the fluid flow was studied numerically with a fixed velocity, a fixed external voltage applied to the duct electrodes and varying remanent flux density (0 T, 1.12 T, 1.32 T and 1.41 T). The aim was to examine the influence of the resulting Lorentz forces on the fluid. In the second study, the fluid flow was studied numerically with varying velocity (0.2 m/s, 0.5 m/s, 1 m/s, 2 m/s and 5 m/s) applied to the duct inlet, a fixed external voltage and a fixed remanent flux density. The aim was to accelerate the fluid inflow velocities with the external voltage and also to enhance thrust productivity. In the third study, the fluid flow was studied numerically with a fixed velocity, varying external voltage (10 V, 20 V, 30 V, 40 V and 100 V) applied to the duct electrodes and a fixed remanent flux density. The aim was to

accelerate the fluid velocity at a temperature of about 10000 K with the applied external electric potentials. From these modellings, numerical results such as the Lorentz force distributions, magnetic flux densities around the fluid, velocity profiles (field vectors and magnitudes) and pressure gradients were obtained along the duct length. The major findings of these studies are as follows:

- When the intensities of the applied magnetic fields were increased in the first study, the results obtained showed that the Hartmann's number and the interaction parameter were increased. This ultimately slowed down the field vectors of the fluid to lower values at the center of the duct and creates M-shaped velocity profiles in the center of the magnetic gap (stagnant region).

- When an electrical potential was also applied to the duct electrodes, the magnitudes of the field vectors were increased at the middle-electrode walls (MPD mode). Therefore, by applying an external load resistor to the duct electrodes, these field vectors can be captured to generate electric power (MHD mode).

- When the selected fluid inflow velocities were increased at the duct inlet in the second study, the results obtained showed that the Reynolds number were increased while the interaction parameters were decreased. Furthermore, the applied magnetic field decelerated the field vectors of each applied fluid inflow to lower values at the center of the duct.

- When an electrical potential was also applied to the duct electrodes, the magnitude of each field vector (applied fluid inflow) arriving at the middle-electrode walls were increased (MPD mode). Consequently, by applying an external load resistor to the duct electrodes, these field vectors can be captured to generate electric power (MHD mode).

- When the temperature of the fluid was increased and the applied voltages to the duct electrodes were varied in the third study, the results obtained showed that the magnitudes of the field vectors arriving at the middle-electrode walls were increased (MPD mode) under a fixed remanent flux density of about 1.41 T. Therefore, by applying an external load resistor to the duct electrodes, these field vectors can be captured to generate electric power (MHD mode).

Considering the above simulation results from the three studies, the interaction between the magnetic field strength and the fluid produce an optimum magnitude of the flow velocity. Additionally, the magnetic flux density used in these simulations serve as a guide towards the selected magnet remanent flux density value used in the experiments. The simulation results could also be used in the design and development of future MHD and MPD systems.

The major findings from the coupling of an MHD system to the South African CCGST stations are as follows:

- When two open circuit MHD models (1 and 2) were modelled theoretically and coupled to the CCGST stations to form the Ankerlig and Gourikwa CCMGST stations (first study), the optimum powers obtained using model 1 MHD unit were 2218 MW and 1235 MW, respectively. Likewise, the optimum powers obtained using model 2 MHD unit were 2910 MW and 1620 MW, respectively.

- When two open circuit MHD models (3 and 4) with external load resistors were modelled theoretically and coupled to both CCGST stations to form the Ankerlig and Gourikwa CCMGST stations (second study), the optimum powers obtained using model 3 MHD unit were 2371 MW and 1320 MW, respectively. Likewise, the optimum powers obtained using model 4 MHD unit were 3067 MW and 1707 MW, respectively.

- When an expansion nozzle was applied between the combustion chamber and the MHD generator, the gas pressure exiting the combustor is reduced and at the same time increases the speed of the plasma (Bernoullis Law) flowing through the generator, thereby increasing the overall generating power of the CCMGST stations.

Based on the outcomes of this investigation, the optimum power results showed that the overall generating efficiency of the Ankerlig and Gourikwa CCMGST stations have been increased. The additional power capacity obtained from models 3 and 4, in which the distance between the MHD duct electrodes was increased showed that the coupling of an MHD power generator to the existing conventional system can help to improve the generation of electricity in South Africa. Furthermore, an MHD generator as a topping unit to the conventional plants can provide alternative energy mix for the current power generation problem in Africa. This method can also help to reduce the atmospheric and environmental pollution (CO emission) that usually occurred when using the conventional system.

The major findings from the inductively coupled plasma and DC arc plasma simulations are as follows:

- The temperature and the velocity magnitude of plasma exiting the ICP torch outlet were 9000 K and 6 m/s, respectively.

- The plasma temperature results obtained at the outlet of the selected torches from the literature ranged from 7900 K to 30000 K. Likewise, the plasma velocity magnitude at the outlet of these torches ranged from 317 m/s to 3000 m/s.

These temperatures and velocities were modelled theoretically to the MHD generator to determine the optimum power. The maximum power was obtained when 1 Ω external load resistor was placed across the generator electrodes (Table 5.3).

7.3.2 Experimental results

This study characterised the behaviour of an MHD power generator prototype when exposed to plasma generated from a DC arc torch within the limitations of the test facility. In doing so, a rectangular duct was constructed and configured in segmented and continuous electrode modes to measure electric power. The DC arc plasma measurements were performed under steady state conditions. However, due to the chaotic nature of the physical processes of the arcing, these measurements encountered challenges in terms of noise. As a result, the study looked at both time and frequency domain analyses. The time domain analysis indicates occurrence of plasma and its more appropriate for the steady state measurements since the noise was random. In addition, when the DC arc plasma was applied, there was an increase in voltage levels compared to the no arc plasma state. By taking the average of the absolute of many experiments, it was easier to minimize the effect of the random noise and clearly observed changes in the voltage levels. The measured output power was consistent with literature. Unlike the time domain analysis, the frequency domain analysis seems to be more robust against the ambient noise and identify the low voltage signals in the measurements.

The key findings from the MHD power generator prototype experiments are as follows:

- In all experiments, the measured terminal voltages from the continuous electrodes and the middle-segmented electrodes were similar.

- The maximum power of about 0.203 mW was obtained when 1 Ω resistor was connected to the middle-segmented electrodes of the MHD generator. This result showed that the effect of Hall current and joule heating is negligible in the segmented mode.

- It can also be deduced that in both numerical and experimental studies, the optimum power was produced when 1 Ω resistor was used. Conclusively, these results validate the measurement approach and operation of MHD generator with segmented electrodes.

- After performing the post-processing with FFT, the frequency content of the measured terminal voltages showed consistency and significant harmonics were observed at frequencies between 0 Hz and 700 Hz.

7.4 Future developments and recommendations

The present research contributed to the pool of knowledge on plasma energy in relation to electric power generation. The outcomes of this research have laid a foundation for further research on plasma conversion system as it has helped in identifying some practical challenges such as limited facilities, as well as some experimental difficulties encountered while testing the MHD power generator prototype. Below are the recommendations for future work:

- The narrow-constricted nozzle of the plasma device can be optimized to fit properly into the inlet of the MHD generator in order to generate more plasma.

- A large MHD generator can be developed and be integrated to the conventional thermal power plants.

- The developed system and the MPD system can be used to create more propulsion for spacecraft's and sea-water thruster's.

- Other categories of MHD system, specifically the disk generator can be developed and tested under thermal plasma.

REFERENCES

Abubakar, M.A. Mohammad, A.A.H. & Bala, I.A. 2016. Thermal Plasma: A Technology for Efficient Treatment of Industrial and Wastewater Sludge. *IOSR Journal of Environmental Science, Toxicology and Food Technology*, 10(11): 63-75.

Ahsan, M. 2014. Numerical analysis of friction factor for a fully developed turbulent flow using k-ε turbulence model with enhanced wall treatment. *Beni-Suef University Journal of Basic and Applied Sciences, 3(4)*: 269-277.

Ajith, K.R. & Jinshah, B.S. 2013. Magnetohydrodynamic Power Generation. *International Journal of Scientific and Research Publications*, 3(6): 1-11.

Altintas, A. & Ozkol, I. 2015. Magneto-hydrodynamics flow of liquid-Metal in circular pipes for externally heated and non-heated cases. *Journal of Applied Fluid Mechanics*, 8(3): 507–514.

Andreev, O., Kolesnikov, Y. & Thess, A. 2007. Corrected Article: Experimental study of liquid metal channel flow under the influence of a nonuniform magnetic field. *Physics of Fluids*, 19(3): 039902_1-12.

Anumaka, M.C. 2014. Explicit Technology of Magnetohydrodynamic (Mhd) Power Generation. *International Journal of Innovative Technology and Research*, 2(4): 1072-1077.

ANSYS Inc, 2015. ANSYS FLUENT 16.2. Theory Guide, USA.

Aoki, L., G Maunsell, M. & Schulz, H. 2012. A magnetohydrodynamic study of behavior in an electrolyte fluid using numerical and experimental solutions. *Engenharia Térmica (Thermal Engineering)*, 11(1-2): 53–60.

Arora, V. Nikhil, V. Suri, N. K. & Arora, P. 2014. Cold Atmospheric Plasma (CAP) in Dentistry. *Dentistry*, 4(1): 1-5.

Asselin, D.J. 2011. Characterization of the near-plume region of a low-current hollow cathode. Unpublished MSc dissertation, Worcester Polytechnic Institute, Worcester.

Axelsson, K., Sergienko, T., Nilsson, H., Brändström, U., Ebihara, Y., Asamura, K. & Hirahara, M. 2012. Spatial characteristics of wave-like structures in diffuse aurora obtained using optical observations. *Annales Geophysicae*, 30(12): 1693-1701.

Ayeleso, A.O. 2014. An Extreme Ultraviolet and Plasma Spectrometer Scientific Payload for a Cubesat. Unpublished MTech dissertation, Cape Peninsula University of Technology, Cape Town.

Ayeleso, A.O., Kahn, M.T.E. & Raji, A.K. 2015. Plasma energy conversion system for electric power generation. *In 2015 International Conference on the Industrial and Commercial Use of Energy (ICUE)*. Cape Town, South Africa. 206–211.

Banerjee, R. 2015. Importance of Magneto Hydro Dynamic Generation. *International Journal of Advanced Research in Electrical, Electronics and Instrumentation Engineering,* 4(7): 6515-6518.

Baranoski, G.V.G., Wan, J., Rokne, J.G. & Bell, I. 2005. Simulating the Dynamics of Auroral Phenomena. *ACM Transactions on Graphics*, 24(1): 37-59.

Barth, J.L., Dyer, C.S. & Stassinopoulos, E.G. 2003. Space, atmospheric, and terrestrial radiation environments. *IEEE Transactions on Nuclear Science*, 50(3): 466-482.

Batsala, M., Chandu, B., Sakala, B., Nama, S. & Domatoti, S. 2012. Inductively Coupled Plasma Mass Spectrometry (ICP-MS). *International Journal of Research in Pharmacy and Chemistry* (IJRPC), 2(3): 671-680.

Berkery, J.W. & Choueiri, E.Y. 2001. Laser Discharge Initiation for Gas-fed Pulsed Plasma Thrusters. In *37th Joint Propulsion Conference*, *Salt Lake City, UT*, July 8-11. 1-9.

Bhuyan, P.J. & Goswami, K.S. 2007. Two-Dimensional and Three-Dimensional Simulation of DC Plasma Torches*. IEEE Transactions on Plasma Science*, 35(6): 1781-1786.

Bogaerts, A., Neyts, E., Gijbels, R. & van der Mullen, J. 2002. Gas discharge plasmas and their applications. *Spectrochimica Acta Part B: Atomic Spectroscopy*, 57(4): 609–658.

Böhlmark, J. 2006. Fundamentals of High Power Impulse Magnetron Sputtering. Unpublished PhD dissertation, Institute of Technology: Linköping University, Linköping, Sweden.

Bonizzoni, G. & Vassallo, E. 2002. Plasma physics and technology; industrial applications. *Vacuum*, 64(3): 327-336.

Boulos, M.I. Fauchais, P. & Pfender, E. 2013. Thermal Plasmas: Fundamentals and Applications: Springer. US.

Braithwait, N.S.J. 2000. Introduction to gas discharges. *Plasma Sources Science Technology*, 9(4): 517-527.

Brown, Neal. 2006. Auroral Facts. In *the Aurora explained* [online]. Available: http://www.alaskascience.com/aurorafacts.htm [Accessed 9 January 2015].

Budtz-Jorgensen, C.V. 2001. Studies of Electrical Plasma Discharges. Unpublished PhD dissertation, Aarhus University, Denmark.

Butt, A.H. & Arshad, A. 2015. Design and analysis of a clustered nozzle configuration and comparison of its thrust. *Student Research Paper Conference*, 2(19): 105-109.

Callen, J.D. 2006. *Fundamentals of Plasma Physics*. Madison: University of Wisconsin.

Casadio, S. & Arino, O. 2011. Monitoring the South Atlantic Anomaly using ATSR instrument series. *Advances in Space Research*, 48(6): 1056-1066.

Castell, R., Iglesias, E. J. & Ruiz-Camach, J. 2004. Glow Discharge Plasma Properties of Gases of Environmental Interest. *Brazilian Journal of Physics*, 34(4B): 1734-1737.

Chau, S.W & Hsu, K.L. 2011. Modelling steady axis-symmetric thermal plasma flow of air by a parallelized magneto-hydrodynamics flow solver. In *Computer & Fluids* 45. *International Conference on Parallel Computational Fluid Dynamics (ParCFD 2010).* Elsevier: 109-115.

Chau, S.W., & Y. Lu, S. & Wang, P.J. 2011. Modelling of axis-symmetric steam plasma flow in a non-transferred torch. *Computer Physics Communication*,182: 152-154.

Chau, S.W., Hsu, S.C. & Chen, S.H. 2016. Modelling of Air Plasma in Direct-Current Torch at Nonatmospheric Pressure. *IEEE Transactions on Plasma Science,* 44(12): 3117-3126.

Chen, F.F. 1984. *Introduction to plasma physics and controlled fusion*. 2nd ed. New York: Plenum Press.

Chen, F.F. 1995. Industrial applications of low-temperature plasma physics. *Physics of Plasmas*, 2(6): 2164-2175.

Chine, B. 2015. 2D Model of a Plasma Torch. *Proceedings of the 2016 COMSOL Conference*, Munich, October 14 – 16.

Cicconardi, S.P. & Perna, A. 2014. Performance Analysis of Integrated Systems Based on MHD Generators. *68th Conference of the Italian Thermal Machines Engineering Association, ATI2013, Energy Procedia*, 45. 1305 – 1314.

Comsol Multiphysics, 2015. *CFD Module User Guide.* Version 5.1. 1-638.

Conde, L. 2014. An Introduction to Plasma Physics and its Space Applications, Department of Applied Physics, ETS Ingenieros Aeronáuticos. Universidad Politécnica de Madrid. [Unpublished course note].

Czapka, T., Mielcarek, W., Warycha, J., Prociow, K. & Mazurek, B. 2008. Plasma Sources with Non-Thermal plasma reactor. *Chemistry Listy,* 10(2): 1314-1317.

Daoud, A. & Kandev, N. 2008. Magneto-hydrodynamics numerical study of DC electromagnetic pump for liquid metal. In *Proceeding of the Comsol conference*, Hannover, Germany, 2008: 1-7.

Dave, P.D. & Joshi, A.K. 2010. Plasma pyrolysis and gasification of plastics waste-a review. *Journal of Scientific & Industrial Research*, 69: 177-179.

Davis, J.R. 2004. Handbook of Thermal Spray Technology. ASM international. Thermal Spray, USA Society.

De Santis, A. & Qamili, E. 2010. Equivalent monopole source of the geomagnetic South Atlantic anomaly. *Pure and Applied Geophysics*, 167(3): 339–347.

Deshpande, N.D., Vidwans, S.S., Mahale, P.R., Joshi, R.S. & Jagtap, K.R. 2014. Theoretical & CFD Analysis of De Laval Nozzle. *International Journal of Modern Physics E*, 2(4): 33-36.

Dhareppagol, V.D. & Saurav, A. 2013. The Future Power Generation with MHD Generators Magneto Hydro Dynamic generation. *International Journal of Advanced Electrical and Electronics Engineering,* 2(6): 2278-8948.

DME, 1996. *Energy in South Africa: information booklet,* Revision 1. Department of Minerals & Energy, Pretoria.

Dropmann, M., Herdrich, G., Laufer, R., Puckert, D., Fulge, H., Fasoulas, S., Schmoke, J., Cook, M. & Hyde, T. W. 2013. A New Inductively Driven Plasma Generator (IPG6)-Setup and Initial Experiments. *IEEE Transactions on Plasma Science.* 41(4): 804–810.

Ducharme, C & Themelis, N. 2010. Analysis of thermal plasma – assisted waste-to energy processes. *Proceedings of the 18th Annual North American Waste-to-Energy Conference NAWTEC*, 18 May 11-13. Orlando, Florida: USA: 1-6.

Düsterer, S. 2002. Laser plasma interaction in droplet targets. Unpublished PhD dissertation, University of Jena, Jena.

Edson, J. & Cohen, H. n.d. Plasmas - the Fourth State of Matter: Characteristics of Typical Plasmas. In *CPEP Fusion Energy Education Web* [online]. Available: http://fusedweb.llnl.gov/CPEP/Chart_Pages/5.Plasma4StateMatter.html [Accessed 5 January 2015].

Energy without Carbon, 2015. Electricity from coal and gas. http://www.energy-without-carbon.org/ElectricityFromCoalAndGas [Accessed 6 December 2016].

Escobar, A.C. 2009. A Langmuir probe instrument for research in the terrestrial Ionosphere. Unpublished MSc dissertation, Pennsylvania State University, United State.

Eskom. 2014. Fact sheet Ankerlig and Gourikwa Gas Turbine Power Stations.

Gedik, E., Kurt, H. & Recebli, Z. 2013. CFD Simulation of Magnetohydrodynamic Flow of a Liquid- Metal Galinstan Fluid in Circular Pipes. *CMES-Computer Modeling in Engineering and Sciences*, 9(1): 23-33.

Goel, P. & Shukla, A. 2015. Magneto Hydrodynamics Power. *International Advanced Research Journal in Science, Engineering and Technology,* 2(1): 105-107.

Grill, A. 1994. *Cold plasma in materials fabrication: from fundamentals to applications*. New York: IEEE Press.

Grill, J. 2018. Guide to Plasma Arc Equipment. [online]. Available: http://weldguru.com/OLDSITE/plasma-arc-equipment.html [Accessed 1 February 2018].

Hardianto, T., Sakamoto, N. & Harada, N. 2008. Three-Dimensional Flow Analysis in a Faraday-Type MHD Generator. *IEEE Transactions on Industry Applications,* 44(4): 1116-1123.

Heirtzler, J.R. 2002. The future of the South Atlantic anomaly and implications for radiation damage in space. *Journal of Atmospheric and Solar-Terrestrial Physics*, 64(16): 1701-1708.

Herdrich, G. & Petkow, D. 2008. High-enthalpy, watercooled and thin-walled ICP sources characterization and MHD optimization. *Journal of Plasma Physics*, 74(3): 391–429.

Huang, R., Fukanuma, H., Uesugi, Y. & Tanaka, Y. 2011. An Improved Local Thermal Equilibrum Model of DC Arc Plasma Torch. *IEEE Transaction on Plasma Scienc*e. 39(10): 1974-1982.

Hunt, J. 1965. Magnetohydrodynamic flow in rectangular ducts. *Journal of Fluid Mechanics*. 21(4): 577–590.

Iceland Aurora Films. 2014. Auroras Explained. [online]. Available: http://www.icelandaurorafilms.com/2014/11/auroras-explained/ [Accessed 9 January 2015].

Ishikawa, M. & Itoh, K. 2003. Three-dimensional constricted electric current near anode and cathode of Faraday MHD generator. *Energy Conversion and Management,* 44: 2111-2124.

Ishikwa, M., Yuhara, M. & Fujino, T. 2007. Three-dimensional computation of magnetohydrodynamics in a weekly ionized plasma with strong MHD interaction. *Journal of Material Processing Technology,* 181(1-3): 254-259.

Islam, M.S., Molla, N.H. & Quddus, E. 2013. Prospect of MHD Generation in Bangladesh. *International Journal of Engineering Research and Applications,* 3(6): 745-748.

Jing, D., Yahojian, Li., Yongxiang, X. & Hongzhi, S. 2011. Numerical simulation of fluid flow and heat transfer in a DC non-transferred arc plasm torch operating under laminar and turbulent conditions. *Plasma Science and Technology*, 13(2): 201-207.

Kagoné, A.K., Koalaga, Z. & Zougmoré, F. 2012. Calculation of air-water vapor mixtures thermal plasmas transport coefficients. *IOP Conference Series: Materials Science and Engineering*, 29(1): 1-15.

Kandev, N. 2012. Numerical Study of a DC Electromagnetic Liquid Metal Pump: Limits of the Model. *Proceeding of the Comsol conference*, Hannover, 2012; 1-6.

Kantrowitz, A.R., Brogan, T.R., Rosa, R.J. & Louis, J.F. 1962. The Magnetohydrodynamics power generator-basic principles, state of the art, and areas of application. *IRE Transactions of Military Electronics,* 6 (1): 78-83.

Kayukawa, N. 2004. Open-cycle Magnetohydrodynamics electrical power generation: a review and future perspectives. *Progress in Energy and Combustion Science,* 30(1): 33–60.

Khan, M.A., Vaddadi, K., Gupta, A. & Vigneshwara, k. 2014. Case Study of MHD Generator for Power Generation and High-Speed Propulsion. *International Journal of Modern Engineering Research*, 4(9): 81-90.

Kletzing, C.A., Scudder, J.D., Dors, E.E. & Curto, C. 2003. Auroral source region: Plasma properties of the high-latitude plasma sheet. *Journal of Geophysical Research*, 108(A10): 1-15.

Kohio, N., Kagoné, A.K., Koalaga, Z., Zougmoré, F. & Njomo, D. 2014. Calculation of transport coefficients of air-water vapor mixtures thermal plasmas used in circuit breakers. *International Journal of Engineering Research*, 3(12): 711-715.

Köritzer, J. 2013. Biophysical effects of cold atmospheric plasma on glial tumor cells. Unpublished PhD dissertation, Ludwig-Maximilians-Universität, München.

Kotova, G.A. 2007. The Earth's plasmasphere: State of studies (a Review). *Geomagnetism and Aeronomy*, 47(4): 409-422.

Laron. 2013. Six years of observing the Earth's magnetosphere. In *transcient.info* [onilne]. Available: http://www.transients.info/2013/09/six-years-of-observing-earths.html# [Accessed 9 January 2015].

Li, P., Barry, G., Castellanos, S., Chan, C., Do, K., Gamez, C. & Kuhn, J., A. 2007. Leon, Power Generation Using Magnetohydrodynamic Generator with a Circulation Flow Driven by Solar-Heat-Induced Natural Convection.
http://cfpub.epa.gov/ncer_abstracts/index.cfm/fuseaction/display.highlight/abstract/8630/report/F

Lieberman, M.A. 2003. A mini-course on the principles of plasma discharges. A short course at the 15th European Summer School on Low Temperature Plasma Physics. 10-16 October 2010, Bad Honnef: Germany. [Unpublished course note].

Lilensten, j., Provan, G., Grimald, S., Brekke, A., Fluckiger, E., Vanlommel, P., Wedlund, C.S., Barthelemy, M. & Garnier, P. 2013. The Planeterrella experiment: from individual initiative to networking. *Journal of Space Weather and Space Climate*, 3(26): 1-9.

Lutz, T.J., Nygren, R.E., Tanaka, T.J., McDonald, J.M., Bauer, F.J., Troncosa, K.P. & Ulrickson, M.A. 2003. Measurements of lithium flow with an EM flow meter in LIMITS. In 20th IEEE/NPSS Symposium on Fusion Engineering, 2003. *20th IEEE/NPSS Symposium on Fusion Engineering*, 2003. 367–370.

Lyons, L.A. 2007. Construction and operation of a Mirror Langmuir Probe diagnostic for the Alcator C-Mod tokamak. Unpublished MSc dissertation, Massachusetts Institute of Technology, Cambridge.

Markusic, T. E. Polzin, K. A. & Dehoyos, A. 2005. Electromagnetic pump for conductive propellant feed systems, *Proceedings of the 29th International Electric Propulsion conference*, Princeton University, November 2005. 1-16.

Martinas, G., Cupsa, O.S., Buzbuchi, N. & Arsenie, A. 2015. Modelling with Finite Volume the Combustion in Direct Injection Natural Gas Engine Using Non-Premixed Combustion Model. In *5th International Conference on innovative Computing Technology (INTECH),* Galicia, Spain, May 20-22. 72-77.

Masood, B., Riaz, M.H. & Yasir, M. 2014. Integration of Magnetohydrodynamics (MHD) Power Generating Technology with Thermal Power Plants for Efficiency Improvement.
World Applied Sciences Journal, 32(7): 1356-1363.

Mavromichalaki, H., Papaioannou, A., Mariatos, G., Papailiou, M., Belov, A., Eroshenko, E., Yanke, V. & Stassinopoulos, E.G. 2007. Cosmic ray radiation effects on space environment associated to intense solar and geomagnetic activity. *IEEE Transactions on Nuclear Science,* 54(4): 1089-1096.

Mayo R. M. & Mills, R. L. 2002. Direct Plasmadynamic Conversion of Plasma Thermal Power to Electricity for Microdistributed Power Applications. *In 40th Annual Power Sources Conference,* Cherry Hill: New Jersey. 1-4.

McClaine, A., Pinsley, J. & Pote, B. 1989. Experimental investigation on the effects of the TRW two stage coal combustors on the performance of the AVCO Mk VI MHD generator. In: *Proceedings of the 24th Intersociety Energy Conversion Engineering Conference.* Washington, DC, USA, 6-11 Aug.

Mendoza Gonzalez, N.Y., Rao, L., Carabin, P., Kaldas, A. & Meunier, J.L. 2009. A three-dimensional model of a DC thermal plasma torch for waste treatment applications. *Proceeding of the 19th International Symposium on Plasma Chemistry*, 27-31 July 2009. Bochum, Germany.

Merlino, L.M. 2007. Understanding Langmuir probe current-voltage characteristics. *American Journal of Physics,* 75(12):1078-1081.

Mgbachi, C.A. 2015. Design Analysis of Magnetohydrodynamic (MHD) Electrical Power Generation Technology. *International Journal of Advancement in Research & Technology*, 4 (10): 103-108.

Miyamoto, K. 2000. *Fundamentals of plasma physics and controlled fusion*. Tokyo: Iwanami Book Service Center.

Murphy, A.B. & Arundelli, C.J. 1994. Transport coefficients of argon, nitrogen, oxygen, argon-nitrogen, and argon-oxygen plasmas. *Plasma Chemistry and Plasma Processing*, 14(4): 451–490.

Murphy, A.B. 1995. Transport coefficients of air, argon-air, nitrogen-air, and oxygen-air plasmas. *Plasma Chemistry and Plasma Processing*, 15(2): 279–307.

Nasa Facts. 2004. National Aeronautics and Space Administration Glenn Research Center Cleveland, Ohio, 44135–3191.

National Instruments, 2014. USER GUIDE-NI USB-6001/6002/6003, Low-Cost DAQ USB Device, USA.

Nehra, V., Kumar, A. & Dwivedi, H.K. 2008. Atmospheric non-thermal plasma sources, *International Journal of Engineering,* 2(1): 53-68.

Nemchinsky, V.A. 1998. Plasma flow in a nozzle during plasma arc cutting. *Journal of Physics, D: Applied Physics,* 31(21): 3102–3107.

NPTEL. 2017. Electrical Rockets-Electric Propulsion. Indian Institute of Technology. [Unpublished lecture note]. Available: Nptel.ac.in/courses/101106046/ [Accessed 25 September 2017].

Okuno, Y., Watanabe, K., Kawasaki, A. & Murakami, T. 2011. Experimental Studies of Seed-Free Pure-Inert-Gas Working MHD Power Generation. In 42nd AIAA Plasmadynamics and Lasers Conference, 27 - 30 June 2011, Honolulu, Hawai.1-7.

Ota, K. Watanabe, Y. Banine, V. & Franken, H. 2006. EUV Source Requirements for EUV Lithography. In *EUV sources for lithography*. Edited by Bakshi, V.B: SPIE Press. 1-1045.

Parsodkar, R.R. 2015. Magneto Hydrodynamics Generator. *International Journal of Advanced Research in Computer Science and Software Engineering,* 5(3): 541-546.

Pollet, B.G., Staffell, I. & Adamson, K.A. 2015. Current energy landscape in the Republic of South Africa. *International Journal of Hydrogen Energy*, 40(46): 16685–16701.

Poonthamil, R., Prakash, S. & Varma, S.A. 2016. Enhancement of Power Generation in Thermal Power Plant Using MHD System. IOSR Journal of Mechanical and Civil Engineering, 13(5): 142–146.

Ramos, J.I. & Winowich, N.S. 1990. Winowich, N.S. & Ramos, I.J. 1990. inite Difference and Finite Elements Methods for MHD Channel Flows. *International Journal of Numerical Methods in Fluid*, 11(6): 907-934.

Richardson, J.D. 2010. *The Solar Wind and Its Interaction with the Interstellar Medium*. Berlin Heidelberg: Springer-Verlag.

Ritchie, W., 1932. Experimental Researches in a voltaic electricity and electromagnetism. *Philosophical Transactions of the Royal Society A*. 122: 279-298.

Robin, L. 2006. Mysterious Radio Hiss Blamed on Space Weather. In s*pace.com* [online]. Available: http://www.space.com/2971-mysterious-radio-hiss-blamed-space-weather.html [Accessed 9 September 2015].

Robot Industrial Supplies. 2018. Plasma ARC Cutting. [online]. Available: http://www.robotindustrial.co.za/thermodyne16a [Accessed 1 February 2018].

Roman, C.R. 2014. Study of the electromagnetic pumping systems of molten metals and molten salts. Docteur De L'Université de Grenoble, France et l'Université Politehnica de Bucarest, Roumanie.

Rucker, H.O. 2008. Introduction to Plasma Physics. Institute of Physics, Karl-Franzens-University Graz: Austria. [Unpublished lecture note]. Available: ftp://ftp.iwf.oeaw.ac.at/pub/pel/plasma%20physics.pdf [Accessed 9 January 2015].

Sawhney, B.K. & Verma, S.S. 1988. Optimum liquid fuel mixture for MHD power generators. *Energy Conversion Management*, 28(2): 137-141.

Sawhney, B.K. & Verma, S.S. 1995. Optimum Power Generation Characteristics of an MHD Generator with Kerosene Oil-Heavy Fuel Oil Mixture as working fluid. *Energy Conversion Management,* 36(5): 343-353.

Sedaghati, R., Rajabi, A.R., Sedaghati, H. & Tazangi, M.M. 2013. A New Technology for Power Generation Based on Kinetic Energy of the Plasma. *International Journal of scientific research and management*, 1(5): 281–284.

Sharma, S. & Gambhir, S. 2015. Magneto Hydro Dynamics Power Generation Techniques. *International Journal of Computing and Corporate Research,* 5(5): 1-10.

Shercliff, J.A. 1953. Steady motion of conducting fluids in pipes under transverse magnetic fields. *Mathematical Proceedings of the Cambridge Philosophical Society,* 49(1): 136-144.

Siingh, D., Singh, R.P., K Kamra, A., N Gupta, P., Singh, R., Gopalakrishnan, V. & Singh, P.A. 2005. Review of electromagnetic coupling between the Earth's atmosphere and the space environment. *Journal of Atmospheric and Solar-Terrestrial Physics*, 67(6): 637-658.

Silinga, C. & Gauché, P. 2014. Scenarios for a South African CSP Peaking System in the Short Term. *Energy Procedia*, 49(Supplement C): 1543–1552.

Sinclair, B.C. 2005. Langmuir Probe Diagnostics of the VASIMR Engine. Unpublished MSc dissertation, Naval Postgraduate School, California.

Singh, S., Chandra, R., Tripathi, S., Rahman, H., Tripathi, P., Jain, A. & Gupta, P. 2014. The bright future of dentistry with cold plasma-Review. *Journal of Dental and Medical Sciences*, 13(10): 6-13.

Sivaram, A.R., Kanimozhivendhan, G., Rajavel, R. & Raj, V.P.D. 2015. Performance Investigation of a closed cycle Magneto Hydrodynamics Power plant with liquid metal as heat source*. Indian Journal of Science and Technology.* 8 (21): 1-6.

Solonenko, O. 2003. *Thermal Plasma Torches and Technologies*. *Volume I, Plasma Torches: Basic Studies and Design.* Cambridge International Science Publishing. Cambridge, UK.

Spalding-Fecher, R. 2011. What is the carbon emission factor for the South African electricity grid? *Journal of Energy in Southern Africa*, 22(4): 8–14.

Stassinopoulos, E.G. & Raymond, J.P. 1988. The space radiation environment for electronics. *IEEE Transactions on Nuclear Science,* 76(11): 1423-1442.

Stern, D.P. 2002. Secrets of the Polar Aurora. Lecture presented in Anchorage, Alaska. Available: http://www.phy6.org/Education/aurora.htm [Unpublished lecture note]. [Accessed 9 January 2015].

Surya Narayana, K.P.S. & Sadhashiva Reddy, K. 2016. Simulation of Convergent Divergent Rocket Nozzle using CFD Analysis, *IOSR Journal of Mechanical and Civil Engineering*, 13 (4): 58-65.

Sutton, G. & Sherman, A. 1965. *Engineering Magnetohydrodynamics*. McGraw-Hill, New York.

Takayanagi, S., Takahashi, K., Sasaki, T., Aso, T. & Harada, N. 2014. Theoretical Power Output from a Capacitive-Coupled Power Extraction Magnetohydrodynamic Generator with a Sinusoidal Alternating Magnetic Field. *Plasma Fusion Research,* 9: 1-3.

The Welding Institute. 2017. Cutting processes - plasma arc cutting - process and equipment considerations. Available: http://www.twi-global.com/technical-knowledge/job-knowledge/cutting-processes-plasma-arc-cutting-process-and-equipment-considerations-051/ [Accessed 16 July 2017].

Tillack, M.S. & Morley, N.B. 1998. *Magnetohydrodynamics: Standard Handbook for Electrical Engineers*. 14th ed. New York: McGraw Hill.

Tobiska, W.K. & Nusinov, A.A. 2000. Status of the draft ISO solar irradiance standard. *Physics and Chemistry of the Earth, Part C: Solar, Terrestrial & Planetary Science*, 25(5-6): 387-388.

Tobiska, W.K. & Nusinov, A.A. 2005. Status of ISO draft international standard for determining solar irradiances (DIS 21348). *Advances in Space Research*, in review. Available: http://www.spacewx.net/pdf/C01_0014_04.pdf [Accessed 7 October 2013].

Tong, J.B., Lu, X., Liu, C.C., Pi, Z.Q., Zhang, R.J. & Qu, X.H. 2016. Numerical simulation and prediction of radio frequency inductively coupled plasma spheroidization. *Applied Thermal Engineering*, 100: 1198-1206.

Trelles, J.P., Chazelas, C., Vardelle, A. & Heberlein, J. V. R. 2009. Arc Plasma Torch Modeling. *Journal of Thermal Spray Technology*, 18(5-6): 728-752.

Valinčius, V. Grigaitienė, V. & Tamošiūnas, A. 2012. Report on the different plasma modules for pollution removal MO 03: Plasma for environ protect. Lithuanian Energy Institute, Lithuania.

Velikhov, E.P., Matveenko, O.G., Panchenko, V.P., Pis'Mennyi, V.D., Yakushev, A.A., Pisakin, A.V., Blokh, A.G., Tkachenko, B.G., Sergeenko, N.M., Zhukov, B.P., Babakov, Y.P., Zhegrov, E.F., Polyakov, V.A., Glukhikh, V.A., Manukyan, G.S., Krylov, V.A., Vesnin, V.A., Parkhomenko, V.A., Sukharev, E.M. & Malashko, Y.I. 1999. Pulsed MHD Power System SAKHALIN-the World largest solid propellant fueled MHD generator of 500 MWe electric power output, In *Proceedings of 13th International Conference on MHD Power Generation and High Temperature*. 12. 387-398.

Venkatramani, N. 2002. Industrial plasma torches and applications, *Current Science*, 83(3): 254-262.

Wang, F. Zhang, J, & Wang, S. 2012. Investigation on flow and heat transfer characteristics in rectangular channel with drop-shaped pin fins. *Propulsion and Power Research*, 1(1): 64-70.

Warra A.A. & Jimoh W.L.O. 2011. Overview of an Inductively Coupled Plasma (ICP) System. *International Journal of Chemical Researc*h (IJCR), 3(2): 41-48.

Weyde, C. 2006. Plasma parameters from the Rosetta LAP instrument. Unpublished MSc dissertation, Uppsala University, Sweden.

Xue, W. Kusumoto, K. & Nezu K. 2005. Relationship between Plasma Arc Cutting Acoustic and Cut Quality. *Science and Technology of Welding and Joining*, 10: 44-49.

Yin, F. Hu, S. Yu, C. & Li, L. 2007. Computational simulation for the constricted flow of argon plasma arc. *Computational Materials Science*, 40: 389-394.

Yongcheol, H. & Han S.U. 2010. Plasma Flame Sustained by Microwaves and Burning Hydrocarbon Fuel: It's Applications, Fuel Injection, Daniela Siano (Ed.). In *InTech* [online]. Available: www.intechopen.com/download/pdf/11345 [Accessed 9 January 2015].

Zhukov, M.F. & Zasypkin, I.M. 2007. *Thermal plasma torches: Design, Characteristics, Application*. Cambridge, Cambridge International Science Publishing Ltd, UK.

APPENDICES

APPENDIX A: Matlab code

A.1 M-file code for calculating the MHD power

```
%%%%%%%%%%%%%%%%%%%%%%%%%%%%%%%%%%%%%%%%%%%%%%%%%%%%%%%%%%%%
%*Ayeleso Ayokunle *                                       %
%*211014788 *                                              %
%                                                          %
% M-file code for calculating the MHD power               %
 %**********************1 ohms *******************************  %
 %%%%%%%%%%%%%%%%%%%%%%%%%%%%%%%%%%%%%%%%%%%%%%%%%%%%%%%%%%%

close all
clear all
clc

RL=1;                                 % External resistance
COND= 432;                            % Electrical conductivity of air
B=1.170;                              % Neodymium permanent remanent flux density
A=0.00327;                            % Electrode surface area
l=0.1;                                % Distance between the electrodes

velocity= 0.0433                      % velocity calculation from the experiment
velocity2=linspace(0.0433,500,10)     % velocity increment

RI=l/(COND*A)                         % Internal resistance
k=RL/(RL+RI)                          % Electrical load factor

voltage=4.735e-03                     % experiment output voltage across 1 ohms resistor
voltage2= velocity2*l*B*k             % voltage from velocity increment
velocity=voltage/(B*l*k)              % Plasma velocity calculation

Power= voltage*A*COND*velocity*B*(1-k)      % MHD system power from experiment
Power2= voltage2*A*COND.*velocity2*B*(1-k)  % MHD system power from velocity increment

I=voltage/RL;                         % Faraday's current
P=voltage*I                           % MHD system power from velocity increment

plot(velocity,Power)                  % Plot of MHD system power from experiment
hold on
plot(velocity2,Power2)                % Plot of MHD system power from velocity increment
```

```
%%%%%%%%%%%%%%%%%%%%%%%%%%%%%%%%%%%%%%%%%%%%%%%%%%%%%%%%%%%%
%*Ayeleso Ayokunle *                                       %
%*211014788 *                                              %
%                                                          %
% M-file code for calculating the MHD power in power plants %
 %                                                         %
 %%%%%%%%%%%%%%%%%%%%%%%%%%%%%%%%%%%%%%%%%%%%%%%%%%%%%%%%%%%

clc; close all;

COND= 20;                             % Plasma conductivity
v=1088;                               % Plasma velocity
B=2.5;                                % Magnetic field
A=1.6;                                % Surface area of the electrodes
l=2;                                  % Distance between the electrodes
```

```
RI=l/(COND*A)                    % Internal resistance
RL=0.1                           % External load resistance
k=RL/(RL+RI)                     % Electrical load factor
Power= COND*v^2*B^2*A*l*k*(1-k)  % MHD power
```

A.2 Fast Fourier Transform code

```
%%%%%%%%%%%%%%%%%%%%%%%%%%%%%%%%%%%%%%%%%%%%%%%%%%%
%                                                                                                  %
%*Ayeleso Ayokunle *                                                                               %
%*211014788 *                                                                                      %
%                                                                                                  %
% *M-file code for Fast Fourier Transform (FFT)*                                                   %
%%%%%%%%%%%%%%%%%%%%%%%%%%%%%%%%%%%%%%%%%%%%%%%%%%%

clc; close all;
set (0,'DefaultAxesFontSize',14)

Voltage2 =[Voltage];                            % Voltage signal of experiments
Fs=2000                                         % Sampling frequency
L=length(Voltage2);                             % Sampling length
mean(Voltage2)                                  % Average of the voltage signal from the experiments
Voltage2abs=abs(Voltage2);                      % Absolute of the voltage signal of the experiment

A=Voltage2(1:119500);                           % Half of the voltage signal from the experiments

Voltage_fftold = abs(fft(Voltage2));            % FFT of the voltage signal of experiment (abs in
                                                % Matlab takes complex magnitude)
Voltage_fftnew = abs(fft(Voltage2abs-mean(Voltage2abs))); % FFT of the absolute of the voltage
                                                % signal

X=((1:119500)*Fs)./239000;                      % Frequency range of the experiments
Y1=Voltage_fftold(1:119500)                     % Half of the FFT of the voltage signal of experiment
Y2=Voltage_fftnew(1:119500)                    % Half of the FFT of the absolute of the voltage signal
Yold=Y1/max(Y1);                                % Normalizing the magnitude of the FFT amplitudes
Ynew=Y2/max(Y2);                                % Normalizing the magnitude of the FFT amplitudes

 %********************************************Plot**********************************************************
figure
plot(X(1:119500),Yold(1:119500),'b')          % Display half of the FFT of the voltage signal
hold on
plot(X(1:119500),Ynew(1:119500),'r');     % Display half of the FFT of the absolute of the voltage signal
legend('FFT of the original data',' FFT of the absolute (original data)')

title('Frequency domain');
xlabel('Frequency (Hz)');
ylabel('Magnitude')
grid on
```

A.3 M-file code for the spectrograms of the measured voltage signal

```
%%%%%%%%%%%%%%%%%%%%%%%%%%%%%%%%%%%%%%%%%%%%%%%%%%%%%%
%*Ayeleso Ayokunle *                                 %
%                                                    %
%*211014788 *                                        %
%                                                    %
% *M-file code for the spectrograms of the voltage signal*   %
%%%%%%%%%%%%%%%%%%%%%%%%%%%%%%%%%%%%%%%%%%%%%%%%%%%%%

clc
close all

Fs=2000;                                  % Sampling frequency
Voltage2= [Voltage];                      % Voltage signal of experiments

nfft = 50000;
mywin = hann(3000);
wvtool(mywin);
olap = 1000;

spectrogram(Voltage2, mywin,olap,nfft,Fs,'yaxis');     % Display the spectrograms of the voltage signal
colorbar;
```

A.4 M-file code for the minimum peak voltage height with arc plasma

```
%%%%%%%%%%%%%%%%%%%%%%%%%%%%%%%%%%%%%%%%%%%%%%%%%%%%%%%%
%*Ayeleso Ayokunle *                                                              %
%                                                                                  %
%*211014788 *                                                                     %
%                                                                                  %
% *M-file code for the minimum peak voltage height with arc plasma *              %
%%%%%%%%%%%%%%%%%%%%%%%%%%%%%%%%%%%%%%%%%%%%%%%%%%%%%%%%

close all;
%clear all;
set (0,'DefaultAxesFontSize',14)

% *******************M-file code used for finding the minimum peak height******************************%

Voltage =[Voltage];                             % Filtered voltage signal
Voltage_abs= abs(Voltage);                      % Absolute value of the filtered voltage signal

% ***************Average of the filtered voltage signal of experiment*************************************%

figure
findpeaks(Voltage_abs(:,1),'MinPeakHeight', 0.00278);          % plots peaks in data
mean(findpeaks(Voltage_abs(:,1),'MinPeakHeight', 0.00278))  % Average of the filtered voltage signal
title('Peak voltage');
xlabel('Time [s]');
ylabel('Voltage [V]')
grid on
```

A.5 M-file code for the minimum peak voltage height without arc plasma

```
%%%%%%%%%%%%%%%%%%%%%%%%%%%%%%%%%%%%%%%%%%%%%%%%%%
%*Ayeleso Ayokunle *                                                    %
%                                                                       %
%*211014788 *                                                           %
%                                                                       %
% *M-file code for the minimum peak voltage height without arc plasma * %
%%%%%%%%%%%%%%%%%%%%%%%%%%%%%%%%%%%%%%%%%%%%%%%%%%

close all;
%clear all;
set (0,'DefaultAxesFontSize',14)

% ******************M-file code used for finding the minimum peak height****************************%

Voltage =[Voltage];                         % Filtered voltage signal
Voltage_abs= abs(Voltage);                  % Absolute value of the filtered voltage signal

% **************Average of the filtered voltage signal of experiment***********************************%

figure
findpeaks(Voltage_abs(:,1),'MinPeakHeight',0.0004);          % plots peaks in data
mean(findpeaks(Voltage_abs(:,1),'MinPeakHeight',0.0004))  % Average of the filtered voltage signal
axis([0 219 -0.04 0.005]);                                   % for axis trimming
title('Peak voltage');
xlabel('Time [s]');
ylabel('Voltage [V]')
grid on
```

APPENDIX B: The assumed systemic offset voltage measured without arc plasma

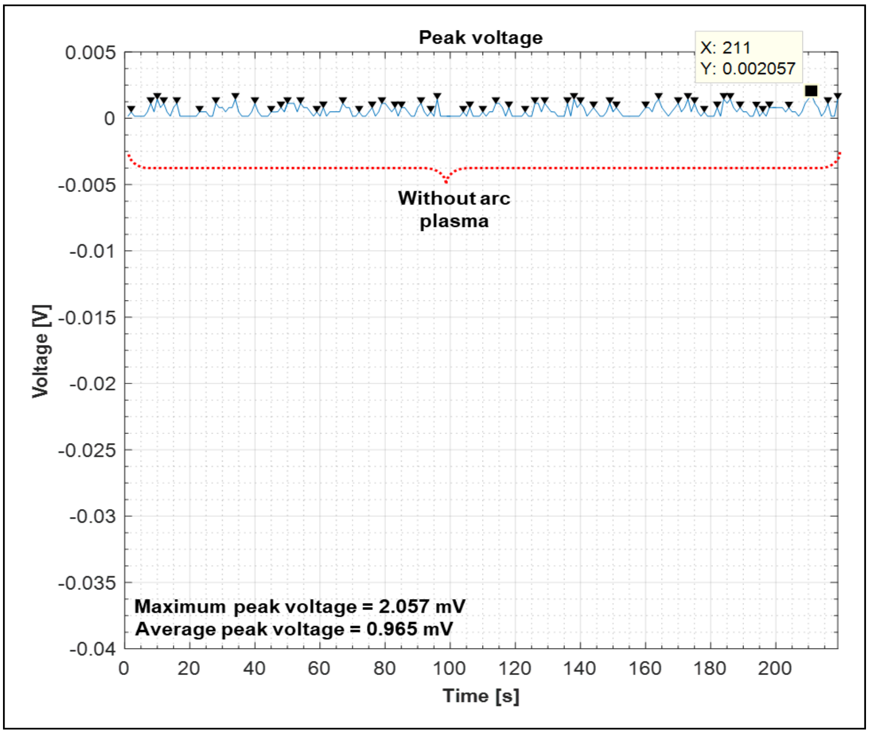

Figure B.1: The systemic offset voltage measured without arc plasma.

APPENDIX C: The electrode surface area

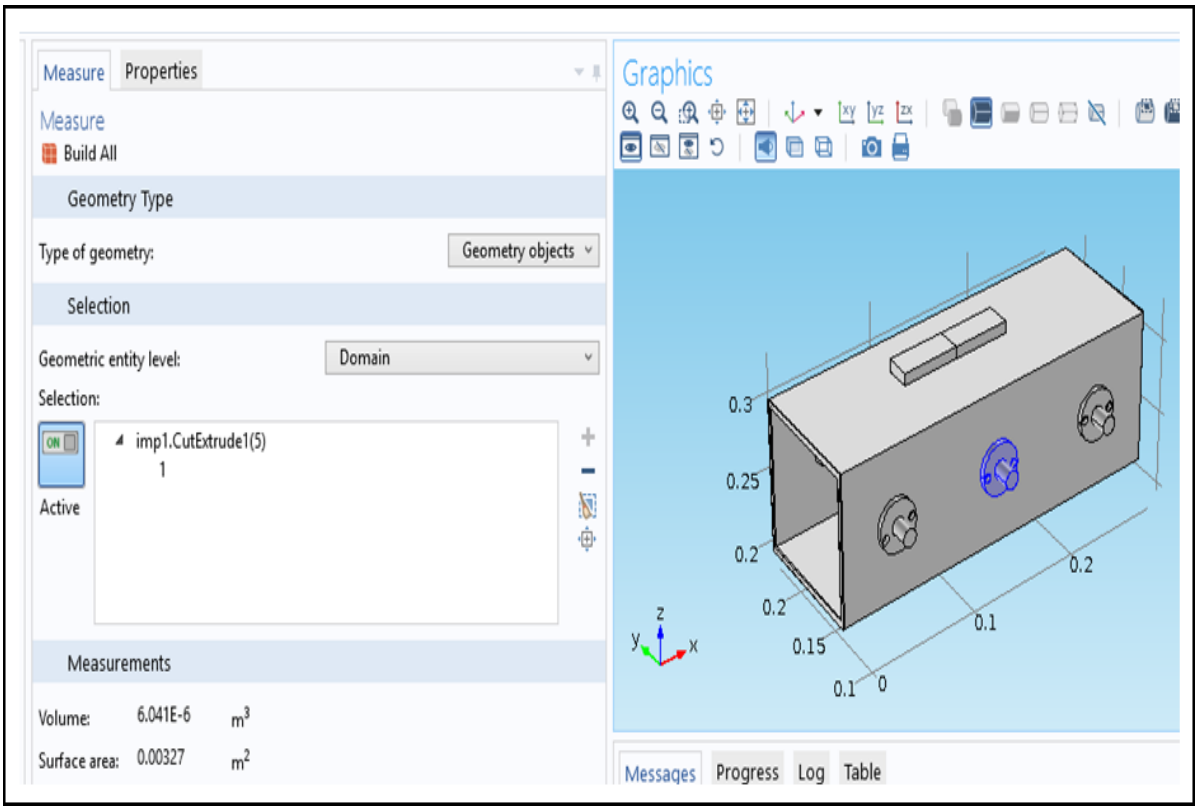

Figure C.1: The electrode surface area.

APPENDIX D: The measurement circuit and Labview NI-DAQ device

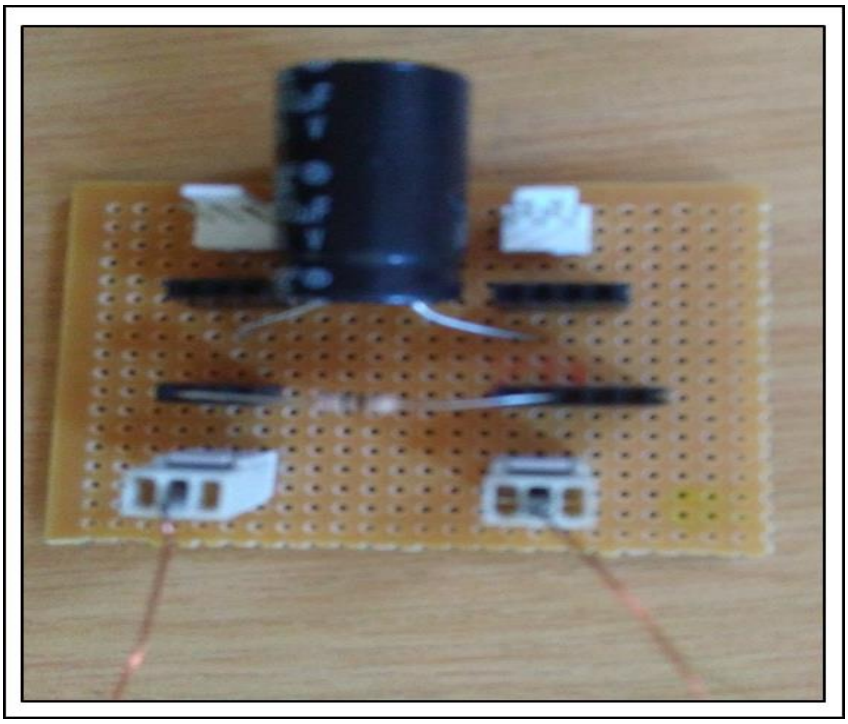

Figure D.1: Measurement circuit.

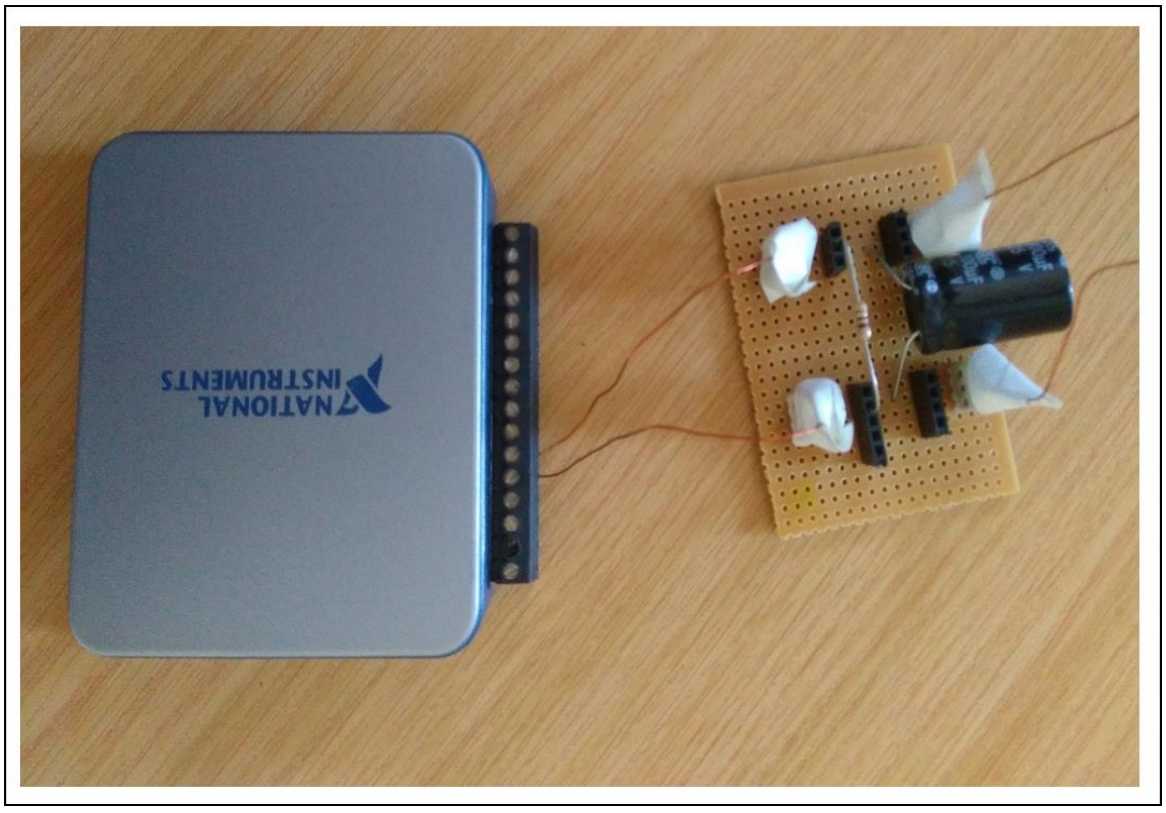

Figure D.2: Photos of the measurement circuit and Labview NI-DAQ device.

Figure D.3: Photos of the measurement circuit and Labview NI-DAQ device inside a plastic case.

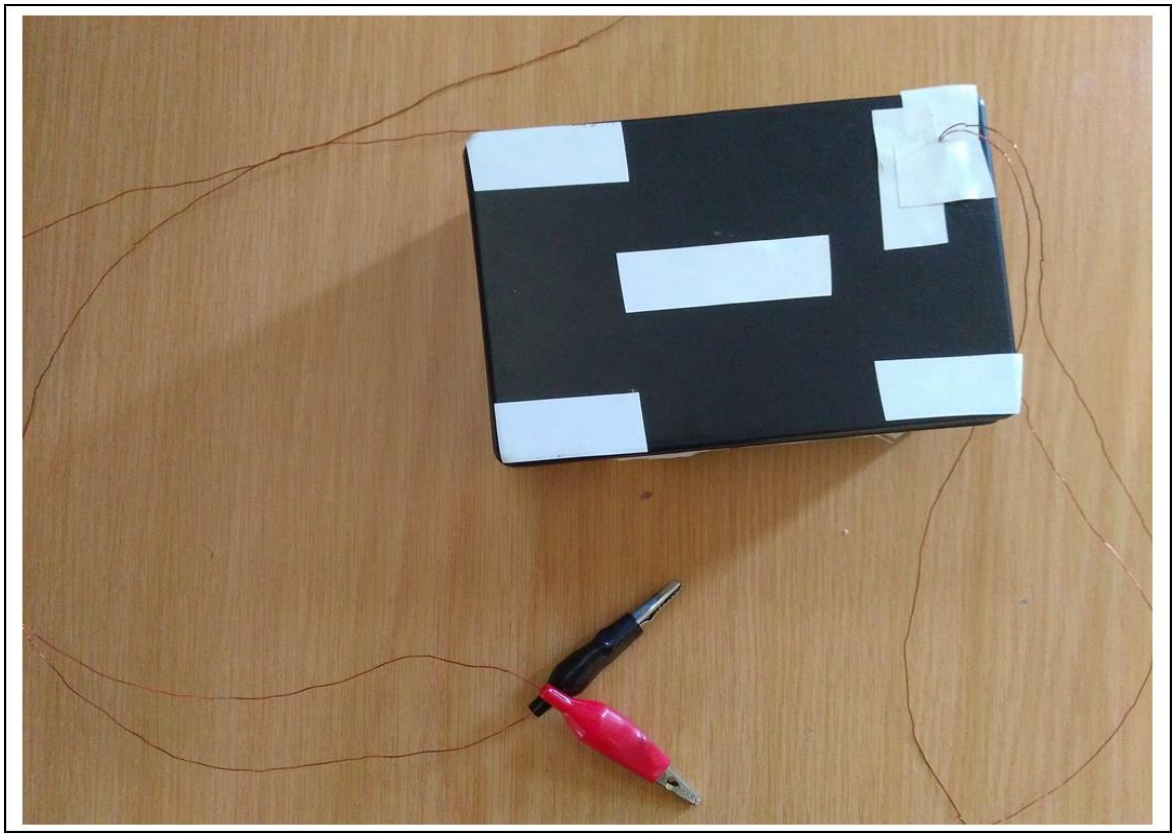

Figure D.4: Photos of a closed box containing the measurement circuit and Labview NI-DAQ device.

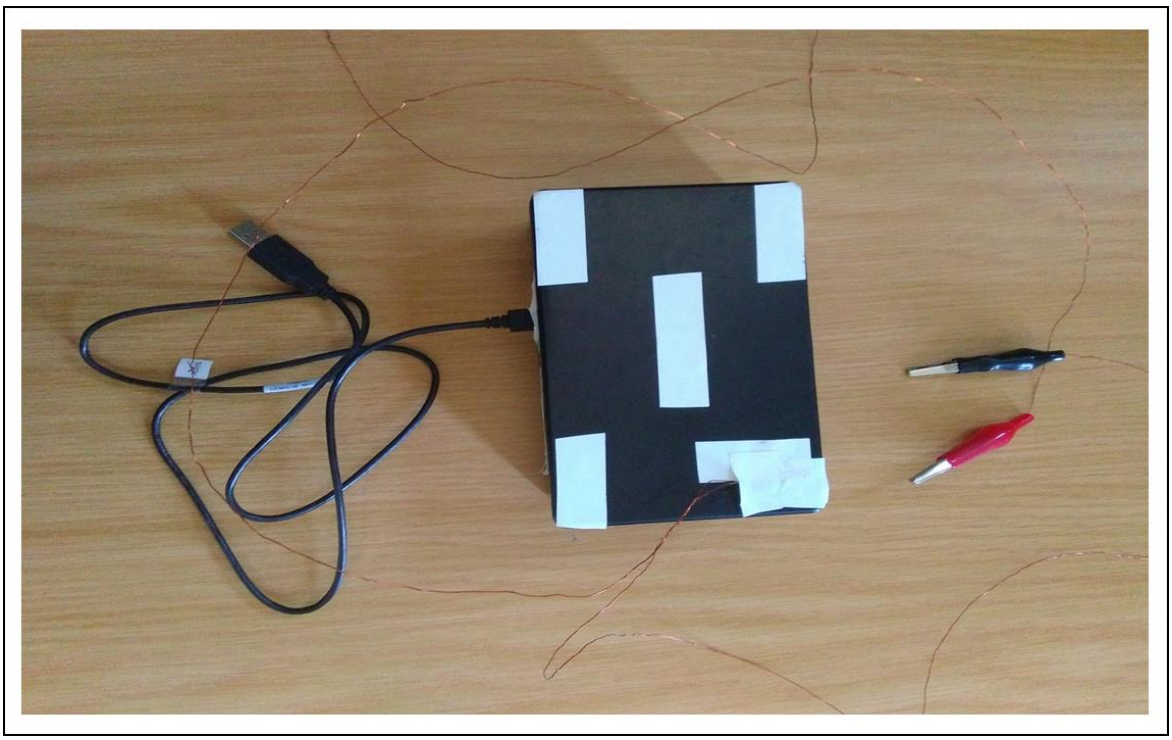

Figure D.5: Photos of a closed box containing the measurement circuit, USB cable, crocodile clips and Labview NI-DAQ device.

APPENDIX E: The DC arc plasma generating unit with MHD power generator prototype

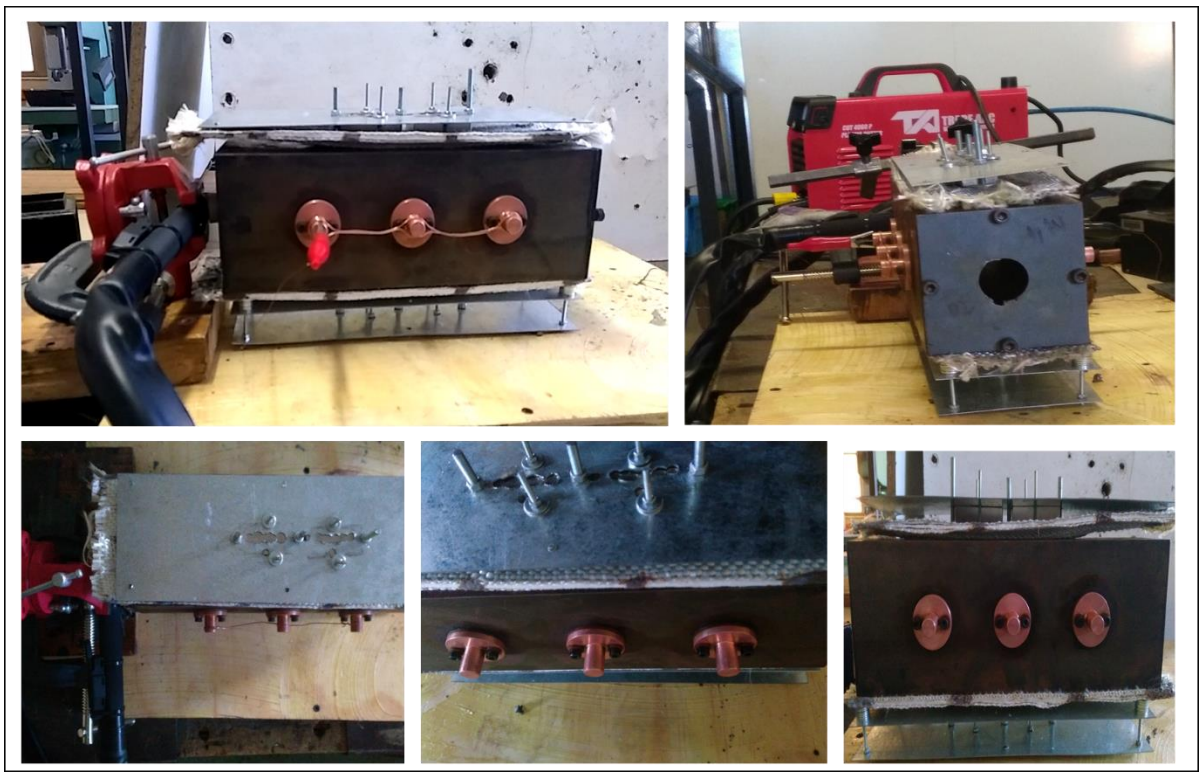

Figure E.1: Photos of the DC arc plasma generating unit with MHD power generation system.

Figure E.2: Photos of the MHD power generation system during the DC arc plasma experiment.

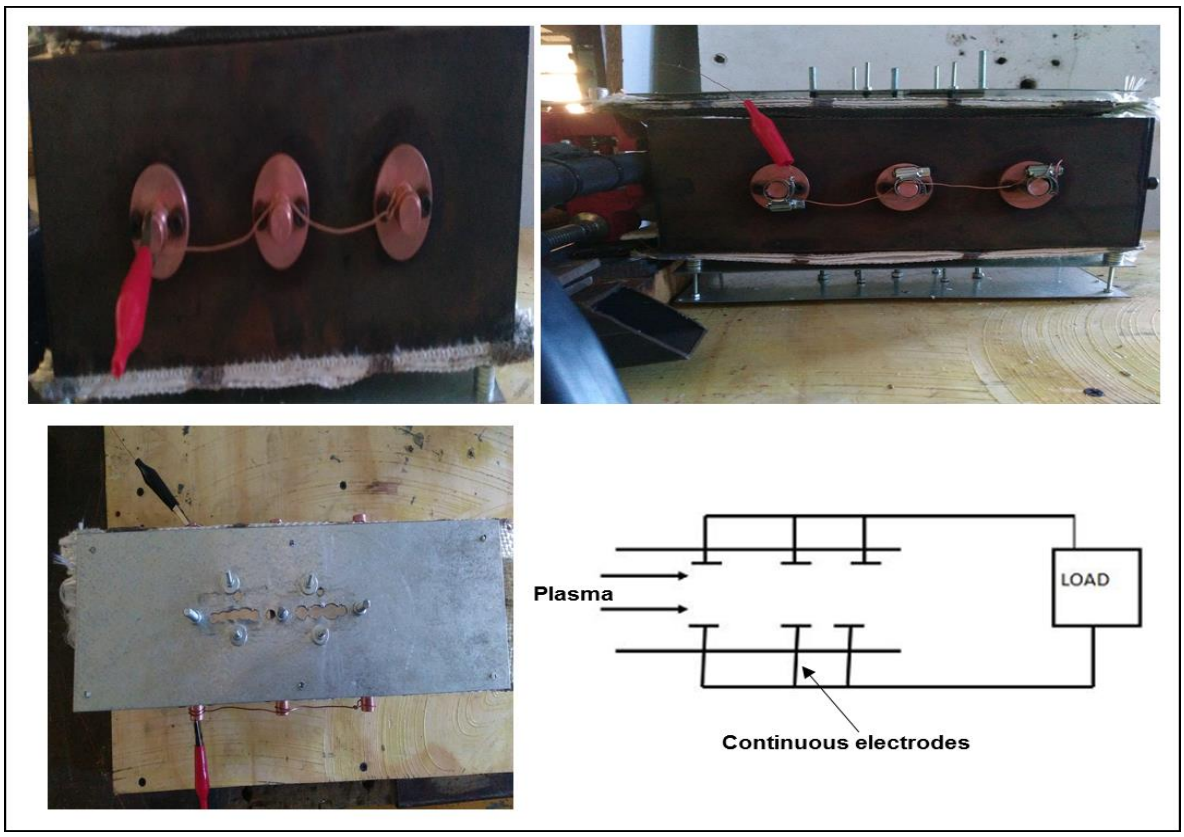

Figure E.3: Photos of the three electrodes connected in continuous mode.

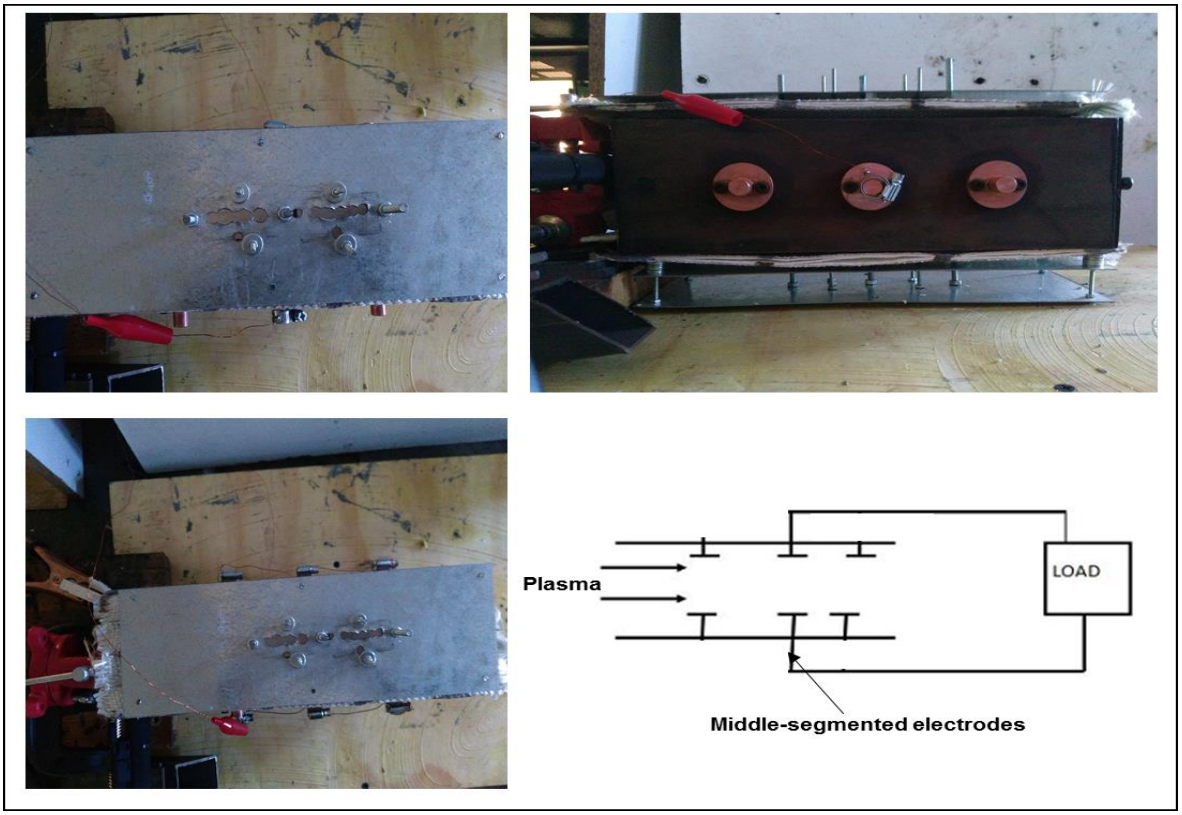

Figure E.4: Photos of the middle electrodes connected in segmented mode.

Figure E.5: Photo of the electrodes after cleaning.

Figure E.6: Photos illustrating the rectangular duct with plasma and the measured terminal voltage (3.7 mV) from a multimeter.

APPENDIX F: Survey of arc temperatures and electron densities (Boulos *et al*., 2013:11)

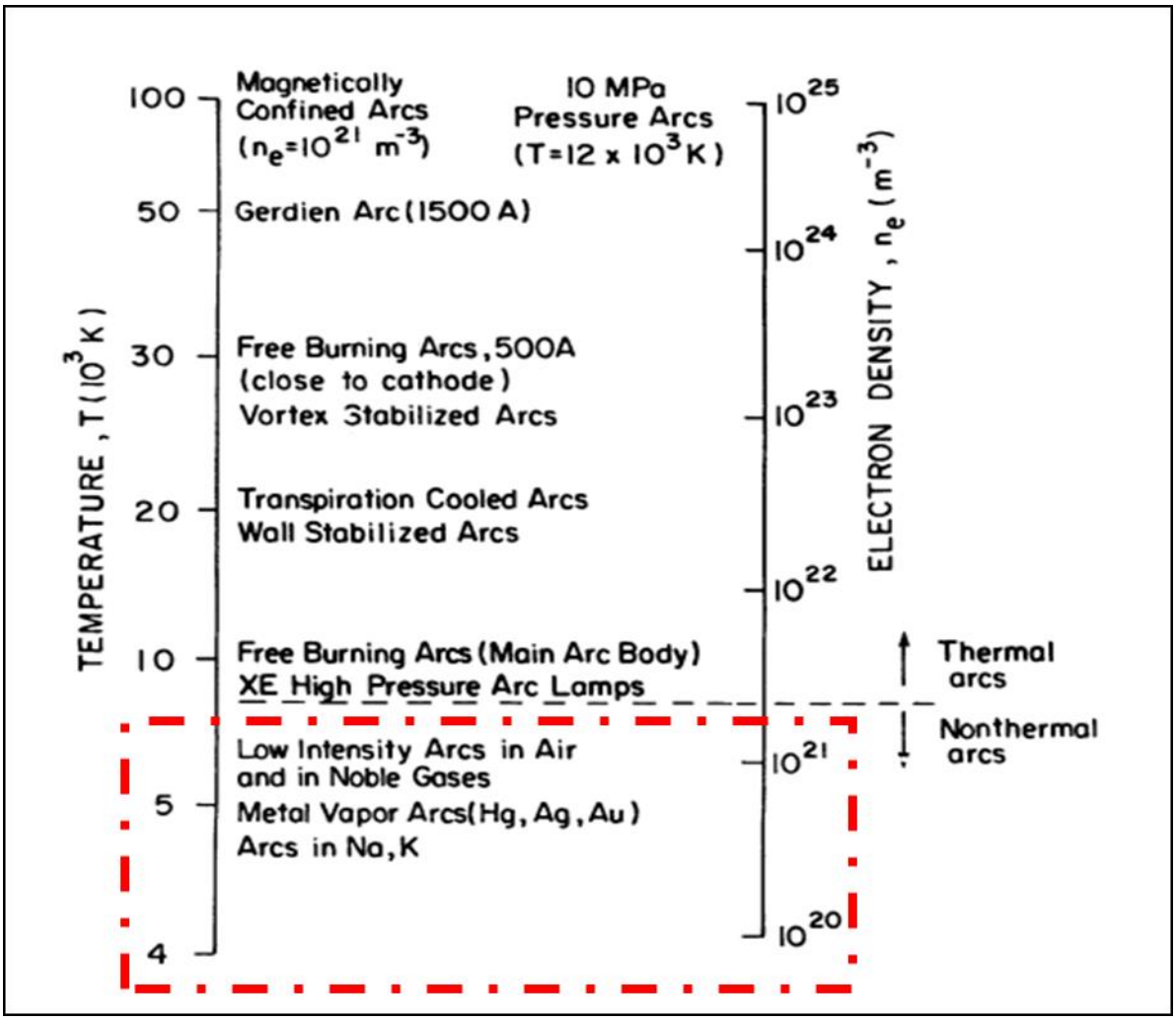

Figure F.1: Survey of arc temperatures and electron densities.